Frequency-Domain Modeling of Harmonic Interactions in Pulse-Width Modulated Voltage-Source Inverter Drives

Der Fakultät für Elektrotechnik und Informatik

der Gottfried Wilhelm Leibniz Universität Hannover

zur Erlangung des akademischen Grades

Doktor-Ingenieur

(abgekürzt: Dr.-Ing.)

genehmigte Dissertation

von

Dipl.-Ing. Malte John

geboren am 03.09.1988

in Emden

2019

1. Referent   Prof. Dr.-Ing. Axel Mertens
2. Referent   Prof. Dr.-Ing. Marco Liserre

Tag der Promotion: 14. März 2019

Vorwort

Diese Arbeit entstand im Rahmen meiner Tätigkeit als wissenschaftlicher Mitarbeiter am Institut für Antriebssysteme und Leistungselektronik (IAL) der Gottfried Wilhelm Leibniz Universität Hannover. An dieser Stelle möchte ich allen Menschen danken, die mich bei meiner Arbeit unterstützt haben.

An erster Stelle möchte ich Prof. Dr.-Ing. Axel Mertens danken. Sie haben mir bereits im Studium den Weg zum WEMPEC an der University of Wisconsin bereitet und sehr lehrreiche fünf Jahre am IAL ermöglicht. Die Zeit in Madison ist für mich persönlich zu einer ganz besonderen Erfahrung geworden.

Herrn Prof. Dr.-Ing. Marco Liserre danke ich für die Übernahme des Koreferats und das Interesse an meiner Arbeit.

Prof. Dr.-Ing. Bernd Ponick möchte ich für die Übernahme des Prüfungsvorsitzes und die gemeinsame Institutszeit danken.

Allen meinen Kollegen und Kolleginnen des Instituts danke ich für die tollen fünf gemeinsamen Jahre. Insbesondere möchte ich Clemens Larivière und Torsten Winkler danken, für die gemeinsame Zeit an unseren praktischen Versuchsaufbauten und die verbundenen amüsanten und erkenntnisreichen Unterhaltungen. Ein besonderer Dank geht an meine Kollegen Jakub Kucka, Stefan Lücke, Marc Dokus, Olga Korolova, Daniel Herwig und Jan Andresen, die mich mit Feedback und Diskussionen zu meiner Arbeit unterstützt haben.

Meiner Mutter Traute John und meinem Vater Wolfgang John danke ich dafür, dass sie mir stets den Rücken frei halten. Meine Frau Stephanie Sykes hat diese Arbeit stets mit mir getragen. Deine liebevolle Unterstützung hat den erfolgreichen Abschluss erst ermöglicht.

Kurzfassung

Die in dieser Arbeit vorgestellte Methodik ermöglicht die Berechnung der Strom- und Spannungsspektren eines Antriebssystems für den eingeschwungenen Zustand unter Berücksichtigung von Wechselwirkungen der Systemkomponenten. Die Darstellung der Signale mittels ihrer Fourier-Koeffizienten bildet die mathematische Grundlage. Die Beschreibung ihrer Systemverknüpfung erfolgt als algebraische Gleichungen, welche im Allgemeinen nichtlinear sind und die Verkopplung der spektralen Komponenten berücksichtigen. Dies ermöglicht die Beachtung der Interaktionen zwischen Wechselrichter, seiner Speisung und Last sowie seiner Regelung und Pulsdauermodulation. Dabei wird die Zeitkontinuität der physikalischen Größen, die Zeitdiskretisierung der Regelung und der entsprechende Umwandlungsprozess einbezogen. Damit trägt diese Arbeit zu einem tieferen Verständnis der Wechselwirkungen innerhalb eines Umrichtersystems bei und ermöglicht die Berechnung der entstehenden Spektren unter Berücksichtigung der Interaktionen, welche in gängigen Frequenzbereichsmodellen vernachlässigt werden.

Als Vereinfachung werden in dieser Arbeit die leistungselektronischen Komponenten als verlustfreie Schalter angenommen, welche diskret einen leitenden und einen sperrenden Zustand annehmen können. Die verwendeten Gleichungen gelten für hart geschaltete Umrichter mit fester Schaltfrequenz. Die Wechselsperrzeit kann für den gesteuerten Betrieb berücksichtigt werden. Diese bleibt allerdings für den geregelten Betrieb vernachlässigt.

Die Interaktion des Umrichtersystems mit einer elektrischen Maschine wird am Beispiel einer permanentmagneterregten Synchronmaschine gezeigt. Andere Maschinentypen werden in dieser Arbeit nicht betrachtet. Die Modellierung erfolgt im rotorfesten Koordinatensystem auf Grundlage der Hauptflussverkettung ohne Sättigung und berücksichtigt den Einfluss von oszillierenden Drehmomenten auf die spektrale Verteilung im gesamten Antriebssystem. Der Wechselrichter wird dabei im gesteuerten Betrieb betrachtet.

Die entwickelten Frequenzbereichsmodelle werden numerisch in Matlab ausgewertet und mit Ergebnissen aus Zeitbereichssimulationen in Simulink verglichen, welche auf den gleichen Annahmen beruhen. Vergleiche zeigen sehr geringe Unterschiede zwischen den Ergebnissen. Eine Validierung der zugrundeliegenden Annahmen erfolgt über den Vergleich mit Messergebnissen. Durch die Rechenleistung sind dem vorgestellten Verfahren, insbesondere bei der Wahl ungünstiger Verhältnisse von Grundfrequenz und Schaltfrequenz, in der numerischen Auswertung bei der Anzahl zu berücksichtigender Harmonische der Systemgröße Grenzen gesetzt.

Schlagworte: Frequenzbereichmodellierung – Oberschwingungs-Wechselwirkungen – pulsdauermodulierte Wechselrichter

Abstract

The method presented in this thesis allows for the calculation of the current and voltage spectra of a drive system for the steady state, while considering the influence of interactions between the system components. The signals are represented by their Fourier coefficients. Their relationships within the system are described by algebraic equations, which are generally nonlinear and they incorporate the coupling of the harmonic components. This ensures the consideration of interactions between the inverter, its feeding source and load, as well as its closed-loop control and pulse-width modulation. The models include the time-continuity of the physical quantities, the time-discretization of the control signals, and their respective conversion processes. As a result, this thesis provides a deeper understanding of the dependencies within a converter system and enables a calculation of the resulting spectra taking into account the aforementioned interactions, which are neglected in established frequency-domain models.

As a simplification, in this work the power electronic components are assumed to be lossless switches, which can conduct and block as discrete states. The equations presented apply to hard-switched converters with fixed switching frequencies. The effect of interlock times is considered in the models for open-loop control. However, it is neglected in the models for closed-loop control.

The interaction of the converter system with an electrical machine is presented for the example of a permanent-magnet synchronous machine. Other machine types are not analyzed in this work. The model is formulated in the rotor reference frame in accordance with the main spatial harmonic of the field components and considers the influence of oscillatory load torque on the spectra of the overall drive system. The inverter is assumed to be in open-loop control in this case.

The frequency-domain models developed in this work are numerically evaluated and they are compared with results from time-doamin simulations in Simulink, which are based on the same assumptions. Comparisons reveal very low differences between the results. A validation of the underlying assumptions is performed by comparison with measurement results. Due to constrains in computational power, especially in cases of unfavorable ratios of fundamental frequency and switching frequency, the presented method is limited in its numerical evaluation regarding the number of considered harmonics and the size of the system.

Keywords: frequency domain modeling – harmonic interactions – pulse-width modulated inverters

Contents

Abbreviations

ADC	analog-to-digital converter
AD-PWM	asymmetrical regularly-sampled double-edge PWM
AFE	active front end
CCM	continuous current mode
CTFT	continuous-time Fourier transform
DCM	discontinuous current mode
DFT	discrete Fourier transform
DPWM	discontinuous pulse-width modulation
DTFT	discrete-time Fourier transform
DUT	device under test
EMF	electromotive force
EMI	electromagnetic interference
ESR	equivalent series resistance
FFT	fast Fourier transform
FPGA	field-programmable gate array
IGBT	insulated-gate bipolar transistor
LE-PWM	leading-edge PWM
LTI	linear time-invariant
ND-PWM	naturally-sampled double-edge PWM
PI	proportional-integral
PLC	programmable logic controller
PLL	phase-locked loop
PMSM	permanent magnet synchronous machine
PWM	pulse-width modulation
SD-PWM	symmetrical regularly-sampled double-edge PWM
SRF-PLL	synchronous reference frame phase-locked loop
SVM	space vector modulation

TEC	two even crossover
TE-PWM	trailing-edge PWM
THD	total harmonic distortion
VSI	voltage source inverter
ZOH	zero-order hold

Nomenclature

Generic Variable Usage Conventions

a, A	constant or variable
$\bar{a}$	mean value
$\boldsymbol{a}$, $\boldsymbol{A}$	matrix
$\boldsymbol{A}^{\mathrm{T}}$	transpose
$x(t)$	continuous-time signal
$x_{\mathrm{s}}(t)$	discrete-time signal
$x[n]$	sampled signal
$\bar{x}(t)$	negated (binary) signal
$\langle x(t) \rangle_T$	moving average of $x(t)$ over the period T
$X(f)$, $X(\omega)$	continuous-time Fourier transform
$X_{\mathrm{s}}(f)$, $X_{\mathrm{s}}(\omega)$	discrete-time Fourier transform
$X[kf_0]$	discrete spectrum (Fourier series)
$X_{,k}$	complex Fourier coefficient of order k
$\hat{X}_{,k}$	magnitude of Fourier coefficient of order k
$\vec{X}$	column vector of complex Fourier coefficients
$\left[\vec{X}\right]_{,k}$	element k of vector $\underline{X}$
$\lvert \Delta X_{,k} \rvert$	difference of complex coefficients
$\Delta \lvert X_{,k} \rvert$	difference of magnitudes

Specific Variables Usage Definitions

$\boldsymbol{A}$	system matrix
$\boldsymbol{C}(\vec{X})$	convolution matrix of vector $\vec{X}$
C	capacitance
C_{ce}	collector-emitter capacitance
C_{gc}	gate-collector capacitance
C_{ge}	gate-emitter capacitance
C_{par}	parasitic capacitance
$C_{\mathrm{par(D)}}$	parasitic diode capacitance
d	duty cycle

e	error
$\boldsymbol{E}$	identity matrix
f	frequency
f_0	fundamental frequency
f_c	control frequency
f_s	sampling frequency
f_{sw}	switching frequency
g	gate signal
g_b	bottom gate signal
g_t	top gate signal
i	current
i_{ac}	ac-side current
i_c	collector current
i_D	diode current
i_{dc}	dc-side current
i_{dcp}	positive-dc-rail current
i_{dcn}	negative-dc-rail current
i_{dis}	disturbance current
i_g	gate current
i_L	inductor current
i_m	machine current
i_T	transistor current
J_m	machine inertia
J	Bessel function of the first kind
k	harmonic order
k_{max}	maximum harmonic order
K_{fr}	friction coefficient
K_P	proportional gain
L	inductance
L_{ac}	ac-side inductance
L_{dc}	dc-side inductance
$L_{par(D)}$	parasitic diode inductance
$L_{par(T)}$	parasitic transistor inductance
m	integer index
m_{max}	maximum value of integer index m
m_{fr}	friction torque
m_i	machine torque
m_l	load torque
M	modulation integer index
n	integer index
n_{max}	maximum value of index n
p	number of pole pairs
p	integer index
p_{max}	maximum value of integer index p
r_D	diode differential resistance

r_T	transistor differential resistance
R	resistance
R_g	gate resistance
R_s	stator resistance
s	switching function
s'	switching function considering interlock times
s''	switching function considering switching transients
$s'_\mathrm{d}, s'_\mathrm{q}$	switching function in dq considering a constant rotation frequency
$s''_\mathrm{d}, s''_\mathrm{q}$	switching function in dq considering a constant rotation frequency and offset angle
t	time
t_{01}	first current zero-crossing time
t_{02}	second current zero-crossing time
T	period
T_0	fundamental period
T_c	control period
T_d	interlock time (dead time)
$T_\mathrm{d(on)}$	turn-on delay time
$T_\mathrm{d(off)}$	turn-off delay time
T_fi	current fall time
T_fv	voltage fall time
T_I	integrator time constant
T_on	turn-on time
T_off	turn-off time
T_ri	current rise time
T_rv	voltage rise time
T_s	sampling period
T_sw	switching period
$\boldsymbol{T}_\mathrm{rot}$	rotation matrix
u	voltage
u_ac	ac-side voltage
u_ce	collector-emitter voltage
u'_ce	collector-auxiliary-emitter voltage
u_D0	diode threshold voltage
u_dc	dc-link voltage
u_dis	disturbance voltage
u_ge	gate-emitter voltage
u_m	machine voltage
u_ref	voltage reference
Δu	voltage error
u_T0	transistor threshold voltage
x_a	aperiodic signal
x_p	periodic signal
x_s	sampled signal
Y	admittance
Z	impedance

δ	Dirac delta function
ε_{c}	constant component of ε_{e}
ε_{e}	electrical rotor angle
ε_{m}	mechanical rotor angle
ε_{t}	time-dependent component of ε_{e}
ΔT	pulse width
θ	phase angle
θ_{iac}	phase angle of the ac-side current
θ_{uac}	phase angle of the ac-side voltage
θ_{uref}	phase angle of the voltage reference
ν	phase number
τ	pulse width
τ_{df}	delay of switching instant falling edge due to interlock time
τ_{dr}	delay of switching instant rising edge due to interlock time
τ_{f}	switching instant falling edge
τ_{r}	switching instant rising edge
ϕ	phase displacement between ac-side voltage and load current
ϕ'	phase displacement between voltage reference and load current
φ_0	reference potential
σ	unit step function
ψ	flux linkage
Ψ_{p}	flux linkage of permanent magnets
ω	radiant frequency
ω_0	fundamental radiant frequency
ω_{e}	electrical radiant frequency
ω_{m}	mechanical radiant frequency
ω_{s}	switching radiant frequency
$\vec{0}$	zero vector
$\mathbf{0}$	zero matrix

Indices

$1, 2, 3$	phase 1,2,3
ac	ac-side
d	d-axis
dc	dc-side
dis	disturbance
l	load
q	q-axis
s	discrete-time
sp	setpoint
α	α-axis
β	β-axis
ν	phase number

1 Introduction

The individual components of drive systems, such as the voltage source inverter (VSI), the passive components, the electrical machine, and the control (Figure 1.1), build closely coupled relationships, resulting in a nonlinear closed-loop system. The accurate assessment of current and voltage harmonics of drive systems is studied to achieve various design goals, for example determination of dc-link capacitor size and lifetime [1, 2], design of grid filters and compliance with grid codes [3], avoiding the excitation of resonances in grid applications [4] and mechanical shafts [5], design of active power filters [6, 7], and many more.

Generally, there are two approaches to evaluate the frequency behavior and the propagation of harmonics. In the first approach, the nonlinear differential equation system can be solved in the time domain by using numerical integration and applying a Fourier transform to the resulting waveforms. Nonlinear effects of the power electronic system can be relatively easily combined, but they can lead to long simulation times. Moreover, the transform is applied on sampled signals using the discrete Fourier transform (DFT) algorithm, which can lead to aliasing when the simulated signals contain a frequency behavior that is higher than half the sampling frequency. When the system contains components with very different time constants, e.g. the small time constant of power electronic switching and the large time constant of an electrical machine, the simulation of transients can become time-consuming. Because the transients cause frequency leakage in the spectrum, it is important to determine when the steady state is achieved, which can be challenging.

In the second approach, the equation system is transformed into the frequency domain providing an algebraic equation system. The formulation of the model is complex, but often provides useful insight into the behavior of the system. The frequency-domain equations can be evaluated more easily for the steady state, which is described by a Fourier series with a discrete spectrum in the form of Fourier coefficients. The exact models in the frequency domain have been developed for power electronic converters for individual aspects, effects, and devices. However, the interactions between the components are often neglected or linearized models are employed.

The goal of this thesis is to develop models that cover the harmonic interactions in a drive system. The models are derived in the frequency domain describing the signals with their Fourier coefficients. The drive system in Figure 1.1 is used in this thesis as a benchmark system. It comprises a three-phase two-level VSI with closed-loop control that drives a permanent magnet synchronous machine (PMSM). The VSI is fed by a diode rectifier, which is represented by its rectified current. The PMSM is loaded by a mechanical load torque. The control assures that
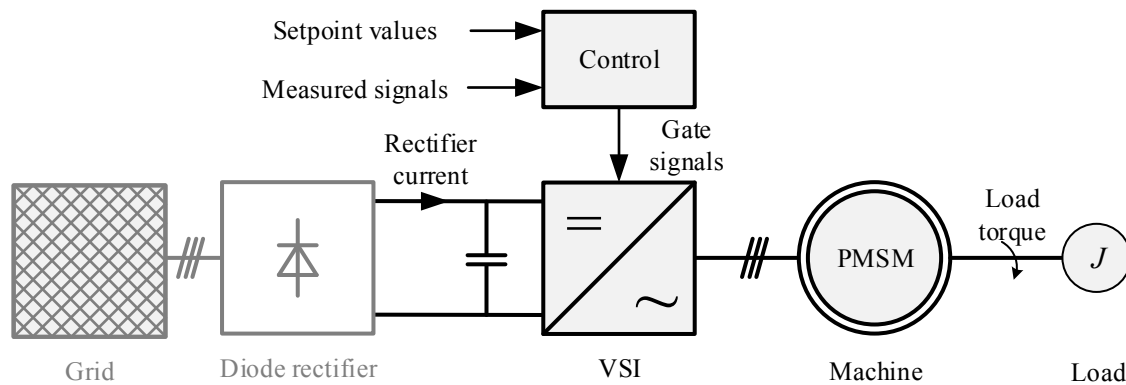
Figure 1.1: Topology of the drive system

the setpoint values are reached. For this, measured signals from the physical system are fed back to the control. The latter influences the system by adjusting the gate signals of the VSI. The following overview of the system provides an identification of the components and their interactions that need to be modeled.

System Overview

The interactions of the signals in the drive system are depicted as a block diagram in Figure 1.2, showing the individual blocks as sub-components that are modeled in the following chapters. The inputs of the system are the rectifier current, the load torque, and the setpoint values of the control. They are represented by red arrows. The black double arrows indicate bidirectional power exchange between the dc link, the VSI, and the PMSM. Because these components describe the behavior of a physical system, they are represented by continuous-time signals. There is an interaction between the dc link and the VSI, which is described by the dc-side signals. The interaction of the VSI and the PMSM is represented by the ac-side signals. The nonlinear behavior of the PMSM describing the interaction of the electrical domain with the mechanical domain and the choice of an appropriate coordinate system are further challenges in the modeling of the drive system.

A closed-loop control is implemented to comply with the demand indicated by the setpoint values. The required voltage and current values are measured by analog sensors and are sampled and held by an analog-to-digital converter (ADC). These unidirectional information signals are indicated by blue arrows. The control provides the required ac-side voltage of the VSI in the form of a duty cycle. Modulating the duty cycle using a pulse-width modulation (PWM) creates the control signals for the power electronic switches. Because the control and the PWM are implemented in a digital unit and the power stage forms an analog unit, both discrete and continuous time signals are present in the system. The following section reviews what kinds of modeling approaches are available in the literature to describe the individual subsystems and to point out the interactions that are not sufficiently covered.
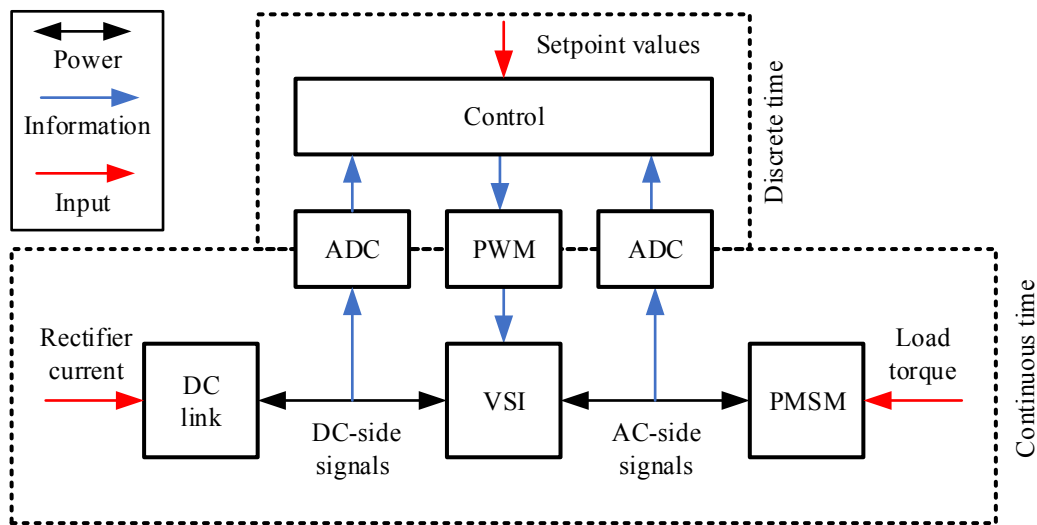
Figure 1.2: Interactions of the signals in the drive system

Frequency-domain Modeling in the Literature

For pulse-width modulated systems, the double Fourier series expression emerged as a standard method to describe the switching behavior of power electronic converters. The method applies for hard-switched converters using fixed switching frequency PWM methods. The double Fourier series approach was originally developed by Bennett [8] and Black [9] for application in communication systems. It was adapted to PWM converters by Bowes and Bird [10]. Further extended by Holmes [11], the method became a standard method to describe the output voltage of PWM VSI, summarized in the comprehensive book of Holmes and Lipo [12]. The results are presented as the ac-side voltage spectrum of the VSI, but in a more general sense the results represent the spectrum that correlates with the switching state of the power electronic components, which is called the switching function spectrum.

The double Fourier series analysis in its original form described by Bowes and Bird [10] and Holmes and Lipo [12] is based on simplifying assumptions:

1. A constant dc-link voltage, i.e. no interaction of dc side and ac side

2. A single frequency modulator input signal, i.e. no interaction with the control loop

3. Ideal switching of the power electronics, i.e. no dead time and lossless switches

For a variable dc-link voltage containing harmonic components, the ac-side voltage spectrum is determined by a convolution of the switching function spectrum and the dc-link voltage spectrum [13], representing the dc-to-ac conversion. McGrath *et al.* [2] showed that an ac-to-dc conversion can be represented similarly and the dc-link current spectrum can be calculated by a convolution of the switching function spectrum and the ac-side current spectrum.

In the last 15 years, adaptions of the double Fourier method and alternative methods were developed for the description of the PWM output spectrum [14], with special emphasis on the incorporation of modulator input signals that contain multiple frequency components [6, 15–17]. Moreover, analytical models were published that allow the incorporation of dead-time effects on the ac output voltage of VSI [18–22]. All these publications developed an input-to-output expression of the PWM block [Figure 1.2]. The interaction of the signals within the power stage of the plant and the influence of the feedback loop of a control system are not considered. Thus, the question arises of how to incorporate the interactions of a closed-loop system.

A wide-spread method of modeling and analyzing PWM converters is the averaging method that was introduced by Wester, Ćuk, and Middlebrook [23–25] for dc/dc-converter topologies and further described by Erickson and Maksimovic [26–29]. The formal mathematical procedure of averaging and linearization process is known as state-space averaging. The approach was adapted to ac/dc power converters by Hiti [30]. The method truncates the high frequency components that are generated by the switching behavior of the converter. Therefore, it requires that the low frequency components of the base band can be separated from the high frequency components of the switching band. This is often true when the switching frequency is much higher than the modulating frequency and aliasing effects are negligible.

The method can be used to develop linearized small-signal models and is often applied in impedance models and small-signal stability analysis [31]. The linearized models allow incorporation of the closed-loop control using linear control theory and use of standard controller design methods, e.g. for grid converters [32] and for drive systems [33]. Corradini *et al.* [34] applied this method to digital control of power converters, taking into account the small-signal delays of the digital controller and the regularly sampled PWM.

Nevertheless, the averaging method simplifies the switching process and is only valid up to approximately half the switching frequency. This can lead to over-simplification, when the switching-band and the base-band components overlap and when sampling effects, such as aliasing, are present. Moreover, no method was found during the literature review that covers the full interaction of the modulation and switching process with the controlled converter system.

The coupling of the power converter and an electrical machine in a drive system leads to a non-linear relationship and an interaction of harmonics between the electrical and the mechanical domain. This means that mechanical load faults can lead to torque oscillations that are propagated into the stator currents [35, 36] and harmonic components of the currents are propagated into the torque of the machine, which can lead to mechanical stress on the rotor shaft [5, 37]. This harmonic behavior is bidirectional and the full spectrum can be predicted when the system is regarded as a closed loop. Whereas Chang *et al.* [38] studied the harmonic interaction of a drive system including an induction machine based on the successive solution of the time-domain equations, there are few publications that model the simultaneous interaction in drive systems in the frequency domain. Arrillaga *et al.* [39] present a frequency-domain model of a synchronous machine, which is modeled in the rotor reference frame. However, the mechanical

speed is assumed to be constant and interactions with the mechanical system are neglected. The coupling of the drive and the electrical machine in one reference frame in the frequency domain, considering the oscillations that are present in the rotor position, has not yet been investigated.

In conclusion, a need for further research was identified that provides a method in the frequency domain covering harmonic interactions within a drive system. This includes the mutual dependencies between physical signals of the power stage as well as interactions with the control signals, introducing nonlinear effects, such as modulation, sampling, and aliasing. The intention is to extend the modeling depth of the steady-state frequency-domain models to that of typical electrical circuit simulator used for power electronic systems, such as *Plecs* and *Simscape*, treating the semiconductors as ideal switches, with a discrete on-state and a discrete off-states.

Overview of this Thesis

The goal of this thesis is to contribute to closing the identified gap in the research area of frequency-domain modeling considering nonlinear interactions. The literature review demonstrates that most approaches describe the drive system components in an input-to-output relationship, neglecting the bidirectional interactions. This thesis addresses the prediction of the harmonic spectrum in a drive system in the frequency domain, including the closed-loop interactions. This thesis seeks to provide a deeper understanding of the harmonic interactions and to develop a modeling approach that allows for calculation of the spectra.

The modeling approach and the general solution process are presented in Chapter 2. The method is adapted to a two-level VSI with open-loop control and linear load in Chapter 3. The questions of how the PWM influences the signals of the physical plant and how these signals interact with each other are addressed.

In Chapter 4 the incorporation of interlock times into the system model are studied. The question arises of how the modified switching behavior affects the signals in the system. The reaction of the plant and the mutual dependency of the signals of the plant and the switching behavior are analyzed.

Chapter 5 demonstrates how the harmonic interaction of the VSI, the PWM, and the plant is changed by application of feedback control. An analysis is conducted of how the solution process is changed by the presence of continuous-time and discrete-time signals and by their mutual dependencies in closed-loop control.

The modeling approach is extended in Chapter 6 to a drive system, by connection of a VSI and a PMSM. Because a standard machine model in the rotor reference frame is chosen, the influence of coordinate transformations on the modeling approach is examined. This chapter addresses the influence of oscillating load torques on the modeling process in the rotating reference frame.

The analytical results developed in this work are compared to results from time-domain simulations. Experimental results are included, obtained from measurements with a prototype converter system. Descriptions of the experimental setup and the measurement equipment are given in the appendix. The thesis is concluded and summarized in Chapter 7.

2 Modeling Approach

The goal of this chapter is to develop a mathematical framework to analyze the interaction of the signals within the drive system and its reaction to external disturbances. The system contains continuous-time signals that represent the quantities of the power level: voltages, currents, rotational speed, and torque. The signals that operate on the control system are discrete-time signals, such as the measured and sampled signals of the power level, the control setpoints, and the signals of the pulse-width modulation.

The first section reviews the frequency-domain representation of signals, starting with the Fourier series and the Fourier transform for continuous-time signals and its extension to discrete-time signals. Then, necessary approximations of the signal are introduced in order to provide the simultaneous numerical solution process presented afterwards. Finally, the validation process is described, which includes the comparison of results from the frequency-domain models with spectra obtained in time-domain simulations and measurements.

The modeling approach developed in this chapter is mainly based on the Fourier analysis and the theory of signal processing taken from the comprehensive books [40] and [41].

2.1 Frequency-Domain Representation of Signals

Continuous-Time Signals

A periodic time-domain signal $x(t)$ can be represented by a complex Fourier series

$$x(t) = \sum_{k=-\infty}^{\infty} X_{,k} \cdot \mathrm{e}^{\mathrm{j}k\omega_0 t}, \quad k \in \mathbb{Z}, \tag{2.1}$$

where $X_{,k} \in \mathbb{C}$ is the complex Fourier coefficient of order k that represents the k-th harmonic of the fundamental angular frequency $\omega_0 = 2\pi f_0$. The Fourier coefficients can be calculated by

$$X_{,k} = \frac{\omega_0}{2\pi} \cdot \int_0^{2\pi/\omega_0} x(t) \cdot \mathrm{e}^{-\mathrm{j}k\omega_0 t} \, \mathrm{d}t \tag{2.2}$$

The Fourier series assigns the periodical signal $x(t)$ to a discrete spectrum $X[kf_0]$, which is represented by the Fourier coefficients. The square brackets $[.]$ indicate that the spectrum is discrete. There are two alternative notations to (2.1), using either real coefficients $(A_{,k}, B_{,k})$ or trigonometric representation with magnitude and phase representation $(\hat{X}_{,k}, \theta_{x,k})$. The conversions between the notations are provided in Appendix A.

The Fourier transform allows the extension of the frequency representation to aperiodic signals $x(t)$, resulting in a continuous spectrum as a function of the frequency f, with

$$X(f) = \int_{-\infty}^{\infty} x(t) \cdot \mathrm{e}^{-\mathrm{j}2\pi ft} \, \mathrm{d}t. \tag{2.3}$$

An alternative notation is introduced, where the spectrum is given as a function of the angular frequency $\omega = 2\pi f$, with

$$X(\omega) = \int_{-\infty}^{\infty} x(t) \cdot \mathrm{e}^{-\mathrm{j}\omega t} \mathrm{d}t. \tag{2.4}$$

In order to distinguish the Fourier transform of a continuous signal from the Fourier transform of a discrete signal, the acronym continuous-time Fourier transform (CTFT) will be used when both types of signals are present.

There is a close relationship between the Fourier series and the Fourier transform, which is illustrated in the following example.

A rectangular pulse, defined by

$$\mathrm{rect}\left(\frac{t}{T}\right) = \begin{cases} 1 & \text{for} & -T/2 \leq t \leq T/2 \\ 0 & \text{otherwise} \end{cases}, \tag{2.5}$$

can be used to represent the status of a switch and with this be used to model the conducting state of a power electronic device, expressed by the switching function $s(t)$. The continuous spectrum for an aperiodic rectangular pulse $s_\mathrm{a}(t)$ with a pulse width of T is given by the si-function, with

$$s_\mathrm{a}(t) = \mathrm{rect}\left(\frac{t}{T}\right) \quad \circ\!\!-\!\!\bullet \quad S_\mathrm{a}(f) = T \cdot \mathrm{si}(\pi T f), \tag{2.6}$$

where $\mathrm{si}(\pi T f) = \sin(\pi T f)/(\pi T f), \pi T f \neq 0$; and $\mathrm{si}(0) = 1$.

Repeating the pulse with a period $T_0 = 1/f_0$ results in a periodic signal of rectangular pulses $s_\mathrm{p}(t)$. The repetition is represented in the time domain by a convolution (represented by the operator $*$) of the aperiodic signal with a sequence of Dirac-pulses δ:

$$s_\mathrm{p}(t) = s_\mathrm{a}(t) * \sum_{k=-\infty}^{\infty} \delta(t - kT_0), \quad k \in \mathbb{Z}. \tag{2.7}$$
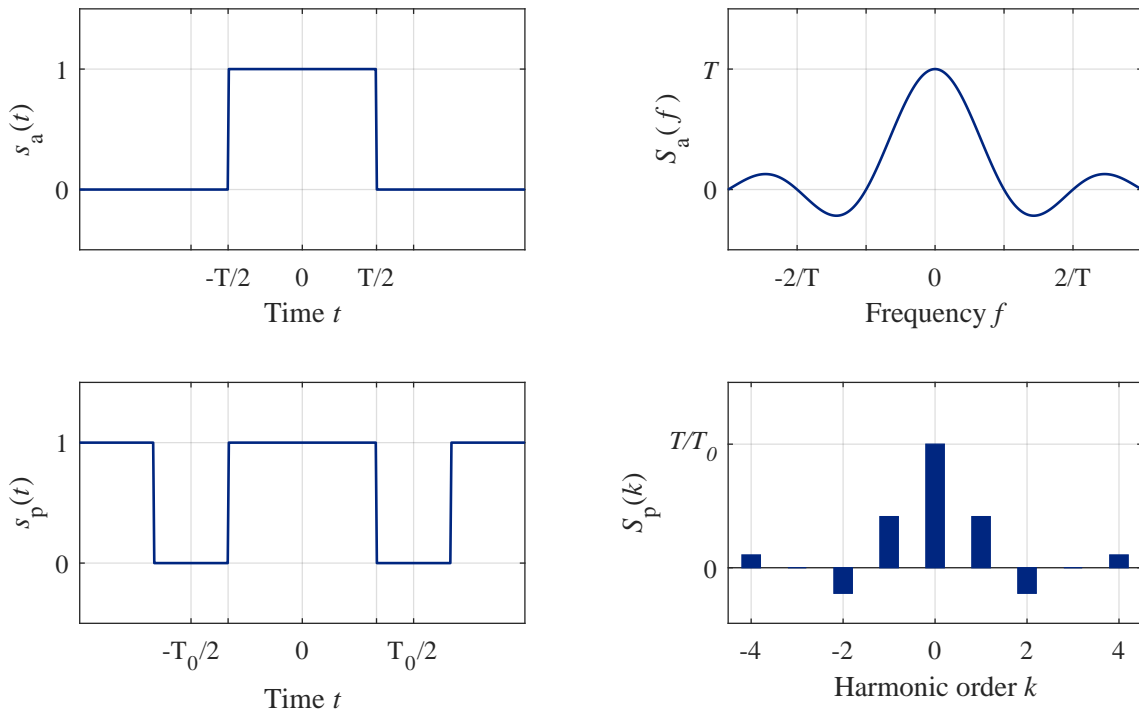
Figure 2.1: Top graph: Waveform of a rectangular pulse with a pulse width of T. Bottom graph: Periodic rectangular signal with a fundamental period of T_0 and a pulse width of $T = 2/3 \cdot T_0$.

Figure 2.2: Top graph: Continuous spectrum of the rectangular from Figure 2.1 top. Bottom graph: discrete spectrum of a periodic rectangular signal depicted in the bottom graph of Figure 2.1 bottom.

Figure 2.1 shows the waveform of the rectangular pulse in the top graph and the periodic pulse train with a pulse width of $T = 2/3 \cdot T_0$ in the bottom graph.

For the calculation of the Fourier transform of (2.7), the convolution theorem

$$x_1(t) * x_2(t) \quad \circ\!\!-\!\!\bullet \quad X_1(f) \cdot X_2(f) \tag{2.8}$$

can be utilized, where a time-domain convolution can be expressed as a multiplication of the spectra. With the Fourier transform of the sequence of Dirac pulses

$$\sum_{k=-\infty}^{\infty} \delta(t - kT_0) \quad \circ\!\!-\!\!\bullet \quad f_0 \cdot \sum_{k=-\infty}^{\infty} \delta(f - kf_0), \quad k \in \mathbb{Z}, \tag{2.9}$$

and the Fourier transform of the aperiodic signal $S_\mathrm{a}(f)$, the Fourier transform of the periodic signal results in a discrete spectrum

$$S_\mathrm{p}(f) = f_0 \cdot S_\mathrm{a}(f) \cdot \sum_{k=-\infty}^{\infty} \delta(f - kf_0) = f_0 \cdot \sum_{k=-\infty}^{\infty} S_\mathrm{a}[kf_0] \cdot \delta(f - kf_0). \tag{2.10}$$

The spectrum is sampled by the Dirac pulses and equals the discrete coefficients of the Fourier series representation $S_{\mathrm{p}}[kf_0]$ of the periodic signal, illustrating the relationship between Fourier series and Fourier transform. The resulting spectrum for the rectangular pulse is shown in Figure 2.2 in the top graph and the discrete spectrum for the periodic waveform is shown in the bottom graph.

Sampling of a continuous Fourier spectrum $X(f)$ is used in this thesis to transfer equations that are developed generally for aperiodic signals to the special case of signals in a periodic steady state, described by complex Fourier coefficients $X_{,k}$.

Discrete-Time Signals

Because the control and modulation of the power converters that are considered in this work are implemented in digital systems, a mixed analysis of continuous and discrete signals is performed. The sampling of a continuous signal $x(t)$ with a sampling period of T_{s} can be represented by multiplication with a sequence of Dirac-pulses, leading to a continuous-time representation of a sampled signal

$$x_{\mathrm{s}}(t) = x(t) \cdot \sum_{n=-\infty}^{\infty} \delta(t - nT_{\mathrm{s}}) = \sum_{n=-\infty}^{\infty} x[nT_{\mathrm{s}}] \cdot \delta(t - nT_{\mathrm{s}}), \quad n \in \mathbb{Z}. \tag{2.11}$$

$x[nT_{\mathrm{s}}]$ is a discrete-time signal sampled at nT_{s}. The application of the Fourier transform in (2.3) to the sampled signal, with

$$X_{\mathrm{s}}(f) = \sum_{n=-\infty}^{\infty} \int_{-\infty}^{\infty} x(t) \cdot \delta(t - nT_{\mathrm{s}}) \cdot \mathrm{e}^{-\mathrm{j}2\pi f nT_{\mathrm{s}}} \, \mathrm{d}t \tag{2.12}$$

$$= \sum_{n=-\infty}^{\infty} x[nT_{\mathrm{s}}] \cdot \mathrm{e}^{-\mathrm{j}2\pi f nT_{\mathrm{s}}}, \tag{2.13}$$

is known as discrete-time Fourier transform (DTFT) and provides a continuous spectrum, which is periodic with the sampling frequency $f_{\mathrm{s}} = 1/T_{\mathrm{s}}$. If the continuous signal $x(t)$ is periodic, the sampled signal is periodic as well. Thus, the spectrum is discrete and can be represented by Fourier coefficients. It should be noted that the fundamental frequency of the discrete-time signal is the greatest common divisor of the sampling frequency and the fundamental frequency of the continuous-time signal $x(t)$. The DTFT has a close relationship with the z-transform, which provides a frequency representation of the sampled signal, with

$$X_{\mathrm{s}}(z) = \sum_{n=-\infty}^{\infty} x[nT_{\mathrm{s}}] \cdot z^{-n}. \tag{2.14}$$

The complex variable z is defined as $z = r \cdot \mathrm{e}^{\mathrm{j}2\pi fT_{\mathrm{s}}}$. For a radius of $r = 1$ the z-transform becomes the DTFT.

Using the analogon of the convolution theorem in (2.8), with

$$x(t) \cdot y(t) \quad \circ\!\!-\!\!\bullet \quad X(f) * Y(f), \tag{2.15}$$

the time-domain multiplication of the continuous signal with a sequence of Dirac pulses in (2.11) can also be expressed as a frequency-domain convolution of the spectrum $X(f)$ with the Fourier transform of the sequence

$$\sum_{n=-\infty}^{\infty} \delta(t - nT_s) \quad \circ\!\!-\!\!\bullet \quad f_s \cdot \sum_{n=-\infty}^{\infty} \delta(f - nf_s), \tag{2.16}$$

resulting in

$$X_s(f) = f_s \cdot X(f) * \sum_{n=-\infty}^{\infty} \delta(f - nf_s). \tag{2.17}$$

With this expression, a frequency-domain consideration of the sampling process is possible and can also be applied to the discrete spectrum of the Fourier coefficients, with

$$X_s[kf_0] = f_s \cdot X[kf_0] * \sum_{n=-\infty}^{\infty} \delta[kf_0 - nf_s], \quad n, k \in \mathbb{Z} \tag{2.18}$$

where f_s is an integer multiple of the fundamental frequency f_0.

In order to illustrate the relationship of the spectrum of a continuous-time and discrete-time signals, Figure 2.3 shows the waveforms of three continuous signals and their sampled equivalent.

1) The top graph shows a continuous signal

$$x_1 = \cos(\omega_0 t) + 0.1 \cdot \cos(5 \cdot \omega_0 t + \pi/7). \tag{2.19}$$

as a solid line. The sampled signal has a sampling frequency of $f_s = 20 \cdot f_0$ and is marked as crosses. Figure 2.4 shows the amplitude of the discrete spectrum for the continuous signal as bars and for the sampled signal as crosses. All frequency components $X_{p1}(kf_0) \neq 0$ have a frequency smaller than the Nyquist frequency of $f_s/2$ and according to the sampling theorem they are correctly represented by the sampled signal. The periodicity of the spectrum with $\pm n \cdot f_s, n \in \mathbb{Z}$ is clearly visible.

2) For a second continuous signal

$$x_2 = x_1 + 0.2 \cdot \cos(16 \cdot \omega_0 t) \tag{2.20}$$

the sampling theorem is not fulfilled as the additional component has a frequency $16 \cdot f_0 > f_s/2$, which leads to aliasing (see middle graphs in Figure 2.3 and Figure 2.4). All frequency components of the periodic signal $X_{p2}(kf_0)$ are present in the spectrum of the sampled signal $X_{s2}(kf_0)$. However, the components with a frequency higher than $f_s/2$ are reflected into the
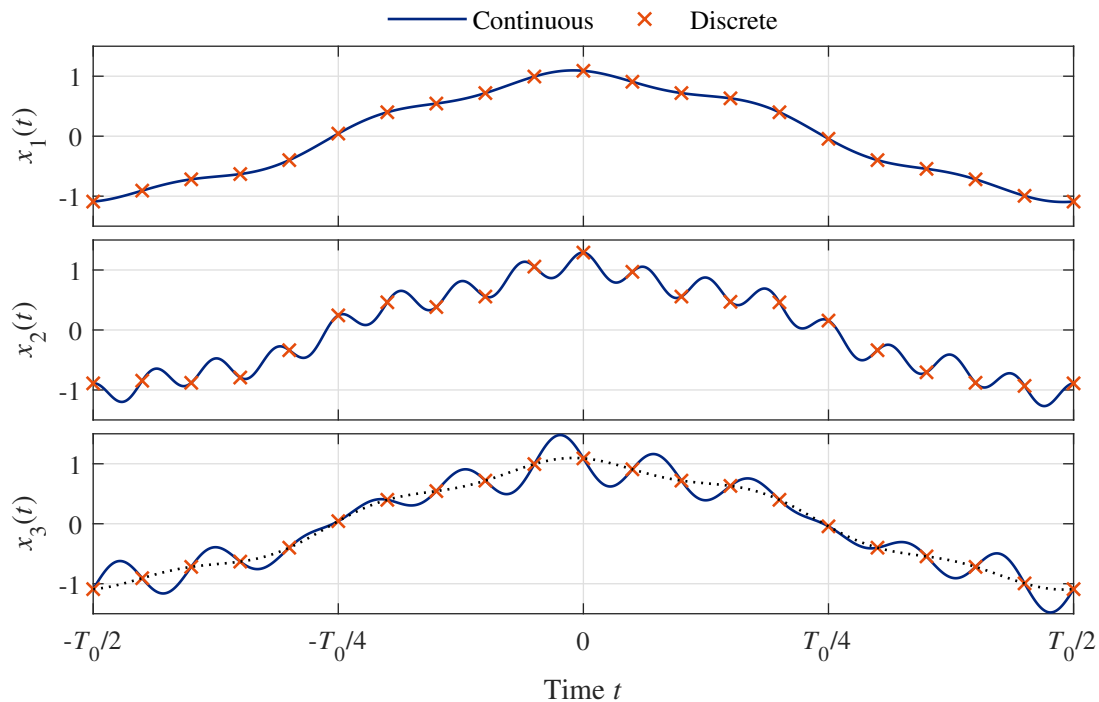
Figure 2.3: Time-domain waveform of continuous-time signals and their sampled equivalents: signal x_1 fulfilling the sampling theorem (top graph), signal x_2 violating the sampling theorem (middle graph), modulated signal x_3, where the sampled values of x_3 are equal to the sampled values of x_1, indicated with a dotted line (bottom graph).
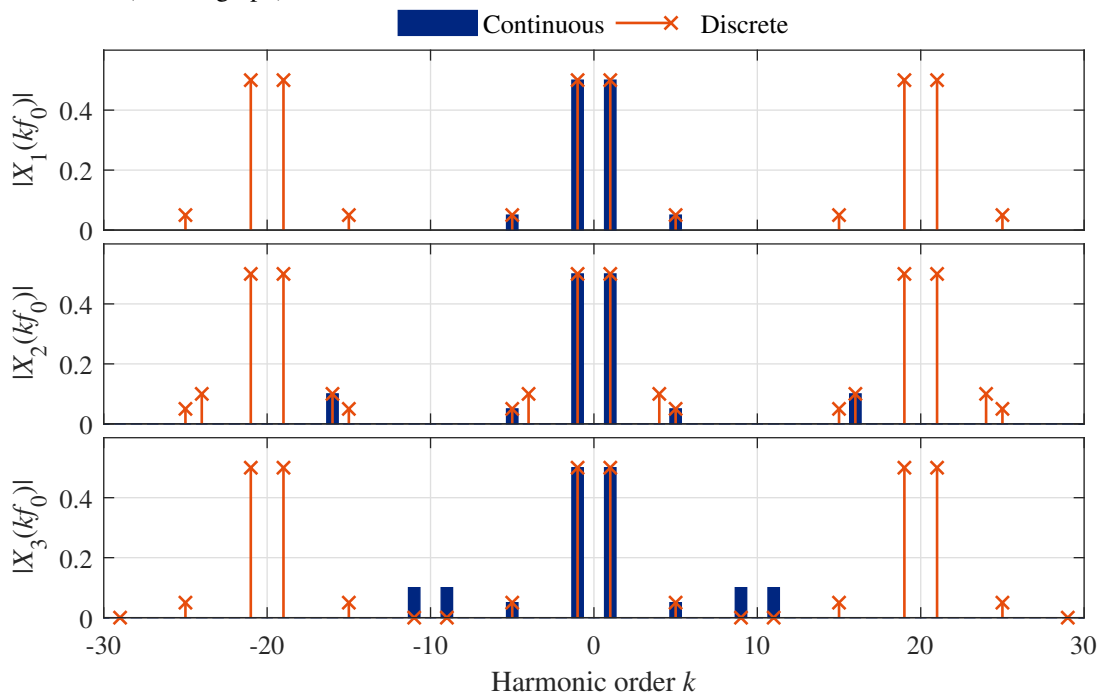

Figure 2.4: Amplitude spectra of the continuous-time signals and their sampled equivalents depicted in Figure 2.3. The spectra of the sampled signals are periodic with the sampling frequency of $f_s = 20 \cdot f_0$. Top graph: Compliance with the sampling theorem results in a correct representation of the spectrum within the sampling frequency interval. Middle graph: violation of the sampling theorem results in aliasing. Bottom graph: The symmetry of the high frequency components around half the sampling frequency results in cancellation in the spectrum of the sampled signal (aliasing occurs, but its effect is desired).

base band. This results in low-frequency components of $\pm(f_{\mathrm{s}} - 16\,f_0)$ that are not present in the spectrum of the continuous signal.

3) Aliasing can be avoided for frequency components that are synchronized with the sampling frequency. If a continuous signal x_3 contains frequency components modulated at half the sampling frequency, with

$$x_3 = x_1 + 0.2 \cdot \cos\left(\omega_0 t + \left(\frac{\omega_{\mathrm{s}}}{2} \cdot t + \frac{\pi}{2}\right)\right) + 0.2 \cdot \cos\left(\omega_0 t - \left(\frac{\omega_{\mathrm{s}}}{2} \cdot t + \frac{\pi}{2}\right)\right), \quad (2.21)$$

the sampling points shown in the bottom graph of Figure 2.3 concur with the crossings of the signal x_3 (solid line) and the signal without amplitude modulation x_1 (dotted line). In other words, the sampling occurs during the zero crossing of the high-frequency component. Therefore, this component is not present in the spectrum of the sampled signal shown in the bottom graph of Figure 2.4. In the frequency domain this can be explained by the aliasing effect that maps the frequency components $(\omega_{\mathrm{s}}/2 + \omega_0)$ to $(\omega_{\mathrm{s}}/2 - \omega_0)$ and vice versa. Complete cancellation results, because these components are symmetrical and of equal amplitude. This fact is used in the feedback control of PWM power converters, where the modulation leads to high-frequency components in the measured signals that are above the Nyquist frequency. These components are not visible in the measured signals when the sampling is synchronized to the center of the PWM pulses [42].

2.2 Numerical Approximation of the Spectrum

From (2.18) in the previous section, we can conclude that the spectra of periodic continuous-time signals and of periodic discrete-time signals can be described by the coefficients of a Fourier series. This includes the sampling process that describes the relationship between the continuous and discrete signals. When considering periodic signals that are not band-limited, the Fourier series contains an infinite number of coefficients. In order to evaluate the interaction of the signals numerically, an approximation of the Fourier series with a limited number of coefficients is required.

The solution of nonlinear time-domain problems is often accomplished by a numerical integration of the differential equations (for continuous systems) or the difference equations (for discrete systems). In order to evaluate the spectral content of the acquired discrete-time signals, a numerical approximation of the Fourier transform can be performed, called DFT. The result is a discrete spectrum

$$X_{\mathrm{s}}(k) = \sum_{n=0}^{N-1} x_{\mathrm{s}}[n] \cdot \mathrm{e}^{-\mathrm{j}k2\pi n/N}, \quad k = 0, ..., N-1, \quad (2.22)$$

which is periodic with the sampling period and therefore approximates the signal up to the

Nyquist frequency of $f_\mathrm{s}/2$ with a limited number of spectral lines. The DFT algorithm requires an evenly sampled sequence $x_\mathrm{s}(n)$ that is an approximation of the continuous signal $x(t)$. If $x(t)$ contains frequencies higher than the Nyquist frequency, the sampling leads to aliasing and the base-band spectrum contains false information, as shown in the previous section.

In order to avoid aliasing, the signals can be described analytically in the frequency domain and a numerical evaluation of the analytical equations provides the approximation of the spectra. All continuous signals considered in this work are finite power signals, that is

$$\frac{1}{T} \cdot \int_T |x(t)|^2 \mathrm{d}t < \infty. \tag{2.23}$$

For finite power signals, the Fourier series converges

$$\sum_{k=-\infty}^{\infty} |X_{,k}|^2 < \infty, \tag{2.24}$$

meaning that the power in the harmonics of high order is negligible [40] and the power of the signal P can be approximated by a Fourier series with a finite number of harmonics k_max, with

$$P = \sum_{k=-\infty}^{\infty} |X_{,k}|^2 \approx \sum_{k=-k_\mathrm{max}}^{k_\mathrm{max}} |X_{,k}|^2. \tag{2.25}$$

However, the deviation $e(t)$ of an approximation $x_\mathrm{app}(t)$ of the signal $x(t)$ with

$$e(t) = x_\mathrm{app}(t) - x(t), \tag{2.26}$$

and

$$x_\mathrm{app}(t) = \sum_{k=-k_\mathrm{max}}^{k_\mathrm{max}} X_{,k} \cdot \mathrm{e}^{\mathrm{j}k\omega_0 t}, \tag{2.27}$$

can have significant errors in points of discontinuities of $x(t)$ that remain even for large numbers of k_max, which is known as the Gibbs phenomenon. Because the evaluation of the developed equation systems in this work is performed on the spectra in a limited frequency band rather than on the reconstruction of the signal in the time domain, (2.27) provides an acceptable approximation. Furthermore, the summation in (2.27) is exact for a band-limited signal, if the maximum frequency in the signal is smaller than $k_\mathrm{max} \cdot f_0$.

This can be demonstrated for a rectangular pulse pattern with a 50 % pulse width and zero average value, which is represented by a Fourier series

$$\mathrm{rect}(t) = \sum_{k=-\infty}^{\infty} \frac{1}{T_0} \cdot \mathrm{si}(k\pi/2), \tag{2.28}$$

with an infinite number of coefficients. Thus, the DFT of the sampled signal contains aliasing.
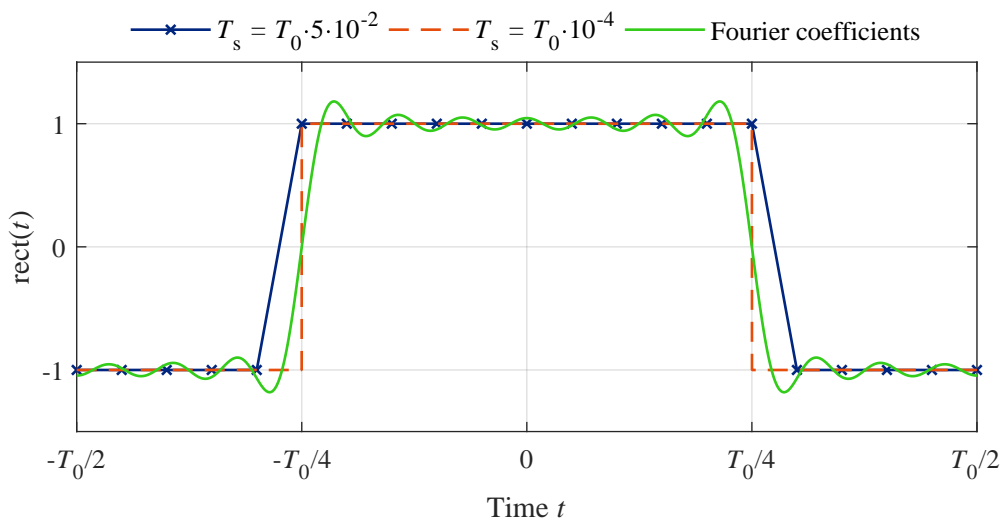
Figure 2.5: Representation of a rectangular pulse. Use of a low number of sampling points (blue crosses) results in a trapezoidal form and a high number of sampling points (dashed orange line) appears in a good representation of the rectangular shape. Using a finite Fourier series representation with $k_{\max} = 15$ reveals significant errors in the points of discontinuities (green solid line).
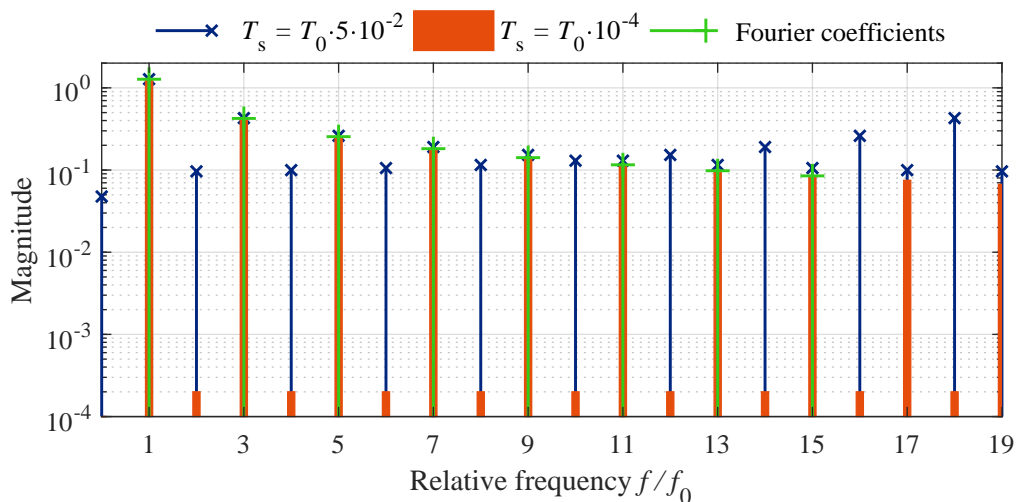

Figure 2.6: DFT of a rectangular pulse described with a low number of sampling points (blue crosses), a high number of sampling points (orange bars) and the coefficients of a Fourier series representation with a maximum order of $k_{\max} = 15$ (green pluses).

Because the rectangular pulse is a finite power signal, the influence of aliasing decreases with higher sampling frequencies. Therefore, the spectral analysis of signals with discontinuities requires very high sampling frequencies, as illustrated by the example in Figure 2.5. The rectangular pulse is plotted for a large sampling period of $T_{\mathrm{s}} = 5 \cdot T_0 \cdot 10^{-2}$ as a solid line with crosses for the sampling points, and for a small sampling period of $T_{\mathrm{s}} = T_0 \cdot 10^{-4}$ as a dashed line. The spectrum obtained by DFT is shown in Figure 2.6 and shows a strong influence of aliasing when using large sampling periods. For a small sampling period, aliasing is reduced to small amplitudes. By contrast, evaluating the coefficients of the Fourier series in (2.28) predicts

the coefficients exactly up to the maximum order k_{max} that the evaluation was performed for. In Figure 2.6 the maximum order is chosen as $k_{\mathrm{max}} = 15$ and the evaluation of the Fourier series is included in Figure 2.5 as a solid line, illustrating the Gibbs phenomenon.

2.3 Simultaneous Solution of the Equation System

The converter systems that will be analyzed in the next chapters contain a number of N unknown signals. The goal is to represent all relationships of the signals in the frequency domain and simultaneously solve the resulting equation system. Two important relationships will be presented in the following section: linear time-invariant (LTI) systems and the frequency-domain convolution.

LTI Systems

The relationship between an input signal $u(t)$ and an output signal $x(t)$ in an LTI system is given as the convolution of the input signal with the impulse response of the system $h(t)$, with

$$x(t) = h(t) * u(t) = \int_{-\infty}^{\infty} h(t - \tau) \cdot u(t) \, \mathrm{d}\tau. \tag{2.29}$$

In the frequency domain this can be expressed by a multiplication of the spectrum of the input signal $X(f)$ with the transfer function of the system $H(f)$, with

$$X(f) = H(f) \cdot U(f). \tag{2.30}$$

If the input signal is periodic and is approximated by a finite Fourier series using (2.27) with a limited number of k_{max} harmonics, the complex Fourier coefficients can be collected in a vector representation

$$\vec{U} = [U_{,-k_{\mathrm{max}}}, .., U_{,-1}, U_{,0}, U_{,1}, .., U_{,k_{\mathrm{max}}}]^{\mathrm{T}} \tag{2.31}$$

with a length of $l = 2\,k_{\mathrm{max}} + 1$. The output of the LTI system results in a Fourier series with the same number of harmonics and the relationship can be written as

$$\vec{X} = \boldsymbol{H} \cdot \vec{U}, \tag{2.32}$$

where the LTI system is represented by a diagonal matrix

$$\boldsymbol{H} = \mathrm{diag}(H_{,-k_{\mathrm{max}}}, .., H_{,-k_{\mathrm{max}}}), \tag{2.33}$$

with the element of harmonic order k

$$H_{,k} = H[kf_0]. \tag{2.34}$$

The output results in a vector of complex Fourier coefficients of the length l, with

$$\vec{X} = [X_{,-k_{\max}}, .., X_{,-1}, X_{,0}, X_{,1}, .., X_{,k_{\max}}]^{\mathrm{T}}. \tag{2.35}$$

Convolution

The multiplication of two time-domain signals $u_1(t)$ and $u_2(t)$ corresponds to a convolution of the spectra in the frequency domain, with

$$x(t) = u_1(t) \cdot u_2(t) \quad \circ\!\!-\!\!\bullet \quad X(f) = U_1(f) * U_2(f). \tag{2.36}$$

If the time-domain signals are periodic, the convolution can be expressed as a summation of shifted products of the discrete spectra

$$X[kf_0] = U_1[kf_0] * U_2[kf_0] = \sum_{m=-\infty}^{\infty} U_1[mf_0] \cdot U_2[(k-m)f_0], \tag{2.37}$$

which is known as linear discrete convolution. For a finite number of harmonics the convolution can be written in a vector representation of the Fourier coefficients, where the convolution output for the harmonic coefficient of order k results in:

$$X_{,k} = \left[\vec{U}_1 * \vec{U}_2\right]_{,k} = \sum_{m=-k_{\max}}^{k_{\max}} U_{1,m} \cdot U_{2,(k-m)}, \quad k - m \geq -k_{\max} \wedge k - m \leq k_{\max}. \tag{2.38}$$

The convolution can then be rearranged into a matrix multiplication

$$\vec{X} = \vec{U}_1 * \vec{U}_2 = \boldsymbol{C}(\vec{U}_1) \cdot \vec{U}_2. \tag{2.39}$$

The complete output of the convolution is a vector $\vec{X}$ of the size $(2\,l - 1)$. Because all signals in this work are limited to the length l, the evaluation of (2.38) will be limited to $k \in \{-k_{\max}, ..., k_{\max}\}$. This truncated form of the linear discrete convolution[1] uses a square convo-

---

[1]This form corresponds to the *Matlab* function *conv* when applying the option *same*.

lution matrix $C(\vec{U}_1)$ of the vector $\vec{U}_1$ that has a size of $l \times l$, with

$$
C(\vec{U}_1) = \begin{bmatrix} U_{1,0} & \cdots & U_{1,-k_{\max}} & & & & \\ U_{1,1} & \cdots & U_{1,(1-k_{\max})} & U_{1,-k_{\max}} & & & \\ \vdots & & \vdots & & \vdots & & \\ U_{1,k_{\max}} & & & \cdots & & & U_{1,-k_{\max}} \\ & & \vdots & & \vdots & & \vdots \\ & & U_{1,k_{\max}} & U_{1,(k_{\max}-1)} & \cdots & & U_{1,-1} \\ & & & U_{1,k_{\max}} & \cdots & & U_{1,0} \end{bmatrix}. \qquad (2.40)
$$

As an example, the time-domain multiplication of two waveforms $u_1(t)$ and $u_2(t)$ is depicted in Figure 2.7. The first graph shows a typical PWM signal as it would result from a modulation index $M = 0.8$, a switching frequency of $f_s = 1000\,\mathrm{Hz}$, and a fundamental frequency of $50\,\mathrm{Hz}$. The second signal has a direct component of 1 superimposed by a high-frequency signal with an amplitude of 0.1 and a frequency of $1050\,\mathrm{Hz}$. The third graph shows the multiplication of the two signals.

The spectra of the signals are shown in Figure 2.8. The spectrum of the first signal is given in the first graph, showing the typical sideband components around multiples of f_s. PWM spectra are analyzed in detail in Chapter 3. The blue lines illustrate the band-limited spectrum with $k_{\max} = 2500\,\mathrm{Hz}/50\,\mathrm{Hz} = 50$ and the red lines represent the full spectrum. The frequency-domain convolution of $\vec{U}_1 * \vec{U}_2$ with the spectrum of the second signal is shown in the third graph for the full convolution matrix. A comparison of the blue lines of the band-limited spectrum with the red lines of the full spectrum reveals that there are deviations not only for the harmonic components above $k_{\max}$, but also for components of the second sideband group around $2000\,\mathrm{Hz}$. This is explained by the convolution of the frequency-components of the third sideband group around $3000\,\mathrm{Hz}$ and the high-frequency component in u_2 at $1050\,\mathrm{Hz}$, which is neglected when using the band-limited spectra. The fourth graph shows the result when using the square convolution matrix as it is given by (2.40).

Inverse Convolution

The inverse convolution, also known as deconvolution, is used in signal processing and image processing to recover the original signal that was filtered by a convolution with a kernel [43]. In order to reverse the process given by (2.36), a time-domain division is performed, which corresponds with an inverse convolution in the frequency domain, with

$$
u_2(t) = \frac{x(t)}{u_1(t)} \quad \circ\!\!-\!\!\bullet \quad U_2(f) = U_1^{-1}(f) * X(f). \qquad (2.41)
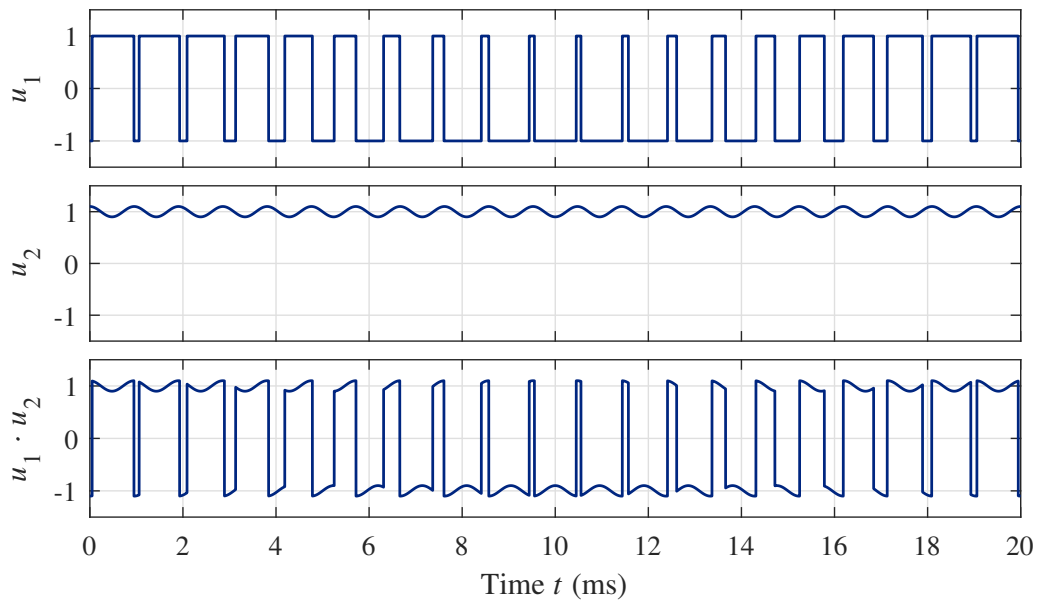$$

Figure 2.7: Time-domain multiplication of a PWM output signal (first graph) with a signal containing a large direct component and smaller high-frequency component (second graph).
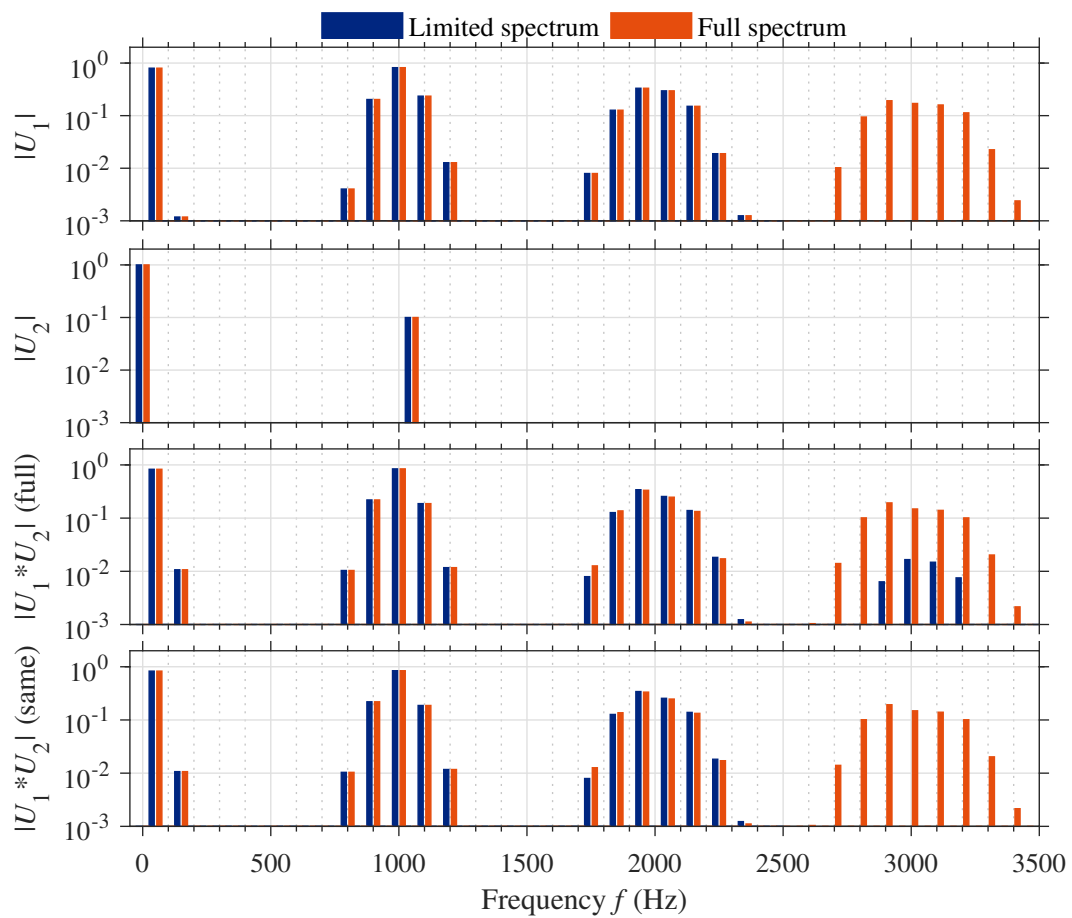

Figure 2.8: Frequency-domain convolution of the spectra of the waveforms in Figure 2.7.

As requirements, the signal $u_1(t)$ must never be zero and $1/u_1(t)$ must be a signal of slow growth [44]. When assuming discrete spectra, an inversion of (2.39) can be performed, with

$$\vec{U}_2 = \boldsymbol{C}^{-1}(\vec{U}_1) \cdot \vec{X}. \tag{2.42}$$

In order to calculate the inverse of the square convolution matrix, it is required that $\boldsymbol{C}(\vec{U}_1)$ is a regular matrix with $\det\left(\boldsymbol{C}(\vec{U}_1)\right) \neq 0$.

Linear Equation System

The N unknown signals of a converter system, represented by the vectors $\vec{X}_n, n \in \{1, 2, ..., N\}$ with vector size l, form a feedback system, where all signals can interact with each other. These relationships are described by a set of N l-dimensional equations $\vec{f}_n : \mathbb{C}^l \to \mathbb{C}^l, n \in \{1, 2, ..., N\}$, as illustrated in Figure 2.9. The input signals, represented by the vectors $\vec{U}_m, m \in \{1, 2, ..., M\}$, are independent of the system signals.
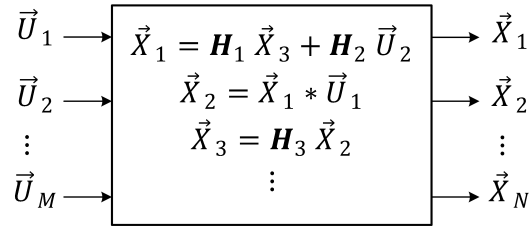

Figure 2.9: Example representation of an linear feedback system with nonreactive input vectors $\vec{U}_1...\vec{U}_M$, output vectors $\vec{X}_1...\vec{X}_N$, and linear transfer functions $\boldsymbol{H}_1...\boldsymbol{H}_3$.

If the relationships of all unknown signals are linear, the system description results in a linear equation system

$$\underbrace{\begin{bmatrix} \boldsymbol{A}_{11} & \dots & \boldsymbol{A}_{1N} \\ \vdots & \dots & \vdots \\ \boldsymbol{A}_{N1} & \dots & \boldsymbol{A}_{NN} \end{bmatrix}}_{\boldsymbol{A}} \cdot \underbrace{\begin{bmatrix} \vec{X}_1 \\ \vdots \\ \vec{X}_N \end{bmatrix}}_{\vec{X}} = \underbrace{\begin{bmatrix} \vec{B}_1 \\ \vdots \\ \vec{B}_N \end{bmatrix}}_{\vec{B}}, \tag{2.43}$$

where $\boldsymbol{A}$ is the coefficient matrix of the dimension $(N \cdot l \times N \cdot l)$, which can be divided into N^2 submatrices $\boldsymbol{A}_{mn}, m, n \in \{1, 2, ..., N\}$ of the size $(l \times l)$. The vector $\vec{X}$ collects all unknown signals and has a length of $N \cdot l$. All input signals are collected in the vector $\vec{B}$, which has a length of $(N \cdot l)$. In the case of a frequency-domain convolution with the harmonics of an unknown signal, the coefficients of the input signal are present in the coefficient matrix.

As an example, an equation system with two input vectors $\vec{U}_1$ and $\vec{U}_2$ and two unknown vectors

$\vec{U}_1$ and $\vec{U}_2$ is given by

$$\begin{cases} \vec{X}_1 * \vec{U}_1 - \vec{X}_2 = \vec{0} \\ \vec{X}_1 + \vec{X}_2 = \vec{U}_2 \end{cases}, \tag{2.44}$$

where $\vec{0}$ is a zero vector of length l. The system contains a convolution of unknown vector $\vec{X}_1$ and input vector $\vec{U}_1$. The equation system can be represented as a linear matrix expression by

$$\underbrace{\begin{bmatrix} \boldsymbol{C}(\vec{U}_1) & -\boldsymbol{E} \\ \boldsymbol{E} & \boldsymbol{E} \end{bmatrix}}_{\boldsymbol{A}} \cdot \underbrace{\begin{bmatrix} \vec{X}_1 \\ \vec{X}_2 \end{bmatrix}}_{\vec{X}} = \underbrace{\begin{bmatrix} \vec{0} \\ \vec{U}_2 \end{bmatrix}}_{\vec{B}}, \tag{2.45}$$

where $\boldsymbol{E}$ denotes the identity matrix. The convolution is represented by the convolution matrix of the input vector $\boldsymbol{C}(\vec{U}_1)$, which is included in the system matrix.

The solution of the equation system requires an inversion of the system matrix, with

$$\vec{X} = \boldsymbol{A}^{-1} \cdot \vec{B}. \tag{2.46}$$

In this thesis, the solution is performed numerically in Matlab using the matrix left divide (`mldivide`) function. The function allows Matlab to choose an appropriate solver depending on the shape and the sparsity of the matrix. A system containing a convolution of two unknown vectors, e.g. $\vec{X}_1 * \vec{X}_2$, is nonlinear and requires a nonlinear solution method.

Nonlinear Equation System

If the overall equation system is nonlinear, a numerical algorithm is required to find the roots of the equation system

$$\begin{cases} \vec{f}_1(\vec{X}_1, ... \vec{X}_N, \vec{U}_1, ... \vec{U}_M) = \vec{0} \\ \quad\quad\quad \vdots \\ \vec{f}_N(\vec{X}_1, ... \vec{X}_N, \vec{U}_1, ... \vec{U}_M) = \vec{0} \end{cases} \tag{2.47}$$

The iterative solution process requires initial values $\vec{X}_{n0}$ for all vectors.

In Chapter 3 a frequency-domain model for a VSI with open-loop control is developed that results in a linear equation system of the form presented in (2.43). When considering closed-loop control in Chapter 5, the simultaneous solution of the resulting nonlinear equation system is required. The initial values of the solution process are calculated in a reduced model that only considers the fundamental frequency component. This approach also applies to the incorporation of nonlinear loads, as shown in Chapter 6 for a drive system with a PMSM.

2.4 Validation Process

The results from the frequency-domain models are compared to results from time-domain simulations and measurement results. In the case of the frequency-domain models, the spectra of the signal X are directly available in the form of complex vectors $\vec{X}_{\text{FD}}$. By contrast, the results of the time-domain simulations and the measurement results are in the form of sampled time-domain values. A fast Fourier transform (FFT) is applied in both cases to calculate the complex spectra in vector representation.

The numerical results of the complex spectra are plotted in the following chapters in their magnitude representation [Appendix A], with

$$\hat{X}_{,k} = 2 \cdot \sqrt{\Re\{X_{,k}\}^2 + \Im\{X_{,k}\}^2} = 2 \cdot |X_{,k}|, \quad k \in \mathbb{N}. \tag{2.48}$$

For a good comparability of a wide range of magnitudes, a logarithmic scale is chosen. Because differences between the results from different models appear smaller in a logarithmic scale than in a linear scale, the differences of the spectra are calculated as an additional comparison tool. There are two definitions of differences that will be used in this thesis. The difference of the complex spectra will be used to compare the spectra of the frequency-domain model $\vec{X}^{\text{FD}}$ and the time-domain model $\vec{X}^{\text{TD}}$. This will be denoted as

$$|\Delta X_{,k}| := \begin{cases} 2 \cdot |X_{,k}^{\text{FD}} - X_{,k}^{\text{TD}}|, & k \neq 0 \\ |X_{,0}^{\text{FD}} - X_{,0}^{\text{TD}}| \end{cases}. \tag{2.49}$$

This method allows to display differences in the models, even when magnitudes are similar. Differences that result from differences in the angle information are indicated in this method.

For a comparison of the results from the frequency-domain models with the spectra of measurement results $\vec{X}^{\text{meas}}$ a second method is utilized. The difference of the magnitude spectra

$$\Delta|X_{,k}| := \begin{cases} 2 \cdot ||\vec{X}_{,k}^{\text{FD}}| - |\vec{X}_{,k}^{\text{meas}}||, & k \neq 0 \\ ||\vec{X}_{,0}^{\text{FD}}| - |\vec{X}_{,0}^{\text{meas}}|| \end{cases}. \tag{2.50}$$

allows to compare the spectra while neglecting differences in the angle information. Although a full validation of the spectra is only possible when considering the complex spectra, this method allows to validate the accuracy of the calculated magnitudes of the frequency-domain model.

A comparison of the angles of the spectra is not used in this thesis, because large differences in the angle information can occur, while the magnitudes of these spectral lines are low. This can lead to misinterpretation. Differences in the angle information are sufficiently covered by the difference of complex spectra $|\Delta\vec{X}|$.

3 VSI with Open-Loop Control

A VSI connects a voltage-stiff[1] dc link to a number of ac phases using semiconductor switches. The single-phase full-bridge VSI depicted in Figure 3.1 is formed by four individually controlled insulated-gate bipolar transistors (IGBTs) with anti-parallel diodes. The converter can be clustered into two half bridges, each of which consist of a top and a bottom transistor-diode pair. Similarly, the three-phase half-bridge VSI depicted in Figure 3.2 consists of three half bridges. The transistors are controlled by their gate signals, which are represented here by a binary signal $g_{t\nu}$ for the top transistor of phase ν and $g_{b\nu}$ for the bottom transistor of phase ν.

The half bridge is the fundamental building block of the VSI and connects a current-stiff[2] ac phase to the dc link. The dc-link capacitor C_{dc} acts as the dc-voltage source and provides two voltage-stiff nodes with a voltage of $u_{dc}/2$ and $-u_{dc}/2$ in reference to the midpoint potential φ_0. By turning the top transistor on and the bottom transistor off, the positive node is connected to the output. By inverting the two gate signals, the negative node can be coupled with the phase output. This results in a positive-voltage and a negative-voltage switching state, respectively. The analytical model for the half bridge as the fundamental building block is developed in Section 3.1 and is used to describe the single-phase VSI and the three-phase VSI.

The ac-side phases of the VSI are connected to a load comprising an inductance, which introduces a low-pass filter. By quickly alternating between the two switching states, the low-pass filtered output voltage is defined by the ratio of the switching intervals. This ratio is called duty

---

[1]A stiff voltage is provided by a capacitive energy storage.
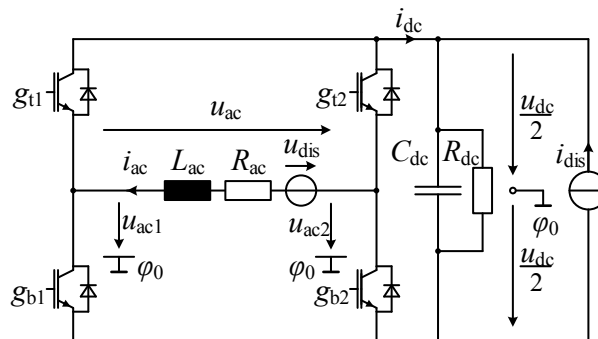[2]An inductive energy storage yields a stiff current.

Figure 3.1: Equivalent circuit of a single-phase full-bridge VSI. It consists of two individually controlled half bridges. The output voltage is the difference of the ac-side voltages of the two half bridges.
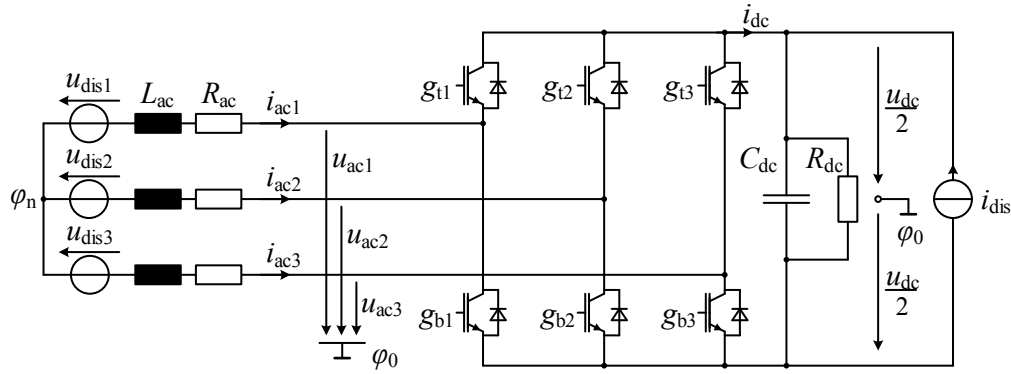
Figure 3.2: Equivalent circuit of a three-phase two-level VSI comprising half bridges

cycle and has approximately a linear relationship with the low-pass filtered output voltage. The generation of the gate signals, representing a low-frequency behavior linear to the duty cycle, is determined in the PWM process, which is analyzed in Section 3.2.

While the PWM process defines the energy conversion between the ac side and the dc side, the two sides form subsystems themselves. As shown in Figure 3.1 and Figure 3.2, these commonly consist of linear components (inductance, capacitor, resistor) and are influenced by disturbance voltages and disturbance currents. The frequency-domain models for these subsystems are developed in Section 3.3 and result in linear transfer functions.

Modeling the VSI with its load and its feeding source as a closed-loop system that describes the interaction of the ac-side signals with the dc-side signals and their reaction to the disturbances in the frequency domain concludes in the simultaneous solution of all equations collected in one equation system. In Section 3.4 the equation system is formulated and numerically solved for the single-phase VSI and the three-phase VSI and validated by time-domain simulations and experimental results.

3.1 Model of One VSI Phase Leg

The model of one half bridge with the phase leg number ν, with $\nu \in \{1, 2\}$ for a single-phase full-bridge inverter and $\nu \in \{1, 2, 3\}$ for a three-phase inverter, is developed on the equivalent circuit shown in Figure 3.3 a. The switching state of the IGBTs is defined by the binary gate signals $g_{\mathrm{t}\nu}(t) \in \{0, 1\}$ and $g_{\mathrm{b}\nu}(t) \in \{0, 1\}$ for the top and bottom IGBT, respectively, and the transistors are switched complementarily with negated gate signals $g_{\mathrm{t}\nu}(t) = \bar{g}_{\mathrm{b}\nu}(t)$. Assuming complementary switching behavior, each phase leg can be replaced by a single-pole double-throw switch (Figure 3.3 b), with the switching function

$$s_\nu(t) = g_{\mathrm{t}\nu}(t) - g_{\mathrm{b}\nu}(t) = 2 \cdot g_{\mathrm{t}\nu}(t) - 1, \quad s_\nu(t) \in \{-1, 1\}. \tag{3.1}$$
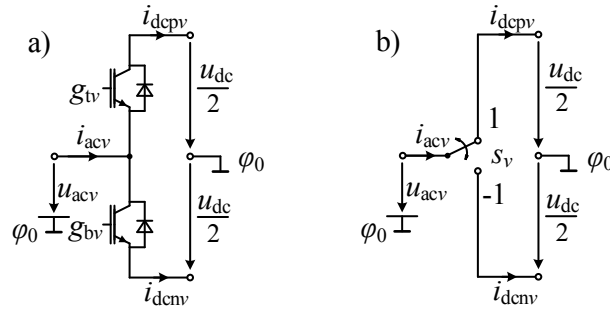
Figure 3.3: Equivalent circuit of one inverter phase leg using **a)** IGBTs **b)** a single-pole double-throw switch

The switching function is used to provide the algebraic connection between the ac-side voltage u_{ac} and the dc-side voltage u_{dc}, with

$$u_{\mathrm{ac}\nu}(t) = \frac{1}{2} \cdot s_\nu(t) \cdot u_{\mathrm{dc}}(t), \tag{3.2}$$

and between the ac-side current i_{ac} and the dc-side current i_{dc}, with

$$i_{\mathrm{dc}\nu}(t) = \frac{i_{\mathrm{dcp}\nu}(t) - i_{\mathrm{dcn}\nu}(t)}{2} = \frac{1}{2} \cdot s_\nu(t) \cdot i_{\mathrm{ac}\nu}(t). \tag{3.3}$$

Note that while considering only a single half bridge, the dc-side current is a mathematical quantity without an equivalent physical current, because there is no return current path. Its physical meaning is given when considering the other half bridges of the topology.

Transforming the equations to the frequency domain, using the convolution theorem in (2.15), yields a convolution of the spectra, with

$$U_{\mathrm{ac}\nu}(f) = \frac{1}{2} \cdot S_\nu(f) * U_{\mathrm{dc}}(f), \tag{3.4}$$

$$I_{\mathrm{dc}\nu}(f) = \frac{1}{2} \cdot S_\nu(f) * I_{\mathrm{ac}\nu}(f). \tag{3.5}$$

Whereas (3.4) and (3.5) are valid for aperiodic signals, a simplified evaluation of the power conversion can be accomplished for the steady state using Fourier coefficients. With the vector representation of the Fourier coefficients in (2.31) and the matrix representation of the convolution in (2.39), the model of a half bridge results in

$$\vec{U}_{\mathrm{ac}\nu} = \frac{1}{2} \cdot \boldsymbol{C}(\vec{S}_\nu) \cdot \vec{U}_{\mathrm{dc}}, \tag{3.6}$$

$$\vec{I}_{\mathrm{dc}\nu} = \frac{1}{2} \cdot \boldsymbol{C}(\vec{S}_\nu) \cdot \vec{I}_{\mathrm{ac}\nu}. \tag{3.7}$$

3.2 Pulse-Width Modulation

PWM is a common method to determine the switching instants of the transistors in order to generate a desired voltage setpoint u_{sp} of the phase output of the half bridges. For clarity, the phase number ν is not included in the following equations of single-phase cases.

The division of the voltage setpoint by half the dc component of the dc-link voltage U_{dc0} defines the duty cycle as

$$d(t) = \frac{u_{sp}(t)}{U_{dc0}/2}. \tag{3.8}$$

A comparison of (3.2) with (3.8) reveals that the ac-side voltage approximates the voltage setpoint when

1. $u_{dc}(t) \approx U_{dc0}$,

2. $d(t) \approx s(t)$.

The first assumption is a valid approximation, because the dc-link voltage is stiff, due to a sufficiently large dc-link capacitance. In order to validate the second assumption, the goal of the PWM process is to provide a fast-switching pattern with a switching period T_{sw} and a short-time average that equals the slowly-varying duty cycle. Introducing the moving average operator $\langle . \rangle_T$ [34], with

$$\langle x(t) \rangle_T = \frac{1}{T} \int_{t-T/2}^{t+T/2} s(\tau) \mathrm{d}\tau, \tag{3.9}$$

the approximation of the PWM process becomes

$$\langle s(t) \rangle_{T_{sw}} = d[nT_{sw}]. \tag{3.10}$$

For carrier-based PWM, the switching function is determined by a comparison of the duty cycle as the input signal to a periodic carrier signal $c(t) \in [-1, 1]$. For the selection of the carrier signal it is required that there be a linear relationship between the duty-cycle and the short-time average of the switching function [13]. If the duty cycle is larger than the carrier signal, the output gate signal $g_t(t) = \bar{g}_b(t)$ is one, otherwise the output is zero. The switching instants are called edges.

It is further assumed that the gradient of the carrier signal is much higher than the gradient of the duty cycle and the duty cycle is limited to $d(t) \in [-1, 1]$. With this, the output signal changes its value twice per cycle and the carrier period is equal to the switching period T_{sw}. The only exceptions are given for the maximum duty cycle values of 1 and -1, where no switching occurs.

A number of different modulation methods exist that differ in their choice of carrier signal and sampling method. For the carrier signal, either a sawtooth signal or a triangular signal are the common choices. Symmetrical carrier signals are preferred because of a lower resulting distortion of the output signal [13]. Using a sawtooth signal, one edge is fixed to the beginning of the carrier period. This modulation type is called single-edge PWM. If the sawtooth signal has a positive slope, as shown in Figure 3.4, the positive edge is fixed and the negative edge is influenced by the duty cycle. This is a modulation type called trailing-edge PWM (TE-PWM). For a negative slope, shown in Figure 3.5, the positive edge is modulated. This is known as leading-edge PWM (LE-PWM).
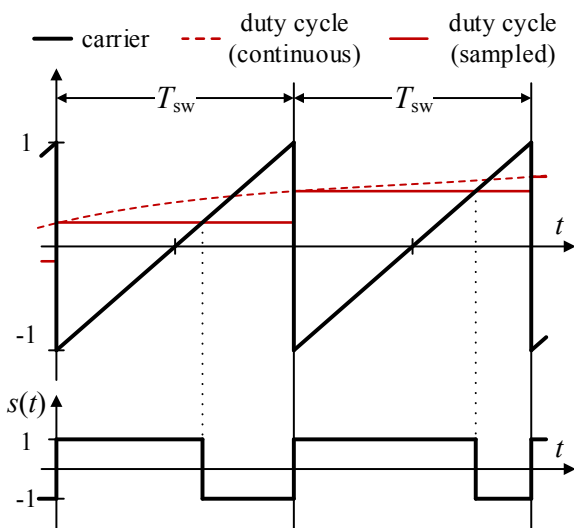

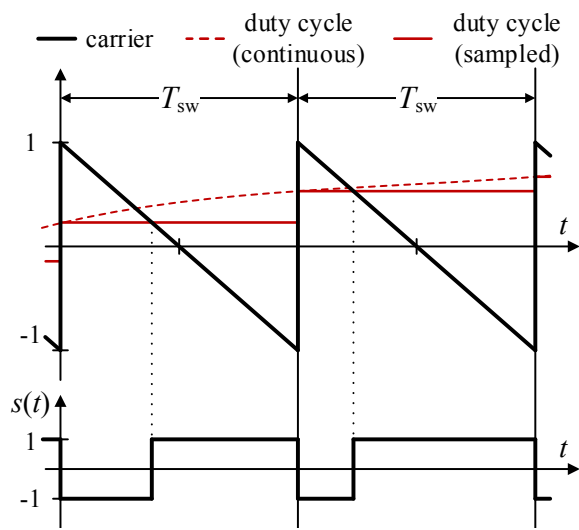**Figure 3.4:** Regularly-sampled trailing-edge PWM (TE-PWM)

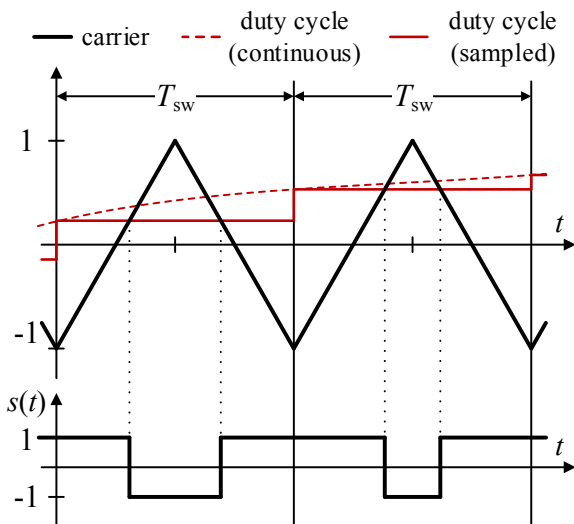**Figure 3.5:** Regularly-sampled leading-edge PWM (LE-PWM)

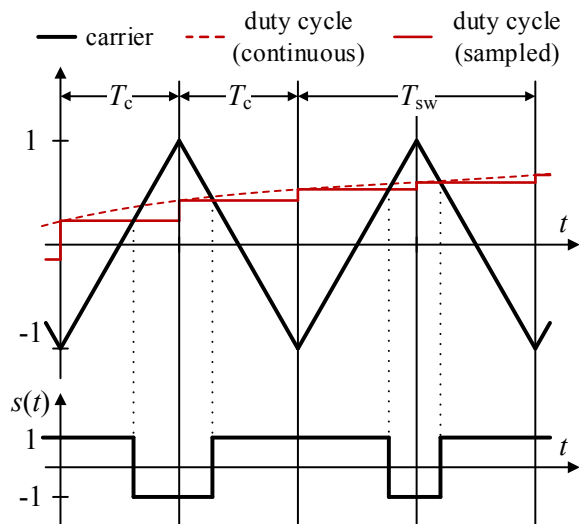**Figure 3.6:** Symmetrical regularly-sampled double-edge PWM (SD-PWM)

Figure 3.7: Asymmetrical regularly-sampled double-edge PWM (AD-PWM)

In digital control systems, the duty cycle is updated once per control period T_c and the duty cycle is sampled and held by the modulation unit, which is called regularly-sampled. For single-edge modulation, the control period is the same as the carrier period $T_{sw} = T_c$. The continuous duty cycle is included in Figure 3.4 and Figure 3.5 as a red, dashed line. The sampling and holding of the duty cycle occurs at the beginning of each carrier period, resulting in the red solid line. The bottom graphs of Figure 3.4 and Figure 3.5 show the resulting switching functions $s(t)$ for regularly-sampled TE-PWM and LE-PWM respectively, which only differ in the placement of the pulse within the switching period. When using an analog modulator, the duty cycle is a time-continuous signal and the modulation process is called naturally-sampled.

The modulation process leads to an output signal that is a distorted image of the input signal. The selection of the modulation type and the preferred modulation and control system (digital or analog) determines the intensity of this distortion. Naturally-sampled PWM has a lower distortion compared to a regularly-sampled implementation [12]. Nevertheless, due to its simpler implementation in the widely used digital low-level control of power converters, only regular sampling is considered in this thesis.

When using a symmetrical triangular carrier, the placement of both edges within the switching period depends on the duty cycle, which explains why it is called double-edge PWM. Sampling the duty cycle at the beginning of the carrier period ($T_{sw} = T_c$) results in a switching pulse that is symmetrically placed within the switching period, as shown in Figure 3.6. This method is called symmetrical regularly-sampled double-edge PWM (SD-PWM). Sampling the duty cycle at the beginning and at the center of the carrier period ($T_{sw} = 2\,T_c$) results in asymmetrical regularly-sampled double-edge PWM (AD-PWM) with an asymmetrically placed switching pulse. In this case, the short-time average of the switching function follows the duty cycle more closely, with

$$\langle s(t)\rangle_{T_{sw}/2} = d[nT_{sw}/2]. \tag{3.11}$$

A triangular signal can be composed of one rising sawtooth signal followed by a falling sawtooth signal [9]. This fact is used to establish the model of double-edge PWM from the models of TE-PWM and LE-PWM, which are easier to analyze. Switching the edges and starting the triangular signal with a falling sawtooth signal followed by a rising sawtooth signal can also be described by a phase shift of the triangular carrier by π.

A comparison of the output spectra of the regularly-sampled PWM methods reveals a lower distortion for the double-edge implementations and the lowest distortion levels for AD-PWM [12]. Nevertheless, both double-edge modulation types are used, because a control frequency that is twice the switching frequency is not feasible in all applications.

3.2.1 Single-Frequency Modulation

The presented modulation methods generate a switching function with a short-time average that approximates the duty cycle. Inevitably, the PWM process generates additional low frequency harmonics of the input signal and high frequency side bands around the switching frequency. In order to evaluate these distortions, which differ significantly between the modulation methods, analyses of the spectra are performed [12].

Under the assumption of sinusoidal modulation, where the duty cycle is a sine wave

$$d(t) = M \cdot \sin(\omega_{\mathrm{d}0} \cdot t + \theta_{d0}) \tag{3.12}$$

with a constant modulation index M, a constant radiant frequency $\omega_{\mathrm{d}0}$ and a phase shift of $\theta_{\mathrm{d}0}$ the ac-side voltage spectrum was analyzed by Bowes and Bird [10] using the double Fourier series approach, which has its theoretical background in the work of Bennett [8] and Black [9]. The results are summarized for and extended to various modulation methods in the comprehensive book of Holmes and Lipo [12]. These represent the ac-side voltage as a double Fourier series under the assumption of a constant dc-link voltage, and therefore they are proportional to the switching function, see (3.8). The carrier signal has constant radiant frequency of ω_{sw} and a phase shift of θ_{sw}.

The output of the modulation process is a switching function $s(t)$ that depends on two variables $x(t)$ and $y(t)$, with

$$\begin{aligned}
(x(t), y(t)) &\longmapsto s(t), \\
x(t) &:= \omega_{\mathrm{sw}} \cdot t + \theta_{\mathrm{sw}}, \\
y(t) &:= \omega_{\mathrm{d}0} \cdot t + \theta_{\mathrm{d}0}.
\end{aligned} \tag{3.13}$$

Periodic waveforms that depend on two variables can be described by a Fourier series extension to two dimensions, called double Fourier series. Its (real) Fourier coefficients A_{mn} and B_{mn} are obtained by solving double integrals, with

$$\begin{aligned}
A_{mn} &= \frac{1}{2\pi^2} \cdot \int_{-\pi}^{\pi} \int_{-\pi}^{\pi} s(x, y) \cdot \cos(mx + ny) \, \mathrm{d}x \, \mathrm{d}y \\
B_{mn} &= \frac{1}{2\pi^2} \cdot \int_{-\pi}^{\pi} \int_{-\pi}^{\pi} s(x, y) \cdot \sin(mx + ny) \, \mathrm{d}x \, \mathrm{d}y
\end{aligned} \tag{3.14}$$

In order to find an analytical expression of the Fourier coefficients, the integration needs to be solved analytically. The expression of the switching function $s(x, y)$ and the corresponding bounds of integration are derived for each modulation method individually based on a graphical interpretation of the so-called unit cell. This process is illustrated in Figure 3.8 for SD-PWM. Each square of the width 2π represents a unit cell, comprising one switching period on the x axis and one duty cycle period one the y axis. The locus of the duty cycle has the form $d(t) = M \cdot \cos(\omega_{\mathrm{d}0} + \theta_{\mathrm{d}0})$ and divides the area of positive (1) and negative (-1) switching

function levels, resulting in a sandglass shape. For natural sampling the switching occurs at the crossing of the linear slope of $\omega_{d0}/\omega_{sw} \cdot t$ (red, dotted line) and the locus of the duty cycle. For regular sampling, the slope is modified into a sampled slope y' (red, solid line). Additionally, a phase correction of the sampling process is implemented that results in an effective sampling at the center of the switching cycle. The resulting switching pattern is included in the bottom graph.

By finding an expression $y \mapsto x$ for the switching instants, the bounds of integration in (3.14) are divided into parts, where the switching function can by substituted by its values (1) and (-1). The graphical representation of the unit cells (Figure 3.8) can help for the development, by transforming the intersections of the locus of the duty cycle and the linear slope. A further substitution $(x, y) \mapsto y'$ is necessary in order to consider the sampling process of SD-PWM and AD-PWM. The results are analytical expressions for the double Fourier coefficients A_{mn} and B_{mn}. The reader is referred to [12] for a detailed derivation of the double Fourier series expressions for various modulation methods.

Regardless of the PWM method, the switching function can be represented by a double Fourier series with the following form:

$$
s(t) = \underbrace{\frac{A_{,00}}{2}}_{\text{dc component}} + \underbrace{\sum_{n=1}^{\infty} \left[A_{,0n} \cos(n(\omega_{d0}t + \theta_{d0})) + B_{,0n} \sin(n(\omega_{d0}t + \theta_{d0})) \right]}_{\text{base-band harmonics}} \ldots
$$

$$
+ \underbrace{\sum_{m=1}^{\infty} \left[A_{,m0} \cos(m(\omega_{sw}t + \theta_{sw})) + B_{,m0} \sin(m(\omega_{sw}t + \theta_{sw})) \right]}_{\text{carrier harmonics}} \ldots
$$
(3.15)

$$
+ \underbrace{\sum_{m=1}^{\infty} \sum_{n=-\infty}^{\infty} \begin{bmatrix} A_{,mn} \cos(m(\omega_{sw}t + \theta_{sw}) + n(\omega_{d0}t + \theta_{d0}))\ldots \\ + B_{,mn} \sin(m(\omega_{sw}t + \theta_{sw}) + n(\omega_{d0}t + \theta_{d0})) \end{bmatrix}}_{\text{side-band harmonics}} \text{[12]},
$$

where $A_{,mn}$ and $B_{,mn}$ are the real Fourier coefficients of the double Fourier series. The indices of summation $m \in \mathbb{N}$ and $n \in \mathbb{Z}$ represent the carrier and duty-cycle harmonic order.

In order to transfer the double Fourier series representation in (3.15) into the single Fourier series approximation, with

$$
s(t) = \sum_{k=-k_{\max}}^{k_{\max}} S_{,k} \cdot e^{jk\omega_0 t},
$$
(3.16)

three steps are performed:

1. The indices of summation are limited to $m = -m_{\max}\ldots m_{\max}$ and $n = -n_{\max}\ldots n_{\max}$.
2. The fundamental frequency of the single Fourier series is selected as the greatest common divisor of the duty cycle frequency and the switching frequency $\omega_0 = \gcd(\omega_{d0}, \omega_{sw})$. For

this, it is assumed that $\omega_{\text{sw}}/\omega_{\text{d0}} \in \mathbb{Q}$.

3. Multiple real double Fourier coefficients $A_{,mn}$ and $B_{,mn}$ of the radiant frequency $m\omega_{\text{sw}} + n\omega_0$ are superimposed in the calculation of a single Fourier coefficient $S_{,k}$ of the radiant frequency $k\omega_0$. All terms that fulfill $k = m + n \cdot \omega_{\text{d0}}/\omega_{\text{sw}}, m \in \mathbb{N}, n \in \mathbb{Z}$ influence the coefficient and build a sum of complex numbers.
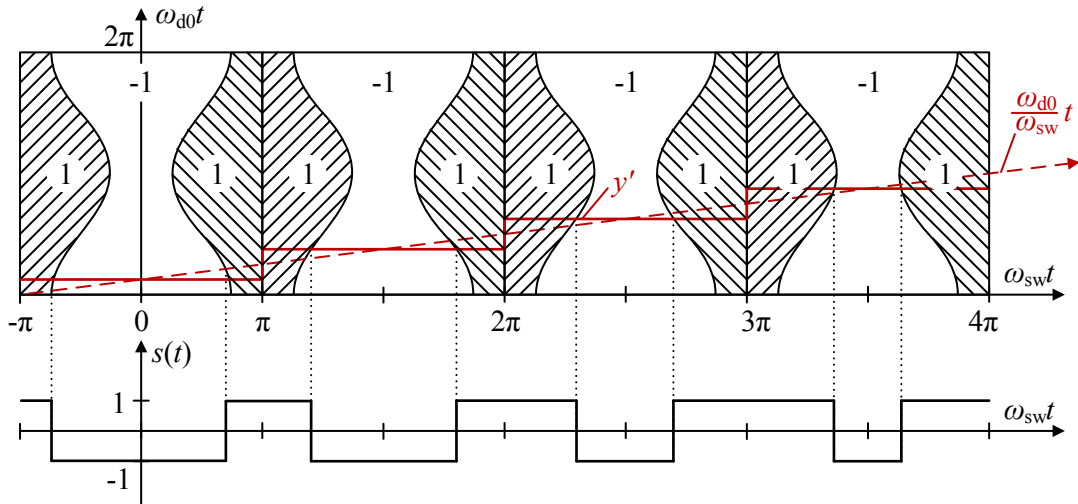

Figure 3.8: Replication of the unit cell for four switching periods and one duty cycle period using SD-PWM with sinusoidal modulation. The bottom graph shows the resulting switching function. The sampling is phase corrected and results at the center of the switching period.
$\omega_{\text{d0}}/\omega_{\text{sw}} = 8, \quad M = 0.5, \quad \theta_{\text{d0}} = 0, \quad \theta_{\text{sw}} = \pi.$

3.2.2 Multiple-Frequency Modulation

Analytical results for the output spectra of modulators with arbitrary band-limited input signals were presented by Song and Sarwate in [15] for the first time, providing a more general representation of the modulator. Alternative approaches were published in recent years [6, 16, 17], allowing the incorporation of multiple harmonics in the input spectrum of the modulator.

The approach by Song and Sarwate originates from a time-domain representation of the pulse pattern using the unit step function (Heaviside function) and is further developed into a frequency-domain representation of the switching function spectrum as a function of the duty-cycle spectrum. The derivation of the approach in [45] is similarly derived in the time domain, but requires a calculation of the switching instants in the time domain prior to the calculation of the switching function spectrum.

The results presented by Song and Sarwate in [15] are developed as Fourier transforms and are reviewed here in a modified notation and with a correction for AD-PWM. They are used to develop the switching function spectrum in the form of Fourier coefficients. For better comparability, the corresponding equation numbers of the reference are given in brackets, where possible.

TE-PWM

Figure 3.9 a) shows the comparison of a sampled duty cycle with a TE-PWM sawtooth carrier for two switching periods. The duty cycle is set to a positive value during the first period and to a negative value during the second period. The output signal $s(t)$ can be divided into a rectangular function $s_\mathrm{c}(t)$ with a constant pulse width of $0.5 \cdot T_\mathrm{sw}$ and a modulated rectangular function $s_\mathrm{dTE}(t, d)$, which has a pulse width that is determined by the sampled values of the duty cycle $d[mT_\mathrm{sw}]$. The duty cycle is sampled at the beginning of each switching period. For TE-PWM the switching function is written as

$$s_\mathrm{TE}(t, d) = s_\mathrm{c}(t) + s_\mathrm{dTE}(t, d) \quad [15, (1)]. \tag{3.17}$$

The signal $s_\mathrm{c}(t)$ is depicted in Figure 3.9 b) and has a value of 1 during the first half of the switching cycle and a value of -1 during the second half of the switching cycle. This is written as

$$s_\mathrm{c}(t) = \begin{cases} 1 & \text{for} & mT_\mathrm{sw} \le t < (m + 1/2)T_\mathrm{sw} \\ -1 & \text{for} & (m + 1/2)T_\mathrm{sw} \le t < (m + 1)T_\mathrm{sw} \end{cases}, \quad m \in \mathbb{Z} \tag{3.18}$$

The duty-cycle-dependent component considers the deviation of the output signal $s_\mathrm{TE}(t, d)$ from $s_\mathrm{c}(t)$ due to the influence of the duty cycle, expressed as

$$s_\mathrm{dTE}(t, \tau) = 2 \cdot \sum_{m=-\infty}^{\infty} \sigma(t - (m + 1/2)T_\mathrm{sw}) - \sigma(t - mT_\mathrm{sw} - \tau_m) \quad [15, (1)], \tag{3.19}$$

where $\sigma(t)$ is the unit step function, defined as

$$\sigma(t) = \begin{cases} 0 & \text{for} & t < 0 \\ 1 & \text{for} & t \ge 0 \end{cases}, \tag{3.20}$$

and τ_m is the pulse width of the switching period m. The pulse width has linear relationship with the duty-cycle value sampled at the beginning of the respective switching cycle, with

$$\tau_m = \frac{1}{2} \cdot T_\mathrm{sw} \cdot (1 + d[mT_\mathrm{sw}]). \tag{3.21}$$

In (3.19) each carrier period comprises a positive and a negative unit step function $\sigma(t)$, illustrated in Figure 3.9 c) for the first switching cycle ($m = 0$) and in Figure 3.9 d) for the second switching cycle ($m = 1$). The two unit step functions are included as blue and green, dashed lines. According to (3.17) the total switching function depicted in Figure 3.9 e) results from the superposition of the components shown in the subplots b) + c) + d).

In order to find an analytical expression of the switching function spectrum for TE-PWM, a
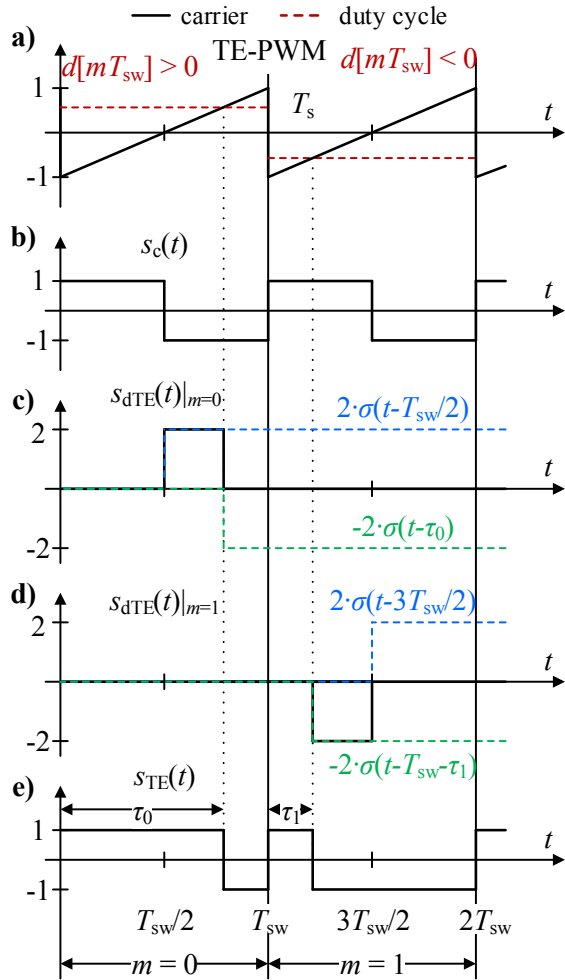
Figure 3.9: Derivation of switching function for TE-PWM:

a) Comparison of a TE-PWM carrier signal with a sampled duty cycle, where $d[mT_{sw}] > 0$ for the first switching period ($n = 0$) and $d[mT_{sw}] < 0$ for the second switching period ($n = 1$).

b) Rectangular function with a duty cycle of 50 %.

c) Duty-cycle-dependent part for ($m = 0$), consisting of two unit-step functions.

d) Duty-cycle-dependent part for ($m = 1$).

e) Resulting switching function comprising b) + c) + d).
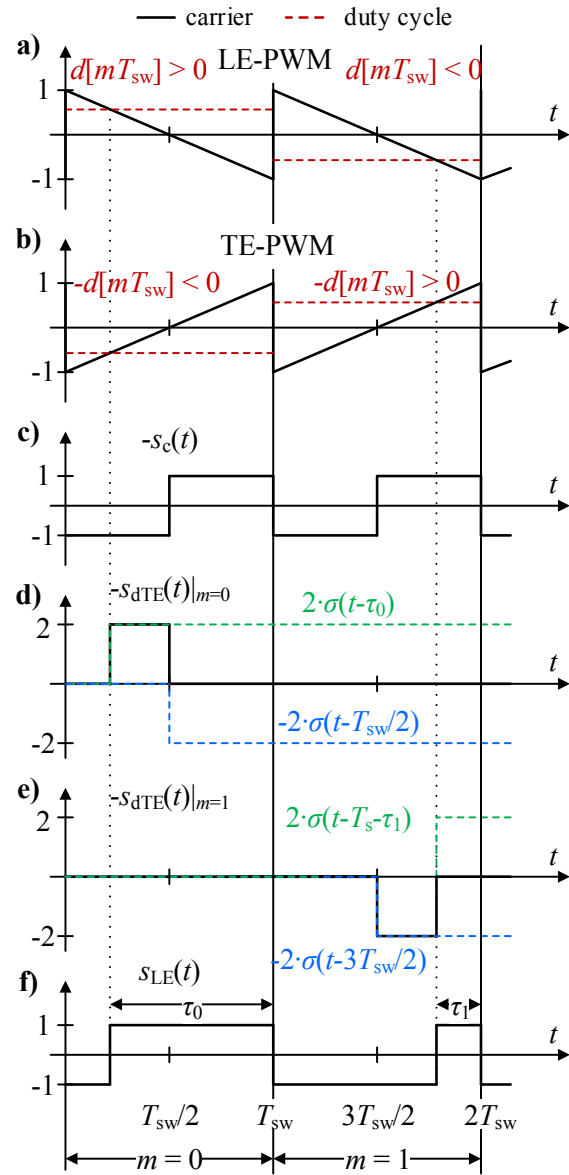
Figure 3.10: Derivation of switching function for LE-PWM:

a) Comparison of an LE-PWM carrier signal with a sampled duty cycle, where $d[mT_{sw}] > 0$ for the first switching period ($n = 0$) and $d[mT_{sw}] < 0$ for the second switching period ($n = 1$).

b) Equivalent description with a TE-PWM carrier signal and an inverted duty cycle.

c) Inverted rectangular function with a duty cycle of 50 %.

d) Inverted duty-cycle-dependent part for TE-PWM in b) and ($m = 0$), consisting of two unit-step functions.

e) Duty-cycle-dependent part for TE-PWM in b) and ($m = 1$).

f) Resulting switching function comprising c) + d) + e).

Fourier transform is applied to the individual components of (3.17), with

$$S_{\mathrm{TE}}(f) = S_{\mathrm{c}}(f) + S_{\mathrm{dTE}}(f), \tag{3.22}$$

The respective vector representation of Fourier coefficients is written as

$$\vec{S}_{\mathrm{LE}} = \vec{S}_{\mathrm{c}} + \vec{S}_{\mathrm{dTE}}. \tag{3.23}$$

Because $s_{\mathrm{c}}(t)$ is a periodic function with a period of T_{sw} it can be described by a Fourier series. Choosing the fundamental period of the Fourier series to an arbitrary value of $T_0 = m \cdot T_{\mathrm{sw}}, m \in \mathbb{Z}$, the Fourier coefficient $S_{\mathrm{c},k}$ of order k of the rectangular function results in

$$S_{\mathrm{c},k} = \begin{cases} \frac{2}{\mathrm{j}\pi(2p+1)} & \text{for} \quad k = (2p+1) \cdot T_0/T_{\mathrm{sw}}, p \in \mathbb{Z} \\ 0 & \text{otherwise} \end{cases}. \tag{3.24}$$

By using the sampling property of the Dirac function, the discrete spectrum can be transformed to a continuous spectrum $S_{\mathrm{c}}(f)$, with

$$S_{\mathrm{c}}(f) = \sum_{p=0}^{\infty} \frac{2}{\mathrm{j}\pi(2p+1)} \cdot [\delta(f - (2p+1)f_{\mathrm{sw}}) - \delta(f + (2p+1)f_{\mathrm{sw}})] \quad [15, (3)], \tag{3.25}$$

For the derivation of the Fourier transform $S_{\mathrm{dTE}}(f, \tau)$ of (3.19), the Fourier transform of the unit step function

$$\Sigma(f) = \frac{1}{2} \cdot \delta(f) + \frac{1}{\mathrm{j}2\pi f} \tag{3.26}$$

and the time-shifting property

$$\sigma(t - \tau) \quad \circ\!\!-\!\!\bullet \quad \Sigma(f) \cdot \mathrm{e}^{-\mathrm{j}2\pi f\tau}, \tag{3.27}$$

are utilized. With this, the Fourier transform $S_{\mathrm{dTE}}(f, \tau)$ results in

$$S_{\mathrm{dTE}}(f, \tau) = \frac{1}{\mathrm{j}\pi f} \cdot \sum_{m=-\infty}^{\infty} \mathrm{e}^{-\mathrm{j}2\pi f \cdot ((m+\frac{1}{2})T_{\mathrm{sw}})} - \mathrm{e}^{-\mathrm{j}2\pi f \cdot (mT_{\mathrm{sw}}+\tau_m)} \quad [15, (4)]. \tag{3.28}$$

Substitution of the pulse width with (3.21) and applying steps of factorization yields

$$S_{\mathrm{dTE}}(f, d) = \frac{1}{\mathrm{j}\pi f} \cdot \sum_{m=-\infty}^{\infty} \mathrm{e}^{-\mathrm{j}2\pi f \cdot ((m+\frac{1}{2})T_{\mathrm{sw}})} - \mathrm{e}^{-\mathrm{j}2\pi f \cdot (mT_{\mathrm{sw}}+\frac{1}{2}T_{\mathrm{sw}}(1+d[mT_{\mathrm{sw}}])} \tag{3.29}$$

$$= \frac{1}{\mathrm{j}\pi f} \cdot \mathrm{e}^{-\mathrm{j}\pi f T_{\mathrm{sw}}} \cdot \sum_{m=-\infty}^{\infty} \mathrm{e}^{-\mathrm{j}2\pi f m T_{\mathrm{sw}}} - \mathrm{e}^{-\mathrm{j}2\pi f \cdot (mT_{\mathrm{sw}}+\frac{1}{2}T_{\mathrm{sw}}d[mT_{\mathrm{sw}}])} \tag{3.30}$$

$$= \frac{1}{\mathrm{j}\pi f} \cdot \mathrm{e}^{-\mathrm{j}\pi f T_{\mathrm{sw}}} \cdot \sum_{m=-\infty}^{\infty} \mathrm{e}^{-\mathrm{j}2\pi f m T_{\mathrm{sw}}} \left(1 - \mathrm{e}^{-\mathrm{j}\pi f T_{\mathrm{sw}} d[mT_{\mathrm{sw}}]}\right) \quad [15, (5)]. \tag{3.31}$$

By applying the Taylor expansion of the exponential function, with

$$1 - e^x = 1 - \sum_{n=0}^{\infty} \frac{x^n}{n!} = -\sum_{n=1}^{\infty} \frac{x^n}{n!}, \tag{3.32}$$

to (3.31) results in:

$$S_{\mathrm{dTE}}(f, d) = \frac{1}{\mathrm{j}\pi f} \cdot e^{-\mathrm{j}\pi f T_{\mathrm{sw}}} \cdot \sum_{m=-\infty}^{\infty} e^{-\mathrm{j}2\pi f m T_{\mathrm{sw}}} \cdot \sum_{n=1}^{\infty} -\frac{(-\mathrm{j}\pi f T_{\mathrm{sw}} \, d[m T_{\mathrm{sw}}])^n}{n!}. \tag{3.33}$$

A rearrangement to

$$S_{\mathrm{dTE}}(f, d) = \frac{1}{\mathrm{j}\pi f} \cdot e^{-\mathrm{j}\pi f T_{\mathrm{sw}}} \cdot \sum_{n=1}^{\infty} -\frac{(-\mathrm{j}\pi f T_{\mathrm{sw}})^n}{n!} \cdot \sum_{m=-\infty}^{\infty} (d[m T_{\mathrm{sw}}])^n \cdot e^{-\mathrm{j}2\pi f m T_{\mathrm{sw}}} \tag{3.34}$$

allows for the extraction of a term $\sum_{m=-\infty}^{\infty} (d[m T_{\mathrm{sw}}])^n \cdot e^{-\mathrm{j}2\pi f m T_{\mathrm{sw}}}$ that corresponds to the DTFT definition in (2.12). The term is called the DTFT of the duty cycle D_{s}, which is a spectrum periodic with the switching frequency f_{sw}. In contrast, the CTFT of the duty cycle is denoted with $D(f)$.

By acknowledging that exponentiation of a signal in the time domain relates to a repeated convolution in the frequency domain, the Fourier transform of the discrete-time duty cycle $(d_{\mathrm{s}}(t))^n$ is written as

$$(d_{\mathrm{s}}(t))^n \quad \circ\!\!-\!\!\bullet \quad \underbrace{D_{\mathrm{s}}(f) * D_{\mathrm{s}}(f) * \ldots * D_{\mathrm{s}}(f)}_{n \text{ times}} =: D_{\mathrm{s}}^{*n}(f). \tag{3.35}$$

$D_{\mathrm{s}}(f)$ is the DTFT of the discrete-time duty cycle. $D_{\mathrm{sw}}^{*n}(f)$ is the Fourier transform of the n-th power of the input signal $(d[m T_{\mathrm{sw}}])^n$, and therefore the n-fold convolution of the duty cycle spectrum with itself.

If the duty cycle spectrum is given as a continuous-time Fourier transform $(d(t))^n \circ\!\!-\!\!\bullet D^{*n}(f)$, the conversion in (2.17) can be applied, which results in

$$\sum_{m=-\infty}^{\infty} (d[m T_{\mathrm{sw}}])^n \cdot e^{-\mathrm{j}2\pi f m T_{\mathrm{sw}}} = D_{\mathrm{s}}^{*n}(f)$$

$$= f_{\mathrm{sw}} \cdot D^{*n}(f) * \sum_{m=-\infty}^{\infty} \delta(f - m f_{\mathrm{sw}}) \tag{3.36}$$

$$= f_{\mathrm{sw}} \cdot \sum_{m=-\infty}^{\infty} D^{*n}(f - m f_{\mathrm{sw}}).$$

Application of (3.36) to (3.34) yields

$$S_{\mathrm{dTE}}(f, D) = \frac{1}{\mathrm{j}\pi f} \cdot \mathrm{e}^{-\mathrm{j}\pi f T_{\mathrm{sw}}} \cdot \sum_{n=1}^{\infty} -\frac{(-\mathrm{j}\pi f T_{\mathrm{sw}})^n}{n!} \cdot f_{\mathrm{sw}} \cdot \sum_{m=-\infty}^{\infty} D^{*n}(f - m f_{\mathrm{sw}}). \quad (3.37)$$

Reduction and rearrangement leads to the final expression of the switching function spectrum as

$$S_{\mathrm{dTE}}(f, D) = \mathrm{e}^{-\mathrm{j}\pi f T_{\mathrm{sw}}} \cdot \sum_{m=-\infty}^{\infty} \sum_{n=1}^{\infty} \frac{(-\mathrm{j}\pi f T_{\mathrm{sw}})^{n-1}}{n!} \cdot D^{*n}(f - m f_{\mathrm{sw}}) \quad [15, (6)]. \quad (3.38)$$

In conclusion, the derivation allows for the expression the switching function spectrum as a function of the duty cycle spectrum containing multiple frequency components: $D(f) \mapsto S_{\mathrm{dTE}}(f)$.

Sampling (3.38) with a frequency $k f_0$, while limiting the indices of summation, leads to an expression for the approximate steady state spectrum using Fourier coefficients:

$$S_{\mathrm{dTE},k} = \mathrm{e}^{-\mathrm{j}\pi k f_0 T_{\mathrm{sw}}} \cdot \sum_{m=-m_{\mathrm{max}}}^{m_{\mathrm{max}}} \sum_{n=1}^{n_{\mathrm{max}}} \frac{(-\mathrm{j}\pi k f_0 T_{\mathrm{sw}})^{n-1}}{n!} \cdot \left[\vec{D}^{*n}\right]_{,(k - m f_{\mathrm{sw}}/f_0)}, \quad (3.39)$$

where an evaluation of the vector $\vec{D}^{*n}$ at the k-th element is denoted as $[\vec{D}^{*n}]_{,k}$. The calculation of the spectrum requires a repeated convolution of the duty cycle spectrum with itself, which is implemented explicitly, with

$$\begin{aligned}
\vec{D}^{*1} &= \vec{D}, \\
\vec{D}^{*n} &= \vec{D}^{*(n-1)} * \vec{D}.
\end{aligned} \quad (3.40)$$

LE-PWM

The derivation of the switching function spectrum for LE-PWM is simplified by using an analogy to TE-PWM. Figure 3.10 a) shows the carrier and the duty cycle for LE-PWM. The resulting switching function is the same as for TE-PWM when applying an inverted duty cycle and inverting the output signal (Figure 3.10 b)): $s_{\mathrm{LE}}(t, d) = -s_{\mathrm{TE}}(t, -d)$. Similar to (3.17), the switching function for LE-PWM can be divided into two components:

$$\begin{aligned}
s_{\mathrm{LE}}(t, d) &= -s_{\mathrm{c}}(t) + s_{\mathrm{dLE}}(t, d), \\
&= -s_{\mathrm{c}}(t) - s_{\mathrm{dTE}}(t, -d).
\end{aligned} \quad (3.41)$$

Figure 3.10 c), d), and e) illustrate how the components $-s_{\mathrm{c}}(t)$ and $s_{\mathrm{dLE}}(t, d)$ can be derived similarly to TE-PWM. Subfigure f) shows the resulting switching function as the superposition of c) + d) + e).

For the derivation of the frequency domain expression

$$S_{\text{LE}}(f, d) = -S_{\text{c}}(f) + S_{\text{dLE}}(f, d), \tag{3.42}$$

the results for are TE-PWM utilized. $S_{\text{c}}(f)$ is the same as for TE-PWM and is given in (3.25). The derivation of the duty-cycle-dependent component is accomplished by modifying (3.33) and following the same steps in the derivation as for TE-PWM, with

$$S_{\text{dLE}}(f, d) = -S_{\text{dTE}}(f, -d) \tag{3.43}$$

$$= -\frac{1}{\text{j}\pi f} \cdot \text{e}^{-\text{j}\pi f T_{\text{sw}}} \cdot \sum_{m=-\infty}^{\infty} \text{e}^{-\text{j}2\pi f m T_{\text{sw}}} \cdot \sum_{n=1}^{\infty} -\frac{(\text{j}\pi f T_{\text{sw}} \, d[m T_{\text{sw}}])^n}{n!} \tag{3.44}$$

$$= -\frac{1}{\text{j}\pi f} \cdot \text{e}^{-\text{j}\pi f T_{\text{sw}}} \cdot \sum_{n=1}^{\infty} -\frac{(\text{j}\pi f T_{\text{sw}})^n}{n!} \cdot \sum_{m=-\infty}^{\infty} (d[m T_{\text{sw}}])^n \cdot \text{e}^{-\text{j}2\pi f m T_{\text{sw}}}, \tag{3.45}$$

$$S_{\text{dLE}}(f, D) = \frac{1}{\text{j}\pi f} \cdot \text{e}^{-\text{j}\pi f T_{\text{sw}}} \cdot \sum_{n=1}^{\infty} \frac{(\text{j}\pi f T_{\text{sw}})^n}{n!} \cdot f_{\text{sw}} \cdot \sum_{m=-\infty}^{\infty} D^{*n}(f - m f_{\text{sw}}). \tag{3.46}$$

$$= \text{e}^{-\text{j}\pi f T_{\text{sw}}} \cdot \sum_{m=-\infty}^{\infty} \sum_{n=1}^{\infty} \frac{(\text{j}\pi f T_{\text{sw}})^{n-1}}{n!} \cdot D^{*n}(f - m f_{\text{sw}}) \quad [15, (42)]. \tag{3.47}$$

The continuous spectrum can again be sampled and approximated with a finite summation to generate the Fourier components for the steady state:

$$S_{\text{dLE},k} = \text{e}^{-\text{j}\pi k f_0 T_{\text{sw}}} \cdot \sum_{m=-m_{\text{max}}}^{m_{\text{max}}} \sum_{n=1}^{n_{\text{max}}} \frac{(\text{j}\pi k f_0 T_{\text{sw}})^{n-1}}{n!} \cdot \left[\vec{D}^{*n}\right]_{(k-m f_{\text{sw}}/f_0)}. \tag{3.48}$$

SD-PWM

The derivation of the switching function for double-edge PWM takes advantage of its close relationship to single-edge PWM. For SD-PWM the switching function can be written as

$$s_{\text{SD}}(t, d) = s_{\text{c}}(t - T_{\text{sw}}/4) + s_{\text{dLE}}(t + T_{\text{sw}}/4, \, d[m T_{\text{sw}}]/2)... \tag{3.49}$$
$$+ s_{\text{dTE}}(t - T_{\text{sw}}/4, \, d[m T_{\text{sw}}]/2) \quad [15],$$

where the first edge is a leading edge and the second edge is a trailing edge. This is illustrated in Figure 3.11 for one switching period, where subfigure a) shows the carrier signal and the duty cycle, which is sampled at the beginning of the switching period. The component of constant duty cycle in subfigure d) differs from TE-PWM (Figure 3.11 b)) in a right shift of $T_{\text{sw}}/4$.

The leading edge of SD-PWM is the same as for LE-PWM when using half the duty cycle ($d[m T_{\text{sw}}]/2$) and a left-shifted LE-PWM carrier by $T_{\text{sw}}/4$, as depicted in Figure 3.11 b). For comparison, the full duty cycle value is included in light red and the unshifted carrier is in-
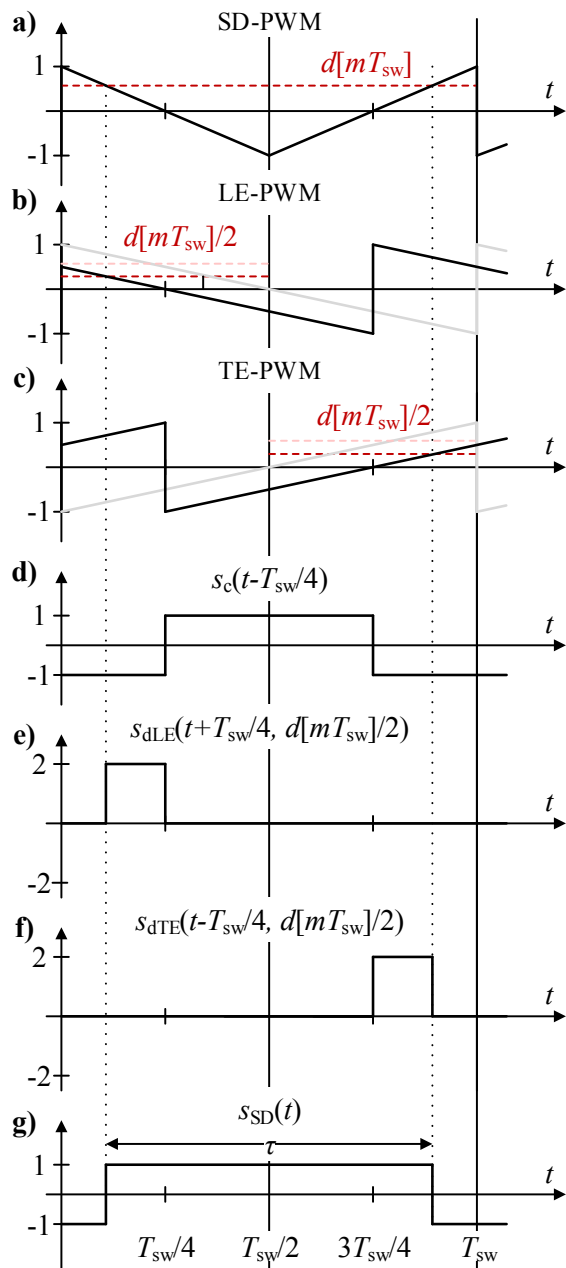
Figure 3.11: Derivation of switching function for SD-PWM:

a) Comparison of an SD-PWM carrier signal (black line) with a sampled duty cycle $d[mT_{sw}] > 0$ (red dashed line).

b) Equivalent description for the leading edge using a LE-PWM carrier signal left-shifted by $T_{sw}/4$. The duty cycle's value is halved.

c) Equivalent description for the trailing edge using a TE-PWM carrier signal right-shifted by $T_{sw}/4$. The duty cycle's value is halved.

d) Rectangular function with a duty cycle of 50 % right-shifted by $T_{sw}/4$.

e) Duty-cycle-dependent part for LE resulting from b).

f) Duty-cycle-dependent part for TE resulting from c).

g) Resulting switching function comprising d) + e) + f).
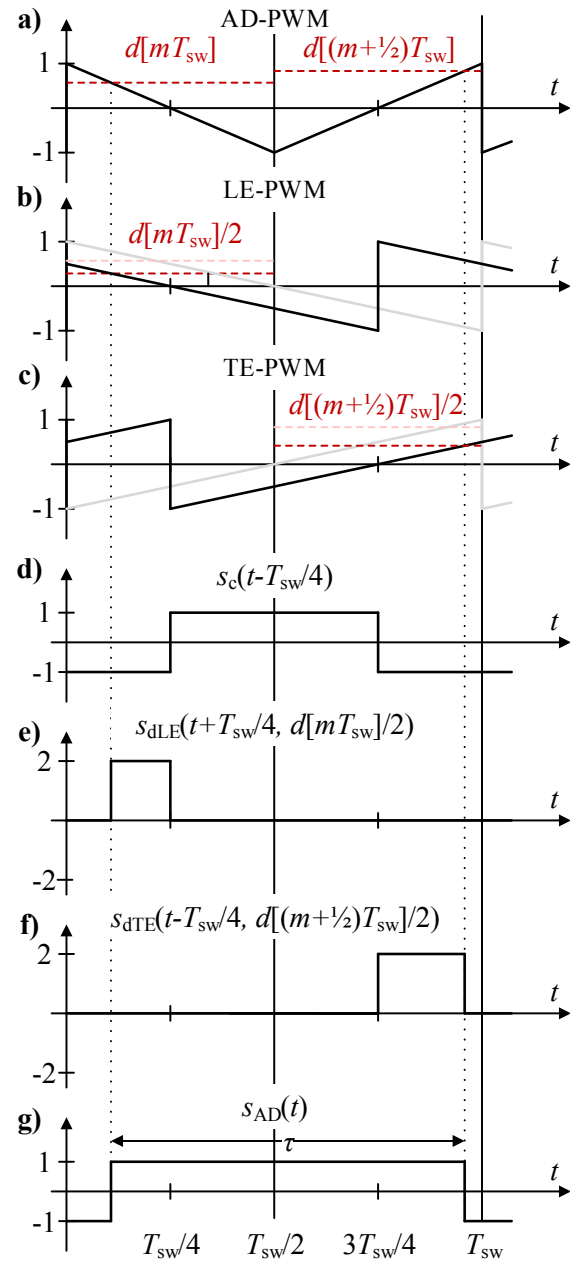
Figure 3.12: Derivation of switching function for AD-PWM:

a) Comparison of an AD-PWM carrier signal (black line) with a sampled duty cycle sampled at mT_{sw} and $(m + 1/2)T_{sw}$ (red dashed line).

b) Equivalent description for the leading edge using a LE-PWM carrier signal left-shifted by $T_{sw}/4$. The duty cycle's value is halved and sampled at mT_{sw}.

c) Equivalent description for the trailing edge using a TE-PWM carrier signal right-shifted by $T_{sw}/4$. The duty cycle's value is halved and sampled at $(m + 1/2)T_{sw}$.

d) Rectangular function with a duty cycle of 50 % right-shifted by $T_{sw}/4$.

e) Duty-cycle-dependent part for LE resulting from b).

f) Duty-cycle-dependent part for TE resulting from c).

**g)** Resulting switching function comprising d) + e) + f).

cluded in gray. The resulting duty-cycle-dependent component of the leading edge $s_{\mathrm{dLE}}(t + T_{\mathrm{sw}}/4,\, d[mT_{\mathrm{sw}}]/2)$ is shown in Figure 3.11 e).

The duty-cycle-dependent component of the trailing edge can be derived similarly. As illustrated in the subfigures c) and f), an equivalent duty-cycle-dependent component $s_{\mathrm{dTE}}(t - T_{\mathrm{sw}}/4,\, d[mT_{\mathrm{sw}}]/2)$ results when applying a comparison of half the duty cycle ($d[mT_{\mathrm{sw}}]/2$) to a right-shifted TE-PWM carrier by $T_{\mathrm{sw}}/4$. The superposition of the subfigures d) + e) + f) yields the total switching function for SD-PWM, depicted in subfigure g).

The Fourier transform of (3.49) results in

$$
\begin{aligned}
S_{\mathrm{SD}}(f, D) = \mathrm{e}^{-j\pi f T_{\mathrm{sw}}/2} \cdot S_{\mathrm{c}}(f) &+ \mathrm{e}^{+j\pi f T_{\mathrm{sw}}/2} \cdot S_{\mathrm{dLE}}(f, d/2)... \\
&+ \mathrm{e}^{-j\pi f T_{\mathrm{sw}}/2} \cdot S_{\mathrm{dTE}}(f, d/2) \quad [15,\,(48)].
\end{aligned}
\tag{3.50}
$$

An analysis of (3.34) and (3.45) reveals that a scaling of the duty cycle by $1/2$ introduces a scaling term of $1/2^n$ into the calculation of the switching function spectra. Therefore, the final equations for TE-PWM and LE-PWM in (3.38) and (3.47) are used with a scaling term of $1/2^n$. This results in

$$
\begin{aligned}
S_{\mathrm{SD}}(f, D) = \mathrm{e}^{-j\pi f T_{\mathrm{sw}}/2} \cdot S_{\mathrm{c}}(f)... & \\
+ \mathrm{e}^{+j\pi f T_{\mathrm{sw}}/2} \cdot \mathrm{e}^{-j\pi f T_{\mathrm{sw}}} \cdot \sum_{m=-\infty}^{\infty} \sum_{n=1}^{\infty} \frac{(j\pi f T_{\mathrm{sw}})^{n-1}}{2^n \cdot n!} \cdot D^{*n}(f - mf_{\mathrm{sw}})... & \\
+ \mathrm{e}^{-j\pi f T_{\mathrm{sw}}/2} \cdot \mathrm{e}^{-j\pi f T_{\mathrm{sw}}} \cdot \sum_{m=-\infty}^{\infty} \sum_{n=1}^{\infty} (-1)^{n-1} \cdot \frac{(j\pi f T_{\mathrm{sw}})^{n-1}}{2^n \cdot n!} \cdot D^{*n}(f - mf_{\mathrm{sw}}). &
\end{aligned}
\tag{3.51}
$$

A further step is introduced by analyzing the summation over n. For odd numbers n it can be stated that $(-1)^{n-1} = 1$ and thus

$$
\begin{aligned}
&(j\pi f T_{\mathrm{sw}})^{n-1} \cdot \mathrm{e}^{+j\pi f T_{\mathrm{sw}}/2} + (-1)^{n-1} \cdot (j\pi f T_{\mathrm{sw}})^{n-1} \cdot \mathrm{e}^{-j\pi f T_{\mathrm{sw}}/2}... \\
&\xrightarrow{n \text{ is odd}} (j\pi f T_{\mathrm{sw}})^{n-1} \cdot \left(\mathrm{e}^{+j\pi f T_{\mathrm{sw}}/2} + \mathrm{e}^{-j\pi f T_{\mathrm{sw}}/2} \right) = (j\pi f T_{\mathrm{sw}})^{n-1} \cdot \cos(\pi f T_{\mathrm{sw}}/2).
\end{aligned}
\tag{3.52}
$$

For even numbers of n it can be stated that $(-1)^{n-1} = -1$ and thus

$$
\begin{aligned}
&(j\pi f T_{\mathrm{sw}})^{n-1} \cdot \mathrm{e}^{+j\pi f T_{\mathrm{sw}}/2} + (-1)^{n-1} \cdot (j\pi f T_{\mathrm{sw}})^{n-1} \cdot \mathrm{e}^{-j\pi f T_{\mathrm{sw}}/2}... \\
&\xrightarrow{n \text{ is even}} (j\pi f T_{\mathrm{sw}})^{n-1} \cdot \left(\mathrm{e}^{+j\pi f T_{\mathrm{sw}}/2} - \mathrm{e}^{-j\pi f T_{\mathrm{sw}}/2} \right) = (j\pi f T_{\mathrm{sw}})^{n-1} \cdot j \cdot \sin(\pi f T_{\mathrm{sw}}/2).
\end{aligned}
\tag{3.53}
$$

Applied to (3.51), the summation can be summarized to

$$S_{\mathrm{SD}}(f, D) = \mathrm{e}^{-\mathrm{j}\pi f T_{\mathrm{sw}}/2} \cdot S_{\mathrm{c}}(f) + \mathrm{e}^{-\mathrm{j}\pi f T_{\mathrm{sw}}}...$$

$$\cdot \sum_{m=-\infty}^{\infty} \sum_{n=1}^{\infty} \frac{(\mathrm{j}\pi f T_{\mathrm{sw}})^{2n-2}}{2^{2n-2}(2n-1)!} \cdot D^{*(2n-1)}(f - m f_{\mathrm{sw}}) \cdot \cos(\pi f T_{\mathrm{sw}}/2)...$$

$$+ \mathrm{j} \cdot \frac{(\mathrm{j}\pi f T_{\mathrm{sw}})^{2n-1}}{2^{2n-1}(2n)!} \cdot D^{*(2n)}(f - m f_{\mathrm{sw}}) \cdot \sin(\pi f T_{\mathrm{sw}}/2) \quad [15, (49)].$$

$$(3.54)$$

In (3.54), odd carrier groups ($n = 1, 3, ...$) are defined by the first part of the summation and even carrier groups ($n = 2, 4, ...$) are defined by the second part of the summation. Sampling is applied to obtain the Fourier coefficient of order k, expressed as

$$S_{\mathrm{SD},k} = \mathrm{e}^{-\mathrm{j}\pi k f_0 T_{\mathrm{sw}}/2} \cdot S_{\mathrm{c},k} + \mathrm{e}^{-\mathrm{j}\pi k f_0 T_{\mathrm{sw}}}...$$

$$\cdot \sum_{m=-m_{\max}}^{m_{\max}} \sum_{n=1}^{n_{\max}} \frac{(\mathrm{j}k\omega_0 T_{\mathrm{sw}}/2)^{2n-2}}{2^{2n-2}(2n-1)!} \cdot \left[\vec{D}^{*(2n-1)}\right]_{(k-m f_{\mathrm{sw}}/f_0)} \cdot \cos(k\omega_0 T_{\mathrm{sw}}/4)...$$

$$+ \mathrm{j} \cdot \frac{(\mathrm{j}k\omega_0 T_{\mathrm{sw}}/2)^{2n-1}}{2^{2n-1}(2n)!} \cdot \left[\vec{D}^{*(2n)}\right]_{(k-m f_{\mathrm{sw}}/f_0)} \cdot \sin(k\omega_0 T_{\mathrm{sw}}/4).$$

$$(3.55)$$

AD-PWM

For AD-PWM, the duty cycle of the second edge is sampled at the center of the switching period. The modulation process is depicted in Figure 3.12, visualizing that the only difference of AD-PWM in comparison to SD-PWM is the duty cycle of the second edge and its influence of the TE-PWM component. The switching function for AD-PWM is described by

$$s_{\mathrm{AD}}(t, d) = s_{\mathrm{c}}(t - T_{\mathrm{sw}}/4) + s_{\mathrm{dLE}}(t + T_{\mathrm{sw}}/4, d[m T_{\mathrm{sw}}]/2)...$$
$$+ s_{\mathrm{dTE}}(t - T_{\mathrm{sw}}/4, d[(m + 1/2)T_{\mathrm{sw}}]/2),$$

$$(3.56)$$

which stands in contrast to the derivation published in [15, p. 2248]. The sampling points of the duty cycle $[m T_{\mathrm{sw}}]$ and $[(m + 1/2)T_{\mathrm{sw}}]$ are included to stress the difference for the trailing edge and the leading edge. The Fourier transform of the switching function in (3.56) results in

$$S_{\mathrm{AD}}(f, d) = \mathrm{e}^{-\mathrm{j}\pi f T_{\mathrm{sw}}/2} \cdot S_{\mathrm{c}}(f) + \mathrm{e}^{-\mathrm{j}\pi f T_{\mathrm{sw}}/2} \cdot S_{\mathrm{TE}}(f, d[(m + 1/2)T_{\mathrm{sw}}]/2)...$$
$$+ \mathrm{e}^{+\mathrm{j}\pi f T_{\mathrm{sw}}/2} \cdot S_{\mathrm{LE}}(f, d[m T_{\mathrm{sw}}]/2)$$

$$(3.57)$$

The influence of the duty cycle's time shift of $T_{\mathrm{sw}}/2$ on the Fourier transform in (3.36) yields:

$$\sum_{m=-\infty}^{\infty} (d[(m+1/2)T_{\mathrm{sw}}])^n \cdot \mathrm{e}^{-\mathrm{j}2\pi f m T_{\mathrm{sw}}} = \mathrm{e}^{\mathrm{j}\pi f T_{\mathrm{sw}}} \cdot D_{\mathrm{s}}^{*n}(f)$$

$$= f_{\mathrm{sw}} \cdot \mathrm{e}^{\mathrm{j}\pi f T_{\mathrm{sw}}} \cdot D^{*n}(f) * \sum_{m=-\infty}^{\infty} \delta(f - m f_{\mathrm{sw}}) \quad (3.58)$$

$$= f_{\mathrm{sw}} \cdot \sum_{m=-\infty}^{\infty} \mathrm{e}^{\mathrm{j}\pi \cdot (f - m f_{\mathrm{sw}}) T_{\mathrm{sw}}} \cdot D^{*n}(f - m f_{\mathrm{sw}}).$$

Its application to (3.34) enables the description of the trailing-edge component for AD-PWM, with

$$S_{\mathrm{dTE}}(f, d[(m+1/2)T_{\mathrm{sw}}]/2)$$

$$= \frac{1}{\mathrm{j}\pi f} \cdot \mathrm{e}^{-\mathrm{j}\pi f T_{\mathrm{sw}}} \cdot \sum_{n=1}^{\infty} -\frac{(-\mathrm{j}\pi f T_{\mathrm{sw}})^n}{n!} \cdot \sum_{m=-\infty}^{\infty} (d[(m+1/2)T_{\mathrm{sw}}]/2)^n \cdot \mathrm{e}^{-\mathrm{j}2\pi f m T_{\mathrm{sw}}}$$

$$= \mathrm{e}^{-\mathrm{j}\pi f T_{\mathrm{sw}}} \cdot \sum_{m=-\infty}^{\infty} \sum_{n=1}^{\infty} \frac{(-\mathrm{j}\pi f T_{\mathrm{sw}})^{n-1}}{2^n \cdot n!} \cdot \sum_{m=-\infty}^{\infty} (d[(m+1/2)T_{\mathrm{sw}}])^n \cdot \mathrm{e}^{-\mathrm{j}2\pi f m T_{\mathrm{sw}}} \quad (3.59)$$

$$= \mathrm{e}^{-\mathrm{j}\pi f T_{\mathrm{sw}}} \cdot \sum_{m=-\infty}^{\infty} \sum_{n=1}^{\infty} \frac{(-\mathrm{j}\pi f T_{\mathrm{sw}})^{n-1}}{2^n \cdot n!} \cdot D^{*n}(f - m f_{\mathrm{sw}}) \cdot \mathrm{e}^{\mathrm{j}\pi \cdot (f - m f_{\mathrm{sw}}) T_{\mathrm{sw}}}.$$

Appying the results from (3.59) and (3.47) to (3.57) results in:

$$S_{\mathrm{AD}}(f, D) = \mathrm{e}^{-\mathrm{j}\pi f T_{\mathrm{sw}}/2} \cdot S_{\mathrm{c}}(f)...$$

$$+ \mathrm{e}^{-\mathrm{j}\pi f T_{\mathrm{sw}}/2} \cdot \mathrm{e}^{-\mathrm{j}\pi f T_{\mathrm{sw}}} \cdot \sum_{m=-\infty}^{\infty} \sum_{n=1}^{\infty} \frac{(-\mathrm{j}\pi f T_{\mathrm{sw}})^{n-1}}{2^n \cdot n!} \cdot D^{*n}(f - m f_{\mathrm{sw}}) \cdot \mathrm{e}^{\mathrm{j}\pi \cdot (f - m f_{\mathrm{sw}}) T_{\mathrm{sw}}}...$$

$$+ \mathrm{e}^{+\mathrm{j}\pi f T_{\mathrm{sw}}/2} \cdot \mathrm{e}^{-\mathrm{j}\pi f T_{\mathrm{sw}}} \cdot \sum_{m=-\infty}^{\infty} \sum_{n=1}^{\infty} \frac{(\mathrm{j}\pi f T_{\mathrm{sw}})^{n-1}}{2^n \cdot n!} \cdot D^{*n}(f - m f_{\mathrm{sw}})$$

$$= \mathrm{e}^{-\mathrm{j}\pi f T_{\mathrm{sw}}/2} \cdot S_{\mathrm{c}}(f)...$$

$$+ \mathrm{e}^{-\mathrm{j}\pi f T_{\mathrm{sw}}/2} \cdot \sum_{m=-\infty}^{\infty} \sum_{n=1}^{\infty} \frac{(-\mathrm{j}\pi f T_{\mathrm{sw}})^{n-1}}{2^n \cdot n!} \cdot D^{*n}(f - m f_{\mathrm{sw}}) \cdot \mathrm{e}^{\mathrm{j}\pi m}...$$

$$+ \mathrm{e}^{-\mathrm{j}\pi f T_{\mathrm{sw}}/2} \cdot \sum_{m=-\infty}^{\infty} \sum_{n=1}^{\infty} \frac{(\mathrm{j}\pi f T_{\mathrm{sw}})^{n-1}}{2^n \cdot n!} \cdot D^{*n}(f - m f_{\mathrm{sw}})$$

$$= \mathrm{e}^{-\mathrm{j}\pi f T_{\mathrm{sw}}/2} \cdot S_{\mathrm{c}}(f)...$$

$$+ \mathrm{e}^{-\mathrm{j}\pi f T_{\mathrm{sw}}/2} \cdot \sum_{m=-\infty}^{\infty} \sum_{n=1}^{\infty} \frac{(\mathrm{j}\pi f T_{\mathrm{sw}})^{n-1}}{2^n \cdot n!} \cdot D^{*n}(f - m f_{\mathrm{sw}}) \cdot \left(1 - (-1)^{m+n}\right).$$

$$(3.60)$$

Sampling is applied to obtain the Fourier coefficient of order k, expressed as

$$S_{\mathrm{AD},k} = \mathrm{e}^{-\mathrm{j}\pi k f_0 T_{\mathrm{sw}}/2} \cdot S_{\mathrm{c},k}\ldots$$
$$+ \mathrm{e}^{-\mathrm{j}\pi k f_0 T_{\mathrm{sw}}/2} \sum_{m=-m_{\max}}^{m_{\max}} \sum_{n=1}^{n_{\max}} \frac{(\mathrm{j}k\omega_0 T_{\mathrm{sw}}/2)^{n-1}}{2^n n!} \cdot \left[\vec{D}^{*n}\right]_{(k-mf_{\mathrm{sw}}/f_0)} \cdot (1-(-1)^{m+n}).$$
$$(3.61)$$

Validation of the AD-PWM Model

In order to validate the correct derivation, (3.61) is evaluated numerically and compared to results from time-domain simulations. The PWM model that is implemented in Simulink is depicted in Figure 3.13, which includes the transformation of the continuous-time duty-cycle into a discrete-time duty-cycle, before the comparison with the carrier signal for generating the switching function. The duty cycle contains a fundamental frequency component with an amplitude of $|D_{,1}| = 0.7$ and a seventh harmonic component with an amplitude of $|D_{,7}| = 0.1$. The carrier to fundamental ratio is $f_{\mathrm{sw}}/f_{d0} = 3000/50 = 60$.

To show the influence of the convolution power of the duty cycle spectrum $D^{*n}(f)$, Figure 3.14 shows $D^{*n}(f)$ for the example case for the first 25 harmonics, including $D^{*1}(f) = D(f)$, $D^{*2}(f) = D(f)*D(f)$, $D^{*3}(f)$, and $D^{*7}(f)$. The graphs illustrate that the spectrum is widened and the amplitudes diminish with an increasing convolution power.

Figure 3.15 shows the amplitude spectrum $|S_{\mathrm{AD},k}|$ for the first 140 harmonics. The first graph visualizes the evaluation of (3.61) for $m_{\max} = 1$ and $n_{\max} = 2$ in blue. The simulation results depicted in red are obtained by applying an FFT to the time-domain waveform of the switching function, which are sampled with a high sampling rate of $5 \cdot 10^9$ to provide precise results. The
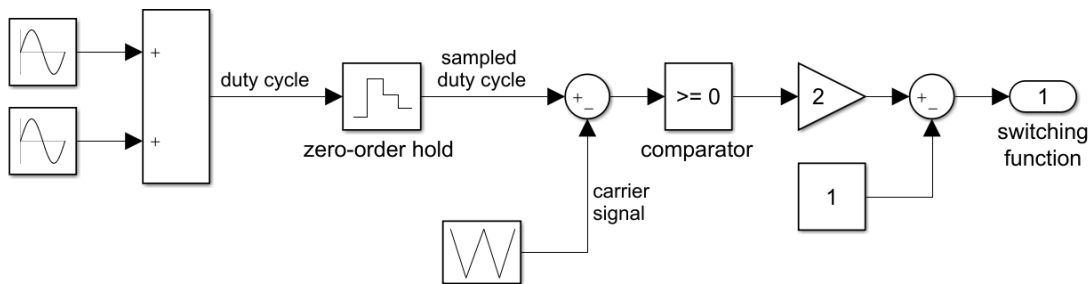

Figure 3.13: Implementation of regularly-sampled double-edge PWM. The superposition of the two sine waves forms the time-continuous duty cycle $d(t)$. The zero-order hold block incorporates the sampling process and the interpolation (the 'hold' function) that are necessary to transform the duty cycle into a discrete-time signal $d_{\mathrm{sw}}(t)$. The sampling frequency of the zero-order hold block is equal to the carrier frequency for SD-PWM and twice the carrier frequency for AD-PWM. The output of the comparator is the gate signal that can be converted to the switching function.
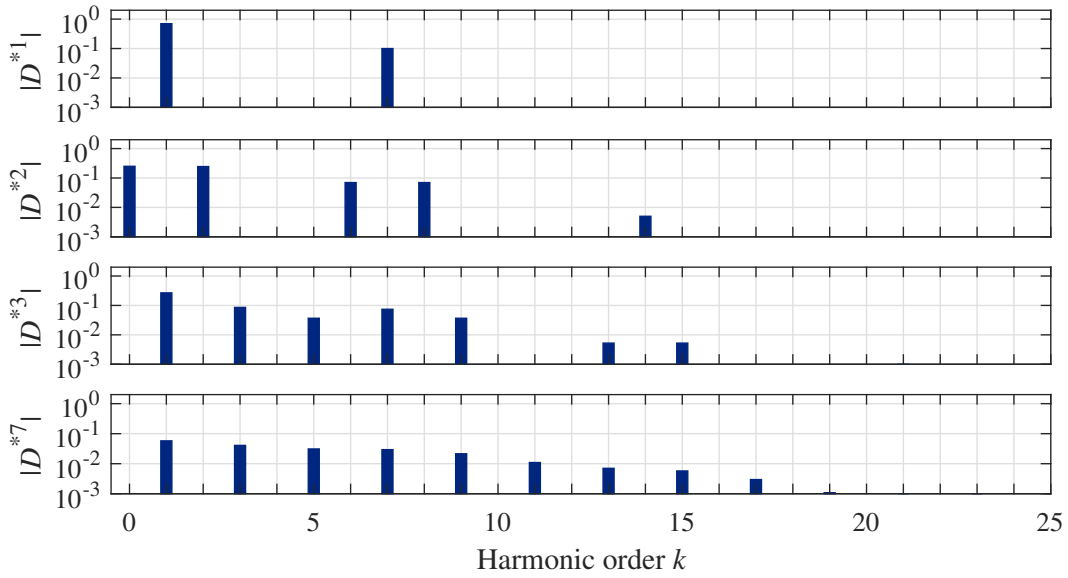
Figure 3.14: Duty cycle spectrum (first graph) and the convolution of the spectrum with itself (second graph), the convolution to the power of three (third graph), and the convolution to the power of seven (fourth graph) for the example case.

black bars in the second graph illustrate the difference of the frequency-domain results $S_{\mathrm{AD},k}^{\mathrm{FD}}$ from the time-domain results $S_{\mathrm{AD},k}^{\mathrm{TD}}$, with

$$|\Delta S_{\mathrm{AD},k}| = |S_{\mathrm{AD},k}^{\mathrm{FD}} - S_{\mathrm{AD},k}^{\mathrm{TD}}|. \tag{3.62}$$

The chosen definition enables to indicate differences resulting from magnitude differences or phase differences of the complex spectra in one variable. The graphs illustrate that large differences are present for the first carrier group, due to the small number of $n_{\mathrm{max}} = 2$. The components of the second carrier are not present in the frequency-domain results because the evaluation is limited to the first carrier group by $m_{\mathrm{max}} = 1$.

By increasing the number of considered side band harmonics to $n_{\mathrm{max}} = 7$ enables to enhance the precision for the first carrier group (third graph). The difference in the first carrier group is reduced to very low levels under 10^{-4} (fourth graph of Figure 3.15). A good approximation of the second is gained by choosing the parameters to $m_{\mathrm{max}} = 2$ and $n_{\mathrm{max}} = 7$ (fifth graph), with differences in the second carrier group under 10^{-3} (sixth graph).

The comparison to time-domain results validates the derived frequency-domain model for AD-PWM. Even higher numbers of m_{max} and n_{max} would result in a further increase of precision and an increased computational effort. The choice depends on the parameters, the system topology, and the requirements of the of the application.

When the duty cycle contains a single frequency component, the method described in this section produces the same results as the double Fourier series approach [15]. Thus, a numerical evaluation of (3.55) for SD-PWM and (3.61) for AD-PWM is used as a standard method in
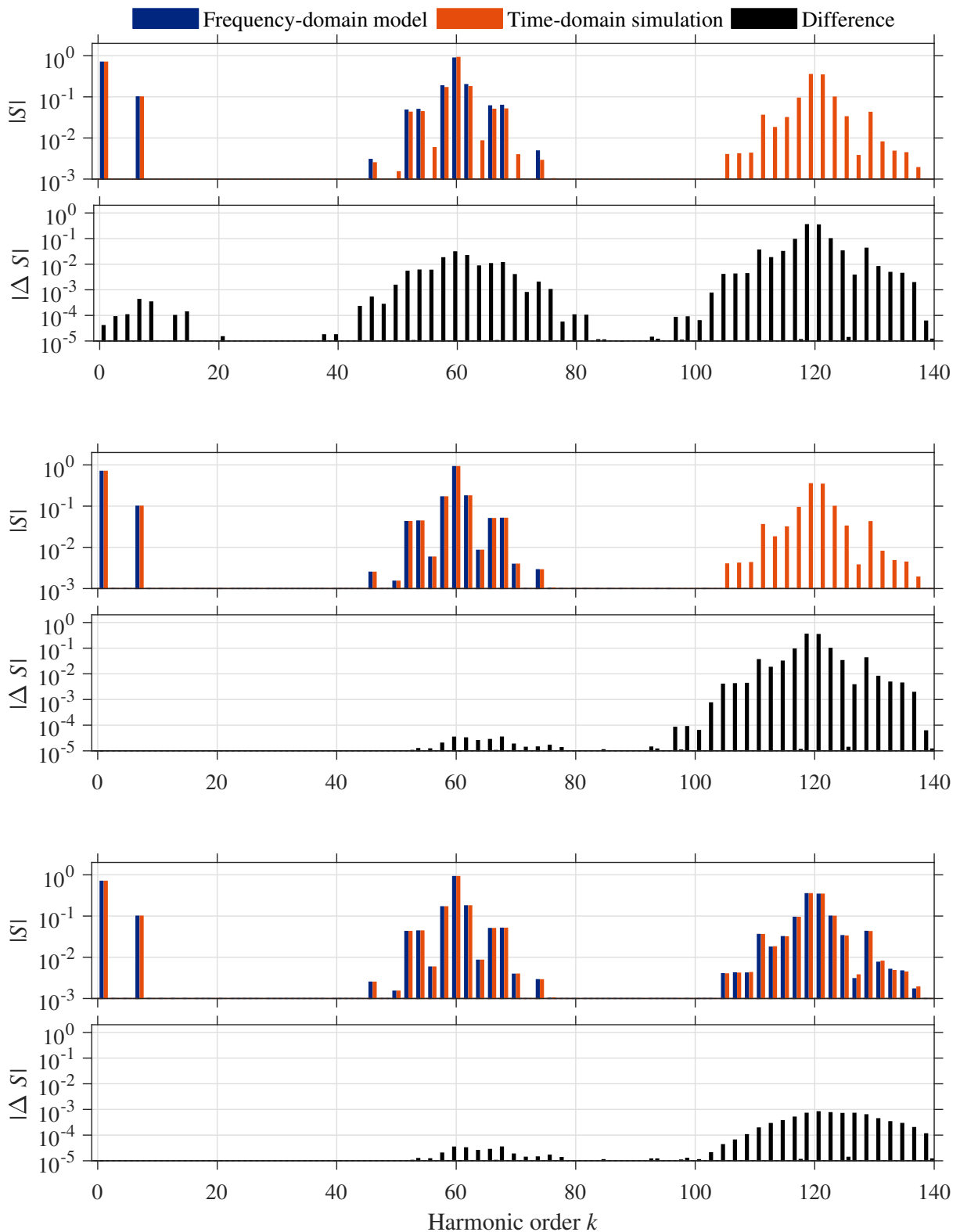
Figure 3.15: Switching function spectrum for AD-PWM with a duty cycle containing a fundamental component of $|D_{,1}| = 0.7$ and a seventh harmonic of $|D_{,7}| = 0.1$. The carrier to fundamental ratio is $f_{\text{sw}}/f_{d0} = 60$. Comparison of frequency-domain results for $m_{\max} = 1$ and $n_{\max} = 2$ with time-domain results (first graph) and their difference based on the complex spectra (second graph). The same comparison is shown in graph three and four for $m_{\max} = 1$ and $n_{\max} = 7$ and in graph five and six for $m_{\max} = 2$ and $n_{\max} = 7$.

this thesis, regardless of the duty cycle containing single-frequency components or multiple-frequency components.

Space Vector Modulation

Van der Broeck *et al.* [46] introduced space vector modulation (SVM) as a PWM method for three-phase VSI that extends the linear modulation range and can lead to lower distortion levels. The method was further analyzed and compared to other continuous and discontinuous PWM methods [47–51].

SVM has a close relationship with regularly-sampled PWM and creates the same switching function spectrum as a carrier based modulation method that has a distorted duty cycle [51]. The equivalent duty cycle of phase ν that would be applied to the carrier-based PWM is called $d_{\mathrm{SVM}\nu}$ and consists of a sinusoidal duty cycle d_ν and an additional zero-sequence component d_0:

$$d_{\mathrm{SVM}\nu}(t) = d_\nu(t) + d_0(t), \quad \nu \in \{1, 2, 3\} \tag{3.63}$$

The PWM process creates a switching pattern of the three switching functions in each switching period in order to generate the desired output voltage vector. The switching states where all half-bridges are connected with the positive dc-link node ($s_1 = s_2 = s_3 = 1$) or the negative dc-link node ($s_1 = s_2 = s_3 = -1$) are called zero-vector states. All other states are called active-vector states. For SVM, the times that the switching pattern remains in the two zero-vector states are chosen to be equally long. This can be implemented by shifting the zero-sequence component of the duty cycle into the center of the maximum and the minimum values of the phase duty cycles in each switching period, with

$$d_0(t) = -\frac{\max(d_1(t), d_2(t), d_3(t)) + \min(d_1(t), d_2(t), d_3(t))}{2} \quad \text{[12].} \tag{3.64}$$

Mouton *et al.* [17] showed that the output spectrum for SVM, as a summation of the two input signals in (3.63), results in the convolution of the side-band spectra that result from two individual PWM processes with the input signals $d_\nu(t)$ and $d_0(t)$. Likewise, other analytical methods describing the PWM process (e.g. [15]) can be used when the spectrum of $d_{\mathrm{SVM}\nu}$ is known.

In the case of single-frequency duty cycles d_ν, the zero-sequence duty cycle results in a triangular wave form with triple frequency and the resulting waveforms are shown in Figure 3.16 for an input duty cycle with an amplitude of 0.9. For duty cycles containing multiple frequencies d_ν, the zero-sequence duty cycle deviates from the triangular waveform. Figure 3.17 shows the resulting waveforms for an input duty cycle containing unsymmetrical fundamental frequency components with amplitude of $\{0.9, 0.45, 0.9\}$ and an additional symmetrical fifth harmonic with an amplitude of 0.3. For a frequency-domain description of SVM for multiple-frequency
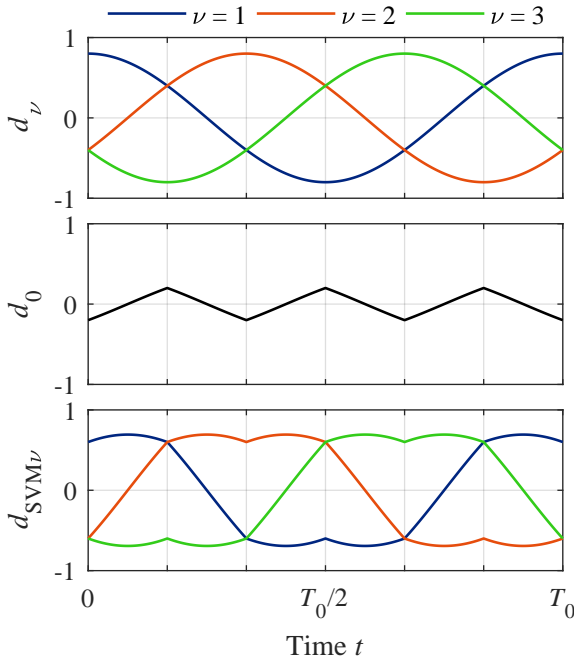
Figure 3.16: Duty cycle for SVM with symmetrical single-frequency input signals. The resulting duty cycle for SVM $d_{\mathrm{SVM}\nu}$ is the superposition of the sinusoidal duty cycle $d_\nu(t)$ and the zero-sequence component d_0, which has a triangular waveform.
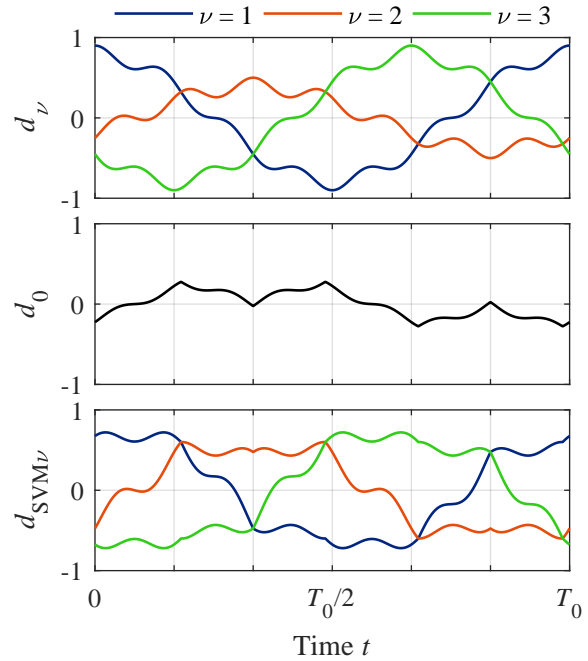
Figure 3.17: Duty cycle for SVM with unsymmetrical multiple-frequency input signals. The zero-sequence component d_0 differs from its original triangular waveform, due to the additional frequency components and the asymmetry in $d_\nu(t)$. $d_{\mathrm{SVM}\nu}$ is the superposition of d_0 and $d_\nu(t)$.

inputs, the Fourier transform of (3.64) is required as a function

$$(D_1(f), D_2(f), D_3(f)) \longmapsto D_0(f). \tag{3.65}$$

No solution of (3.65) for SVM with multiple-frequency input signals was found either in the literature review or in this thesis, due to the absence of general Fourier transforms of the min and max functions.

3.3 Linear Electrical Components

The relationship of the ac-side and dc-side signals are described in (3.4)-(3.5) by a nonlinear interaction with the switching function. In contrast, the relationship between the currents and voltages within one side is often linear. The ac-side impedance defines the relationship of the ac-side current and the ac-side voltage. Depending on the application, the ac-side impedance represents a grid filter, a motor stray inductance or a passive load. In a similar way, the dc-link capacitor and an optional load in the dc link define the relationship of the dc-side current and the dc-side voltage. These components can often be modeled as linear devices. When exceeding the

normal operating area or the defined frequency range where the chosen modeling assumptions are valid, these components have an increasing nonlinear behavior, which might require consideration in the modeling depth. The nonlinear behavior that is introduced in electrical machines is further discussed in Chapter 6.

When the components form LTI systems, they can be described in the frequency domain by continuous transfer functions, which can be obtained using a Laplace transform of the system's differential equations or the two-port network theory. By sampling the continuous transfer functions, discrete transfer functions described by Fourier coefficients are obtained. In the following section, the ac-side impedance and the dc link are used as examples for the derivation of the transfer functions of the linear components.

3.3.1 AC-Side Subsystem

For the single-phase ac-side impedance depicted in Figure 3.1, the ac-side subsystem is described by a differential equation

$$R_{\mathrm{ac}} \cdot i_{\mathrm{ac}}(t) + L_{\mathrm{ac}} \cdot \frac{\mathrm{d}}{\mathrm{d}t} i_{\mathrm{ac}}(t) = u_{\mathrm{dis}}(t) - u_{\mathrm{ac1}}(t) + u_{\mathrm{ac2}}(t), \tag{3.66}$$

with a resistance R_{ac} and an inductance L_{ac}.

The linear components can be described in the frequency domain for each harmonic component independently, where the equation of the k-th harmonic results in

$$(R_{\mathrm{ac}} + \mathrm{j}k\omega_0 L_{\mathrm{ac}}) \cdot I_{\mathrm{ac}} = U_{\mathrm{dis}} - U_{\mathrm{ac1}} + U_{\mathrm{ac2}}. \tag{3.67}$$

A combined notation for all harmonics results in a vector representation

$$\boldsymbol{Z}_{\mathrm{ac}} \cdot \vec{I}_{\mathrm{ac}} = \vec{U}_{\mathrm{dis}} - \vec{U}_{\mathrm{ac1}} + \vec{U}_{\mathrm{ac2}}, \tag{3.68}$$

where the impedance is described by a diagonal matrix

$$\boldsymbol{Z}_{\mathrm{ac}} = \mathrm{diag}(Z_{\mathrm{ac},-k_{\mathrm{max}}}, .., Z_{\mathrm{ac},k_{\mathrm{max}}}), \tag{3.69}$$

with the diagonal elements

$$Z_{\mathrm{ac,k}} = (R_{\mathrm{ac}} + \mathrm{j}k\omega_0 L_{\mathrm{ac}}), \quad k \in \{-k_{\mathrm{max}}, ..., k_{\mathrm{max}}\}. \tag{3.70}$$

Alternatively, an admittance representation

$$\boldsymbol{Y}_{\mathrm{ac}} = \mathrm{diag}(Y_{\mathrm{ac},-k_{\mathrm{max}}}, .., Y_{\mathrm{ac},k_{\mathrm{max}}}) \tag{3.71}$$

can be used, with the diagonal elements

$$Y_{\text{ac,k}} = 1/Z_{\text{ac,k}} = 1/(R_{\text{ac}} + jk\omega_0 L_{\text{ac}}), \quad k \in \{-k_{\max}, \ldots, k_{\max}\}, \tag{3.72}$$

and the ac-side subsystem is described by the linear equation system

$$\vec{I}_{\text{ac}} = \boldsymbol{Y}_{\text{ac}} \cdot \left(\vec{U}_{\text{dis}} - \vec{U}_{\text{ac1}} + \vec{U}_{\text{ac2}}\right). \tag{3.73}$$

Extending the approach to the symmetrical three-phase impedance depicted in Figure 3.2 yields a differential equation system for the time domain, with

$$R_{\text{ac}} \cdot \begin{bmatrix} i_{\text{ac1}}(t) \\ i_{\text{ac2}}(t) \\ i_{\text{ac3}}(t) \end{bmatrix} + L_{\text{ac}} \cdot \frac{\mathrm{d}}{\mathrm{d}t} \begin{bmatrix} i_{\text{ac1}}(t) \\ i_{\text{ac2}}(t) \\ i_{\text{ac3}}(t) \end{bmatrix} = \frac{1}{3} \cdot \begin{bmatrix} 2 & -1 & -1 \\ -1 & 2 & -1 \\ -1 & -1 & 2 \end{bmatrix} \cdot \begin{bmatrix} u_{\text{dis1}}(t) - u_{\text{ac1}}(t) \\ u_{\text{dis2}}(t) - u_{\text{ac2}}(t) \\ u_{\text{dis3}}(t) - u_{\text{ac3}}(t) \end{bmatrix}, \tag{3.74}$$

and a linear equation system in the frequency domain, with

$$\begin{bmatrix} \vec{I}_{\text{ac1}} \\ \vec{I}_{\text{ac2}} \\ \vec{I}_{\text{ac3}} \end{bmatrix} = \frac{1}{3} \cdot \begin{bmatrix} 2\boldsymbol{Y}_{\text{ac}} & -\boldsymbol{Y}_{\text{ac}} & -\boldsymbol{Y}_{\text{ac}} \\ -\boldsymbol{Y}_{\text{ac}} & 2\boldsymbol{Y}_{\text{ac}} & -\boldsymbol{Y}_{\text{ac}} \\ -\boldsymbol{Y}_{\text{ac}} & -\boldsymbol{Y}_{\text{ac}} & 2\boldsymbol{Y}_{\text{ac}} \end{bmatrix} \cdot \begin{bmatrix} \vec{U}_{\text{dis1}} - \vec{U}_{\text{ac1}} \\ \vec{U}_{\text{dis2}} - \vec{U}_{\text{ac2}} \\ \vec{U}_{\text{dis3}} - \vec{U}_{\text{ac3}} \end{bmatrix}. \tag{3.75}$$

Three-Phase LCL Grid Filter

For converter applications that require a low distortion of the ac-side current, higher order filters are applied, enhancing the damping of high order harmonics. A symmetrical filter can be regarded as the two-port network depicted in Figure 3.18, which can represent a third-order LCL grid filter connecting the independent three-phase voltage vectors of the grid $\vec{U}_{\text{g}} = [\vec{U}_{\text{g1}}, \vec{U}_{\text{g2}}, \vec{U}_{\text{g3}}]^{\text{T}}$ and the converter $\vec{U}_{\text{ac}} = [\vec{U}_{\text{ac1}}, \vec{U}_{\text{ac2}}, \vec{U}_{\text{ac3}}]^{\text{T}}$. The symmetrical impedance of the LCL filter can be calculated from a single-phase equivalent circuit (Figure 3.19), resulting for the harmonic order k in:

$$\begin{aligned} Z_{1,k} &= R_1 + jk\omega_0 L_1, \\ Z_{2,k} &= R_{\text{d}} + \frac{1}{jk\omega_0 C_{\text{f}}}, \\ Z_{3,k} &= R_2 + jk\omega_0 L_2, \end{aligned} \tag{3.76}$$

where L_1 and R_1 are the grid-side inductance and resistance, C_{f} and R_{d} are the filter capacitance and the series damping resistance, and L_2 and R_2 are the converter-side inductance and resistance.

Using the two-port admittance representation, the vectors of the grid voltages and the converter voltages are the two input variables, and the vectors of the grid currents $\vec{I}_{\text{g}} = [\vec{I}_{\text{g1}}, \vec{I}_{\text{g2}}, \vec{I}_{\text{g3}}]^{\text{T}}$ and the converter currents $\vec{I}_{\text{ac}} = [\vec{I}_{\text{ac1}}, \vec{I}_{\text{ac2}}, \vec{I}_{\text{ac3}}]^{\text{T}}$ are the outputs, with
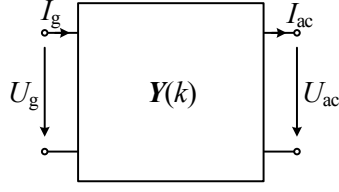
Figure 3.18: Filter as a two-port network

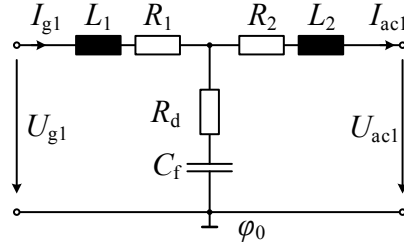**Figure 3.19:** Single-phase impedance model of the LCL-filter

$$
\begin{bmatrix} \vec{I}_{g1} \\ \vec{I}_{g2} \\ \vec{I}_{g3} \end{bmatrix} = \frac{1}{3} \cdot \begin{bmatrix} 2\boldsymbol{Y}_{11} & -\boldsymbol{Y}_{11} & -\boldsymbol{Y}_{11} \\ -\boldsymbol{Y}_{11} & 2\boldsymbol{Y}_{11} & -\boldsymbol{Y}_{11} \\ -\boldsymbol{Y}_{11} & -\boldsymbol{Y}_{11} & 2\boldsymbol{Y}_{11} \end{bmatrix} \cdot \begin{bmatrix} \vec{U}_{g1} \\ \vec{U}_{g2} \\ \vec{U}_{g3} \end{bmatrix} + \frac{1}{3} \cdot \begin{bmatrix} 2\boldsymbol{Y}_{12} & -\boldsymbol{Y}_{12} & -\boldsymbol{Y}_{12} \\ -\boldsymbol{Y}_{12} & 2\boldsymbol{Y}_{12} & -\boldsymbol{Y}_{12} \\ -\boldsymbol{Y}_{12} & -\boldsymbol{Y}_{12} & 2\boldsymbol{Y}_{12} \end{bmatrix} \cdot \begin{bmatrix} \vec{U}_{ac1} \\ \vec{U}_{ac2} \\ \vec{U}_{ac3} \end{bmatrix}
$$

$$
\begin{bmatrix} \vec{I}_{ac1} \\ \vec{I}_{ac2} \\ \vec{I}_{ac3} \end{bmatrix} = \frac{1}{3} \cdot \begin{bmatrix} 2\boldsymbol{Y}_{21} & -\boldsymbol{Y}_{21} & -\boldsymbol{Y}_{21} \\ -\boldsymbol{Y}_{21} & 2\boldsymbol{Y}_{21} & -\boldsymbol{Y}_{21} \\ -\boldsymbol{Y}_{21} & -\boldsymbol{Y}_{21} & 2\boldsymbol{Y}_{21} \end{bmatrix} \cdot \begin{bmatrix} \vec{U}_{g1} \\ \vec{U}_{g2} \\ \vec{U}_{g3} \end{bmatrix} + \frac{1}{3} \cdot \begin{bmatrix} 2\boldsymbol{Y}_{22} & -\boldsymbol{Y}_{22} & -\boldsymbol{Y}_{22} \\ -\boldsymbol{Y}_{22} & 2\boldsymbol{Y}_{22} & -\boldsymbol{Y}_{22} \\ -\boldsymbol{Y}_{22} & -\boldsymbol{Y}_{22} & 2\boldsymbol{Y}_{22} \end{bmatrix} \cdot \begin{bmatrix} \vec{U}_{ac1} \\ \vec{U}_{ac2} \\ \vec{U}_{ac3} \end{bmatrix} .
$$

$$(3.77)$$

One possible way to calculate the elements of the diagonal matrices $\boldsymbol{Y}_{11}, \boldsymbol{Y}_{12}, \boldsymbol{Y}_{21}, \boldsymbol{Y}_{22}$, is to calculate the elements of the impedance representation first, with

$$
\begin{aligned}
Z_{11,k} &= \left.\frac{U_{g,k}}{I_{g,k}}\right|_{I_{ac,k}=0} = Z_{1,k} + Z_{2,k}, \\
Z_{12,k} &= \left.\frac{U_{g,k}}{I_{ac,k}}\right|_{I_{g,k}=0} = -Z_{2,k}, \\
Z_{21,k} &= \left.\frac{U_{ac,k}}{I_{g,k}}\right|_{I_{ac,k}=0} = Z_{2,k}, \\
Z_{22,k} &= \left.\frac{U_{ac,k}}{I_{ac,k}}\right|_{I_{g,k}=0} = -Z_{2,k} - Z_{3,k},
\end{aligned}
\tag{3.78}
$$

followed by a transformation to the admittance representation, with

$$
Y_{11,k} = \frac{Z_{22,k}}{\det(\boldsymbol{Z}_{,k})}, \quad Y_{12,k} = \frac{-Z_{12,k}}{\det(\boldsymbol{Z}_{,k})}, \quad Y_{21,k} = \frac{-Z_{21,k}}{\det(\boldsymbol{Z}_{,k})}, \quad Y_{22,k} = \frac{Z_{11,k}}{\det(\boldsymbol{Z}_{,k})}, \tag{3.79}
$$

where the determinant is $\det(\boldsymbol{Z}_{,k}) = -(Z_{1,k} \cdot Z_{2,k} + Z_{1,k} \cdot Z_{3,k} + Z_{2,k} \cdot Z_{3,k})$.

3.3.2 DC-Link Subsystem

The voltage-stiff dc link in Figure 3.1 and Figure 3.2 consists of large capacitance C_{dc} and an optional resistive load, modeled with a resistance R_{dc}. The differential equation that connects the dc-side current i_{dc} and a dc-side disturbance current i_{dis} with the dc-side voltage u_{dc} results

in

$$C_{\mathrm{dc}} \cdot \frac{\mathrm{d}u_{\mathrm{dc}}(t)}{\mathrm{d}t} = i_{\mathrm{dc}}(t) + i_{\mathrm{dis}}(t). \tag{3.80}$$

The parasitic inductance that results from the connection of the power electronic devices to the dc-link capacitor and the equivalent series resistance (ESR) of the capacitor are neglected in this model.

The vector representation in the frequency domain is

$$\vec{U}_{\mathrm{dc}} = \boldsymbol{Z}_{\mathrm{dc}} \cdot (\vec{I}_{\mathrm{dc}} + \vec{I}_{\mathrm{dis}}), \tag{3.81}$$

where the diagonal matrix

$$\boldsymbol{Z}_{\mathrm{dc}} = \mathrm{diag}(Z_{\mathrm{dc},-k_{\max}}, .., Z_{\mathrm{dc},k_{\max}}) \tag{3.82}$$

represents the dc-side impedance for each harmonic, with the elements

$$Z_{\mathrm{dc,k}} = \frac{1}{\frac{1}{R_{\mathrm{dc}}} + \mathrm{j}k\omega_0 C_{\mathrm{dc}}}. \tag{3.83}$$

With no resistive load ($1/R_{\mathrm{dc}} = 0$) the dc-side impedance has a singularity for $k = 0$. In this case, the dc component of the dc-link voltage U_{dc0} is defined by boundary conditions, e.g. the power flow, and is regarded as a disturbance variable instead of as an unknown variable in the solution of the equation system.

3.4 Numerical Evaluation for VSI with Open-Loop Control

The relationships of the signals of a converter system form a closed loop, illustrated in the block diagram in Figure 3.20, where the ac-side signals (u_{ac}, i_{ac}) influence the dc-side signals (u_{dc}, i_{dc}) and vice versa. This energy conversion is defined by the convolution with the switching function spectrum. For self-commutated converters with open-loop control, the switching function is independent of the converter currents and voltages and can be regarded as a disturbance variable. For this reason, the equation system of the frequency-domain model is linear, with

$$\boldsymbol{A} \cdot \vec{X} = \vec{B}, \tag{3.84}$$

where $\boldsymbol{A}$ is the coefficient matrix, $\vec{X}$ is the vector of the unknown signals, and $\vec{B}$ is the vector of the known signals (disturbances). By limiting the number of considered harmonics to $k_{\max}$, each unknown signal is represented as a vector of the length $l = 2 \cdot k_{\max} + 1$. If the equation system contains N unknown signals, the coefficient matrix has a size of ($Nl \times Nl$).
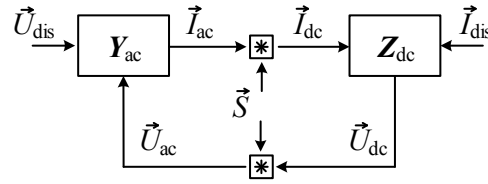
Figure 3.20: Block diagram of the harmonic interaction in a VSI with open-loop control

The equation system can be numerically solved in Matlab, using the automatic solver optimization of the matrix left divide (mldivid) function. In the solution process, Matlab performs an optimization, depending on the sparsity of $\boldsymbol{A}$ and $\vec{B}$. Considering a large number of harmonics, the solution process becomes time-consuming and the risk of numerical inaccuracy increases. In order to increase the accuracy and the computation speed or allow for the consideration of a larger number of harmonics, a compact system description with a small number of unknown signals is preferable.

In the following section, the equation system for the single-phase VSI is developed in a compact structure that enhances the solution process. The numerical evaluation is used to show the successful calculation of the interaction for sine-triangle modulation using SD-PWM and AD-PWM. The method is extended to a three-phase VSI and the numerical evaluation shows the incorporation of a duty cycle containing multiple frequency components.

3.4.1 Single-Phase VSI

The single-phase full-bridge VSI in Figure 3.1 consists of two half bridges, described by the switching functions s_1 and s_2. Because the voltage seen by the load is the difference of the output voltages of the half bridges $u_{\mathrm{ac}} = u_{\mathrm{ac1}} - u_{\mathrm{ac2}}$, the desired setpoint is described by a single duty cycle.

Nevertheless, there are different approaches to switching the second half bridge in relation to the first half bridge in order to reach this goal. These approaches are called modulation strategies here, to avoid confusion with the choice of the modulation method, such as AD-PWM. Switching the second half bridge with the inverted signal of the first half bridge $\bar{s}_1(t) = s_2(t)$ is called bipolar modulation and leads to an output voltage that has two levels $u_{\mathrm{ac}} \in \{-u_{\mathrm{dc}}, u_{\mathrm{dc}}\}$.

The modulation strategy known as unipolar modulation can be obtained by either inverting the duty cycle or the carrier signal of the second half bridge. Because the switching instants of the two half bridges occur at different times, the output voltage contains an additional zero-voltage level, with $u_{\mathrm{ac}} \in \{-u_{\mathrm{dc}}, 0, u_{\mathrm{dc}}\}$. This leads to a significantly improved spectrum and even to a complete cancellation of the side band harmonics for odd carrier multiples in the case of N-PWM and AD-PWM [12]. However, bipolar modulation might be preferred in some applications, due to a lower electromagnetic interference (EMI) impact on the load [32].

Using the vector representation in (3.6) and (3.7) for the two half bridges and the linear model of the ac-side and dc-side subsystems in (3.73) and (3.81), the single-phase VSI can be described by four equations, with

$$\vec{U}_{\text{ac}} = \vec{U}_{\text{ac1}} - \vec{U}_{\text{ac2}} = \frac{1}{2} \cdot \boldsymbol{C}(\vec{S}_1 - \vec{S}_2) \cdot \vec{U}_{\text{dc}}, \tag{3.85}$$

$$\vec{I}_{\text{ac}} = \boldsymbol{Y}_{\text{ac}} \cdot \left(\vec{U}_{\text{dis}} - \vec{U}_{\text{ac}} \right), \tag{3.86}$$

$$\vec{U}_{\text{dc}} = \boldsymbol{Z}_{\text{dc}} \cdot \left(\vec{I}_{\text{dis}} + \vec{I}_{\text{dc}} \right), \tag{3.87}$$

$$\vec{I}_{\text{dc}} = \vec{I}_{\text{dc1}} - \vec{I}_{\text{dc2}} = \frac{1}{2} \cdot \boldsymbol{C}(\vec{S}_1 - \vec{S}_2) \cdot \vec{I}_{\text{ac}}. \tag{3.88}$$

These equations are valid for all presented modulation methods and modulation strategies. Transferring the equations in the matrix form of (3.84) results in

$$\underbrace{\begin{bmatrix} \boldsymbol{E} & \boldsymbol{0} & -\frac{1}{2} \cdot \boldsymbol{C}(\vec{S}_1 - \vec{S}_2) & \boldsymbol{0} \\ \boldsymbol{Y}_{\text{ac}} & \boldsymbol{E} & \boldsymbol{0} & \boldsymbol{0} \\ \boldsymbol{0} & \boldsymbol{0} & \boldsymbol{E} & -\boldsymbol{Z}_{\text{dc}} \\ \boldsymbol{0} & -\frac{1}{2} \cdot \boldsymbol{C}(\vec{S}_1 - \vec{S}_2) & \boldsymbol{0} & \boldsymbol{E} \end{bmatrix}}_{\boldsymbol{A}} \cdot \underbrace{\begin{bmatrix} \vec{U}_{\text{ac}} \\ \vec{I}_{\text{ac}} \\ \vec{U}_{\text{dc}} \\ \vec{I}_{\text{dc}} \end{bmatrix}}_{\vec{X}} = \underbrace{\begin{bmatrix} \vec{0} \\ \boldsymbol{Y}_{\text{ac}} \cdot \vec{U}_{\text{dis}} \\ \boldsymbol{Z}_{\text{dc}} \cdot \vec{I}_{\text{dis}} \\ \vec{0}. \end{bmatrix}}_{\vec{B}}, \tag{3.89}$$

where $\boldsymbol{C}(.)$ is the convolution matrix defined in (2.40), $\boldsymbol{E}$ denotes the identity matrix, and $\boldsymbol{0}$ is the zero matrix. All elements of the matrix $\boldsymbol{A}$ are sub-matrices of the size $l \times l$. The form in (3.89) illustrates that the spectra of the switching functions have to be independent of the unknown signals, in order to create a linear equation system.

By eliminating three of the four variables, the equation system can be reduced to a quarter of the size. When choosing the dc-link voltage as the remaining variable, the equation system results in

$$\boldsymbol{A} = \boldsymbol{E} + \frac{1}{4} \cdot \boldsymbol{Z}_{\text{dc}} \cdot \boldsymbol{C}(\vec{S}_1 - \vec{S}_2) \cdot \boldsymbol{Y}_{\text{ac}} \cdot \boldsymbol{C}(\vec{S}_1 - \vec{S}_2),$$

$$\vec{X} = \vec{U}_{\text{dc}}, \tag{3.90}$$

$$\vec{B} = \boldsymbol{Z}_{\text{dc}} \cdot \left(\vec{I}_{\text{dis}} + \frac{1}{2} \cdot \boldsymbol{C}(\vec{S}_1 - \vec{S}_2) \cdot \boldsymbol{Y}_{\text{ac}} \cdot \vec{U}_{\text{dis}} \right).$$

The system matrix in (3.90) is dense and the number of elements is 16 times smaller than the sparse system matrix in (3.89). The reduction is beneficial for the numerical evaluation, especially when considering a large number of harmonics.

A benefit of choosing the dc-link voltage as the remaining variable is that boundary conditions for the dc-link voltage can be easily implemented. For example, the goal is to integrate a simplified model of an active front-end that controls the dc component of the dc-link voltage to U_{dc0} and injects additional harmonic currents into the dc link. Figure 3.21 illustrates how the
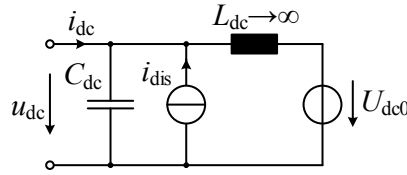
Figure 3.21: Equivalent circuit of the dc link in steady state, incorporating a fixed dc component of the dc-link voltage U_{dc0} represented by a voltage source that is connected to the capacitance via an infinite inductance. Harmonic disturbance currents can be considered by a current source i_{dis}.

incorporation results in the equivalent circuit of the dc link, using an ideal dc voltage source U_{dc0} and an inductor with infinity inductance L_{dc} and a disturbance current source i_{dis}. In time-domain simulations this is problematic, because a finite inductance L_{dc} must be chosen, which introduces a resonant circuit with the dc-link capacitance. For small inductance values the current of the voltage source contains unwanted harmonic components and for large values of L_{dc} the time constant of the resonant circuit is large, resulting in large simulation times to reach the steady state. In the frequency-domain model, the row of the equation system describing the dc component can simply be replaced by

$$\boldsymbol{A}\big|_{k=0} = [0, \ldots, 0, 1, 0, \ldots, 0], \quad \vec{B}\big|_{k=0} = U_{\mathrm{dc0}}. \tag{3.91}$$

The analytical results are presented for an example system with the parameters listed in Table 3.1. Unipolar modulation and AD-PWM are used with a switching frequency of 1 kHz. A single-frequency duty cycle with a frequency of $f_{\mathrm{d0}} = 50\,\mathrm{Hz}$ and a modulation index of $M = 0.4$ is applied. The fundamental frequency of the model is $f_0 = \gcd(f_0, f_{\mathrm{sw}}) = 50\,\mathrm{Hz}$. The switching function spectra result from evaluation of (3.61), where the PWM model considers $m_{\mathrm{max}} = 4$ carrier harmonics, $n_{\mathrm{max}} = 10$ sideband harmonics and the maximum harmonic order is $k_{\mathrm{max}} = 90$.

A disturbance voltage introduces a first harmonic component (50 Hz) with an amplitude of $\hat{u}_{\mathrm{dis},1}$ and a seventh harmonic component (350 Hz) with an amplitude of $\hat{u}_{\mathrm{dis},7}$ and zero phase-shift. The duty cycle of the first half bridge has a phase relation to the disturbance voltage of θ_{d0} and the second half bridge of $\theta_{\mathrm{d0}} + \pi$ (unipolar modulation). Solving the linear equation system (3.90) yields the dc-link voltage spectrum, which is used further to calculate the ac-side voltage, ac-side current, and dc-side current spectra.

The analytical spectra are compared in Figure 3.22 to results of time-domain simulations in Simulink/Plecs. The differences between the complex spectra are depicted in Figure 3.23. The first graph shows the magnitude of the switching function spectrum of the first half bridge $|\vec{S}_1|$. The spectrum contains the fundamental component at 50 Hz, and four carrier sideband groups around multiples of the switching frequency. There is a very good conformity between the results for the switching function spectrum.

Choosing a finite inductance of $L_{\mathrm{dc}} = 10\,\mathrm{mH}$ to connect the constant voltage source U_{dc0} to the
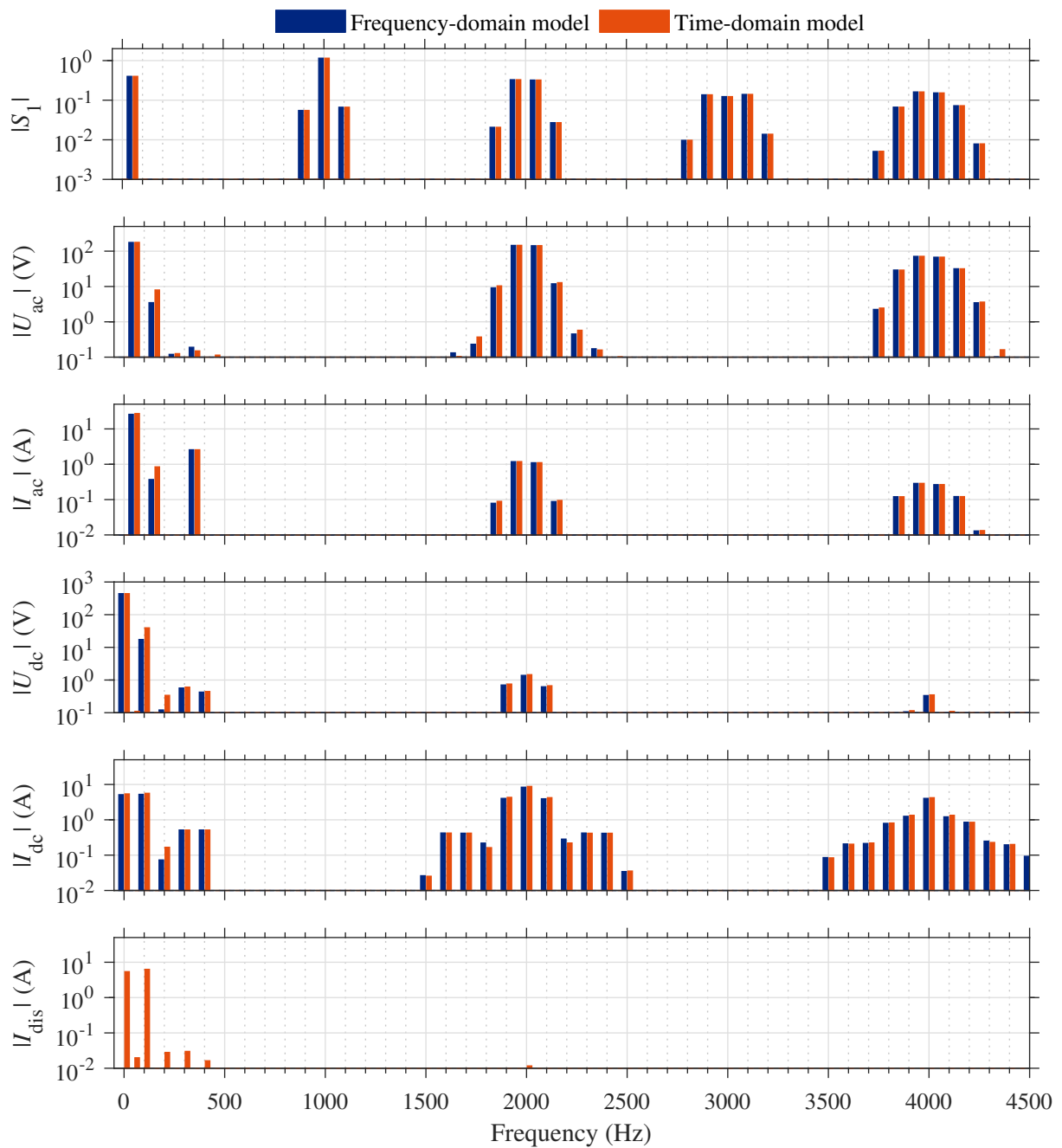
Figure 3.22: Comparison of frequency-domain model and time-domain simulations for a single-phase VSI with open-loop control for unipolar modulation and AD-PWM and $f_0 = f_{d0} = 50\,\text{Hz}$; $f_{sw} = 1\,\text{kHz}$. There is an introduction of harmonic disturbance currents in the simulation model that influences the currents and voltages of the system, due to the finite inductance coupling the dc link to a constant voltage source.
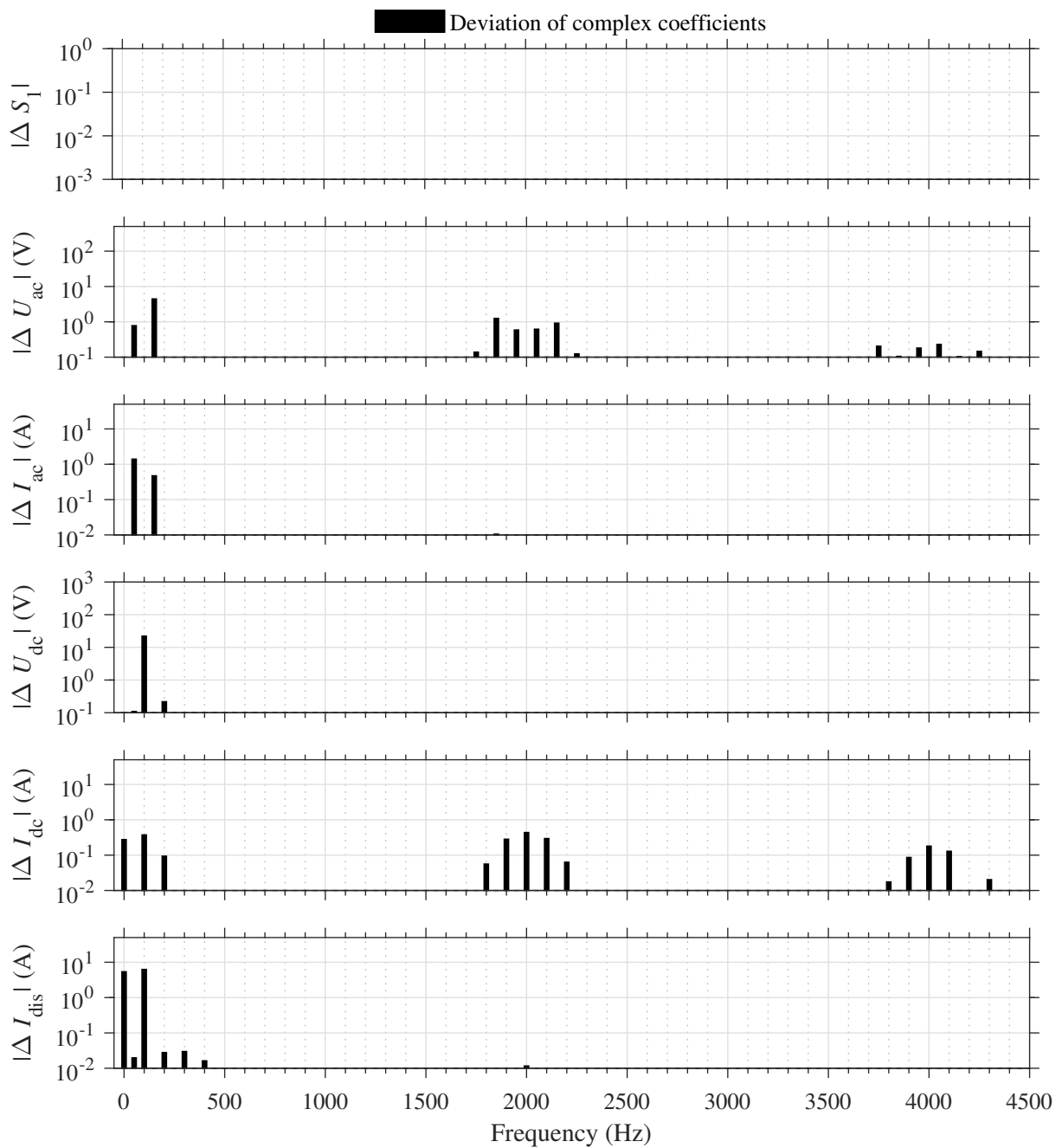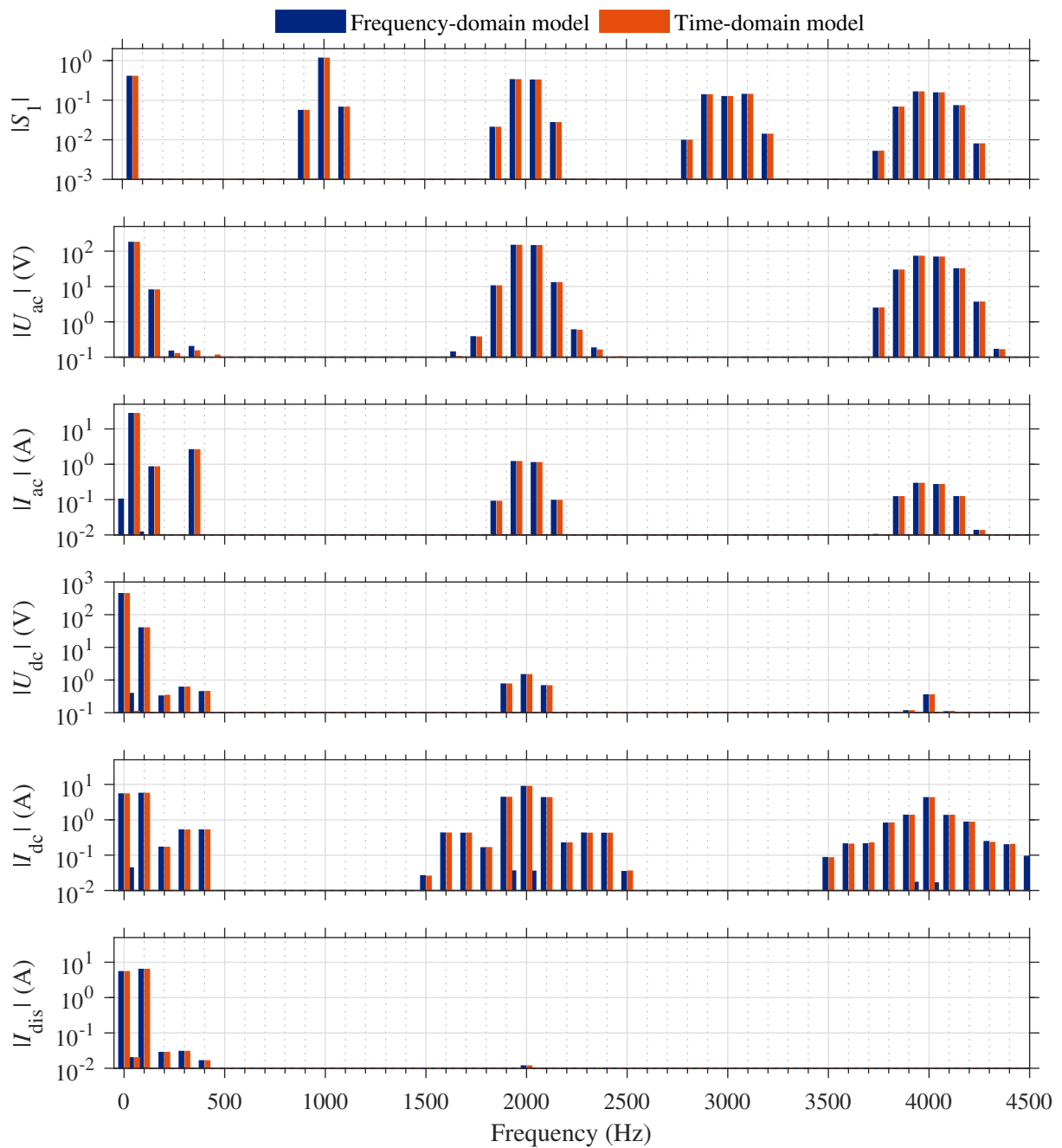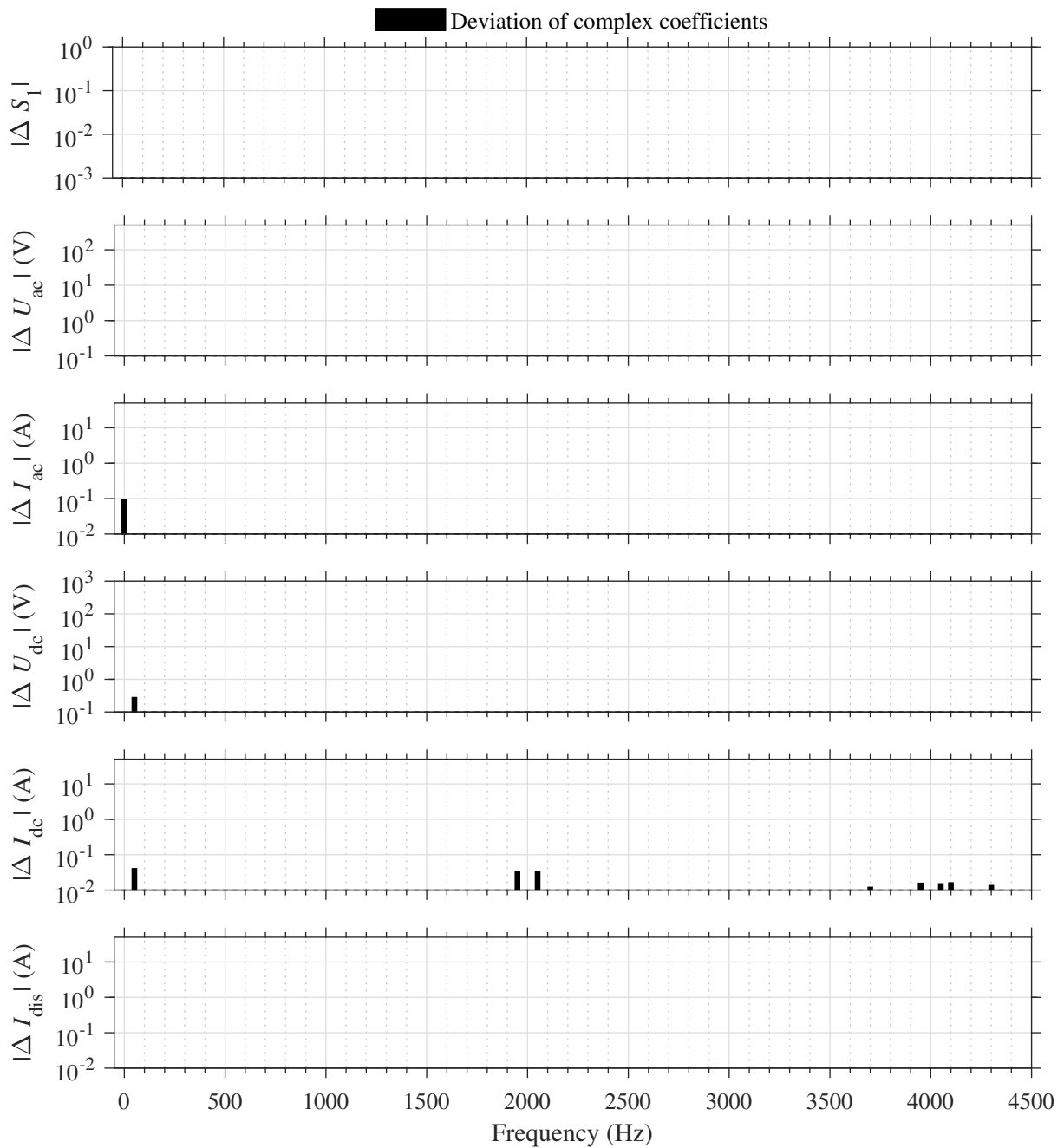
Figure 3.23: Differences of the complex spectra shown in Figure 3.22 for a single-phase VSI with open-loop control for unipolar modulation and AD-PWM and $f_0 = f_{d0} = 50\,\text{Hz}$; $f_{sw} = 1\,\text{kHz}$. There is an introduction of harmonic disturbance currents in the simulation model that influences the currents and voltages of the system, due to the finite inductance coupling the dc link to a constant voltage source.

Figure 3.24: Comparison of frequency-domain model and time-domain simulations for a single-phase VSI with open-loop control for unipolar modulation and AD-PWM and $f_0 = f_{d0} = 50\,\mathrm{Hz}$; $f_{sw} = 1\,\mathrm{kHz}$. The disturbance current that is simulated in the time-domain model is used as an input in the frequency-domain model.

Figure 3.25: Differences of the complex spectra shown in Figure 3.24 for a single-phase VSI with open-loop control for unipolar modulation and AD-PWM and $f_0 = f_{d0} = 50\,\text{Hz}$; $f_{sw} = 1\,\text{kHz}$. The disturbance current that is simulated in the time-domain model is used as an input in the frequency-domain model.

Table 3.1: Parameters of the single-phase VSI with open-loop control

Parameter	Symbol	Value
AC filter resistance	R_{ac}	$0.2\,\Omega$
AC filter inductance	L_{ac}	$10\,\mathrm{mH}$
Switching frequency	f_{sw}	$1\,\mathrm{kHz}$
Control frequency	f_{c}	$2\,\mathrm{kHz}$
Duty-cycle frequency	f_{d0}	$50\,\mathrm{Hz}$
Modulation index	M	0.4
Duty-cycle phase shift	θ_{d0}	$-20°$
DC link capacitance	C_{dc}	$480\,\mu\mathrm{F}$
DC-link voltage	U_{dc0}	$440\,\mathrm{V}$
DC-link inductance	L_{dc}	$10\,\mathrm{mH}$
Amplitude of disturbance voltage at f_{d0}	$\hat{u}_{\mathrm{dis,1}}$	$188\,\mathrm{V}$
Amplitude of disturbance voltage at $7 \cdot f_{\mathrm{d0}}$	$\hat{u}_{\mathrm{dis,7}}$	$56\,\mathrm{V}$
Fundamental frequency	f_0	$50\,\mathrm{Hz}$
Maximum harmonic order	k_{max}	90
Maximum carrier order	m_{max}	4
Maximum sideband order	n_{max}	10

dc link in the time-domain simulation model, results in an introduction of harmonic disturbance currents into the dc link (last graph in Figure 3.22). This leads to visible deviations for all current and voltage spectra of the system, as these harmonic components are further propagated to the ac side. By injecting these disturbance current harmonics into the frequency-domain model, it can be shown that they are the cause of the deviations: Figure 3.24 and Figure 3.25 show the complex spectra of the two models and their differences when the same disturbance current is used in both models. There is a good conformity in all signals. The carrier sideband groups around odd switching frequency multiples are canceled out in the voltage and current spectra, due to the unipolar modulation technique. The seventh harmonic component introduced by the disturbance voltage is visible in the ac-side current spectrum and is further propagated to the dc-side current and dc-link voltage as a sixth and eighth harmonic component. A comparison of the switching function spectrum with the ac-side voltage spectrum $|\vec{U}_{\mathrm{ac}}|$ in the second graph reveals the influence of the harmonics that are present in the dc-link voltage spectrum $|\vec{U}_{\mathrm{dc}}|$, illustrating the importance of considering the convolution of the switching function and dc-link voltage spectra. The same can be concluded by looking at the influence of the ac-side current spectrum $|\vec{I}_{\mathrm{ac}}|$ on the dc-side current spectrum $|\vec{I}_{\mathrm{dc}}|$.

3.4.2 Three-Phase VSI

The analytical model of the three-phase VSI in Figure 3.2 with open-loop control results in a linear equation system with a sparse structure:

$$
\boldsymbol{A} = \begin{bmatrix}
\boldsymbol{E} & \boldsymbol{0} & \boldsymbol{0} & \boldsymbol{0} & \boldsymbol{0} & \boldsymbol{0} & -\frac{1}{2}\boldsymbol{C}(\vec{S}_1) & \boldsymbol{0} \\
\boldsymbol{0} & \boldsymbol{E} & \boldsymbol{0} & \boldsymbol{0} & \boldsymbol{0} & \boldsymbol{0} & -\frac{1}{2}\boldsymbol{C}(\vec{S}_2) & \boldsymbol{0} \\
\boldsymbol{0} & \boldsymbol{0} & \boldsymbol{E} & \boldsymbol{0} & \boldsymbol{0} & \boldsymbol{0} & -\frac{1}{2}\boldsymbol{C}(\vec{S}_3) & \boldsymbol{0} \\
\frac{2}{3}\boldsymbol{Y}_{\mathrm{ac}} & -\frac{1}{3}\boldsymbol{Y}_{\mathrm{ac}} & -\frac{1}{3}\boldsymbol{Y}_{\mathrm{ac}} & \boldsymbol{E} & \boldsymbol{0} & \boldsymbol{0} & \boldsymbol{0} & \boldsymbol{0} \\
-\frac{1}{3}\boldsymbol{Y}_{\mathrm{ac}} & \frac{2}{3}\boldsymbol{Y}_{\mathrm{ac}} & -\frac{1}{3}\boldsymbol{Y}_{\mathrm{ac}} & \boldsymbol{0} & \boldsymbol{E} & \boldsymbol{0} & \boldsymbol{0} & \boldsymbol{0} \\
-\frac{1}{3}\boldsymbol{Y}_{\mathrm{ac}} & -\frac{1}{3}\boldsymbol{Y}_{\mathrm{ac}} & \frac{2}{3}\boldsymbol{Y}_{\mathrm{ac}} & \boldsymbol{0} & \boldsymbol{0} & \boldsymbol{E} & \boldsymbol{0} & \boldsymbol{0} \\
\boldsymbol{0} & \boldsymbol{0} & \boldsymbol{0} & \boldsymbol{0} & \boldsymbol{0} & \boldsymbol{0} & \boldsymbol{E} & -\boldsymbol{Z}_{\mathrm{dc}} \\
\boldsymbol{0} & \boldsymbol{0} & \boldsymbol{0} & -\frac{1}{2}\boldsymbol{C}(\vec{S}_1) & -\frac{1}{2}\boldsymbol{C}(\vec{S}_2) & -\frac{1}{2}\boldsymbol{C}(\vec{S}_3) & \boldsymbol{0} & \boldsymbol{E}
\end{bmatrix},
$$

$$
\vec{X} = \begin{bmatrix}
\vec{U}_{\mathrm{ac1}} \\
\vec{U}_{\mathrm{ac2}} \\
\vec{U}_{\mathrm{ac3}} \\
\vec{I}_{\mathrm{ac1}} \\
\vec{I}_{\mathrm{ac2}} \\
\vec{I}_{\mathrm{ac3}} \\
\vec{U}_{\mathrm{dc}} \\
\vec{I}_{\mathrm{dc}}
\end{bmatrix}, \qquad
\vec{B} = \begin{bmatrix}
\vec{0} \\
\vec{0} \\
\vec{0} \\
\frac{1}{3}\boldsymbol{Y}_{\mathrm{ac}}\left(2\vec{U}_{\mathrm{dis1}} - \vec{U}_{\mathrm{dis2}} - \vec{U}_{\mathrm{dis3}}\right) \\
\frac{1}{3}\boldsymbol{Y}_{\mathrm{ac}}\left(-\vec{U}_{\mathrm{dis1}} + 2\vec{U}_{\mathrm{dis2}} - \vec{U}_{\mathrm{dis3}}\right) \\
\frac{1}{3}\boldsymbol{Y}_{\mathrm{ac}}\left(-\vec{U}_{\mathrm{dis1}} - \vec{U}_{\mathrm{dis2}} + 2\vec{U}_{\mathrm{dis3}}\right) \\
\boldsymbol{Z}_{\mathrm{dc}}\vec{I}_{\mathrm{dis}} \\
\vec{0}
\end{bmatrix}. \tag{3.92}
$$

Again, a reduction of the system's size can be obtained by eliminating variables, resulting in a full system matrix, with

$$
\begin{aligned}
\boldsymbol{A} = \boldsymbol{E} + \frac{1}{6}\boldsymbol{Z}_{\mathrm{dc}} \Big[& \boldsymbol{C}(\vec{S}_1)\boldsymbol{Y}_{\mathrm{ac}}\left(\boldsymbol{C}(\vec{S}_1) - \frac{1}{2}\boldsymbol{C}(\vec{S}_2) - \frac{1}{2}\boldsymbol{C}(\vec{S}_3)\right) \dots \\
& + \boldsymbol{C}(\vec{S}_2)\boldsymbol{Y}_{\mathrm{ac}}\left(-\frac{1}{2}\boldsymbol{C}(\vec{S}_1) + \boldsymbol{C}(\vec{S}_2) - \frac{1}{2}\boldsymbol{C}(\vec{S}_3)\right) \dots \\
& + \boldsymbol{C}(\vec{S}_3)\boldsymbol{Y}_{\mathrm{ac}}\left(-\frac{1}{2}\boldsymbol{C}(\vec{S}_1) - \frac{1}{2}\boldsymbol{C}(\vec{S}_2) + \boldsymbol{C}(\vec{S}_3)\right) \Big],
\end{aligned}
$$

$$
\vec{X} = \vec{U}_{\mathrm{dc}}, \tag{3.93}
$$

$$
\begin{aligned}
\vec{B} = \boldsymbol{Z}_{\mathrm{dc}} \cdot \Big[& \vec{I}_{\mathrm{dis}} + \frac{1}{6}\boldsymbol{C}(\vec{S}_1)\boldsymbol{Y}_{\mathrm{ac}}\left(2\vec{U}_{\mathrm{dis1}} - \vec{U}_{\mathrm{dis2}} - \vec{U}_{\mathrm{dis3}}\right) \dots \\
& + \frac{1}{6}\boldsymbol{C}(\vec{S}_2)\boldsymbol{Y}_{\mathrm{ac}}\left(-\vec{U}_{\mathrm{dis1}} + 2\vec{U}_{\mathrm{dis2}} - \vec{U}_{\mathrm{dis3}}\right) \dots \\
& + \frac{1}{6}\boldsymbol{C}(\vec{S}_3)\boldsymbol{Y}_{\mathrm{ac}}\left(-\vec{U}_{\mathrm{dis1}} - \vec{U}_{\mathrm{dis2}} + 2\vec{U}_{\mathrm{dis3}}\right) \Big].
\end{aligned}
$$

The equation system is numerically evaluated for two example cases.

Case I

Case I shows the harmonic interactions of the system when the dc link is fed by a six-pulse diode rectifier (Figure 3.26). The ac phases of the VSI are connected to a symmetrical three-phase RL load. The presented case shows the incorporation of different fundamental frequencies of the subsystems. The grid feeding the diode rectifier operates at a grid frequency of $f_g = 50\,\text{Hz}$. Thus, harmonic currents with frequencies of $n \cdot 6 \cdot f_g, n \in \mathbb{N}$ are injected into the dc link. These are implemented in the frequency-domain model in a nonreactive current source i_{dis}. Hence, the equivalent circuit of Figure 3.2 represents the frequency-domain model for Case I. For reasons of comparability, the same disturbance current harmonics are used in the frequency-domain model as in the time-domain model and they represent the dominant harmonics that are measured in the experimental system.
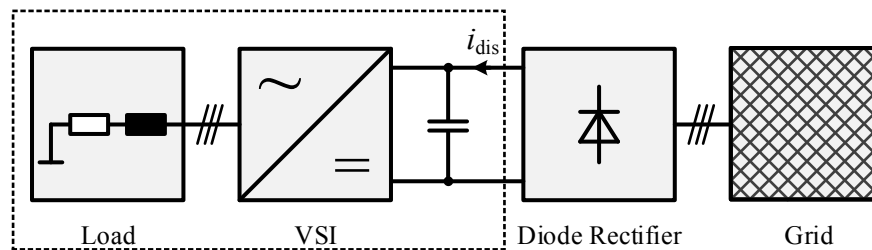
Figure 3.26: Experimental setup for Case I. The ac-side outputs of a three-phase VSI are connected to a passive RL load. The dc link is fed by three-phase diode rectifier that is connected to the utility grid.

The frequency of the sinusoidal duty cycle is set to $f_{\text{d0}} = 40\,\text{Hz}$. The switching frequency is chosen to $f_{\text{sw}} = 3\,\text{kHz}$. This results in a fundamental frequency of $f_0 = \gcd(f_g, f_{\text{d0}}, f_{\text{sw}}) = 10\,\text{Hz}$. The PWM model in (3.61) is evaluated with $m_{\max} = 1$ carrier harmonics, $n_{\max} = 10$ sideband harmonics and the maximum harmonic order is $k_{\max} = 340$. Subsequently, the linear model of the model in (3.93) is evaluated. The parameters are summarized in Table 3.2.

A comparison of the spectra resulting from the frequency-domain model to results from time-domain simulations is shown in Figure 3.27. Accordingly, Figure 3.28 shows the differences of the complex coefficients between both models. The first graph shows the switching function spectrum of phase 1, which incorporates a fundamental frequency component and the first carrier sideband group at f_{sw}. The disturbance current spectrum depicted in the last graph introduces harmonic currents as multiples of $300\,\text{Hz}$, which are propagated to the dc-link voltage. Accordingly, the ac-side voltage spectrum contains harmonic components that result from the convolution of the switching function and the dc-link voltage spectra. The resulting low-frequency harmonics have frequencies of $n \cdot 6 \cdot f_g \pm m \cdot f_{\text{d0}}, m, n \in \mathbb{N}$ and are not integer multiples of the duty-cycle frequency, illustrating the importance of choosing the correct fundamental frequency of the Fourier series.

In Figure 3.29, the spectra are depicted as a comparison of frequency-domain results and experimental results, with the same order for the spectra as in the previous figures. The differences

Table 3.2: Parameters of the three-phase VSI with open-loop control for Case I

Parameter	Symbol	Value
Fundamental frequency	f_0	10 Hz
Grid frequency	f_g	50 Hz
Duty-cycle frequency	f_{d0}	40 Hz
AC-side resistance 1	R_{ac}	5 Ω
AC-side inductance 1	L_{ac}	20 mH
Switching frequency	f_{sw}	3 kHz
Control frequency	f_c	6 kHz
Grid voltage (line-to-line rms)	U_g	400 V
DC-link voltage (dc component)	U_{dc0}	555 V
DC-link capacitance	C_{dc}	480 µF
Modulation index	M	0.6
Duty cycle phase shift	θ_{d0}	0
Maximum harmonic order	k_{max}	340
Maximum carrier order	m_{max}	1
Maximum sideband order	n_{max}	10

of the magnitude spectra are included in Figure 3.30. For the measurement results, the switching function is calculated by utilizing its relationship with the gate signals (see (3.1)). The gate voltage signals have a voltage level of 5 V and are measured at the input of the gate driver. The unit-free switching function is then obtained by dividing the measured voltage by twice the average value:

$$s(t) = \frac{u_{gt}(t) - u_{gb}(t)}{2 \cdot \bar{u}_{gt}} \tag{3.94}$$

The bottom plot shows the spectrum of the disturbance current in green, which was measured using a Rogowski coil. Note that the dc component cannot be measured with a Rogowski coil. The influence of the rectifier is included in the frequency-domain models as a nonreactive current source i_{dis} using the measured values of the dominant harmonics, with frequencies $n \cdot 6 \cdot f_g, n = 1, ..., 10$, are used as inputs.

The modeling results and the measurement results show generally good conformity. Differences become apparent when the influence of nonlinear effects are increased. Previously the switching function was analyzed under the assumption of an ideal switching behavior. In reality the switching behavior is distorted by nonlinearities that are commonly known as dead-time effects, including an interlock time that is introduced to the gate signals to prevent simultaneous conduction of both transistors of a half bridge. The interlock time is chosen to $T_d = 1 \, \mu s$ for the measurement results depicted in Figure 3.29. An increase of the interlock time to $T_d = 10 \, \mu s$ leads to the spectrum shown in Figure 3.31. Additional frequency components become evident in the ac-side voltage, which are further propagated to the ac-side current depending on the load parameters. These components are not predicted by the frequency-domain model. The influence of interlock times obviously requires a closer consideration and is further analyzed in Chapter 4.
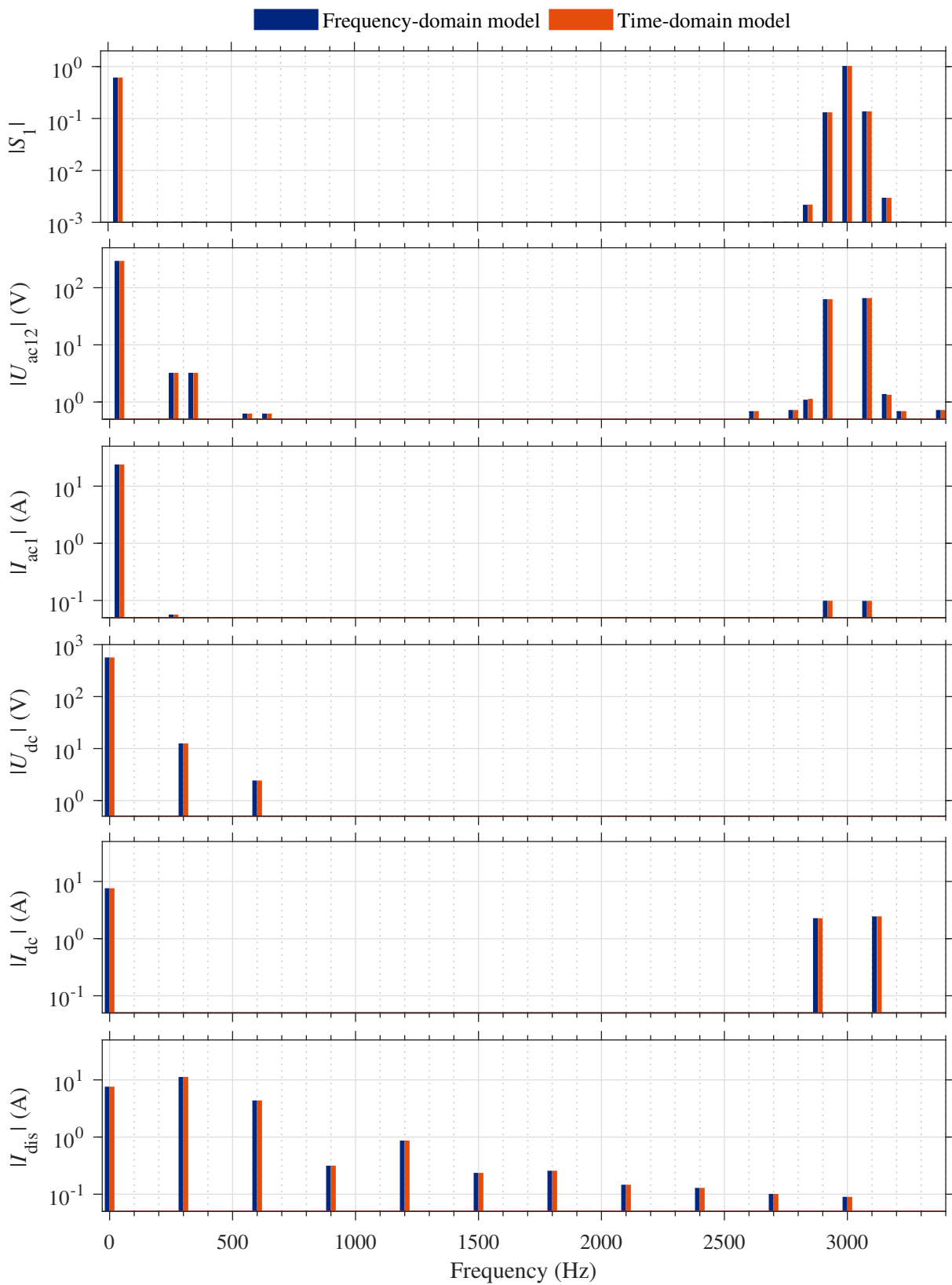
Figure 3.27: Comparison of frequency-domain model and time-domain simulations for a three-phase VSI with open-loop control for Case I with AD-PWM, $f_0 = 10\,\text{Hz}$, $f_{d0} = 40\,\text{Hz}$; $f_{sw} = 3\,\text{kHz}$. The disturbance current spectrum represents the diode rectifier, which introduces harmonic currents at multiples of $300\,\text{Hz}$.
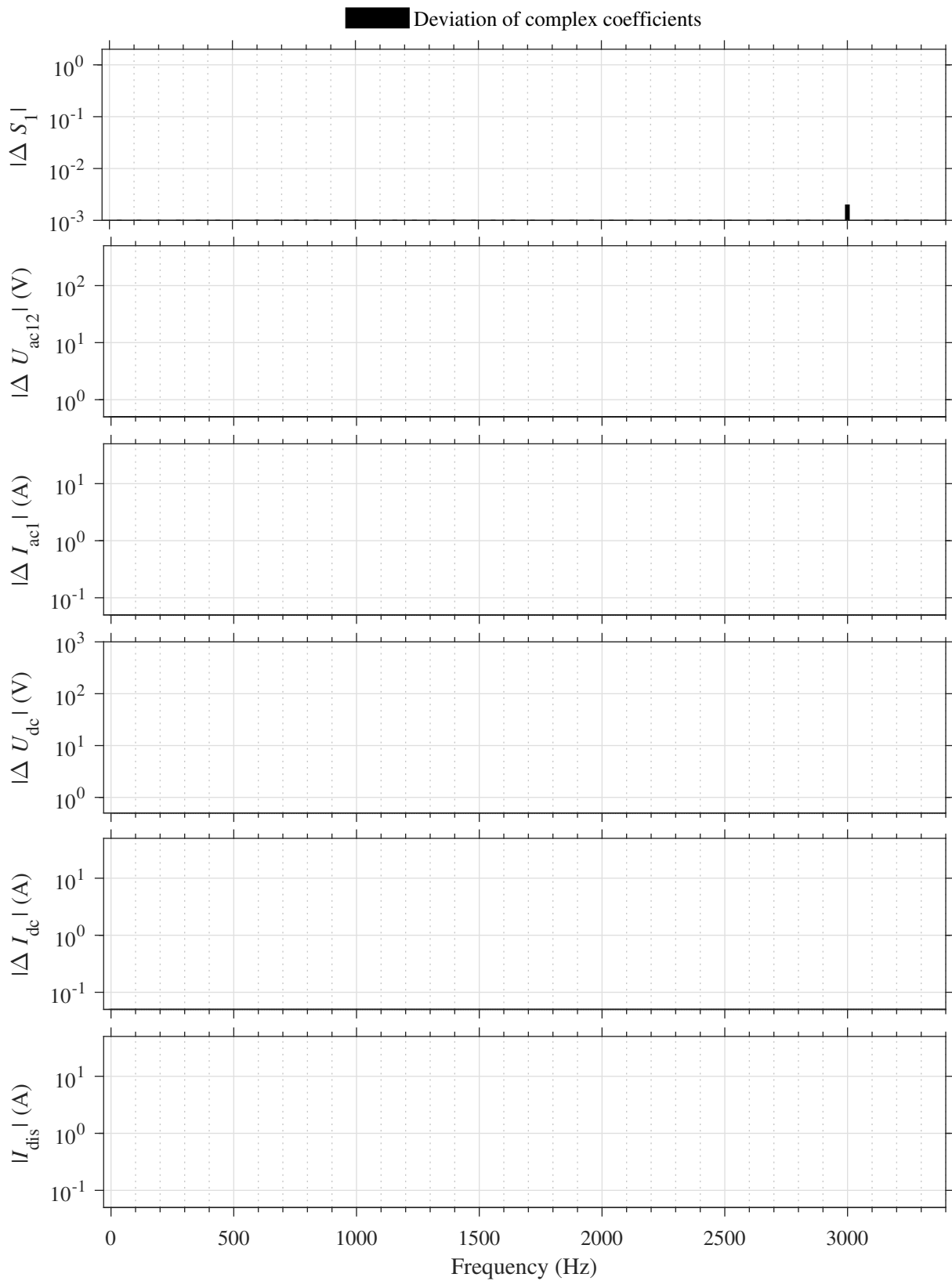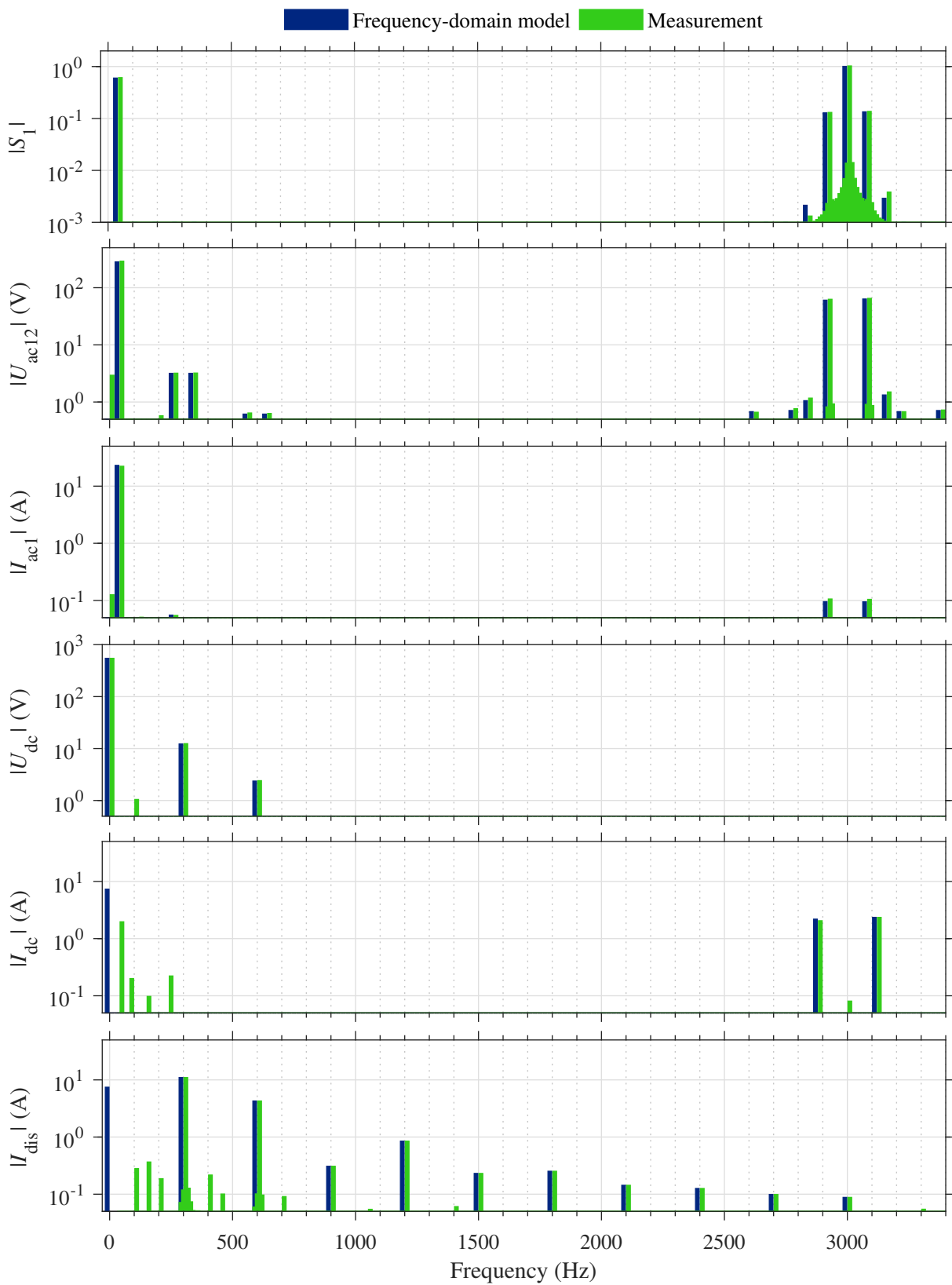
Figure 3.28: Differences of the complex spectra shown in Figure 3.27 for a three-phase VSI with open-loop control for Case I with AD-PWM, $f_0 = 10\,\text{Hz}$, $f_{\text{d0}} = 40\,\text{Hz}$; $f_{\text{sw}} = 3\,\text{kHz}$.

Figure 3.29: Comparison of frequency-domain model and measurements for a three-phase VSI with open-loop control for Case I with AD-PWM, $f_0 = 10\,\text{Hz}$, $f_{\text{d}0} = 40\,\text{Hz}$; $f_{\text{sw}} = 3\,\text{kHz}$. $T_{\text{d}} = 1\,\mu\text{s}$, in contrast to Figure 3.31.
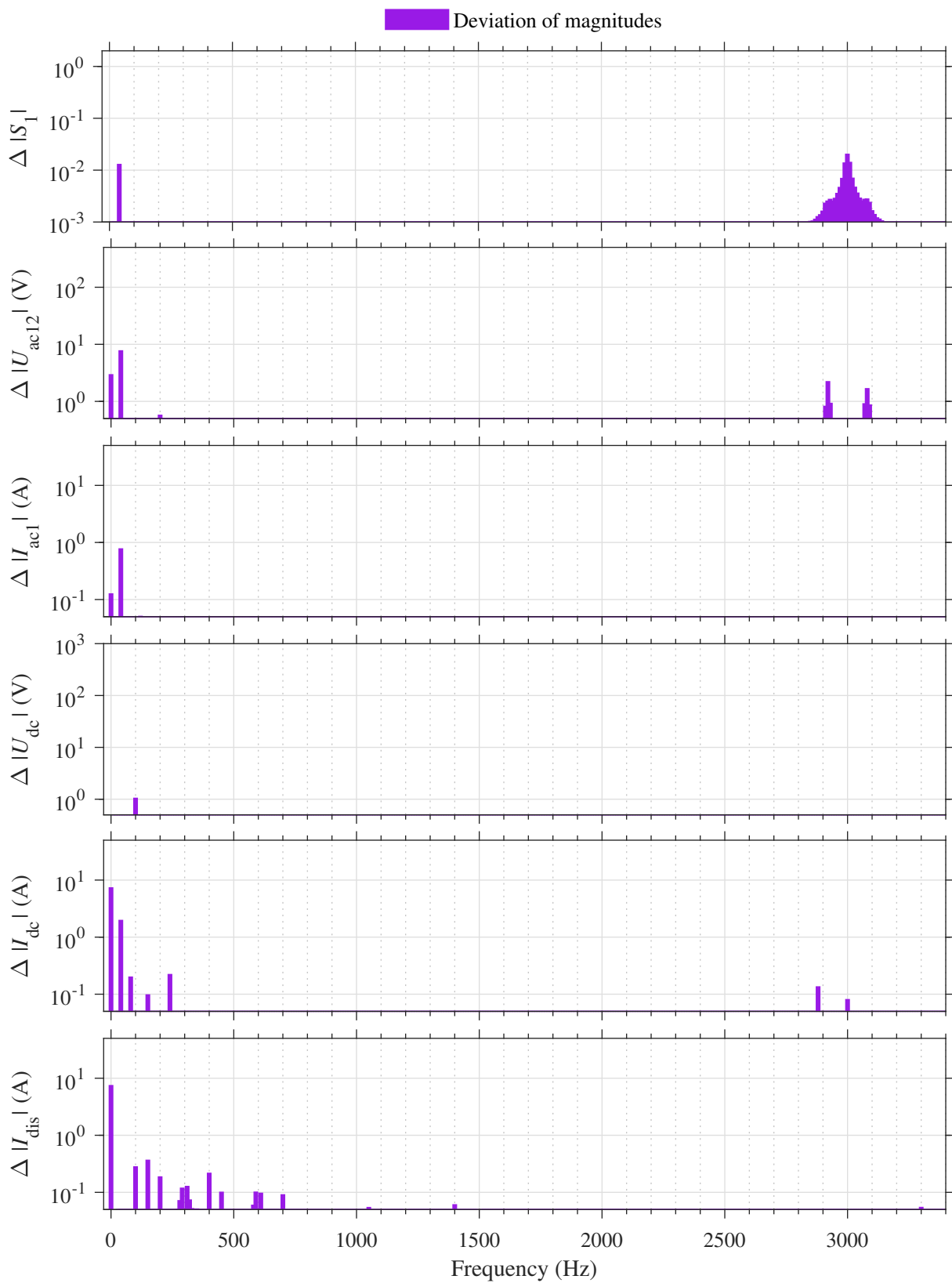
Figure 3.30: Differences of the magnitude spectra shown in Figure 3.29 for a three-phase VSI with open-loop control for Case I with AD-PWM, $f_0 = 10\,\text{Hz}$, $f_{d0} = 40\,\text{Hz}$; $f_s = 3\,\text{kHz}$, and $T_d = 1\,\text{µsw}$.
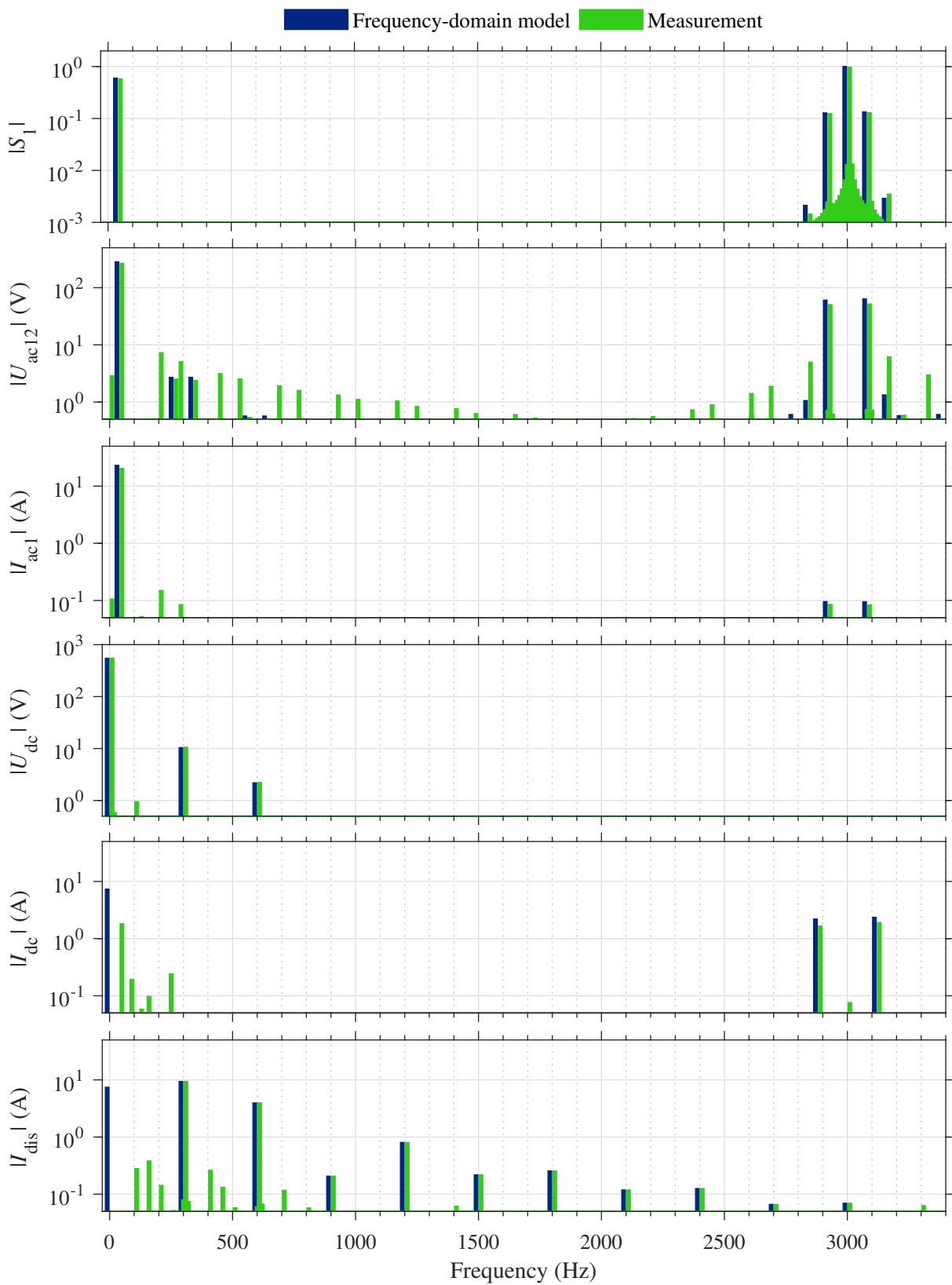
Figure 3.31: Spectrum for a three-phase VSI with open-loop control for Case I with AD-PWM, $f_0 = 10\,\text{Hz}$, $f_{d0} = 40\,\text{Hz}$; $f_{sw} = 3\,\text{kHz}$. $T_d = 10\,\mu\text{s}$, in contrast to Figure 3.29.

Case II

In Case II a three-phase VSI is fed by a direct voltage source on the dc-side and the ac-side phases are connected to an LCL-filter that is terminated by a resistive load (Figure 3.32). In order to show the influence of a duty cycle containing multiple frequencies, Case II uses additional frequency components at the fifth and seventh multiples of the fundamental frequency, with

$$d(t) = M_1 \cdot \cos\left(\omega_0 t + \theta_1\right) + M_5 \cdot \cos\left(\omega_0 t + \theta_5\right) + M_7 \cdot \cos\left(\omega_0 t + \theta_7\right). \tag{3.95}$$

The PWM model for SD-PWM with multiple-frequency modulation in (3.55) is evaluated with the parameters $m_{\max} = 1$ and $n_{\max} = 10$. The highest harmonic order is $k_{\max} = 90$. The parameters of the system are summarized in Table 3.3.
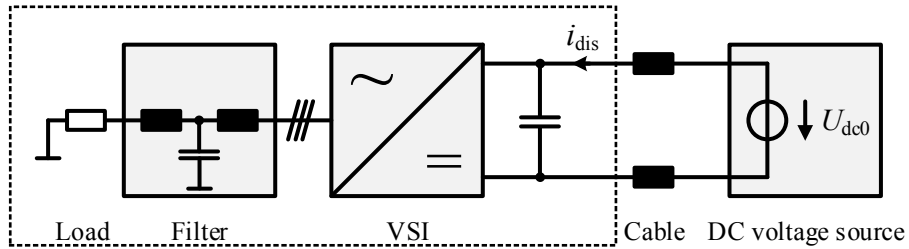
Figure 3.32: Experimental setup for Case II. The dc link is fed by a constant voltage source that is connected via a long cable.

The incorporation of a three-phase LCL-filter described by the admittance matrices ($\boldsymbol{Y}_{21}$ and $\boldsymbol{Y}_{22}$) in (3.77) leads to a minor change in the equation system, with

$$
\begin{aligned}
\boldsymbol{A} = \boldsymbol{E} + \frac{1}{6} \cdot \boldsymbol{Z}_{\mathrm{dc}} \cdot \bigg[&\boldsymbol{C}(\vec{S}_1) \cdot \boldsymbol{Y}_{22} \cdot \left(\boldsymbol{C}(\vec{S}_1) - \frac{1}{2} \cdot \boldsymbol{C}(\vec{S}_2) - \frac{1}{2} \cdot \boldsymbol{C}(\vec{S}_3) \right) \dots \\
& + \boldsymbol{C}(\vec{S}_2) \cdot \boldsymbol{Y}_{22} \cdot \left(-\frac{1}{2} \cdot \boldsymbol{C}(\vec{S}_1) + \boldsymbol{C}(\vec{S}_2) - \frac{1}{2} \cdot \boldsymbol{C}(\vec{S}_3) \right) \dots \\
& + \boldsymbol{C}(\vec{S}_3) \cdot \boldsymbol{Y}_{22} \cdot \left(-\frac{1}{2} \cdot \boldsymbol{C}(\vec{S}_1) - \frac{1}{2} \cdot \boldsymbol{C}(\vec{S}_2) + \boldsymbol{C}(\vec{S}_3) \right) \bigg], \\
\vec{X} = \vec{U}_{\mathrm{dc}}, & \\
\vec{B} = \boldsymbol{Z}_{\mathrm{dc}} \cdot \bigg[&\vec{I}_{\mathrm{dis}} + \frac{1}{6} \cdot \boldsymbol{C}(\vec{S}_1) \cdot \boldsymbol{Y}_{21} \cdot \left(2 \cdot \vec{U}_{\mathrm{dis1}} - \vec{U}_{\mathrm{dis2}} - \vec{U}_{\mathrm{dis3}} \right) \dots \\
& + \frac{1}{6} \cdot \boldsymbol{C}(\vec{S}_2) \cdot \boldsymbol{Y}_{21} \cdot \left(-\vec{U}_{\mathrm{dis1}} + 2 \cdot \vec{U}_{\mathrm{dis2}} - \vec{U}_{\mathrm{dis3}} \right) \dots \\
& + \frac{1}{6} \cdot \boldsymbol{C}(\vec{S}_3) \cdot \boldsymbol{Y}_{21} \cdot \left(-\vec{U}_{\mathrm{dis1}} - \vec{U}_{\mathrm{dis2}} + 2 \cdot \vec{U}_{\mathrm{dis3}} \right) \bigg].
\end{aligned}
\tag{3.96}
$$

The resulting spectra are depicted in Figure 3.33 as a comparison of the frequency-domain model to time-domain simulations and with their respective difference of complex coefficients in Figure 3.34. Likewise, a comparison of the frequency-domain model to measurements is performed in Figure 3.35 and respective differences of magnitude spectra are shown in Figure 3.36.
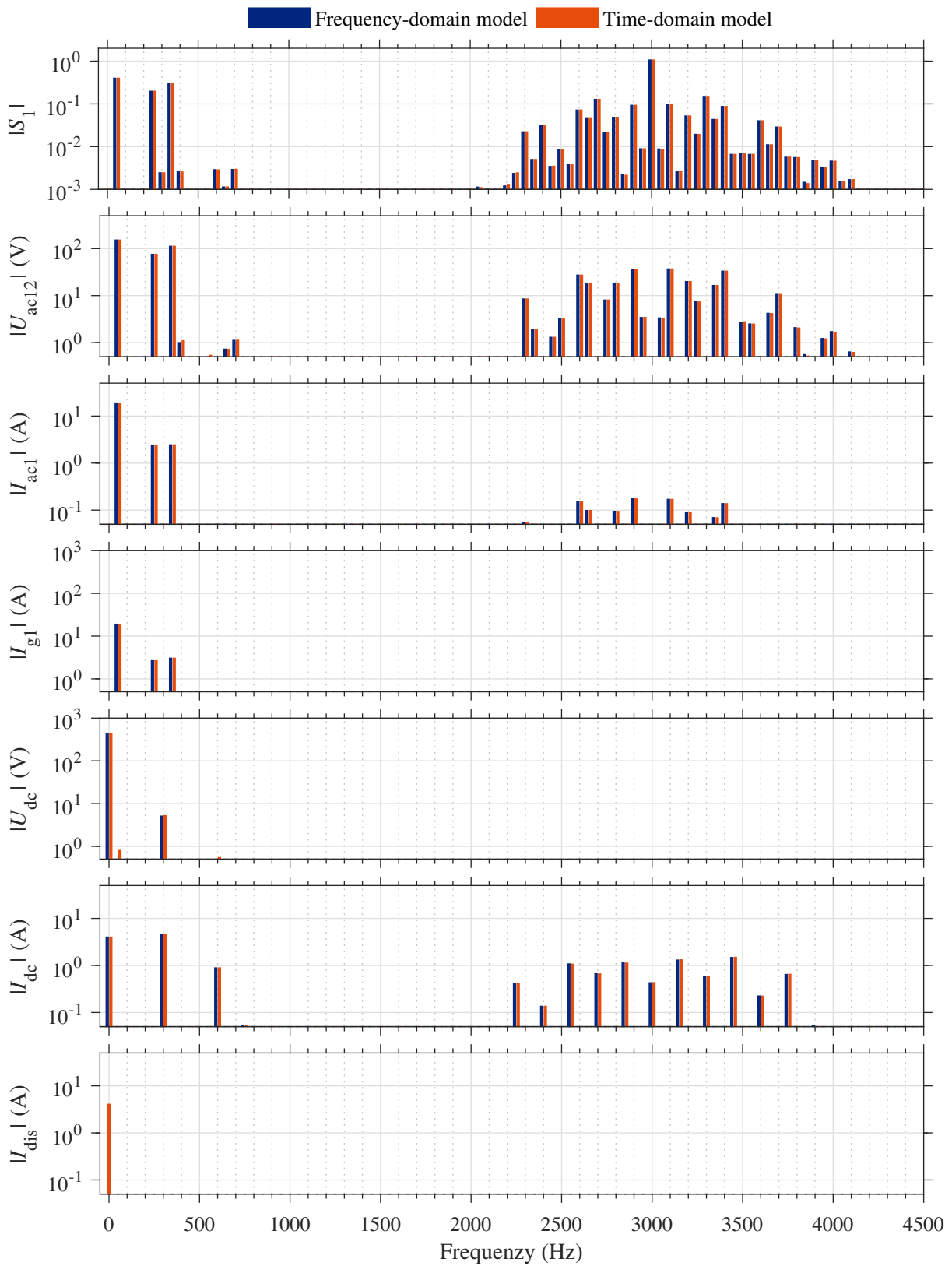
Figure 3.33: Comparison of frequency-domain model and time-domain simulations for a three-phase VSI with open-loop control for Case II. The duty cycle contains components 1, 5, and 7 times the fundamental frequency of 50 Hz. $f_{sw} = 3\,kHz$ (SD-PWM).
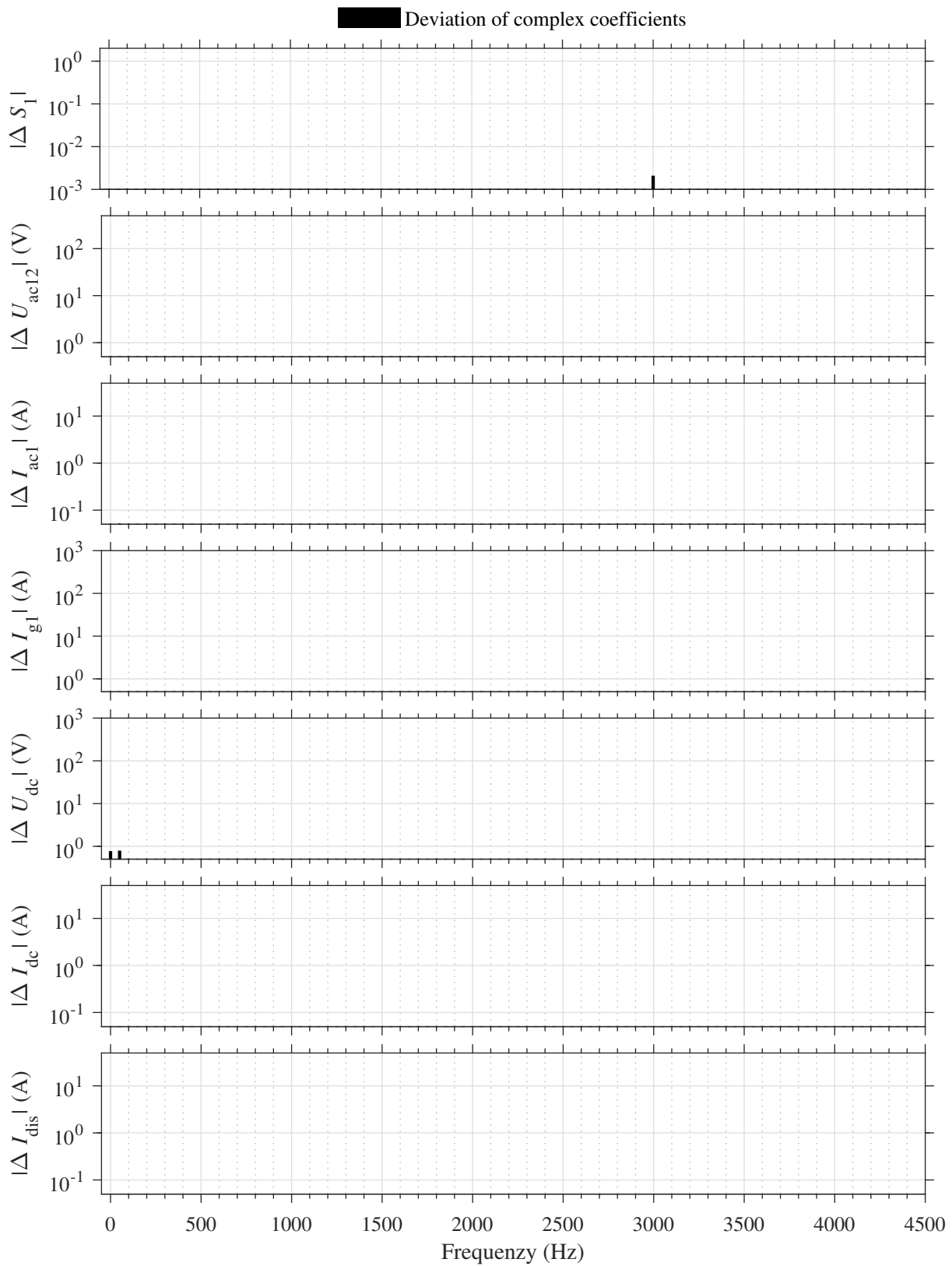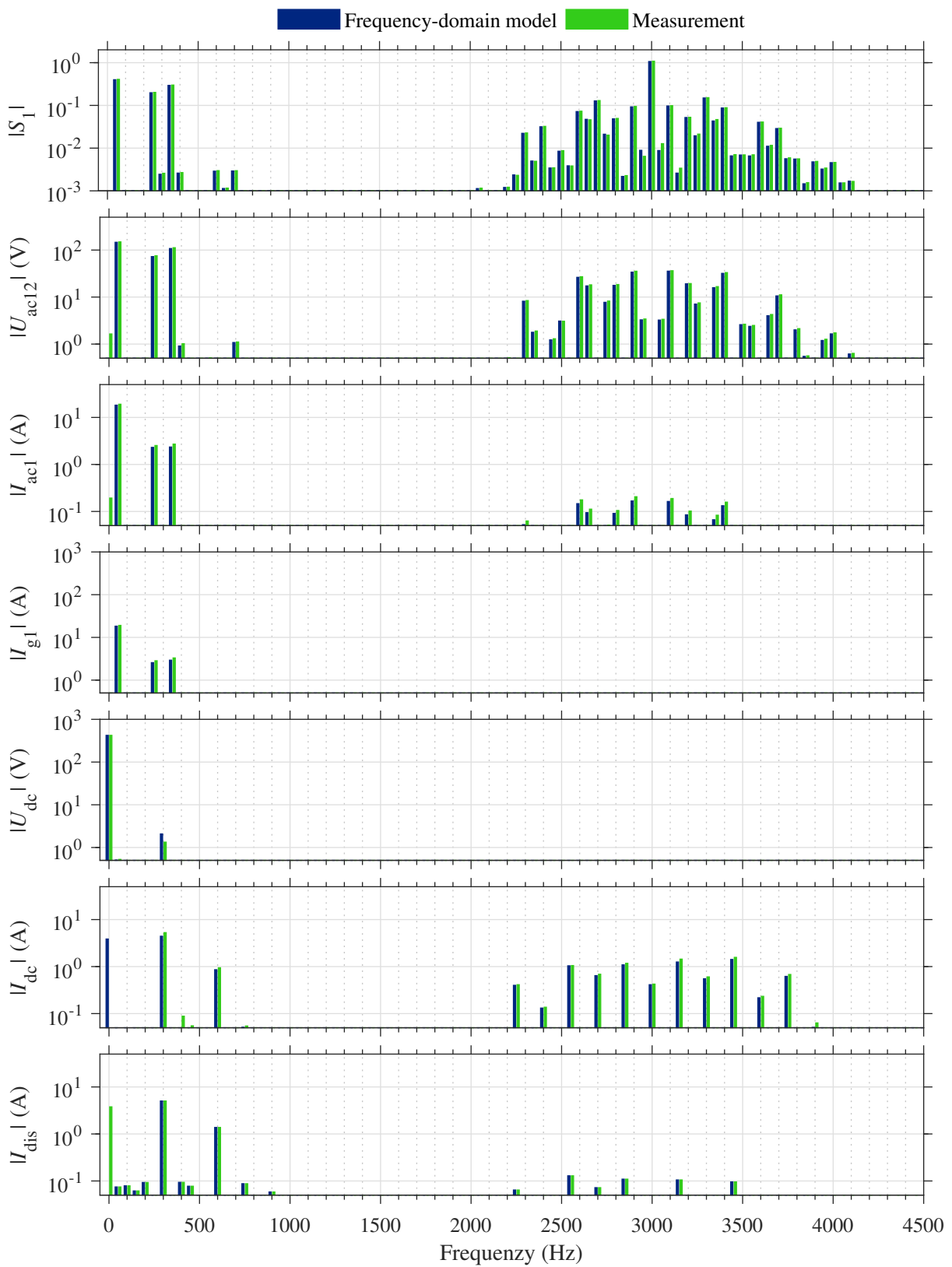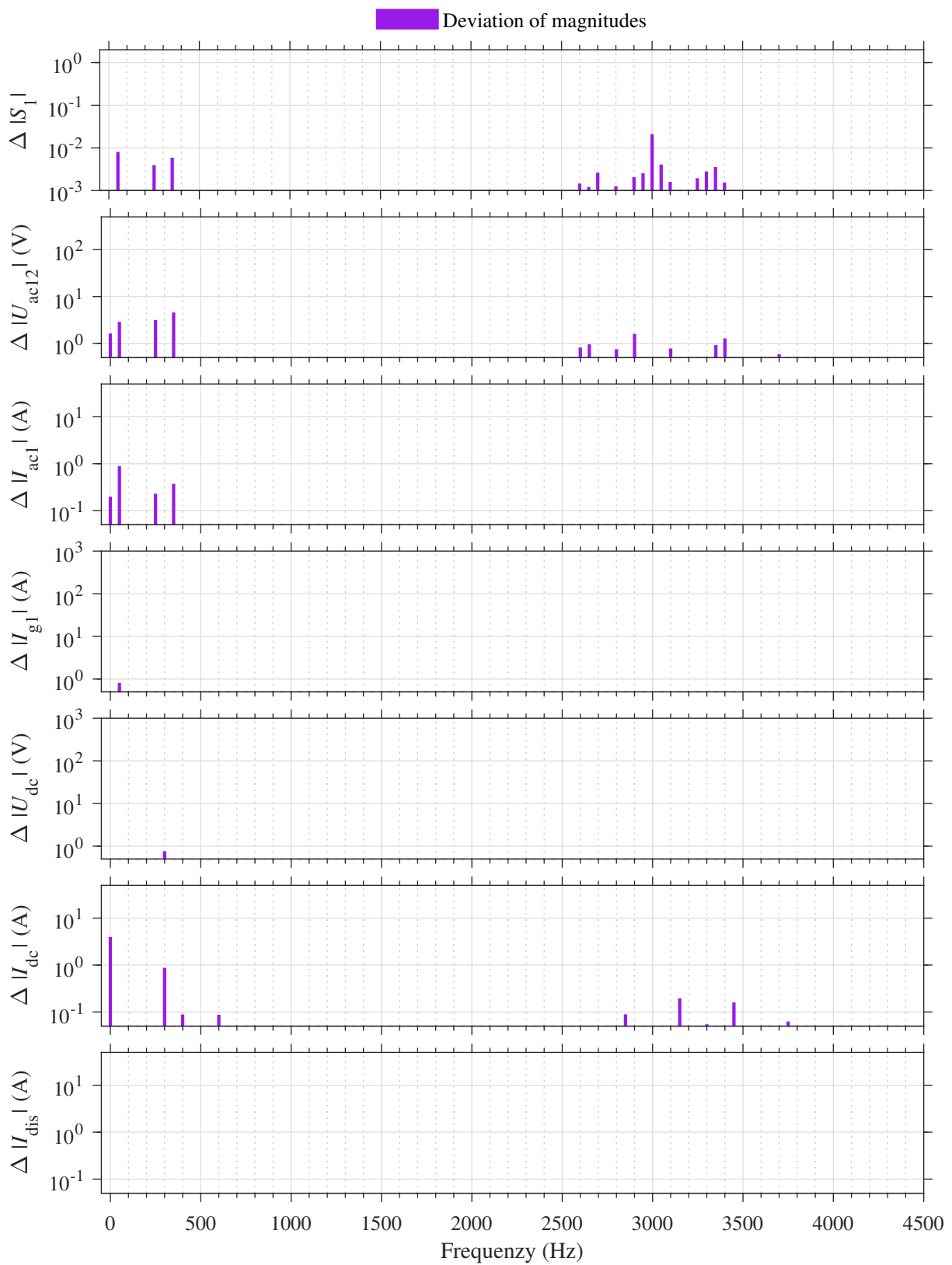
Figure 3.34: Differences of the complex spectra shown in Figure 3.33 for a three-phase VSI with open-loop control for Case II. The duty cycle contains components 1, 5, and 7 times the fundamental frequency of 50 Hz. $f_{\text{sw}} = 3\,\text{kHz}$ (SD-PWM).

Figure 3.35: Comparison of frequency-domain model and measurements for a three-phase VSI with open-loop control for Case II. The duty cycle contains components 1, 5, and 7 times the fundamental frequency of 50 Hz. $f_{sw} = 3\,\text{kHz}$ (SD-PWM).

Figure 3.36: Differences of the magnitude spectra shown in Figure 3.35 for a three-phase VSI with open-loop control for Case II. The duty cycle contains components 1, 5, and 7 times the fundamental frequency of 50 Hz. $f_{sw} = 3\,kHz$ (SD-PWM).

Table 3.3: Parameters of the three-phase VSI with open-loop control for Case II

Parameter	Symbol	Value
Fundamental frequency	f_0	50 Hz
Duty-cycle frequency	f_{d0}	50 Hz
AC-side resistance 1	R_1	3 Ω
AC-side inductance 1	L_1	4.22 mH
AC-side resistance 2	R_2	0.1 Ω
AC-side inductance 2	L_2	6.75 mH
Damping resistance	R_d	1.5 Ω
Filter capacitance	C_f	10 μF
Switching frequency	f_{sw}	3 kHz
Control frequency	f_c	3 kHz
Modulation index at $1 \cdot \omega_{d0}$	M_1	0.4
Modulation index at $5 \cdot \omega_{d0}$	M_5	0.2
Modulation index at $7 \cdot \omega_{d0}$	M_7	0.3
Phase shift at $1 \cdot \omega_{d0}$	θ_1	0
Phase shift at $5 \cdot \omega_{d0}$	θ_5	$\pi/5$
Phase shift at $7 \cdot \omega_{d0}$	θ_7	$\pi/4$
DC-link capacitance	C_{dc}	480 μF
DC-link voltage	U_{dc0}	440 V
Maximum harmonic order	k_{max}	90
Maximum carrier order	m_{max}	1
Maximum sideband order	n_{max}	10

The additional components in the duty cycle result in a broad carrier sideband spectrum, which is visible in the switching function spectrum in the first graph.

The frequency components of the switching function spectrum are present in the line-to-line ac-side voltage in the second graph, with the exception of zero-sequence components. Because there are no harmonic disturbance signals present in the system, all harmonic components in the system are caused by the PWM process. The low-pass effect of the third-order filter is clearly visible in a comparison of the ac-side voltage, the ac-side current, and the grid-side current spectra. The bottom graph shows the spectrum of the disturbance current that is introduced by the dc-voltage source.

3.5 Discussion

This chapter introduced a modeling approach that describes the harmonic interactions in VSI systems, including their reaction to external disturbances and including the influence of the PWM process. In order to describe the interaction of the ac-side and the dc-side quantities, a switching function was introduced, which describes the state of conduction of the half bridge. The switching function characterizes both the relationship of the ac-side voltages and the dc-link voltage, as well as the ac-side currents and the dc-side current. This fact is true independently of the chosen modulation method.

For linear loads, the frequency-domain model of the VSI with open-loop control is linear. The solution of the linear equation system is a standard method in numerical computing, which is generally robust and fast. Even an analytical inversion of the system matrix is conceivable, which can further enhance the numerical evaluation.

When the existing frequencies of the system signals are non-integer ratios, the size of the equation system can become very large. For an inconvenient choice of duty-cycle frequency and switching frequency, the fundamental frequency, as their greatest common divisor, has a small value. This results in a large system matrix, even though the system is not more complicated than for other sets of parameters.

The comparison of numerical results from frequency-domain models and time-domain models shows very good conformity, proving a correct derivation of the equations and correct implementation in the numerical solution process. The results illustrate the interaction of the signals. In the presence of harmonic disturbances, the ac-side voltage spectrum and the dc-side current spectrum deviate from the spectrum of the switching function. Although the switching function spectrum is a legitimate measure for the PWM performance, it is recommended to include the system interaction by evaluation of the voltage and current spectra.

Experimental results showed a good accordance with the analytical results. Nevertheless, deviations are present in the spectra, motivating the analysis of nonlinear effects in the switching behavior of the VSI, which is conducted in the following chapter.

4 Nonlinearities of Power Electronic Switches

In the previous chapter, the power electronic components were considered to be ideal switches assuming infinite response time and neglecting losses. The actual performance differs from the ideal switch model due to a number of nonlinear influences:

- Interlock times

- Turn-on and turn-off times due to parasitic capacitances

- Forward voltage drops

The resulting nonlinear distortions are collectively called dead-time effects [52]. Among these effects, the interlock times (also known as blanking times or dead times) are considered to have the largest impact [53]. A large number of publications analyze their effect and propose compensation methods, refer to [54, 55] for an overview of compensation methods and further references.

In Section 4.1 the analysis of the interlock times is reviewed and it is shown that the effect can be directly incorporated into the switching function. As a result, the modeling approach introduced in Chapter 3 can be extended with the influence of interlock times. The other non-linear effects lead to further deviations of the switching behavior. Their influence is briefly analyzed in Section 4.3 and their incorporation into the frequency domain model is discussed. The frequency-domain models are evaluated numerically in Section 4.2 and compared to time-domain simulations and experimental results.

4.1 Modeling the Effect of Interlock Times

The two transistors of a half bridge are turned on complementarily using inverted gate signals for the top and bottom switch $g_t = \bar{g}_b$. Due to a finite turn-off time of the transistors, a simultaneous conduction of both transistors and a short circuit of the feeding dc link could result. This can potentially destroy the dc-link capacitor and the IGBT modules. An interlock time is introduced as a prevention method, delaying the rising edge of the gate signals by T_d.
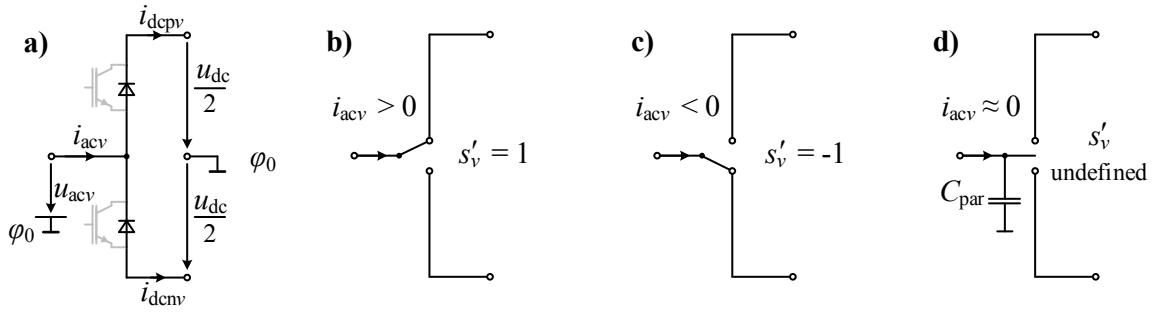
Figure 4.1: Switching function model during interlock times: **a)** half bridge   **b)** switch position 1 for $i_{ac\nu} > 0$
    c) switch position -1 for $i_{ac\nu} > 0$ **d)** undefined switch position for $i_{ac\nu} \approx 0$

As introduced in Chapter 3, the switching function represents the conduction state of a half bridge. During the interlock times, both transistors of the half bridge are turned off (Figure 4.1 a). The stiff phase current commutates to one of the freewheeling diodes, depending on the sign of the current. As a result, the conduction state of the half bridge during the interlock times is equal to the conduction state of the diodes. Thus, the relationship between the gate signals and the switching function in (3.1) is no longer valid. As illustrated in Figure 4.1, the half bridge can be modeled during the interlock times using a current-dependent switching function $s'_\nu(t)$, with

$$s'_\nu(t) = \left\{ \begin{array}{ccc} 1 & \text{for} & i_{ac\nu} > 0 \\ -1 & \text{for} & i_{ac\nu} < 0 \\ \text{undefined} & \text{for} & i_{ac\nu} = 0 \quad (\text{only in DCM}) \end{array} \right\}, \quad (\text{during interlock times}). \quad (4.1)$$

As indicated by Figure 4.1 d), the phase current cannot be assigned to neither the top diode nor the bottom diode and the output voltage is determined by the voltage of the parasitic capacitance. The influence of this discontinuous current mode (DCM) due to small phase currents charging the parasitic capacitances is further discussed in Section 4.3.

When DCM can be neglected, only the two switch positions b) and c) in Figure 4.1 have to be considered. For very small phase currents, the conduction state during the interlock time is influenced by the parasitic capacitance C_{par} of the half bridge. Outside the interlock times, the switching function is independent of the phase currents and defined by the gate signals, with

$$s'_\nu(t) = s_\nu(t), \quad (\text{equation only valid outside interlock times}). \quad (4.2)$$

Figure 4.2 shows the gate signals g_t (first graph) and g_b (second graph) when the leading edges of the gate signals are delayed by an interlock time T_d. The modified switching function s' in the third graph corresponds to the gate signals with zero interlock time. The actual switching function s' (fourth graph) that reflects the conduction state of the half bridge including the interlock times depends on the sign of the phase current, which is positive in Figure 4.2 a) and negative in Figure 4.2 b). During the interlock time, the ideal switching function deviates from
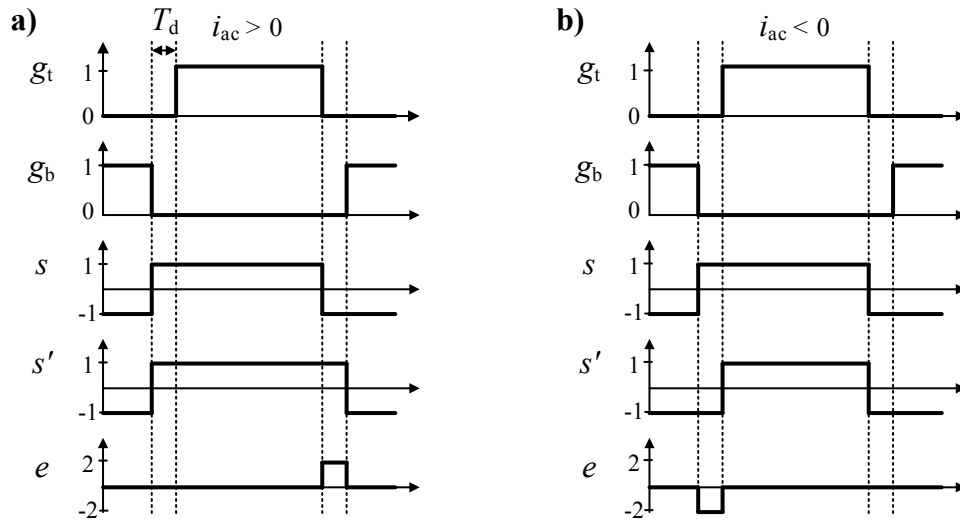
Figure 4.2: Top and bottom gate signals g_t and g_b, ideal switching function s, modified switching function considering interlock times s', and their deviation $e(t)$ for **a)** positive phase currents and **b)** negative phase currents.

the actual switching function and generates a modeling error e (fifth graph), with

$$e_\nu(t) = s'_\nu(t) - s_\nu(t). \tag{4.3}$$

The error function is a square-wave signal with a width of T_d. Its sign equals the sign of the phase current. The error function represents the deviation from the desired waveform, which results in the distortion of the phase voltage $\Delta u_{\mathrm{ac}\nu}$, with

$$\Delta u_{\mathrm{ac}\nu}(t) = \frac{1}{2} \cdot e_\nu(t) \cdot u_{\mathrm{dc}}(t). \tag{4.4}$$

This error voltage leads to:

- A lower fundamental frequency component for loads in motor operation

- A higher fundamental frequency component for loads in generator operation

- An introduction of odd order harmonics

- A widening of the carrier side bands

At the same time, the interlock time introduces a dc-side current error of

$$\Delta i_{\mathrm{dc}\nu}(t) = \frac{1}{2} \cdot e_\nu(t) \cdot i_{\mathrm{ac}\nu}(t). \tag{4.5}$$

4.1.1 Influence of the Phase Currents

By applying the averaging operator over one switching period to (4.4) and assuming a constant dc-link voltage of U_{dc0} results in an average ac-side voltage error of

$$\langle \Delta u_{\mathrm{ac}\nu}(t) \rangle_{T_{\mathrm{sw}}} = f_{\mathrm{sw}} \cdot \frac{1}{2} \cdot U_{\mathrm{dc0}} \cdot \int_{T_{\mathrm{sw}}}^{t+T_{\mathrm{sw}}} e_\nu(\tau)\,\mathrm{d}\tau = f_{\mathrm{sw}} \cdot T_{\mathrm{d}} \cdot U_{\mathrm{dc0}} \cdot \mathrm{sign}(i_{\mathrm{ac}\nu}(t)) \quad [56]. \tag{4.6}$$

A Fourier decomposition of the square wave signal yields the rms value of the k-th harmonic component of

$$|\Delta U_{\mathrm{ac},k}| = \frac{1}{\sqrt{2}} \cdot \frac{4}{\pi} \cdot \frac{1}{k} \cdot f_{\mathrm{sw}} \cdot T_{\mathrm{d}} \cdot U_{\mathrm{dc0}}, \quad k \in \{1,3,5,...\} \tag{4.7}$$

and shows the generation of odd-numbered harmonics. Similarly, the dc-side current error in (4.5) can be expressed with its average value (also see [57]):

$$\begin{aligned}
\langle \Delta i_{\mathrm{dc}}(t) \rangle_{T_{\mathrm{sw}}} &= f_{\mathrm{sw}} \cdot \frac{1}{2} \cdot \int_{T_{\mathrm{sw}}}^{t+T_{\mathrm{sw}}} (i_{\mathrm{ac1}}(\tau) \cdot e_1(\tau) + i_{\mathrm{ac1}}(\tau) \cdot e_2(\tau) + i_{\mathrm{ac3}}(\tau) \cdot e_3(\tau))\,\mathrm{d}\tau \\
&= f_{\mathrm{sw}} \cdot T_{\mathrm{d}} \cdot (|i_{\mathrm{ac1}}(t)| + |i_{\mathrm{ac2}}(t)| + |i_{\mathrm{ac3}}(t)|).
\end{aligned} \tag{4.8}$$

Note that the product of error function and phase current always results in positive values, because the sign of the error function is determined by the sign of the phase current.

Jeong and Park [58] presented a quantitative prediction of the fundamental ac-side voltage $U_{\mathrm{ac},1}$ in an rms phasor representation. The model is reviewed here and extended to three-phase systems including disturbance voltages, with the equivalent circuit introduced in Chapter 3 (Figure 3.2). Assuming a symmetrical impedance and allowing generally asymmetrical voltages, the ac-side current phasors result in

$$\begin{bmatrix} \underline{I}_{\mathrm{ac1},1} \\ \underline{I}_{\mathrm{ac2},1} \\ \underline{I}_{\mathrm{ac3},1} \end{bmatrix} = \underline{Y}_{\mathrm{ac},1} \cdot \begin{bmatrix} 2 & -1 & -1 \\ -1 & 2 & -1 \\ -1 & -1 & 2 \end{bmatrix} \cdot \begin{bmatrix} \underline{U}_{\mathrm{dis1},1} - \underline{U}_{\mathrm{ac1},1} \\ \underline{U}_{\mathrm{dis2},1} - \underline{U}_{\mathrm{ac2},1} \\ \underline{U}_{\mathrm{dis3},1} - \underline{U}_{\mathrm{ac3},1} \end{bmatrix}. \tag{4.9}$$

The ac-side voltage of phase ν under the influence of interlock times can be decomposed into a voltage reference $\underline{U}_{\mathrm{ref}\nu,1}$ and a voltage error $\Delta\underline{U}_{\mathrm{ac}\nu,1}$, with

$$\underline{U}_{\mathrm{ac}\nu,1} = \underline{U}_{\mathrm{ref}\nu,1} + \Delta\underline{U}_{\mathrm{ac}\nu,1}. \tag{4.10}$$

The voltage reference is determined by the modulation process and results in an rms phasor representation of

$$\underline{U}_{\mathrm{ref}\nu,1} = \frac{1}{\sqrt{2}} \cdot M_\nu \cdot \frac{U_{\mathrm{dc0}}}{2} \cdot \mathrm{e}^{\mathrm{j}\theta_{\mathrm{ref}\nu}}, \tag{4.11}$$
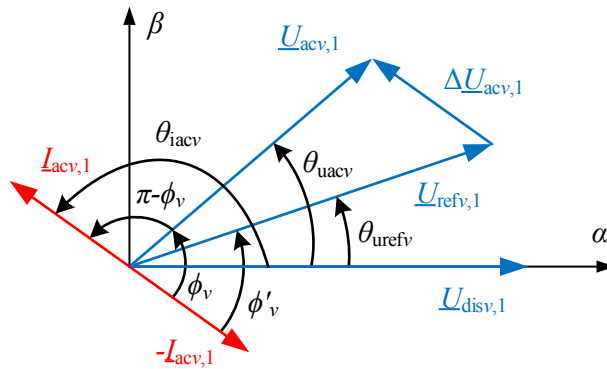
Figure 4.3: Phasor diagram of the fundamental frequency model considering interlock times, based on [58]. The ac-side voltage equals the reference voltage distorted by an error voltage. The phase angle of the error voltage is the same as the phase angle of the ac-side current.

where $\theta_{\mathrm{ref}\nu}$ is the phase angle of the reference voltage. The magnitude of the fundamental voltage error is given in (4.7) with $k = 1$. The sign function of the ac-side current determines that the voltage error phasor is aligned with the ac-side current phasor:

$$\Delta \underline{U}_{\mathrm{ac}\nu,1} = \frac{\sqrt{2} \cdot 2}{\pi} \cdot f_{\mathrm{sw}} \cdot T_{\mathrm{d}} \cdot U_{\mathrm{dc}0} \cdot e^{\mathrm{j}\theta_{\mathrm{iac}\nu}}, \tag{4.12}$$

where $\theta_{\mathrm{iac}\nu}$ is the phase angle of the ac-side current.

The phasor relationships are illustrated in Figure 4.3, where the disturbance voltage is aligned with the alpha axis. The voltage error is in phase with the ac-side current. The phasor diagram introduces the phase angle ϕ_ν, which is defined as the angle between the ac-side voltage $\underline{U}_{\mathrm{ac}\nu,1}$ and the load current $-\underline{I}_{\mathrm{ac}\nu,1}$, with

$$\phi_\nu = \theta_{\mathrm{uac}\nu} - \theta_{\mathrm{iac}\nu} + \pi, \tag{4.13}$$

where $\theta_{\mathrm{uac}\nu}$ is the phase angle of the ac-side voltage. For a passive load the phase angle of the load current is determined by the argument of the complex load impedance: $\phi_\nu = \arg(\underline{Z}_{\mathrm{ac},1})$.

The phase angle ϕ'_ν of the reference voltage with respect to the load current is defined as

$$\phi'_\nu = \theta_{\mathrm{uref}\nu} - \theta_{\mathrm{iac}\nu} + \pi. \tag{4.14}$$

The information provided by ϕ'_ν is the relation of the voltage reference and the fundamental component of the ac-side current, which determines the phase of the voltage error when the harmonic content is negligible. For considering the influence of harmonic phase currents, it is useful to introduce the zero-crossing times t_{01} and t_{02} of the ac-side current, which are the roots

of the ac-side current's Fourier series:

$$i_{\mathrm{ac}\nu}(t) = \sum_{k=-k_{\max}}^{k_{\max}} I_{\mathrm{ac}\nu,k} \cdot \mathrm{e}^{\mathrm{j}k\omega_0 t}, \tag{4.15}$$

$$i_{\mathrm{ac}\nu}(t_{01}) \overset{!}{=} 0, \tag{4.16}$$

$$i_{\mathrm{ac}\nu}(t_{02}) \overset{!}{=} 0. \tag{4.17}$$

In a first step, a single-frequency sinusoidal current is regarded and (4.15) can be written as

$$i_{\mathrm{ac}\nu}(t) = 2 \cdot |I_{\mathrm{ac}\nu,1}| \cdot \cos(\omega_0 \cdot t + \theta_{\mathrm{iac}\nu}). \tag{4.18}$$

The zero crossing $i_{\mathrm{ac}\nu}(t_{01}) \overset{!}{=} 0$ occurs at the time t_{01} when the argument of the cosine function equals $-\pi/2$, thus:

$$\omega_0 \cdot t_{01} + \theta_{\mathrm{iac}\nu} = -\pi/2. \tag{4.19}$$

The second zero-crossing time t_{02} has a fixed relationship with the first zero-crossing time, with

$$\omega_0 \cdot t_{02} = \omega_0 \cdot t_{01} + \pi, \tag{4.20}$$

due to the symmetry of the cosine function. The relationships of the angles are illustrated in Figure 4.4 with the time-domain waveforms of the voltage reference and the ac-side current. The relationship of the phase angle ϕ' and the zero-crossing time results in

$$\phi' = \theta_{\mathrm{uref}\nu} + \omega_0 \cdot t_{01} - \pi/2. \tag{4.21}$$

By using the calculation of the current zero crossings in (4.15)-(4.17), the phase angle ϕ' in
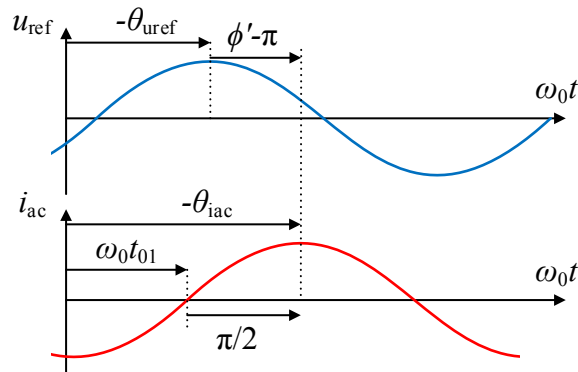

Figure 4.4: Definition of zero crossing angles for sinusoidal currents and voltages: The voltage reference in blue is described by a cosine function with a phase lag of θ_{uref} to the reference point $\omega_0 t = 0$. The ac-side current in red is a cosine function with a phase lag of θ_{iac}, which is alternatively described by the zero-crossing angle $\omega_0 t_{01} = -\theta_{\mathrm{iac}} - \pi/2$. The phase difference of the voltage reference and the ac-side current describes the angle $\phi' - \pi$.

(4.21) describes the current zero crossing under the influence harmonic phase currents. In the following derivation of the switching function spectrum it is assumed that the current changes its sign twice per fundamental period, which is called two even crossover (TEC) mode [18, 22], where the two current zero crossings are symmetrical and (4.20) is valid for harmonic currents.

4.1.2 Switching Function Spectrum Considering Interlock Times

The averaging method in (4.6) and (4.8) is an approximation of the spectrum neglecting the influence of the switching harmonics. The influence of the switching behavior is described by the switching function. Assuming continuous current mode (CCM), the modified definition of the switching function in (4.1) and (4.2) allows for incorporation of the effect of interlock times directly into the calculation of the ac-side voltage spectrum and the dc-side current spectrum using the convolution method in (3.6) and (3.7), resulting in

$$\vec{U}_{\mathrm{ac}\nu} = \frac{1}{2} \cdot \boldsymbol{C}(\vec{S'}_{\nu}) \cdot \vec{U}_{\mathrm{dc}}, \tag{4.22}$$

$$\vec{I}_{\mathrm{dc}\nu} = \frac{1}{2} \cdot \boldsymbol{C}(\vec{S'}_{\nu}) \cdot \vec{I}_{\mathrm{ac}\nu}. \tag{4.23}$$

Therefore, an analytical description of the switching function spectrum under the influence of interlock times $\vec{S'}$ is required.

An analytical model of the ac-side voltage spectrum considering interlock times was first presented by Wu *et al.* [18] for a single-phase full-bridge inverter with inductive load, based on double Fourier analysis. A further method based on double Fourier series was proposed by Koeslag *et al.* [19]. This method assumes single-frequency duty cycles and incorporates the influence of finite turn-on and turn-off times by consideration of the gate-drain capacitance and the parasitic switching-node capacitance.

An alternative method of deriving the ac-side voltage spectrum under the influence of interlock times is derived by Moore *et al.* [21]. The method is based on the PWM model introduced by Cox [14] and assumes a sinusoidal duty cycle and a passive RL load. Although not mentioned by the authors, the results represent the switching function, because they are derived as a dimensionless quantity $v(t)$ for a constant dc-link voltage of $U_{\mathrm{dc0}} = 2\,\mathrm{V}$. The equality is expressed through

$$v(t) := \frac{u_{\mathrm{ac}}(t)}{U_{\mathrm{dc0}}/2} \mathbin{\hat{=}} s'_{\nu}(t). \tag{4.24}$$

Using the same mathematical approach, the dc-side current spectrum is derived in the Ph.D. thesis by Ainslie-Malik [20].

As shown in Chapter 3, the same switching function can be used for the calculation of both the

ac-side voltage and the dc-side current. This is also true during the interlock times in CCM. Thus, the results given in [21] can be used in a modified notation to represent the switching function $s'_\nu(t)$ of phase ν.

In this thesis, it is proposed to interpret the results presented in [21] as a switching function spectrum, which allows for the utilization of the convolution method in (4.22) and (4.23) and simultaneously incorporates the effect of interlock times and harmonic disturbances. The resulting block diagram of the signal interactions is depicted in Figure 4.5. Because the switching function spectrum including interlock times depends on the sign of the phase current, the equation system is nonlinear. The following section deals with the determination of the phase current's zero crossings that is required by the method.
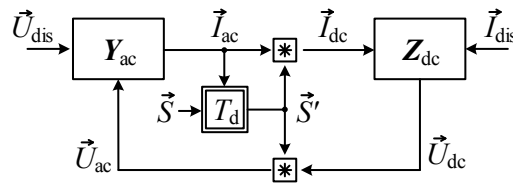

Figure 4.5: Extension of the block diagram in Figure 3.20 showing the interaction of the signals under the influence of interlock times.

Derivation of the Switching Function Spectrum

The switching process under the influence of the interlock times is mathematically expressed according to the times defined in Figure 4.6. Using a sequence of unit step functions (see (3.20)) the switching function without interlock times of phase ν can be written as

$$s_\nu(t) = 1 - 2 \cdot \sum_{m=-\infty}^{\infty} \sigma(t - mT_{\text{sw}} - \tau_{\text{f}\nu m}) - \sigma(t - mT_{\text{sw}} - \tau_{\text{r}\nu m}) \quad \text{[21, (3)]}, \quad (4.25)$$

where the switching instants with respect to the beginning of the m-th switching period are $\tau_{\text{f}\nu m}$ for the falling edge and $\tau_{\text{r}\nu m}$ for the rising edge. These times have a linear relationship with the duty cycle, with

$$
\begin{aligned}
\tau_{\text{f}\nu m} &= \frac{1}{4} \cdot (1 + d_\nu[mT_{\text{sw}}]) \cdot T_{\text{sw}} \quad \text{[21, (9)]}, \\
\tau_{\text{r}\nu m} &= \frac{1}{4} \cdot (3 - d_\nu[(m + 1/2)T_{\text{sw}}]) \cdot T_{\text{sw}} \quad \text{[21, (10)]}.
\end{aligned}
\tag{4.26}
$$

The application of interlock times to the rising edges of the gate signals modifies the expression of the switching function to

$$s'_\nu(t) = 1 - 2 \cdot \sum_{m=-\infty}^{\infty} \sigma(t - mT_{\text{sw}} - \tau_{\text{f}\nu m} - \tau_{\text{df}\nu m}) - \sigma(t - mT_{\text{sw}} - \tau_{\text{r}\nu m} - \tau_{\text{dr}\nu m}). \quad (4.27)$$
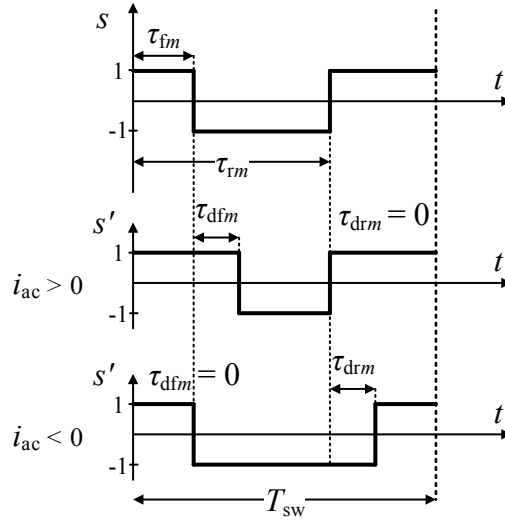
Figure 4.6: Top graph: Ideal switching function s, with the time interval of the falling edge $\tau_{\mathrm{f}m}$ and the rising edge $\tau_{\mathrm{r}m}$ in reference to the beginning of the m-th switching cycle. **Middle graph:** Modified switching function s' for positive phase currents, where the falling edge is delayed by $\tau_{\mathrm{df}m}$ due to interlock times. **Bottom graph:** Modified switching function s' for negative phase currents, where the rising edge is delayed by $\tau_{\mathrm{dr}m}$ due to interlock times.

The influence of interlock times is considered by delaying the switching process by the times $\tau_{\mathrm{df}\nu m}$ and $\tau_{\mathrm{dr}\nu m}$ for the falling and rising edges of the switching function respectively, with

$$
\begin{aligned}
\tau_{\mathrm{df}\nu m} &= \frac{1}{2} \cdot (1 + \psi_\nu[mT_{\mathrm{sw}}]) \cdot T_{\mathrm{d}}, \\
\tau_{\mathrm{dr}\nu m} &= \frac{1}{2} \cdot (1 - \psi_\nu[(m+1/2)T_{\mathrm{sw}}]) \cdot T_{\mathrm{d}} \quad [21, (13)\text{-}(14)].
\end{aligned}
\tag{4.28}
$$

Here, the choice function $t \mapsto \psi(t)$ considers the influence of the sign of the phase current. In addition to [21], a phase displacement of the voltage reference in reference to the other signals of the system is considered. This enables to incorporate the relationship of the voltage reference with other signals, such as an external disturbance voltage and the dc-link voltage. Because the voltage reference is covered in this thesis in the more general sense of the duty cycle, the phase angle $\theta_{\mathrm{d}0\nu}$ is used in replacement of the angle of the reference voltage $\theta_{\mathrm{uref}\nu}$ in (4.14). Using this equation, the phase current changes its sign twice per cycle at a zero-crossing angle $\angle I_{\mathrm{ac}\nu} = -\phi'_\nu + \theta_{\mathrm{d}0\nu} + \pi$ and the choice function can be written as

$$
\begin{aligned}
\psi_\nu(t) &= \mathrm{sign}(i_{\mathrm{ac}\nu}(t)) = \mathrm{sign}(\cos(\omega_0 t + \angle I_{\mathrm{ac}\nu})) \\
&= \mathrm{sign}(\cos(\omega_0 t - \phi'_\nu + \theta_{\mathrm{d}0\nu} + \pi)) = -\mathrm{sign}(\cos(\omega_0 t - \phi'_\nu + \theta_{\mathrm{d}0\nu})).
\end{aligned}
\tag{4.29}
$$

The function has a rectangular waveform with a periodicity of $2\pi/\omega_0$,

$$
\psi_\nu(t) = \begin{cases} 1 & \text{for} \quad (\frac{\pi}{2} + \phi'_\nu - \theta_{\mathrm{d}0\nu}) < \omega_0 t < (\frac{3\pi}{2} + \phi'_\nu - \theta_{\mathrm{d}0\nu}) \\ -1 & \text{for} \quad (-\frac{\pi}{2} + \phi'_\nu - \theta_{\mathrm{d}0\nu}) < \omega_0 t < (\frac{\pi}{2} + \phi'_\nu - \theta_{\mathrm{d}0\nu}) \end{cases}.
\tag{4.30}
$$

In a later step of the derivation process, a time-shifted choice function is utilized, with

$$\psi_\nu(t - \frac{\theta_{\mathrm{d}0\nu}}{\omega_0}) = \begin{cases} 1 & \text{for} & (\frac{\pi}{2} + \phi'_\nu) < \omega_0 t < (\frac{3\pi}{2} + \phi'_\nu) \\ -1 & \text{for} & (-\frac{\pi}{2} + \phi'_\nu) < \omega_0 t < (\frac{\pi}{2} + \phi'_\nu) \end{cases} . \tag{4.31}$$

Due to a simplified derivation in the following steps, the choice function in (4.29) is applied with values of $i_{\mathrm{ac}\nu}(t)$ sampled at the beginning of the switching cycle and at the center of the switching cycle. This introduces a modeling error when the sign of the current changes within a PWM period.

In the following derivation of the switching function spectrum, the duty cycle is limited to a single frequency sine wave, with

$$d_\nu[mT_{\mathrm{sw}}] = M_\nu \cdot \cos(m\omega_0 T_{\mathrm{sw}} + \theta_{\mathrm{d}0\nu}). \tag{4.32}$$

The Fourier transform $S'_\nu(\omega) \bullet\!\!-\!\!\circ s'_\nu(t)$ of the modified switching function in (4.27) is derived by applying the Fourier transform of the time-shifted unit step function (3.26) and (3.27). With $\omega = 2\pi f \neq 0$ this results in:

$$S'_\nu(\omega) = -\frac{2}{\mathrm{j}\omega} \cdot \sum_{m=-\infty}^{\infty} \mathrm{e}^{-\mathrm{j}\omega(mT_{\mathrm{sw}} + \tau_{\mathrm{f}\nu m} + \tau_{\mathrm{df}\nu m})} - \mathrm{e}^{-\mathrm{j}\omega(mT_{\mathrm{sw}} + \tau_{\mathrm{r}\nu m} + \tau_{\mathrm{dr}\nu m})} \quad [21, (39)]. \tag{4.33}$$

Application of (4.26), (4.28), and (4.32) to (4.33) yields:

$$S'_\nu(\omega) = -\frac{2}{\mathrm{j}\omega} \cdot \sum_{m=-\infty}^{\infty} \mathrm{e}^{-\mathrm{j}\omega mT_{\mathrm{sw}}}...$$
$$\cdot \left[\quad \mathrm{e}^{-\frac{1}{4}\mathrm{j}\omega T_{\mathrm{sw}}} \cdot \mathrm{e}^{-\mathrm{j}\omega\frac{1}{4}(T_{\mathrm{sw}}M_\nu \cos(m\omega_0 T_{\mathrm{sw}} + \theta_{\mathrm{d}0\nu}) + 2\omega T_{\mathrm{d}}\psi_\nu[mT_{\mathrm{sw}}])} \cdot \mathrm{e}^{-\frac{1}{2}\mathrm{j}\omega T_{\mathrm{d}}} \quad ... \right.$$
$$\left. - \mathrm{e}^{-\frac{3}{4}\mathrm{j}\omega T_{\mathrm{sw}}} \cdot \mathrm{e}^{\mathrm{j}\omega\frac{1}{4}(T_{\mathrm{sw}}M_\nu \cos((m+1/2)\omega_0 T_{\mathrm{sw}} + \theta_{\mathrm{d}0\nu}) + 2\omega T_{\mathrm{d}}\psi_\nu[(m+1/2)T_{\mathrm{sw}}])} \cdot \mathrm{e}^{-\frac{1}{2}\mathrm{j}\omega T_{\mathrm{d}}} \right]. \tag{4.34}$$

The definition of

$$z_\nu(\omega) := -\frac{1}{4}\omega T_{\mathrm{sw}} M_\nu$$
$$\lambda_\nu := -\frac{2T_{\mathrm{d}}}{T_{\mathrm{sw}} M_\nu} \tag{4.35}$$

allows for a more compact notation:

$$S'_\nu(\omega) = -\frac{2}{\mathrm{j}\omega} \cdot \sum_{m=-\infty}^{\infty} \mathrm{e}^{-\mathrm{j}\omega mT_{\mathrm{sw}}} \cdot \mathrm{e}^{-\frac{1}{2}\mathrm{j}\omega T_{\mathrm{d}}}...$$
$$\cdot \left[\quad \mathrm{e}^{-\frac{1}{4}\mathrm{j}\omega T_{\mathrm{sw}}} \cdot \mathrm{e}^{\mathrm{j}z_\nu(\omega)\cdot(\cos(m\omega_0 T_{\mathrm{sw}} + \theta_{\mathrm{d}0\nu}) - \lambda_\nu\psi_\nu[mT_{\mathrm{sw}}])} \quad ... \right.$$
$$\left. - \mathrm{e}^{-\frac{3}{4}\mathrm{j}\omega T_{\mathrm{sw}}} \cdot \mathrm{e}^{-\mathrm{j}z_\nu(\omega)\cdot(\cos((m+1/2)\omega_0 T_{\mathrm{sw}} + \theta_{\mathrm{d}0\nu}) - \lambda_\nu\psi_\nu[(m+1/2)T_{\mathrm{sw}}])} \right]. \tag{4.36}$$

Use of the Poisson re-summation formula, with

$$\sum_{m=-\infty}^{\infty} h(m) = \sum_{m=-\infty}^{\infty} \int_{-\infty}^{\infty} e^{j2\pi m\tau} \cdot h(\tau)\, d\tau \quad \text{[21, (17)]} \tag{4.37}$$

allows for the expression of (4.36) as

$$S'_\nu(\omega) = -\frac{2}{j\omega} \sum_{m=-\infty}^{\infty} \int_{-\infty}^{\infty} e^{j2\pi m\tau} \cdot e^{-j\omega\tau T_{\mathrm{sw}}} \cdot e^{-\frac{1}{2}j\omega T_{\mathrm{d}}} \cdot Q(\tau)\, d\tau \quad \text{[21, (40)]}, \tag{4.38}$$

where

$$Q(\tau) = \quad e^{-\frac{1}{4}j\omega T_{\mathrm{sw}}} \cdot e^{jz_\nu(\omega)\cdot(\cos(\omega_0\tau T_{\mathrm{sw}}+\theta_{\mathrm{d}0\nu})-\lambda_\nu\psi_\nu(\tau T_{\mathrm{sw}}))} \cdots$$
$$- e^{-\frac{3}{4}j\omega T_{\mathrm{sw}}} \cdot e^{-jz_\nu(\omega)\cdot((\omega_0(\tau+1/2)T_{\mathrm{sw}}+\theta_{\mathrm{d}0\nu})-\lambda_\nu\psi_\nu((\tau+1/2)T_{\mathrm{sw}}))}. \tag{4.39}$$

Substitution of $t = \tau T_{\mathrm{sw}}$ yields:

$$S'_\nu(\omega) = -\frac{2}{j\omega T_{\mathrm{sw}}} \sum_{m=-\infty}^{\infty} \int_{-\infty}^{\infty} e^{j2\pi mt/T_{\mathrm{sw}}} \cdot e^{-j\omega t} \cdot e^{-\frac{1}{2}j\omega T_{\mathrm{d}}} \cdot q(t)\, dt, \tag{4.40}$$

with

$$q(t) = \quad e^{-\frac{1}{4}j\omega T_{\mathrm{sw}}} \cdot e^{jz_\nu(\omega)\cdot(\cos(\omega_0 t+\theta_{\mathrm{d}0\nu})-\lambda_\nu\psi_\nu(t))} \cdots$$
$$- e^{-\frac{3}{4}j\omega T_{\mathrm{sw}}} \cdot e^{-jz_\nu(\omega)\cdot((\omega_0(t+T_{\mathrm{sw}}/2)+\theta_{\mathrm{d}0\nu})-\lambda_\nu\psi_\nu(t+T_{\mathrm{sw}}/2))}. \tag{4.41}$$

The exponentials include the periodic functions $\cos(\omega_0 t + \theta_{\mathrm{d}0\nu})$ and $\psi(t)$, which have a periodicity of $2\pi/\omega_0$. Thus, an expression as a Fourier series is possible. The Fourier series is introduced in the following general form

$$e^{jz_\nu(\omega)(\cos(\omega_0 t)-\lambda_\nu\psi_\nu(t-\frac{\theta_{\mathrm{d}0\nu}}{\omega_0}))} = \sum_{n=-\infty}^{\infty} C_n(z_\nu, \lambda_\nu, \phi'_\nu) \cdot e^{jn\omega_0 t}, \tag{4.42}$$

where C_n is the Fourier coefficient of harmonic order n and z_ν and λ_ν are parameters. It is indicated that there is a dependency on ϕ'_ν through the choice function ψ_ν, which is clarified by the following equations. The coefficients are calculated by applying (2.2), with

$$C_n(z_\nu, \lambda_\nu, \phi'_\nu) = \frac{\omega_0}{2\pi} \cdot \int_0^{2\pi/\omega_0} e^{jz_\nu(\cos(\omega_0 t)-\lambda_\nu\psi_\nu(t-\frac{\theta_{\mathrm{d}0\nu}}{\omega_0}))} \cdot e^{-jn\omega_0 t}\, dt$$
$$= \frac{\omega_0}{2\pi} \cdot \left(\int_{(-\frac{\pi}{2}+\phi'_\nu)/\omega_0}^{(\frac{\pi}{2}+\phi'_\nu)/\omega_0} e^{jz_\nu(\cos(\omega_0 t)+\lambda_\nu)} \cdot e^{-jn\omega_0 t}\, dt \cdots \right.$$
$$\left. + \int_{(\frac{\pi}{2}+\phi'_\nu)/\omega_0}^{(\frac{3\pi}{2}+\phi'_\nu)/\omega_0} e^{jz_\nu(\cos(\omega_0 t)-\lambda_\nu)} \cdot e^{-jn\omega_0 t}\, dt \right). \tag{4.43}$$

In the next step, the Jacobi-Anger identity

$$e^{jz_\nu \cos(\omega_0 t)} = \sum_{p=-\infty}^{\infty} j^p \cdot J_p(z_\nu) \cdot e^{jp\omega_0 t} \tag{4.44}$$

is applied, where $J_p(z_\nu)$ is the p-th order Bessel function of the first kind with the argument z_ν. This yields

$$C_n(z_\nu, \lambda_\nu, \phi'_\nu) = \frac{\omega_0}{2\pi} \cdot \left(\int_{(-\frac{\pi}{2}+\phi'_\nu)/\omega_0}^{(\frac{\pi}{2}+\phi'_\nu)/\omega_0} e^{jz_\nu\lambda_\nu} \cdot e^{-jn\omega_0 t} \cdot \sum_{p=-\infty}^{\infty} j^p \cdot J_p(z_\nu) \cdot e^{jp\omega_0 t} \, dt \, ... \right.$$
$$\left. + \int_{(\frac{\pi}{2}+\phi'_\nu)/\omega_0}^{(\frac{3\pi}{2}+\phi'_\nu)/\omega_0} e^{-jz_\nu\lambda_\nu} \cdot e^{-jn\omega_0 t} \cdot \sum_{p=-\infty}^{\infty} j^p \cdot J_p(z_\nu) \cdot e^{jp\omega_0 t} \, dt \right) . \tag{4.45}$$

Since p and t are independent variables, the integral of the sum is equivalent to the sum of integrals:

$$C_n(z_\nu, \lambda_\nu, \phi'_\nu) = \frac{\omega_0}{2\pi} \cdot \sum_{p=-\infty}^{\infty} j^p \cdot J_p(z_\nu)...$$
$$\cdot \underbrace{\left(e^{jz_\nu\lambda_\nu} \cdot \int_{(-\frac{\pi}{2}+\phi'_\nu)/\omega_0}^{(\frac{\pi}{2}+\phi'_\nu)/\omega_0} e^{-j(n-p)\omega_0 t} \, dt + e^{-jz_\nu\lambda_\nu} \cdot \int_{(\frac{\pi}{2}+\phi'_\nu)/\omega_0}^{(\frac{3\pi}{2}+\phi'_\nu)/\omega_0} e^{-j(n-p)\omega_0 t} \, dt \right)}_{A_{pn}} . \tag{4.46}$$

The summation is further analyzed for the term in the brackets A_{pn} for the case $p = n$, with

$$A_{pn}(z_\nu, \lambda_\nu, \phi'_\nu) = \frac{\pi}{\omega_0} \cdot \left(e^{jz_\nu\lambda_\nu} + e^{-jz_\nu\lambda_\nu} \right)$$
$$= \frac{2\pi}{\omega_0} \cdot \cos(z_\nu\lambda_\nu), \tag{4.47}$$

and for the case $p \neq n$:

$$A_{pn}(z_\nu, \lambda_\nu, \phi'_\nu) = e^{jz_\nu\lambda_\nu} \cdot \frac{1}{-j(n-p)\omega_0} \left(e^{-j(n-p)\frac{\pi}{2}} - e^{j(n-p)\frac{\pi}{2}} \right) \cdot e^{-j(n-p)\phi'} ...$$
$$+ e^{-jz_\nu\lambda_\nu} \cdot \frac{1}{-j(n-p)\omega_0} \left(e^{-j(n-p)\frac{3\pi}{2}} - e^{-j(n-p)\frac{\pi}{2}} \right) \cdot e^{-j(n-p)\phi'}$$
$$= \left(e^{jz_\nu\lambda_\nu} - e^{-jz_\nu\lambda_\nu} \right) \cdot e^{-j(n-p)\phi'} \cdot \frac{1}{-j(n-p)\omega_0} \left(e^{-j(n-p)\frac{\pi}{2}} - e^{j(n-p)\frac{\pi}{2}} \right) \tag{4.48}$$
$$= 2j \cdot \sin(z_\nu\lambda_\nu) \cdot e^{-j(n-p)\phi'} \cdot \frac{1}{-j(n-p)\omega_0} \cdot e^{j(n-p)\frac{\pi}{2}} \cdot \left(e^{-j(n-p)\pi} - 1 \right)$$
$$= \sin(z_\nu\lambda_\nu) \cdot e^{j(p-n)\phi'} \cdot \frac{2}{(p-n)\omega_0} \cdot j^{n-p} \cdot \left((-1)^{p-n} - 1 \right) .$$

This allows for the expression of the Fourier coefficient in (4.46) as:

$$C_n(z_\nu, \lambda_\nu, \phi_\nu') = \quad \mathrm{j}^n \cdot \cos(z_\nu \lambda_\nu) \cdot J_n(z_\nu)...$$

$$+ \mathrm{j}^n \cdot \sin(z_\nu \lambda_\nu) \cdot \sum_{\substack{p=-\infty \\ p \neq n}}^{\infty} \frac{1}{\pi(p-n)} \cdot J_p(z_\nu) \cdot \mathrm{e}^{\mathrm{j}(p-n)\phi'} \cdot ((-1)^{p-n} - 1). \quad (4.49)$$

Before inserting this result (4.40), the time-shift property is applied to (4.42), with

$$\mathrm{e}^{\mathrm{j}z_\nu(\cos(\omega_0 t + \theta_{\mathrm{d}0\nu}) - \lambda_\nu \psi(t))} = \sum_{n=-\infty}^{\infty} C_n(z_\nu, \lambda_\nu, \phi_\nu') \cdot \mathrm{e}^{\mathrm{j}n\omega_0 t} \cdot \mathrm{e}^{\mathrm{j}n\theta_{\mathrm{d}0\nu}}, \quad (4.50)$$

the exponentials in (4.41) can be expressed by the Fourier coefficients, with

$$q(t) = \mathrm{e}^{-\frac{1}{4}\mathrm{j}\omega T_{\mathrm{sw}}} \cdot \sum_{n=-\infty}^{\infty} C_n(z_\nu, \lambda_\nu, \phi_\nu') \cdot \mathrm{e}^{\mathrm{j}n\omega_0 t} \cdot \mathrm{e}^{\mathrm{j}n\theta_{\mathrm{d}0\nu}t}...$$

$$-\mathrm{e}^{-\frac{3}{4}\mathrm{j}\omega T_{\mathrm{sw}}} \cdot \sum_{n=-\infty}^{\infty} C_n(-z_\nu, \lambda_\nu, \phi_\nu') \cdot \mathrm{e}^{\mathrm{j}n\omega_0 t} \cdot \mathrm{e}^{\mathrm{j}n\omega_0 T_{\mathrm{sw}}/2} \cdot \mathrm{e}^{\mathrm{j}n\theta_{\mathrm{d}0\nu}t}. \quad (4.51)$$

Inserting (4.51) into (4.40) yields:

$$S_\nu'(\omega, \phi_\nu') = -\frac{2}{\mathrm{j}\omega T_{\mathrm{sw}}} \cdot \mathrm{e}^{-\frac{1}{2}\mathrm{j}\omega T_{\mathrm{d}}} \sum_{m=-\infty}^{\infty} \sum_{n=-\infty}^{\infty} \int_{-\infty}^{\infty} \mathrm{e}^{-\mathrm{j}(\omega - \omega_{mn})}...$$

$$\cdot \left[\mathrm{e}^{-\frac{1}{4}\mathrm{j}\omega T_{\mathrm{sw}}} \cdot C_n(z_\nu, \lambda_\nu, \phi_\nu') - \mathrm{e}^{-\frac{3}{4}\mathrm{j}\omega T_{\mathrm{sw}}} \cdot C_n(-z_\nu, \lambda_\nu, \phi_\nu') \cdot \mathrm{e}^{\mathrm{j}n\omega_0 T_{\mathrm{sw}}/2} \right] \cdot \mathrm{e}^{\mathrm{j}n\theta_{\mathrm{d}0\nu}t} \, \mathrm{d}t, \quad (4.52)$$

where $\omega_{mn} = n\omega_0 + m\omega_s$ [21, (45)].

This equation can be interpreted as a Fourier transform

$$S_\nu'(\omega, \phi_\nu') = \int_{-\infty}^{\infty} s_\nu'(t, \phi_\nu') \mathrm{e}^{-\mathrm{j}\omega} \, \mathrm{d}t \quad (4.53)$$

with the time-domain function

$$s_\nu'(t, \phi_\nu') = -\frac{2}{\mathrm{j}\omega T_{\mathrm{sw}}} \cdot \mathrm{e}^{-\frac{1}{2}\mathrm{j}\omega T_{\mathrm{d}}} \sum_{m=-\infty}^{\infty} \sum_{n=-\infty}^{\infty} ... \quad (4.54)$$

$$\cdot \left[\mathrm{e}^{-\frac{1}{4}\mathrm{j}\omega T_{\mathrm{sw}}} \cdot C_n(z_\nu, \lambda_\nu, \phi_\nu') - \mathrm{e}^{-\frac{3}{4}\mathrm{j}\omega T_{\mathrm{sw}}} \cdot C_n(-z_\nu, \lambda_\nu, \phi_\nu') \cdot \mathrm{e}^{\mathrm{j}n\omega_0 T_{\mathrm{sw}}/2} \right] \cdot \mathrm{e}^{\mathrm{j}\omega_{mn}} \cdot \mathrm{e}^{\mathrm{j}n\theta_{\mathrm{d}0\nu}t}.$$

Being in the form of a double Fourier series with Fourier coefficients $\vec{S}_{\nu,mn}'(\phi_\nu')$, the equation is written as:

$$s_\nu'(t, \phi_\nu') = \sum_{m=-\infty}^{\infty} \sum_{n=-\infty}^{\infty} \underline{S}_{\nu,mn}'(\phi_\nu') \cdot \mathrm{e}^{\mathrm{j}\omega_{mn}t} \cdot \mathrm{e}^{\mathrm{j}n\theta_{\mathrm{d}0\nu}}. \quad (4.55)$$

It is indicated that the coefficients depend on the current zero crossing, which is expressed by

the phase angle ϕ'_ν defined in (4.14). The Fourier coefficients are:

$$
\underline{S}'_{\nu,mn}(\phi'_\nu) = -\frac{2}{\mathrm{j}\omega_{mn}T_{\mathrm{sw}}} \cdot \mathrm{e}^{-\frac{1}{2}\mathrm{j}\omega_{mn}T_{\mathrm{d}}}\dots
$$
$$
\cdot\left[\mathrm{e}^{-\frac{1}{4}\mathrm{j}\omega_{mn}T_{\mathrm{sw}}}\cdot C_n\left(z_\nu,\lambda_\nu,\phi'_\nu\right) - \mathrm{e}^{-\frac{3}{4}\mathrm{j}\omega_{mn}T_{\mathrm{sw}}}\cdot C_n\left(-z_\nu,\lambda_\nu,\phi'_\nu\right)\cdot \mathrm{e}^{\mathrm{j}n\omega_0 T_{\mathrm{sw}}/2}\right]. \tag{4.56}
$$

Due to the properties of the Bessel function, with $J_n(-z_\nu) = J_n(z_\nu)\cdot(-1)^n, n\in\mathbb{N}$, and the properties of trigonometric functions, with $\cos(-z_\nu\lambda_\nu) = \cos(z_\nu\lambda_\nu)$ and $\sin(-z_\nu\lambda_\nu) = -\sin(z_\nu\lambda_\nu)$, it can be shown that

$$
C_n(z_\nu,\lambda_\nu,\phi'_\nu) = C_n(-z_\nu,\lambda_\nu,\phi'_\nu)\cdot(-1)^n, n\in\mathbb{N}. \tag{4.57}
$$

This allows for a more compact expression of (4.56), with

$$
\underline{S}'_{\nu,mn}(\phi'_\nu) = \frac{2}{\mathrm{j}\omega_{mn}T_{\mathrm{sw}}}\cdot \mathrm{e}^{-\frac{1}{2}\mathrm{j}\omega_{mn}T_{\mathrm{d}}}\cdot \mathrm{e}^{-\frac{1}{4}\mathrm{j}\omega_{mn}T_{\mathrm{sw}}}\cdot C_n\left(-z_\nu,\lambda_\nu,\phi'_\nu\right)\cdot\left((-1)^m - (-1)^n\right). \tag{4.58}
$$

Application of (4.49) and re-substitution of (4.35) yields:

$$
\begin{aligned}
\underline{S}'_{\nu,mn}(\phi'_\nu) = \quad &\frac{2}{\mathrm{j}\Omega_{mn}}\cdot J_n\left(\frac{1}{4}\Omega_{mn}M_\nu\right)\cdot\cos\left(\frac{1}{2}\Omega_{mn}M_\nu\frac{T_{\mathrm{d}}}{T_{\mathrm{sw}}}\right)\dots \\
&\cdot \mathrm{e}^{-\frac{1}{4}\mathrm{j}\Omega_{mn}}\cdot \mathrm{e}^{-\frac{1}{2}\mathrm{j}\Omega_{mn}\frac{T_{\mathrm{d}}}{T_{\mathrm{sw}}}}\cdot \mathrm{j}^n\cdot\left((-1)^m - (-1)^n\right)\dots \\
&+\frac{2}{\mathrm{j}\Omega_{mn}}\cdot\sum_{\substack{p=-\infty\\p\neq n}}^{\infty} J_p\left(\frac{1}{4}\Omega_{mn}M_\nu\right)\cdot\sin\left(\frac{1}{2}\Omega_{mn}M_\nu\frac{T_{\mathrm{d}}}{T_{\mathrm{sw}}}\right)\dots \\
&\cdot\frac{\mathrm{e}^{\mathrm{j}(p-n)\phi'_\nu}}{\pi(p-n)}\cdot \mathrm{e}^{-\frac{1}{4}\mathrm{j}\Omega_{mn}}\cdot \mathrm{e}^{-\frac{1}{2}\mathrm{j}\Omega_{mn}\frac{T_{\mathrm{d}}}{T_{\mathrm{sw}}}}\cdot \mathrm{j}^n\cdot F_{mnp},
\end{aligned} \tag{4.59}
$$
$$
F_{mnp} := (1 - (-1)^{p-n})\cdot((-1)^m + (-1)^p),
$$
$$
\Omega_{mn} := \omega_{mn}\cdot T_{\mathrm{sw}}\quad [21, (49\text{-}50)].
$$

Because of the assumption $\omega\neq 0$ in (4.33), the results are valid for $\omega_{mn}\neq 0$. In [20] it is shown that the average value of the function $s'_\nu(t)$ is zero, which means that the superposition of all components that contribute to $\omega_{mn} = 0$ is zero.

In order to incorporate the modified switching function spectrum into the frequency-domain models, it is necessary to transform the information into the vector representation $\vec{\underline{S}}'$, where the rows describe harmonics of the fundamental frequency f_0. Its Fourier series is described by

$$
s'_\nu(t) = \sum_{k=-k_{\max}}^{k_{\max}} \underline{S}'_{\nu,k}(\phi'_\nu)\cdot \mathrm{e}^{\mathrm{j}k\omega_0 t}. \tag{4.60}
$$

A comparison of (4.55) with the required form in (4.60) reveals that all combinations of m and n that fulfill $m\cdot\omega_{\mathrm{sw}} + n\cdot\omega_{\mathrm{d}0} = k\cdot\omega_0$ are superposed in the k-th harmonic component. Limiting

the indeces of summation in (4.55) to $m = [-m_{\max}, ..., m_{\max}]$ and $n = [-n_{\max}, ..., n_{\max}]$ enables a numerical evaluation. The modified switching function spectrum depends on the system signals through the current zero crossing in the form of the phase angle ϕ'. Due to the nonlinear interactions of the ac-side current and the modified switching function, an iterative solution process is implemented.

Whereas the results in (4.59) are only valid for sinusoidal duty cycles, the method presented by Chierchie *et al.* [22] provides the ac-side voltage spectrum for multiple-frequency duty cycles using a TE-PWM model based on the results in [15]. Similarly, the results are derived for a constant dc-link voltage and represent the switching function spectrum, although not indicated by the authors.

Iterative Solution Process

By solving the nonlinear equation system (4.9)-(4.12) an estimation of the phase current zero crossing is obtained based on the fundamental frequency components. The phase angle ϕ' is then given in (4.14). The information about the zero crossing is required in the switching function model in the form of the phase angle ϕ'_ν. The calculation assumes that the output current of the inverter is nearly sinusoidal [58]. Especially when large harmonic components are present in the current, the deviation of the actual zero crossing from the calculation becomes considerable.

Using the phase angle ϕ' of the fundamental frequency model as a starting value makes it possible to solve the linear equation system of the VSI under the influence of interlock times. The resulting phase current spectrum allows for the recalculation of the current zero crossings by solving (4.15).

In an iterative process (Figure 4.7), the spectrum of the ac-side current is recalculated until the deviation of the newly calculated phase angle ϕ' from an old calculation is smaller than a defined boundary $\Delta\phi_{\max}$.

4.2 Numerical Evaluation

A numerical evaluation of the frequency-domain models including the influence of interlock times is presented in this section.

The case study uses the same topology and set of parameters as Case I in Section 3.4, with a three-phase VSI that is connected to an RL load on the ac side. The dc link is fed by a six-pulse diode rectifier. A switching frequency of $2\,\mathrm{kHz}$ is used with AD-PWM as the modulation method. The parameters are given in Table 4.1.
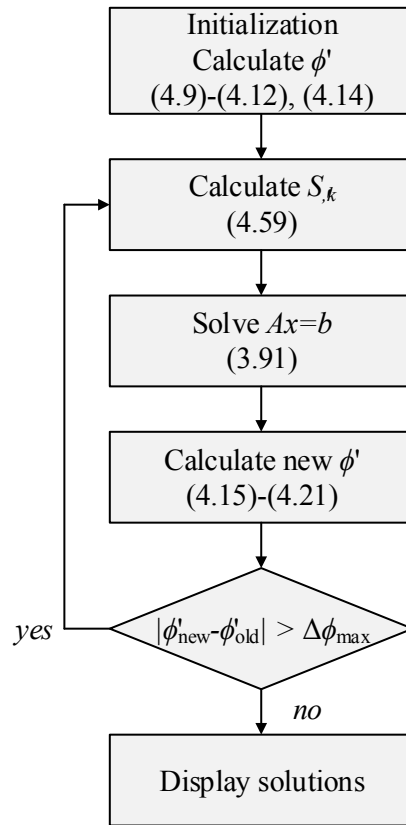
Figure 4.7: Program flow chart of the iterative calculation of the converter spectrum under the influence of inter-lock times. An estimation of ϕ' is initially calculated using a fundamental frequency model. In the following iteration process, the modified switching function is calculated and applied in the linear frequency-domain model of the VSI. The obtained ac-side current spectrum allows for the recalculation of ϕ' for an improved estimation. The process is stopped when the variation of the iteratively calculated phase angle ϕ' is smaller than a predefined maximum deviation ε.

The first step of the evaluation process is to compare the results from the frequency-domain model with time-domain simulations, while the ac-side current is idealized to a symmetrical sinusoidal three-phase system. Due to this modeling simplification, the load behaves like a current source and the zero-crossing angle ϕ' is independent of the behavior of the VSI. The zero crossing angle is chosen to $\phi' = \angle \underline{Z}_{ac}$ and the amplitude of the phase current is set to $\hat{i}_{ac} = (M \cdot U_{dc0})/(2 \cdot |\underline{Z}_{ac}|)$.

The disturbance current spectrum $\vec{I}_{dis}$ that results from the rectifier is taken from the time-domain simulations and is included in the frequency-domain model as an independent input signal. Because the zero-crossing angle is known, the modified switching function spectrum $\vec{S}'_\nu$ can be calculated a priori using (4.59). This allows for the calculation of the dc-side current spectrum, the dc-link voltage spectrum and the ac-side voltage spectra from the ac-side current spectrum in a linear process:

$$\vec{I}_{ac\nu} \xrightarrow{(4.23)} \vec{I}_{dc} = \sum_\nu \vec{I}_{dc\nu} \xrightarrow{(3.81)} \vec{U}_{dc} \xrightarrow{(4.22)} \vec{U}_{ac\nu}. \tag{4.61}$$

Table 4.1: Parameters of the example system for evaluating the influence of interlock times.

Parameter	Symbol	Value
Fundamental frequency	f_0	$10\,\mathrm{Hz}$
Grid frequency	f_g	$50\,\mathrm{Hz}$
Duty-cycle frequency	f_d0	$40\,\mathrm{Hz}$
AC filter resistance	R_ac	$5\,\Omega$
AC filter inductance	L_ac	$20\,\mathrm{mH}$
Switching frequency	f_sw	$3\,\mathrm{kHz}$
Control frequency	f_c	$6\,\mathrm{kHz}$
Dead time	T_d	$10\,\mathrm{\mu s}$
Grid voltage (line-to-line rms)	U_g	$400\,\mathrm{V}$
DC-link voltage (dc component)	U_dc0	$555\,\mathrm{V}$
DC-link capacitance	C_dc	$480\,\mathrm{\mu F}$
Modulation index	M	0.6
Fundamental phase shift	θ_0	0
Maximum harmonic order	k_max	500
Maximum carrier order	m_max	1
Maximum sideband order	n_max	90
	p_max	90

Figure 4.8 shows a comparison of the results from the frequency-domain model with results from time-domain simulations. The first graph shows the magnitudes of the modified switching function spectrum. Because it is a fictive signal that cannot be measured in a system, the modified switching function spectra for the time-domain simulations are calculated from the ac-side voltage and the dc-link voltage signals and application of an FFT, with

$$S_1[kf_0] = \mathcal{FFT}\left\{2 \cdot \frac{u_\mathrm{ac1}[n]}{u_\mathrm{dc}[n]}\right\}. \tag{4.62}$$

The fundamental frequency of the signals is the greatest common divisor of the fundamental frequencies of the two subsystems, with $f_0 = \gcd(f_\mathrm{g}, f_\mathrm{d0}) = 10\,\mathrm{Hz}$. Therefore, the FFT of the simulation results and measurement results are based on a time range of $100\,\mathrm{ms}$. There are some minor deviations between the models that have an amplitude lower than the limit of the deviations of the complex spectra plotted in Figure 4.9. The good conformity between the models indicates that the frequency-domain model is correctly implemented and the angle information is accurate.

The second graph shows the line-line ac-side voltage spectrum. It contains all frequency components of the switching function spectrum with the exception of the zero-sequence components (multiples of $3 \cdot f_\mathrm{d0}$). Deviations are visible for the same spectral components as for the switching function spectrum. Additional frequency components are present in the ac-side voltage spectrum, due to the convolution of the switching function spectrum with the dc-link voltage spectrum (fourth graph). There are frequency components visible that result either from harmonic dc-link voltage components or from the influence of interlock times.
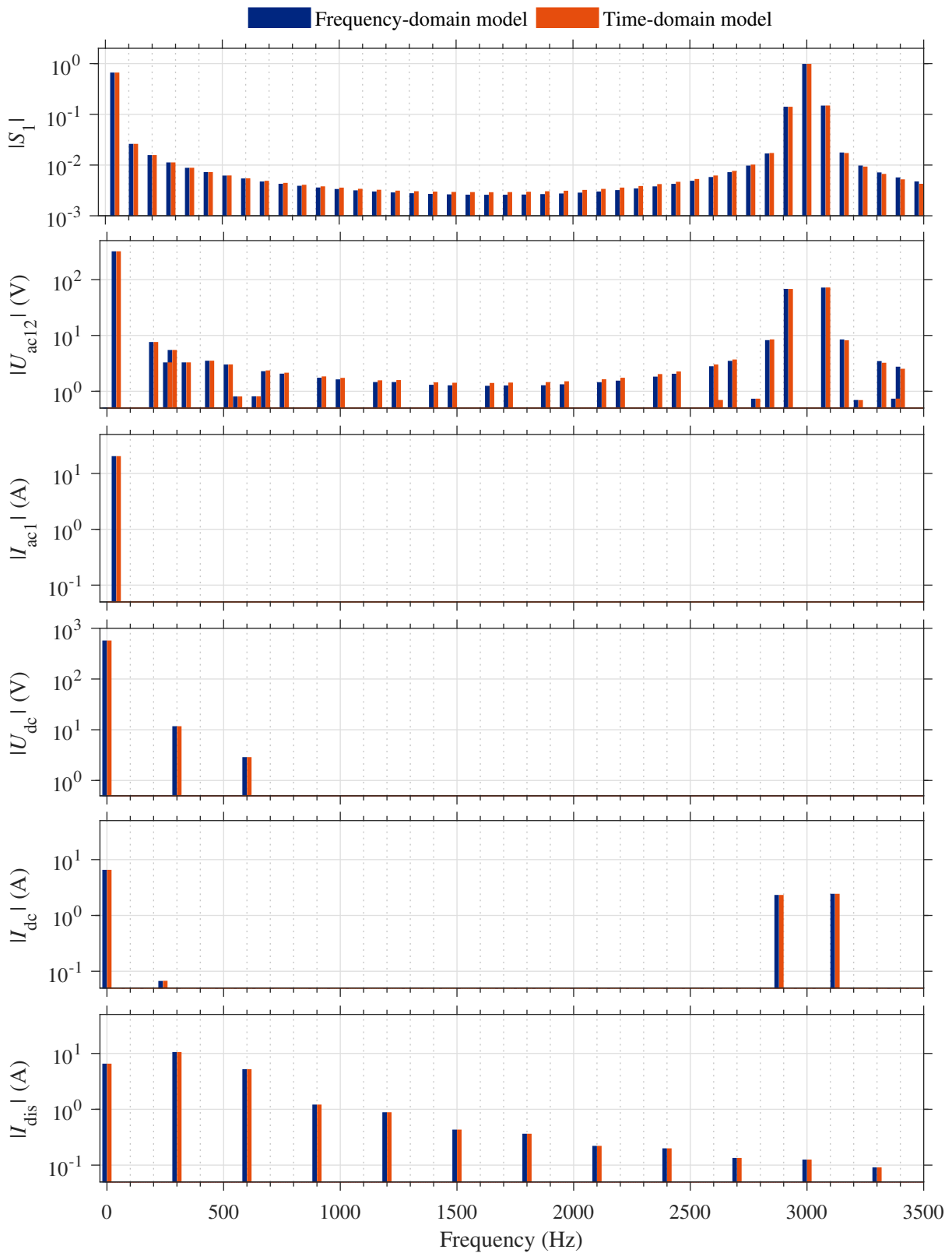
Figure 4.8: Comparison of the results for the frequency-domain model (blue) and the time-domain model. The ac-side currents are idealized as symmetrical, sinusoidal currents impressed by current sources. Parameters: $f_{sw} = 3\,\text{kHz}$, $f_{d0} = 40\,\text{Hz}$, $f_{g0} = 50\,\text{Hz}$, $T_d = 10\,\mu\text{s}$.
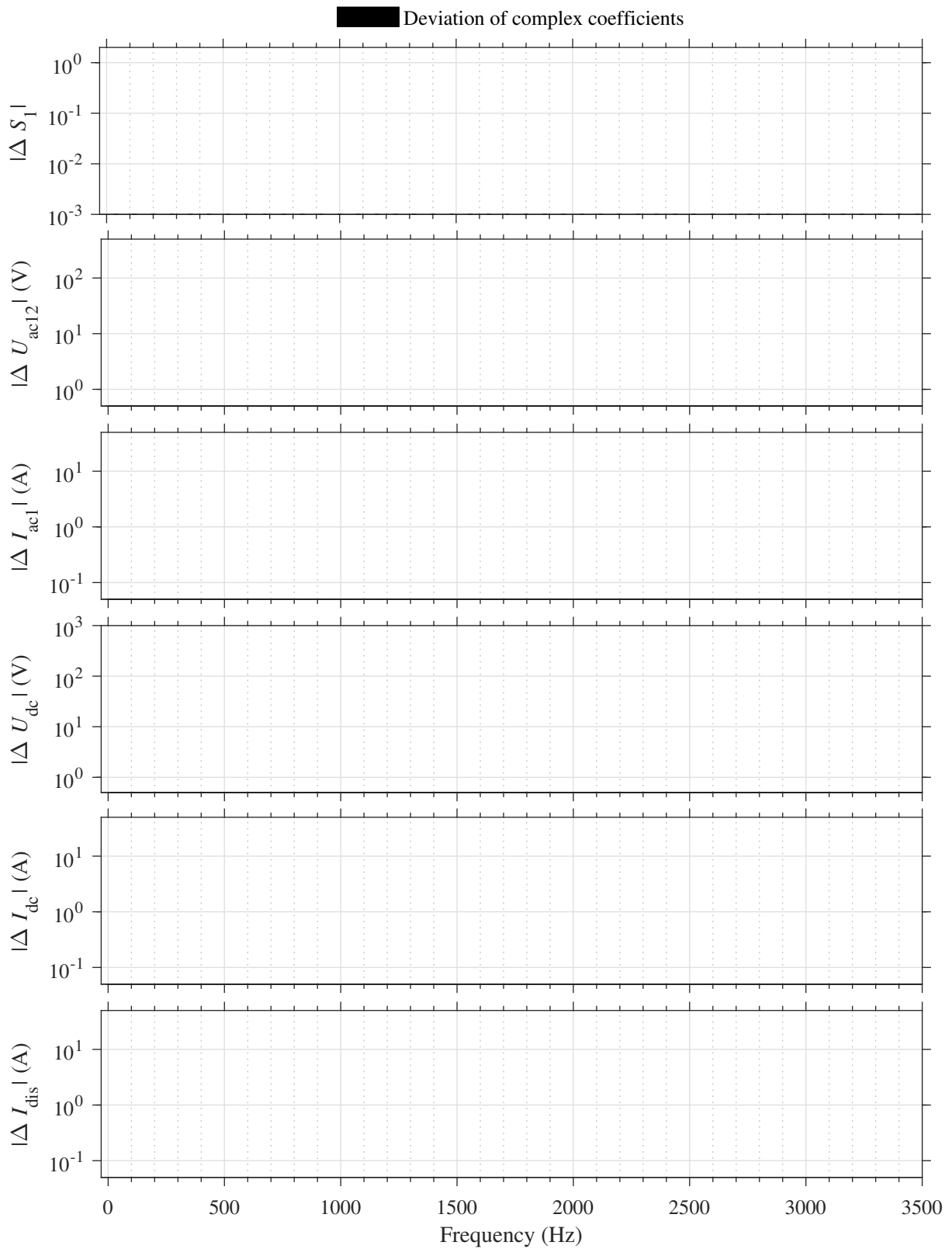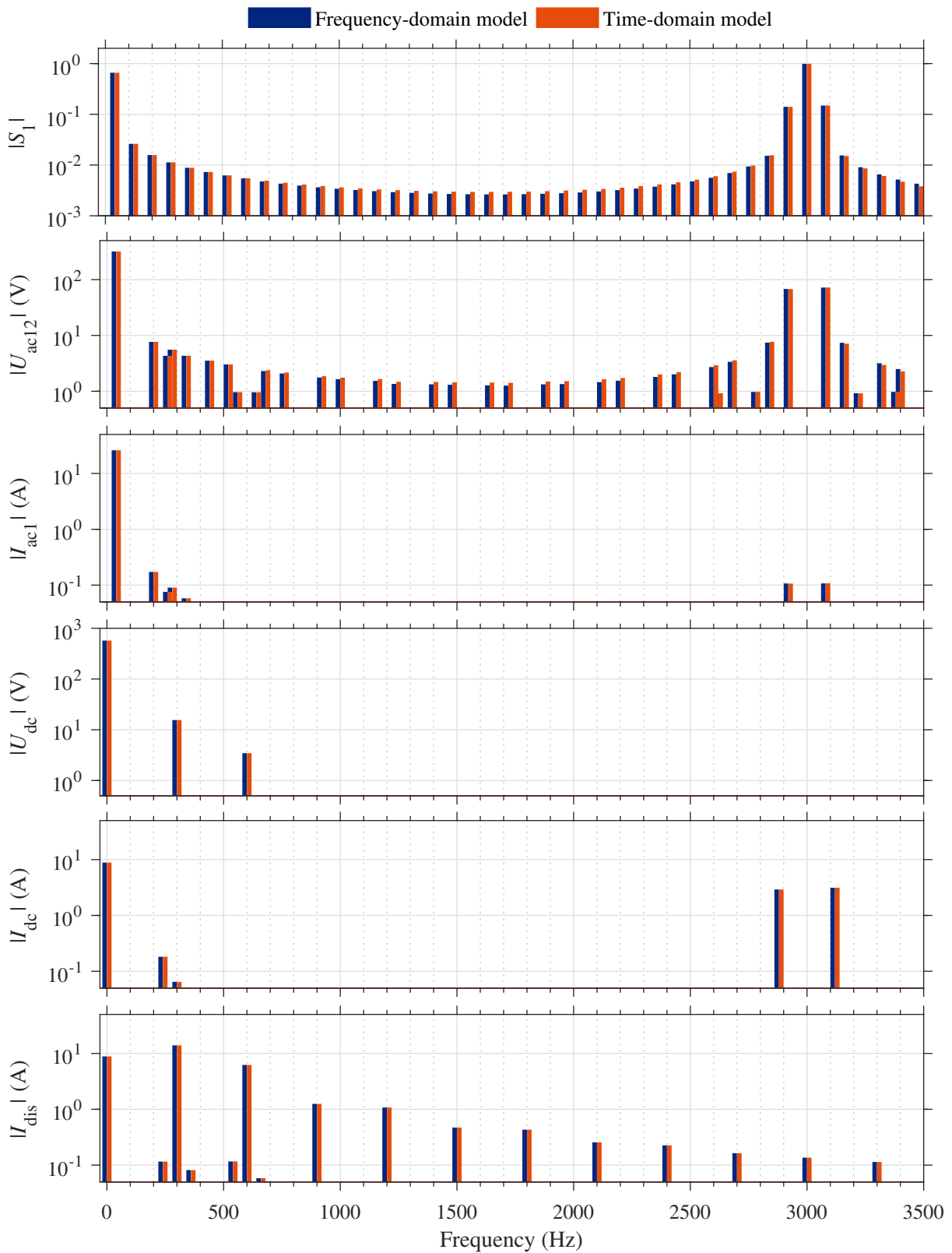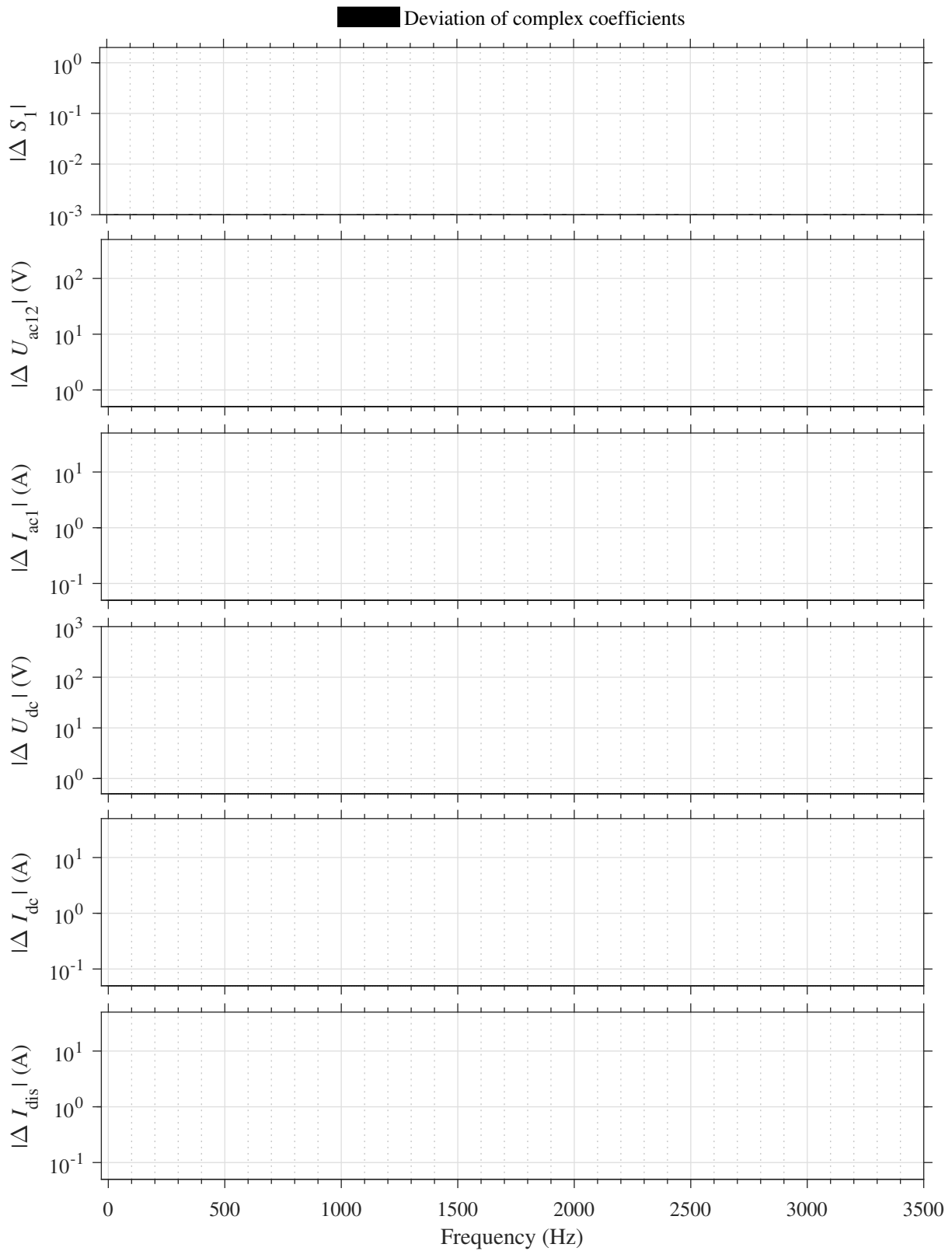
Figure 4.9: Deviation of the complex spectra of the frequency-domain model from the time-domain model shown in Figure 4.8. Parameters: $f_{\mathrm{sw}} = 3\,\mathrm{kHz}$, $f_{\mathrm{d}0} = 40\,\mathrm{Hz}$, $f_{\mathrm{g}0} = 50\,\mathrm{Hz}$, $T_{\mathrm{d}} = 10\,\mathrm{\mu s}$.

Figure 4.10: Comparison of the results for the frequency-domain model (blue) and the time-domain model. The ac-side currents contain harmonic components, feeding a symmetrical RL load. Parameters: $f_{\text{sw}} = 3\,\text{kHz}$, $f_{\text{d}0} = 40\,\text{Hz}$, $f_{\text{g}0} = 50\,\text{Hz}$, $T_{\text{d}} = 10\,\mu\text{s}$.

Figure 4.11: Deviation of the complex spectra of the frequency-domain model from the time-domain model shown in Figure 4.10. Parameters: $f_{sw} = 3\,\text{kHz}$, $f_{d0} = 40\,\text{Hz}$, $f_{g0} = 50\,\text{Hz}$, $T_d = 10\,\mu\text{s}$.
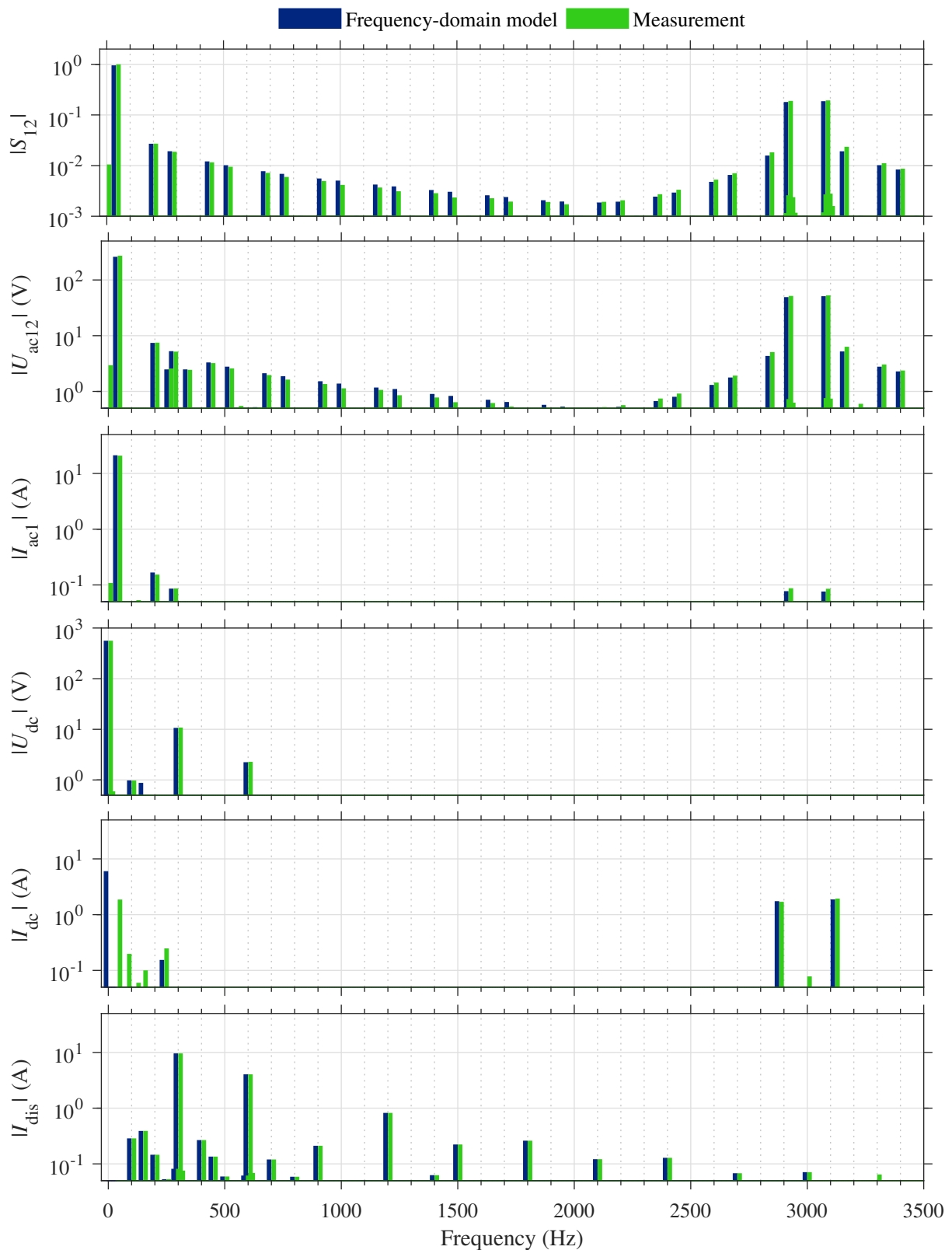
Figure 4.12: Comparison of frequency-domain model and measurements for a three-phase VSI with interlock times. Parameters: $f_{sw} = 3\,\text{kHz}$, $f_{d0} = 40\,\text{Hz}$, $f_{g0} = 50\,\text{Hz}$, $T_d = 10\,\mu\text{s}$.
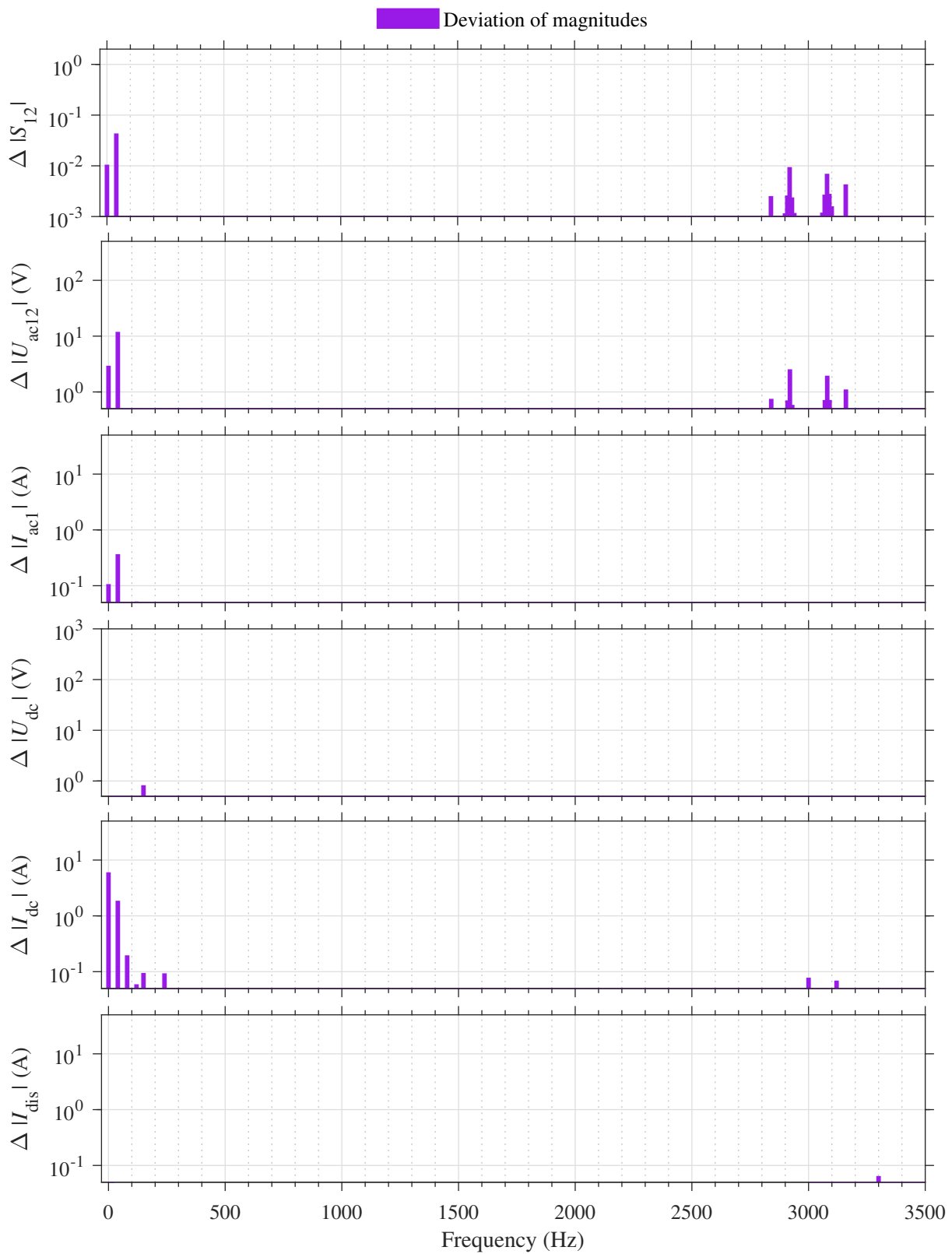
Figure 4.13: Deviations of the magnitude spectra shown in Figure 4.12. Parameters: f_{sw} = 3 kHz, f_{d0} = 40 Hz, f_{g0} = 50 Hz, T_d = 10 µs.

For the correct calculation of the harmonic components in the ac-side currents when applying an RL load to the phase outputs, the iteration process introduced in Figure 4.7 is used. The initial calculation of ϕ' is based on the fundamental frequency model described by (4.9)-(4.14). In the iteration process, the modified switching function spectrum in (4.59) is evaluated. Subsequently, it is applied to the linear equation system described in (3.93), where $\vec{S}_\nu$ is substituted by $\vec{S}'_\nu$. Figure 4.10 shows the resulting magnitude spectra. Additional frequency components are visible for the ac-side current and the dc-side current. The deviation of the complex spectra shown in Figure 4.11 indicates a successful implementation of the iterative solution process.

A comparison of Figure 4.8 with the results from Chapter 3 in Figure 3.27 illustrates the influence of the interlock times on the switching function spectrum, generating odd order harmonics. The superposition of harmonic components that result from the interlock times and from the disturbance currents are visible in the ac-side voltage and ac-side current.

The comparison of spectra taken from the frequency-domain model and measurements is included in Figure 4.12. Figure 4.13 shows the deviation of the magnitude spectra. The measured disturbance current spectrum I_{dis} is used as an input of the frequency-domain model, which differs from the disturbance current that was used previously in the time-domain simulations and frequency-domain models [Figure 4.8-Figure 4.11] explaining differences in the spectra. The switching function of the measurements is reproduced according to (4.62). The first graph shows the line-to-line switching function spectrum $S_{12} = S_1 - S_2$. A comparison with the ac-side voltage spectrum illustrates the odd harmonic components of $f_{\mathrm{d}0}$ that are introduced by the dead time effects. The harmonic components that result from the disturbance current as multiples of $6 \cdot f_g$ are present in the ac-side voltage, but are missing in the switching function spectrum.

According to (4.7), the influence of the interlock times on the harmonic components of the baseband ($f << f_{\mathrm{sw}}/2$) is expected to be unvarying for constant products $f_{\mathrm{sw}} \cdot T_{\mathrm{d}}$. This expectation is reviewed using measurement results for varying values of interlock times of $10\,\mu\mathrm{s}$, $5\,\mu\mathrm{s}$, and $1\,\mu\mathrm{s}$, while retaining a constant product $f_{\mathrm{sw}} \cdot T_{\mathrm{d}} = 0.001$. The switching frequencies are adapted to $1\,\mathrm{kHz}$, $2\,\mathrm{kHz}$, and $10\,\mathrm{kHz}$, respectively. In order to ensure a sufficiently large ratio of $f_{\mathrm{sw}}/f_{\mathrm{d}0}$, the duty-cycle frequency is lowered to $f_{\mathrm{d}0} = 1\,\mathrm{Hz}$ and the modulation index is set to $M = 0.025$. Figure 4.14 shows the ac-side voltage spectra for the three measurements and a comparison to results from the frequency-domain model. For small values of T_{d}, the influence on the voltage harmonics is decreased significantly in the measurements. This indicates the increased relevance of further nonlinear effects, such as the device turn-on and turn-off times. For small values of T_{d}, the switching transitions and delay times manipulate the output voltage for a considerable time span of the interlock times.
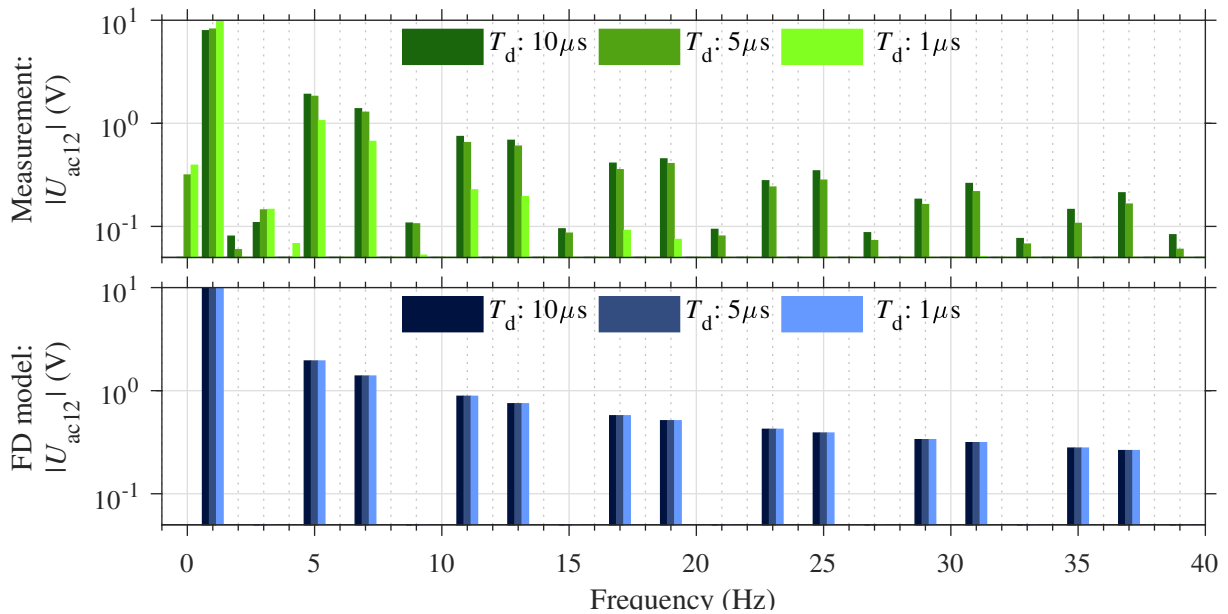
Figure 4.14: Measured ac-side voltage spectra (top graph) and spectra from frequency-domain model (bottom graph) for constant products of switching frequency and interlock time $f_{\mathrm{sw}} \cdot T_{\mathrm{d}} = 1\mathrm{e}\text{-}3$, and $(f_{\mathrm{sw}}, T_{\mathrm{d}})$ set to $(1\,\mathrm{kHz}, 10\,\mu\mathrm{s})$, $(2\,\mathrm{kHz}, 5\,\mu\mathrm{s})$, and $(10\,\mathrm{kHz}, 1\,\mu\mathrm{s})$. Parameters: $f_{\mathrm{d}0} = 1\,\mathrm{Hz}$, $M = 0.025$.

4.3 Other Nonlinear Effects

This section briefly reviews the nonlinear effects of turn-on and turn-off times and forward voltage drops of the semiconductor devices. A discussion of their influence on the inverter spectrum and possible methods to incorporate the effects into a frequency-domain model are included.

4.3.1 Turn-on and turn-off times

The switching process has so far been modeled as a rectangular function with two levels (-1, 1) and zero transition time between the levels. Consequently, infinite voltage and current gradients in the switching instants are assumed. In reality, there are finite transition times between the two switching states of a power semiconductor due to a limited gate current and a required charging time of parasitic capacitances within the semiconductor device [59, 60]. The turn-on time T_{on} represents the time necessary for the transistor to switch from the blocking state to the conduction state. The turn-off time T_{off} represents the time to reverse the states. The characteristic switching transients of a power transistor can be measured using the circuit depicted in Figure 4.15. The following generic waveforms use the naming conventions as introduced in [60].

A generic turn-on process of an IGBT is depicted in Figure 4.16, measured for the mod-
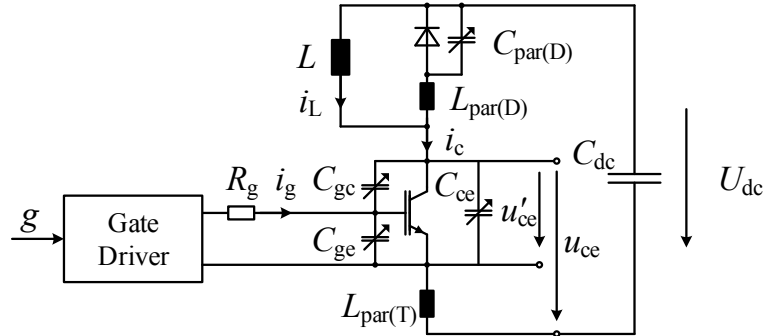
Figure 4.15: Electric circuit to characterize power transistors (cf. [60]): By turning the transistor on, the stiff voltage U_{dc} of the large capacitance C_{dc} causes an increasing current through the inductance L. At a desired current level, the transistor is switched off and the current commutates to the freewheeling diode. Shortly after, the transistor is turned on again. Due to the large time constant of the inductor, the turn-off and turn-on processes are performed at similar current levels. The circuit diagram includes the parasitic capacitances of the transistor $C_{\text{ce}}, C_{\text{gc}}, C_{\text{ge}}$, the parasitic inductance of the transistor $L_{\text{par(T)}}$ and the parasitic capacitance and inductance of the diode $C_{\text{par(D)}}$ and $L_{\text{par(D)}}$. The capacitances are functions of the voltage and the temperature.

ule Infineon FF1000R17IE4 at a dc-link voltage of $U_{\text{dc}} = 500\,\text{V}$ and an inductor current of $I_{\text{L}} = 1000\,\text{A}$. The graphs show the gate-emitter voltage u_{ge} in the top graph, the collector current i_{c} in the middle graph and the collector-emitter voltage u_{ce} in the bottom graph. The measurement starts at $t = 0$ and is triggered by the rising input signal at the input of the gate driver. There is a small delay of 100 ns until the rise of the voltage at the input of the gate unit. During the following turn-on delay time of $T_{\text{d(on)}} \approx 600\,\text{ns}$ the gate-emitter voltage increases. Once the threshold voltage is reached, the commutation of the inductor current is initiated. This process defines the current rise time of T_{ri}, which lasts approximately 500 ns. The collector current exceeds the level of the inductor current due to the diode reverse recovery current. During the current rise time, the measurement of the collector-emitter voltage shows an intermittent level. However, this is caused by the voltage drop over the parasitic inductance. With an estimated inductance value of 40 nH, the influence is corrected and plotted as the red voltage curve, approximating the collector-auxiliary-emitter voltage u_{ce}'. Therefore, it can be stated that the collector-emitter voltage stays at high level until the collector current reaches its peak value and the diode builds up the blocking voltage. The gate-collector capacitance C_{gc} is discharged and thus the collector-emitter voltage decreases in a voltage fall time of $T_{\text{fv}} \approx 250\,\text{ns}$. Due to a decreasing space-charge zone in the device, the gate-collector capacitance C_{gc} increases during this step [59, 60].

The turn-off process of the same module under the same boundary conditions is depicted in Figure 4.17. The gate-emitter voltage falls almost 200 ns after the gate driver input signal is set to its low level. During the following turn-off delay time $T_{\text{d(off)}} \approx 1300\,\text{ns}$, the capacitance C_{gc} is charged and C_{ge} is discharged, until the gate-emitter voltage reaches the value where the collector current equals the saturation current. During the following voltage-rise time of $T_{\text{rv}} \approx 400\,\text{ns}$, the space-charge region is built up and the gate-collector capacitance decreases
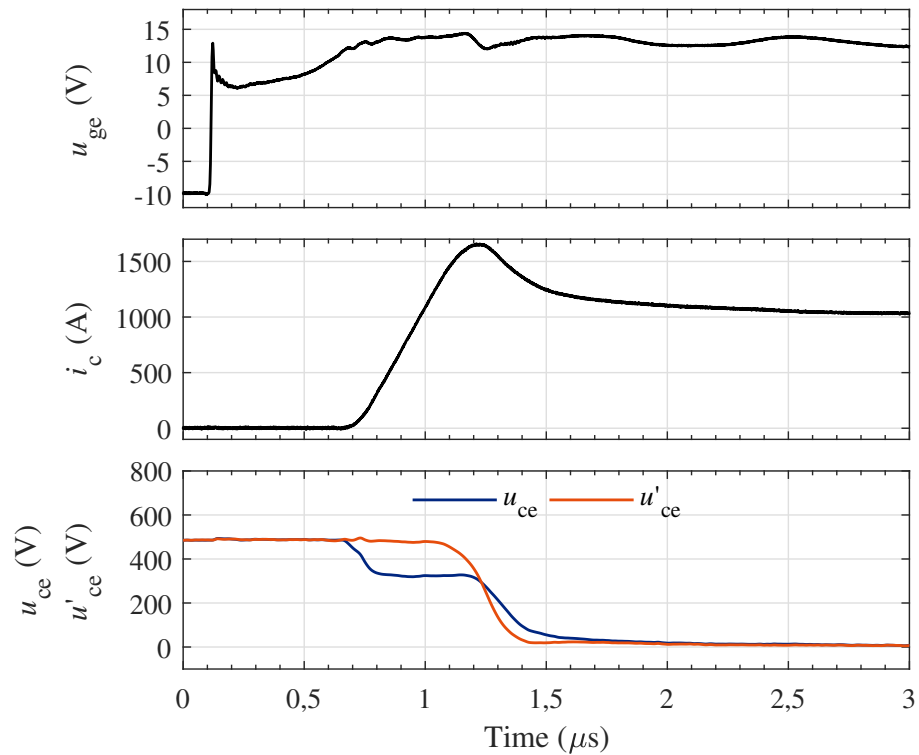
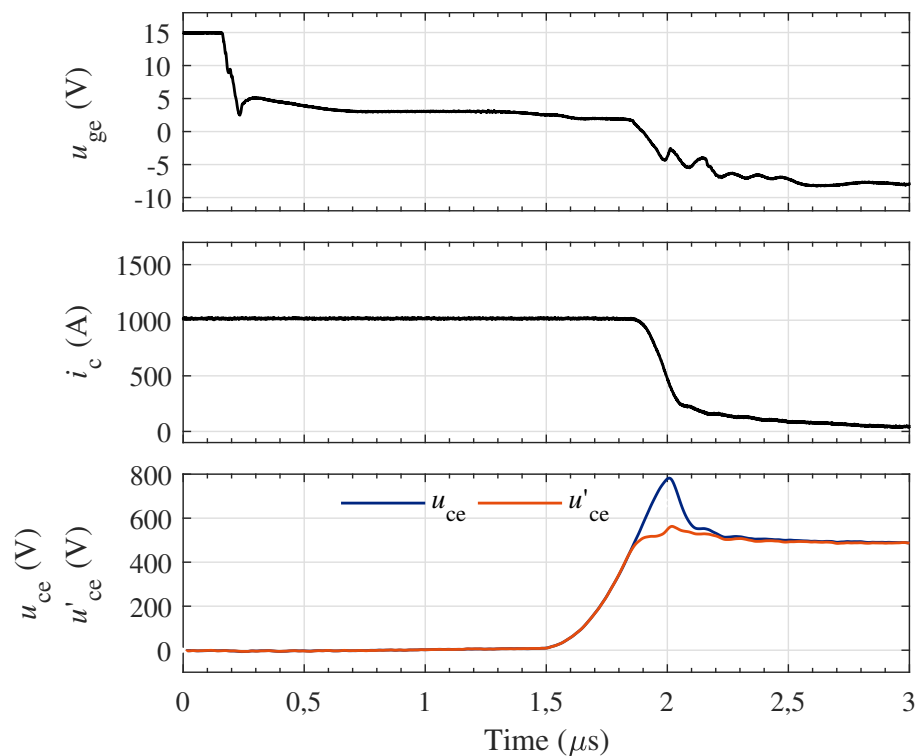**Figure 4.16:** Turn-on process of the IGBT module Infineon FF1000R17IE4, with $i_\text{L} = 1000\,\text{A}$, $U_\text{dc} = 500\,\text{V}$.

Figure 4.17: Turn-off process of the IGBT module Infineon FF1000R17IE4, with $i_\text{L} = 1000\,\text{A}$, $U_\text{dc} = 500\,\text{V}$.

and is charged. Consequently, the collector-emitter voltage rises. Subsequently, the load current commutates to the diode and the collector current decreases during this current fall time T_{fi}. The collector-emitter voltage exceeds the blocking voltage by a voltage peak that is due to the voltage drop over parasitic inductances. The characteristic tail current is visible for $t = 2...3\,\mu\mathrm{s}$, which is caused by recombination of charge carriers that remained within the drift zone of the IGBT after its turn off [59, 60].

The switching transients include time intervals where there is a simultaneous current conduction and a large voltage drop across the semiconductors, generating switching losses. During the commutation, the conduction state cannot be assigned to either the top or the bottom path and thus the process cannot be represented by a lossless switch s. The switching transients are often modeled as an equivalent constant [52,56,61–63] or linear error function [61,63]. The nonlinear switching transient is considered in [19].

In the following schematic model, the finite switching times are represented by a modified switching function s''. The turn-on process is divided into a turn-on delay time $T_{\mathrm{d(on)}}$ where the collector-emitter voltage is at high level and a voltage-fall time T_{fv} that can be approximated by a constant gradient. Similarly, the IGBT turn off can be described by a turn-off delay time $T_{\mathrm{d(off)}}$ where the collector-emitter voltage is at low level and a voltage-rise time T_{rv} with constant voltage gradient. This approximation neglects the different delay times for the current commutation and the nonlinearity of the parasitic capacitances. The turn-on and turn-off processes are mainly determined by the operating point (blocking voltage, load current, and temperature), the gate current, and the device-specific threshold voltage and voltage-dependent parasitic capacitances.

Figure 4.18 shows the switching process schematically for a half bridge. At the beginning the bottom transistor is conducting a positive current i and the switching state described by the switching function is $s = -1$. The transition to the switching state 1 is performed by turning the bottom transistor off and turning the top transistor on after an interlocking time of T_{d} (transition a) $\rightarrow$ b)). Due to the finite turn-off time, the transition is delayed and the modified switching function s'' differs from the ideal switching function s, as indicated by the deviation area A_1 of the error e. The turn-off delay results in a rectangular deviation and the voltage rise time is approximated by a triangular shape. The reverse switching transition from 1 to -1 begins with changing the top gate signal to zero, as shown at c). The top diode keeps conducting the phase current, resulting in a rectangular deviation e. At the end of the interlock time at d), the bottom transistor is turned on. The turn-on delay time and the voltage-fall time cause an extension of the deviation area A_2. The same switching process is shown in the steps e)-h) for negative inductor currents, where the same principle applies and the deviation areas have inverse signs.

For very low inductor currents, the switching transition is governed by an equivalent capacitance called switching-node capacitance of the half bridge [19]: In order to commutate the inductor current to the freewheeling diode, the parasitic capacitance of the diode $C_{\mathrm{par(D)}}$ has to be charged and the collector-emitter capacitance of the bottom IGBT has to be discharged [see Figure 4.15]. For this, the inductor current splits up between the top and the bottom path and charges the collector-emitter capactitance of the IGBT and the capacitance of the freewheeling
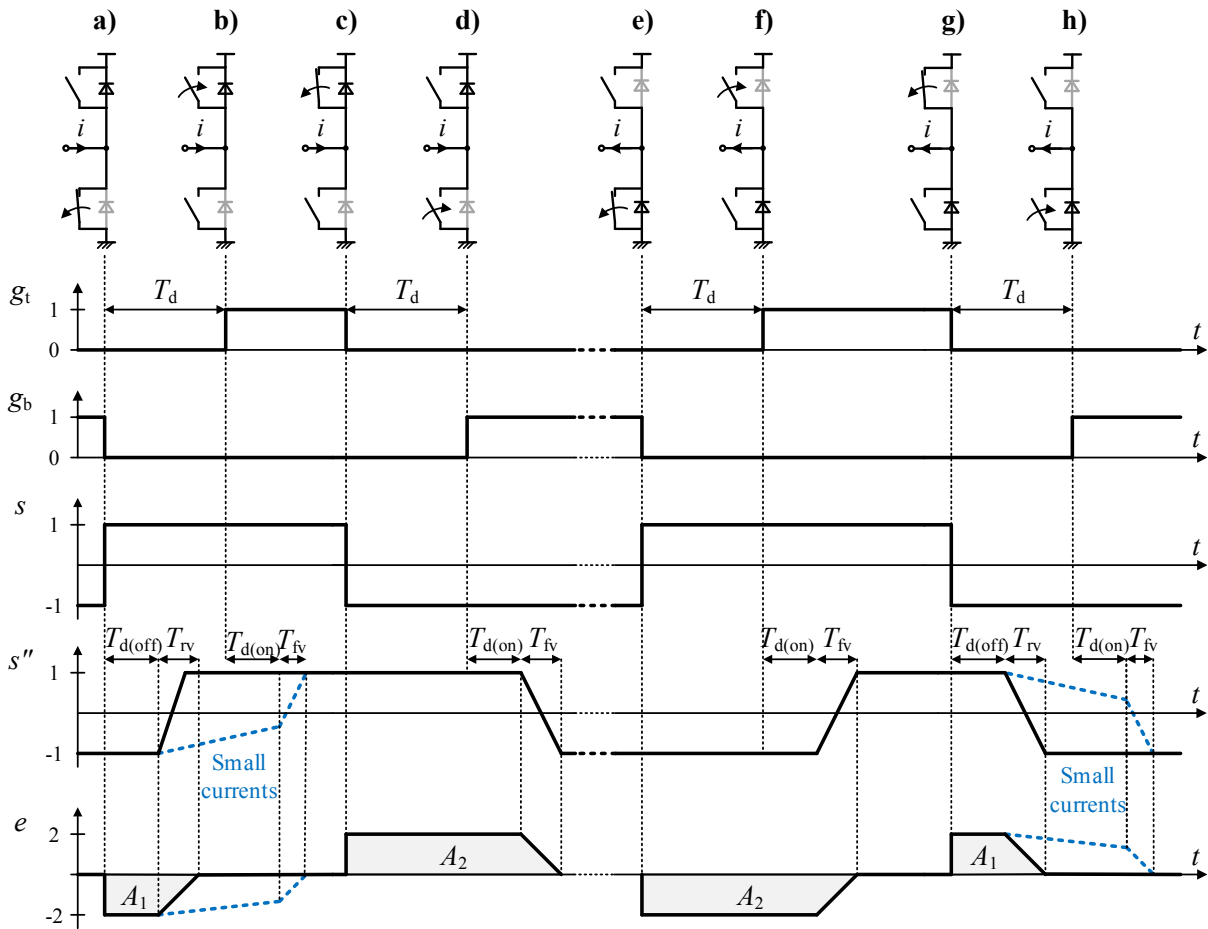
Figure 4.18: Representation of transistor turn-on and turn-off times in a modified switching function s''. The leading edges of the gate signals g_t and g_b are delayed by interlock times T_d. The transitions a)-d) show the commutation process for positive phase currents and the transitions e)-h) for negative phase currents.

diodes simultaneously. For a half bridge, the switching node capacitance represents the parallel connection of the parasitic capacitances of the two IGBTs and the two diodes. Whenever the current flow path changes, the switching node capacitance has to change polarity. For very low inductor currents, the charging time can be in the range of the interlock time. The resulting switching function slope is included in Figure 4.18 as a blue dashed line. The voltage rise time is extended due to the required charging time of the switching node capacitance. The switching transition is terminated by the switch-on process of the transistor anti-parallel to the diode, as shown at b) and h). The switching function model neglects that the inductor current cannot be assigned to a single current flow path (top or bottom). Therefore, an error is introduced for the calculation of the dc-side current. However, the influence is considered to be low, because the value of the current is very low.

The switching-node capacitance is often assumed constant [53, 56, 61, 64], because the average error over one switching period, rather than the shape of the transient is of interest. The impact of

the effect is limited to the low frequency operation of ac drives when both the output frequency and the voltage are low [65].

Under the assumption of $T_{\mathrm{d(on)}} >> T_{\mathrm{fv}}$ and $T_{\mathrm{d(off)}} >> T_{\mathrm{rv}}$, the error areas are assumed in [52, 56, 65] to be rectangular and the average value of the error pulses over one switching period can be written as

$$\langle e(t) \rangle_{T_{\mathrm{sw}}} = \frac{A_1 + A_2}{T_{\mathrm{sw}}} \approx 2 \cdot \frac{T_{\mathrm{d}} + T_{\mathrm{on}} - T_{\mathrm{off}}}{T_{\mathrm{sw}}} \cdot \mathrm{sign}(i_{\mathrm{ac}}). \tag{4.63}$$

Consequently, the turn-on and turn-off times can intensify (turn-on delay) and attenuate (turn-off delay, switching-node capacitance) the influence of dead-time effects. Whereas average models are proposed in [52, 55, 56, 65], Koeslag *et al.* [19] developed an analytical model for output voltage including finite transition times by applying the double Fourier method. The model includes an approximation of the voltage-dependent parasitic capacitances. An incorporation of the transition times requires the adaption of the edges $\tau_{\mathrm{dr}\nu m}$ and $\tau_{\mathrm{df}\nu m}$ in (4.27) regarding the areas A_1 and A_2 in Figure 4.18. Due to the nonlinear dependency of the capacitances on the operating point (phase current, dc-link voltage, and device temperature), this adaption is challenging. Additionally, the parameters of the capacitances are often not provided by the device manufacturer, requiring an additional measurement. Nevertheless, the assumption of $T_{\mathrm{d(on)}} >> T_{\mathrm{fv}}$ and $T_{\mathrm{d(off)}} >> T_{\mathrm{rv}}$ results in square-shaped areas that are easier to model than the trapezoidal shape and $T_{\mathrm{d(on)}}$ and $T_{\mathrm{d(off)}}$ could be approximated as constant parameters, resulting in a more accurate model in comparison to a model that neglects the transition times.

4.3.2 Forward voltage drops

The forward voltage drops across the semiconductor devices introduce a deviation of the ac-side voltage from the model described by (3.2). The current equation in (3.3) is not affected. The equivalent circuit of a half bridge including the forward voltage drops is depicted in Figure 4.19. The states of conduction of the top (t) and bottom (b) path are modeled by the switching function s. The voltages across the IGBTs are represented by a differential resistance r_{T} and a threshold voltage U_{T0}, with

$$u_{\mathrm{T}}(t) = U_{\mathrm{T0}} + r_{\mathrm{T}} \cdot i_{\mathrm{T}}(t). \tag{4.64}$$

Respectively, the voltages across the diodes are represented by a differential resistance r_{D} and a threshold voltage U_{D0}, with

$$u_{\mathrm{D}}(t) = U_{\mathrm{D0}} + r_{\mathrm{D}} \cdot i_{\mathrm{D}}(t). \tag{4.65}$$

It is assumed that the top and bottom devices have equal parameters. Lossless diodes are included in the equivalent circuit to model the unidirectional current flow in each semiconductor.
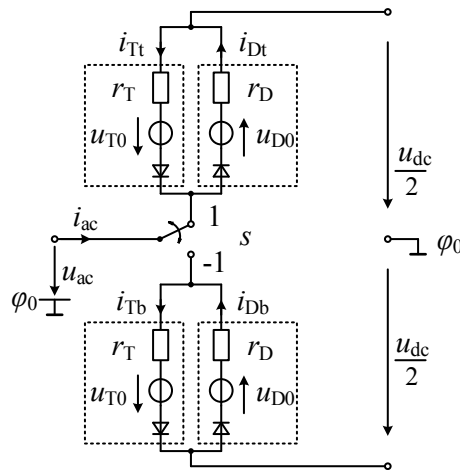
Figure 4.19: Equivalent circuit of a half bridge including forward voltage drops of the semiconductor devices. The conduction state of the top and bottom path is modeled with the switching function s. The forward voltage drop is included for each component as a series connection of its differential resistance, its threshold voltage, and an lossless diode.

Table 4.2: Value of the ac-side voltage in dependence of the switching function and the current sign.

$s(t)$	$\psi(t)$	$u_{\text{ac}}(t)$ in (4.66)	$u_{\text{ac}}(t)$ in (4.67)
1	1	$\frac{1}{2} \cdot u_{\text{dc}}(t) + u_{\text{D}}(t)$	$\frac{1}{2} \cdot u_{\text{dc}}(t) + U_{\text{D0}} + r_{\text{D}} \cdot i_{\text{ac}}(t)$
1	-1	$\frac{1}{2} \cdot u_{\text{dc}}(t) - u_{\text{T}}(t)$	$\frac{1}{2} \cdot u_{\text{dc}}(t) - U_{\text{T0}} + r_{\text{T}} \cdot i_{\text{ac}}(t)$
-1	1	$-\frac{1}{2} \cdot u_{\text{dc}}(t) + u_{\text{T}}(t)$	$-\frac{1}{2} \cdot u_{\text{dc}}(t) + U_{\text{T0}} + r_{\text{T}} \cdot i_{\text{ac}}(t)$
-1	-1	$-\frac{1}{2} \cdot u_{\text{dc}}(t) - u_{\text{D}}(t)$	$-\frac{1}{2} \cdot u_{\text{dc}}(t) - U_{\text{D0}} + r_{\text{D}} \cdot i_{\text{ac}}(t)$

The ac-side voltage has a dependency on the switching state and additionally on the sign of the phase current $\psi(t) = \text{sign}(i_{\text{ac}}(t))$. The value of the ac-side voltage is summarized in the third column of Table 4.2 for combinations of s and ψ. A time-domain equation that reproduces these combinations is given by

$$u_{\text{ac}} = s(t) \cdot \left(\frac{1}{2} \cdot u_{\text{dc}}(t) + \frac{s(t) \cdot \psi(t) + 1}{2} \cdot u_{\text{D}}(t) + \frac{s(t) \cdot \psi(t) - 1}{2} \cdot u_{\text{T}}(t) \right). \qquad (4.66)$$

In modeling and compensation of dead-time effects, the current-dependent voltage drop is often considered of minor importance [52, 56, 64] and in some cases the complete voltage drop is neglected due to its minor influence [62, 66]. A frequency-domain model that provides an expression of (4.66) with Fourier coefficients was not found in the literature review. The following equations provide an approach to express the voltage drops in the frequency domain.

By analysis of Figure 4.19, the voltage drops $u_{\text{D}}(t)$ and $u_{\text{T}}(t)$ can be expressed as functions of the ac-side current, which are summarized in the fourth column of Table 4.2. It is emphasized

that the influence of the resistive component is proportional to $i_{\mathrm{ac}}(t)$ and the influence of the threshold voltage changes with the sign of the ac-side current $\psi(t)$. Applied to (4.66), this results in

$$
\begin{aligned}
u_{\mathrm{ac}} = {} & \frac{1}{2} \cdot s(t) \cdot u_{\mathrm{dc}}(t) + \frac{s(t) \cdot \psi(t) + 1}{2} \cdot U_{\mathrm{D0}} \cdot s(t) + \frac{s(t) \cdot \psi(t) + 1}{2} \cdot r_{\mathrm{D}} \cdot i_{\mathrm{ac}}(t) ... \\
& + \frac{s(t) \cdot \psi(t) - 1}{2} \cdot U_{\mathrm{T0}} \cdot s(t) - \frac{s(t) \cdot \psi(t) - 1}{2} \cdot r_{\mathrm{T}} \cdot i_{\mathrm{ac}}(t).
\end{aligned}
\tag{4.67}
$$

With the introduction of

$$
\bar{U}_0 := \frac{U_{\mathrm{T0}} + U_{\mathrm{D0}}}{2}, \quad \Delta U_0 := \frac{U_{\mathrm{T0}} - U_{\mathrm{D0}}}{2}, \quad \bar{r} := \frac{r_{\mathrm{T}} + r_{\mathrm{D}}}{2}, \quad \Delta r := \frac{r_{\mathrm{T}} - r_{\mathrm{D}}}{2}
\tag{4.68}
$$

it is possible to express (4.67) as

$$
u_{\mathrm{ac}} = \frac{1}{2} \cdot s(t) \cdot u_{\mathrm{dc}}(t) + \bar{U}_0 \cdot \psi(t) - \Delta U_0 \cdot s(t) + \bar{r} \cdot i_{\mathrm{ac}}(t) - \Delta r \cdot \psi(t) \cdot s(t) \cdot i_{\mathrm{ac}}(t).
\tag{4.69}
$$

It is notable that the influence of the voltage can be divided into four components:

1. A component $\bar{U}_0 \cdot \psi(t)$, which is proportional to the average threshold voltage, and which depends on the sign of the ac-side current. The sign of sinusoidal currents is a square wave and introduces harmonics of odd order into the ac-side voltage.

2. A component $\Delta U_0 \cdot s(t)$, which is proportional to the deviation of the threshold voltages, and which depends on the switching function.

3. A component $\bar{r} \cdot i_{\mathrm{ac}}(t)$, which introduces a resistive behavior.

4. A component $\Delta r \cdot \psi(t) \cdot s(t) \cdot i_{\mathrm{ac}}(t)$, which is proportional to the deviation of the differential resistance. It depends on the product of the ac-side current, the ac-side current sign and the switching function.

When the characteristics of the diode and the IGBT are similar, it is possible to assume that $\Delta U_0 \approx 0$ and $\Delta r \approx 0$. With these assumptions, an application of a Fourier transformation to (4.69) yields

$$
U_{\mathrm{ac}}(f) = \frac{1}{2} \cdot S(f) * U_{\mathrm{dc}}(f) + \bar{U}_0 \cdot \Psi(f) + \bar{r} \cdot I_{\mathrm{ac}}(f).
\tag{4.70}
$$

4.4 Discussion

In this chapter the influence of interlocking times on the switching function spectrum was analyzed. A method was presented that allows for the incorporation of the effect of interlock times directly into the switching function spectrum and the calculation of the spectra considering both the interlock times and harmonic disturbances. The results of this chapter extend previous work [19, 21, 22] that provided the analytical models of the ac-side voltage spectrum for a constant dc-link voltage and sinusoidal phase currents.

Interlock times result in the generation of odd order harmonics of the fundamental frequency in the switching function spectrum. For harmonic orders that are a multiple of three, the components form zero-sequence components in a three-phase system and therefore cancel out in the line-to-line voltages and they are not present in the line currents. The interlock times also lead to a widening of the switching sidebands and there is no clear separation between baseband harmonics and the switching sidebands.

Under the influence of interlock times, there is a dependency of the switching function on the zero-crossing times of the ac-side current, which results in a nonlinear equation system. Numerical results were presented and validated by time-domain simulations and experiments. Because the analytical models assume two current zero crossings per fundamental cycle, deviations occur when the assumption is not valid due to large current harmonics.

Parasitic capacitances of the semiconductors impact the shape of the output voltages during the finite switching transients. They generally lead to an attenuation of the harmonics generated by the interlock times. The semiconductor forward voltage drop cause odd numbered harmonic components that add to the harmonics generated by the other nonlinear effects.

5 VSI with Closed-Loop Control

Closed-loop control utilizes the feedback of measured or estimated output signals of the plant to shape its input signals, achieving a desired control goal. This results in a mutual dependency between the signals of the control system and the plant. A simplified control loop is illustrated in Figure 5.1a as a block diagram. The output variable x is measured by a sensor and fed back to the control system as the sensed output signal x'. A comparison to the setpoint signal x_{sp} results in the control error Δx. A controller amplifies the control error, generating the control command u_{sp}. An actuator executes the command, influencing the input of the plant and shaping the output signal x in order to reach the desired control goal. When designed correctly, deviations in the output signal from the setpoint signal that result from the influence of a disturbance signal l are compensated by the controller through the control command, creating a robust and stable system.
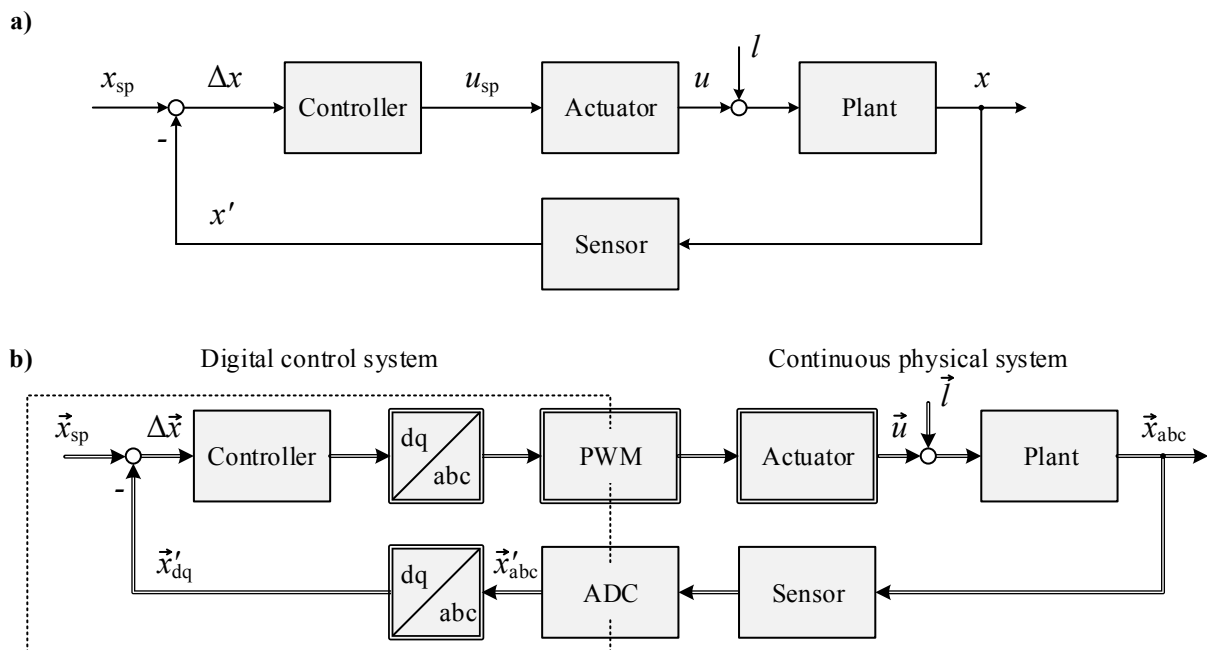
Figure 5.1: Block diagram of a physical system with closed-loop control: **a)** Fundamental structure. **b)** Extension to a three-phase converter system. The signals that are vectors are illustrated with double lines. Nonlinear blocks are drawn with double frames. The control is implemented digitally in rotating coordinates, requiring a hybrid model of discrete and continuous signals in multiple coordinate systems.

Figure 5.1b shows the extension of the block diagram to a three-phase system, where the control is implemented in rotating coordinates in a digital subsystem. The physical model of the three-phase system is modeled with continuous signals in abc coordinates. A conversion into digital signals is required at the input of the control system. At its output, the digital-to-analog conversion is performed inherently by the PWM block, which transforms the discrete-time duty cycle into a continuous-time switching function. Consequently, a hybrid modeling approach is required that incorporates discrete and continuous signals simultaneously. Moreover, the transformation into rotating coordinates, which is implemented in the digital control system, requires consideration in the modeling process.

The VSI as the actuator was modeled in Chapter 3 using an idealized switching function and in Chapter 4 with a modified switching function incorporating nonlinear effects. It was assumed that the input of the modulator, i.e. the duty cycle, was an independent signal and could be calculated a priori. For closed-loop control, the duty cycle is a dependent signal determined in the control process, which interacts with the signals of the plant. Due to the PWM and the switching process, this interaction is nonlinear.

It was found that the frequency-domain modeling of the interaction between PWM, control, and plant is not sufficiently covered in the literature. Approaches that model the PWM in great detail are available, but they do not cover the influence of the feedback. These are the PWM models that were reviewed in Chapter 3 [12, 14, 15, 17]. Other approaches that cover the interaction are based on linearization or contain linearized models of the PWM and the switching process. Almér and Jönsson [67] develop a dynamic phasor model that accounts for the closed-loop control of dc-dc converters by averaging and by truncation of high-frequency components. Corradini et al. [34] present discrete-time average models for dc-dc converters that incorporate sampling and aliasing effects under small-signal assumptions. A linearization enables the use of standard control theory methods, such as Bode plot and Nyquist stability theorem. The aliasing of unsynchronized frequency components that are near the sampling frequency are discussed by Yue et al [68]. These unwanted beat-frequency components are incorporated under small-signal assumptions by mapping the high-frequency components to the baseband using a crossed frequency matrix.

The goal of this chapter is to develop the mathematical framework for calculation of the spectrum of the signals including the harmonic interactions due to the feedback control. The control is developed for the example of closed-loop current control of a three-phase VSI. In Section 5.1 the individual components of the control loop are analyzed as a block-wise input-to-output description. The influence of quantization is excluded in the models developed in this thesis. Its influence is briefly discussed in Section 5.2. Section 5.3 describes a modification to the PWM models introduced in Chapter 3 that is necessary to allow a hybrid model of discrete-time and continuous-time signals. The evaluation of the total equation system requires nonlinear solution methods, which is described in Section 5.4.

5.1 Control Components

Digital control can be implemented on software-based controllers (e.g. microcontrollers) or hardware-based controllers (e.g. FPGAs) [34]. In this thesis, the control structure is split into a software-based control for the setpoint generation implemented in a CPU and the evaluation of the ADCs and the PWM implemented on an FPGA. The system structure and the interaction of the control unit with the power stage are depicted in Figure 5.2 as a block diagram. The continuous-time signals $i_{ac}(t)$ and $u_{dc}(t)$ are measured by analog sensors and converted into discrete-time signals $i'_{ac}[n]$ and $u'_{dc}[n]$ by an ADC such as a $\Delta\Sigma$ modulator. A digital decimator provides the attenuation of the quantization error and the downsampling to the control frequency. The signals $i'_{ac}[n]$ and $u'_{dc}[n]$ are sampled with the control frequency and utilized in the CPU. The output of the controller is the duty cycle $d[n]$. The PWM process is implemented in the FPGA and transforms the duty cycle into an equivalent switching function $s[n]$.

Analytical models of the PWM and plant were previously analyzed in Chapter 3. This section studies the measurement system and the digital control. All subsystems are given in an input-to-output description in the frequency domain.
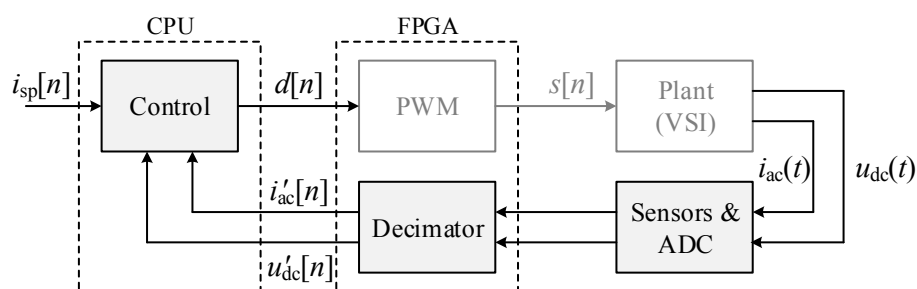
Figure 5.2: Overview of system's interactions for closed-loop control. The blocks ADC, decimator, and control are analyzed in this section, whereas the blocks PWM and plant were previously introduced in Chapter 3.

5.1.1 Measurement System

The structure of the measurement system that is used to track a continuous signal of the plant $x(t)$ is depicted in Figure 5.3. An analog sensor transforms the signal into a low-voltage or low-current equivalent, which is further converted into a digital signal using a $\Delta\Sigma$ converter. Decimation is the collective process of low-pass filtering and downsampling [69], which is applied to the digital signal on an FPGA. Finally, the low-pass filtered signal $x'[n]$ is sampled with the control frequency and transferred to the control unit.

The sensors can be described by a specified accuracy, an offset error, and a characteristic frequency behavior that can be regarded as linear up to a cut-off frequency f_{cut}. Assuming a correction of the offset error and a sufficiently large accuracy, these impact factors are neglected
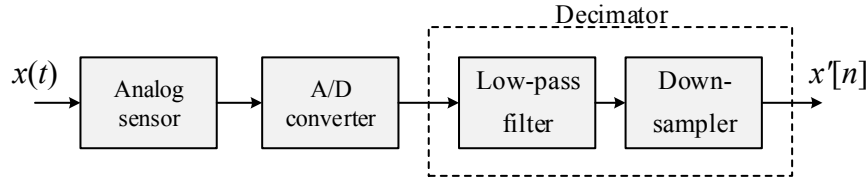
Figure 5.3: Structure of the measurement system

in the following modeling approach. Even though the bandwidth of the sensor is usually large ($f_{\text{cut}} >> k_{\text{max}} \cdot f_0$), a considerable error of the angle information can occur for the components around the switching frequency. Therefore, the analog sensors are represented by the transfer function of a first-order low-pass filter

$$H_{\text{sensor}}(\omega) = \frac{1}{\text{j}\omega/f_{\text{cut}} + 1}. \tag{5.1}$$

Refer to Appendix B for information about the measurement devices of the experimental setup.

The $\Delta\Sigma$ modulator transforms the analog signal into a 1-bit digital signal, where the density of the ones is proportional to the magnitude of the analog signal. The 1-bit resolution causes a high quantization noise. Using a sampling frequency that is much higher than the control frequency (oversampling), the noise is mainly present in the high frequency range. The noise is attenuated in a further step using digital low-pass filters. The high sampling frequency also reduces the requirements of the input anti-aliasing filter. The cut-off frequency of the anti-aliasing filter is in the range of half the clock frequency of the delta-sigma modulator, which results in several MHz and allows a negligence in the models [70].

The output spectrum of the modulator in the z domain $Y(z)$ consists of an input signal spectrum $X(z)$ affected by the signal transfer function $H_x(z)$ and a noise spectrum $E(z)$ affected by the noise transfer function $H_e(z)$, with

$$\begin{aligned} Y(z) &= H_x(z) \cdot X(z) + H_e(z) \cdot E(z) \\ &= z^{-1} \cdot X(z) + (1 - z^{-1})^L \cdot E(z) \quad \text{[69]}, \end{aligned} \tag{5.2}$$

where L is the order of the modulator. The noise spectrum represents a white noise process that is uncorrelated with the input signal spectrum. The signal transfer function $H_x(z)$ has unity gain for all frequencies and introduces a phase delay. The influence can be estimated by assuming a signal frequency of $f = 10\,\text{kHz}$ and a sampling frequency of $f_{\Delta\Sigma\text{s}} = 10\,\text{MHz}$, which results in the low value of $-0.4°$.

Figure 5.4 shows the noise transfer function $H_e(z)$ for a first-order and a second-order $\Delta\Sigma$ modulator in dB for the same sampling frequency of $f_{\Delta\Sigma\text{s}} = 10\,\text{MHz}$. The graphs illustrate that the noise spectrum is significantly shifted to higher frequencies, especially for the second-order modulator. The high-frequency noise is removed in the digital filtering process. The quantization noise at low frequencies is insignificant. At a frequency of $f = 10\,\text{kHz}$ the noise is
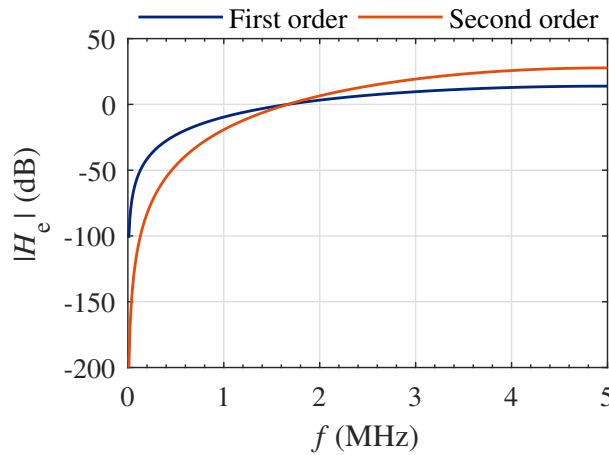
Figure 5.4: Noise transfer function of a first-order and second-order $\Delta\Sigma$ modulator for a sampling frequency of $f_{\Delta\Sigma s} = 10\,\text{MHz}$, cf. [69].

attenuated to -200 dB for the second-order $\Delta\Sigma$ modulator. It is concluded that the influence of the $\Delta\Sigma$ modulator can be neglected in the models that consider frequencies up to several kHz.

The tasks of the decimator are to remove the quantization noise in the high frequency range, apply anti-aliasing filters for the upper end of the signal bandwidth, and provide downsampling to the control frequency while increasing the word size of the signal. Multistage decimators can be applied where the individual stages are optimized to fulfill these different purposes [71]. The reduction of quantization noise is often performed in the first stage by sinc filters of order $K > 1$, which have a transfer function of

$$H_{\text{sinc}K}(z) = \left(\frac{1}{N} \frac{1 - z^{-N}}{1 - z^{-1}} \right)^K \qquad [71], \tag{5.3}$$

where $N = f_{\Delta\Sigma s}/f_D$ is the decimation, $f_{\Delta\Sigma s}$ is the sampling frequency of the $\Delta\Sigma$ modulator, and f_D is the intermediate decimation frequency. In the second stage a low-pass filter can be incorporated to shape the desired transfer characteristic at the upper end of the signal bandwidth. For second-order $\Delta\Sigma$ modulators, sinc filters of order $K \geq 3$ are recommended for effective prevention of aliasing [72]. To provide decimation to the control frequency, an accumulate-and-dump circuit [71] can be applied in the third stage, which is a sinc filter with its transfer function given by (5.3) with $K = 1$. The second and the third stage are optional. The total transfer function of the decimator is called H_{dec}, which is a diagonal matrix $\boldsymbol{H}_{\text{dec}}$ for the vector representation of Fourier coefficients.

The output of the decimator is sampled with the sampling period T_s. The sampling process is represented by a multiplication of the continuous signal $x(t)$ with a sequence of Dirac pulses δ described in (2.11), which results in the sampled signal $x_s(t)$, with

$$x_s(t) = x(t) \cdot \sum_{n=-\infty}^{\infty} \delta(t - nT_s). \tag{5.4}$$
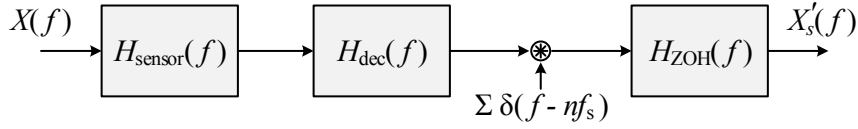
Figure 5.5: Block diagram of the measurement system as it is modeled in the frequency domain.

In the frequency domain the sampling is represented by a convolution of the spectrum of the continuous signal $X_s[kf_0]$ with a sequence of Dirac pulses, which is described in (2.18). In the vector representation, this is expressed as a convolution of the signal vector $\vec{X}$ and a vector H_s that contains ones at the elements of order $nT_s/T_0, n \in \mathbb{Z}$:

$$\vec{X}_s = \vec{H}_s * \vec{X}. \tag{5.5}$$

The sampling process is commonly synchronized with the PWM period, minimizing the influence of switching harmonics in the sensed signals [42]. This avoids aliasing of switching harmonics, even when digital filters are not applied. See Chapter 3 and Figure 2.4 for an explanation of the beneficial effect of synchronization.

The sampled signals are held in the control system for one control period, which can be modeled by application of a zero-order hold (ZOH) block to each output of the measurement system. The continuous transfer function of the ZOH is

$$H_{\mathrm{ZOH}}(\omega) = \mathrm{e}^{-\mathrm{j}\omega T_s/2} \cdot \mathrm{si}(\omega T_s/2). \tag{5.6}$$

In the vector representation of Fourier coefficients the ZOH is a diagonal matrix $\boldsymbol{H}_{\mathrm{ZOH}}$, with the k-th diagonal element

$$H_{\mathrm{ZOH},k} = \mathrm{e}^{-\mathrm{j}k\omega_0 T_c/2} \cdot \mathrm{si}(k\omega_0 T_s/2). \tag{5.7}$$

The resulting model of the measurement system is illustrated in Figure 5.5 as a block diagram and the discrete output spectrum in the vector representation is calculated with

$$\vec{X}'_s = \boldsymbol{H}_{\mathrm{ZOH}} \cdot \left(\boldsymbol{C}(\vec{H}_s) \cdot \boldsymbol{H}_{\mathrm{dec}} \cdot \boldsymbol{H}_{\mathrm{sensor}} \cdot \vec{X} \right). \tag{5.8}$$

Figure 5.6 presents an example that illustrates the significance of the correct modeling of sampling and filtering. The input of the measurement system represents a typical ac-side current signal, with a large fundamental component at $f_0 = 50\,\mathrm{Hz}$ and a switching spectrum. The sidebands are visible around the first and second carrier groups at $f_{\mathrm{sw}} = 2500\,\mathrm{Hz}$ and $2 \cdot f_{\mathrm{sw}} = 5000\,\mathrm{Hz}$, respectively. The switching process is synchronized with the sampling process of the measurement system to avoid aliasing of the switching harmonics [42]. Additionally, the input signal contains a component at $f_{\mathrm{dis}} = 2100\,\mathrm{Hz}$ that is unsynchronized with the sampling process, representing an external disturbance. The influence of a sensor is neglected in this example. There are a number of sampling and filtering methods available:
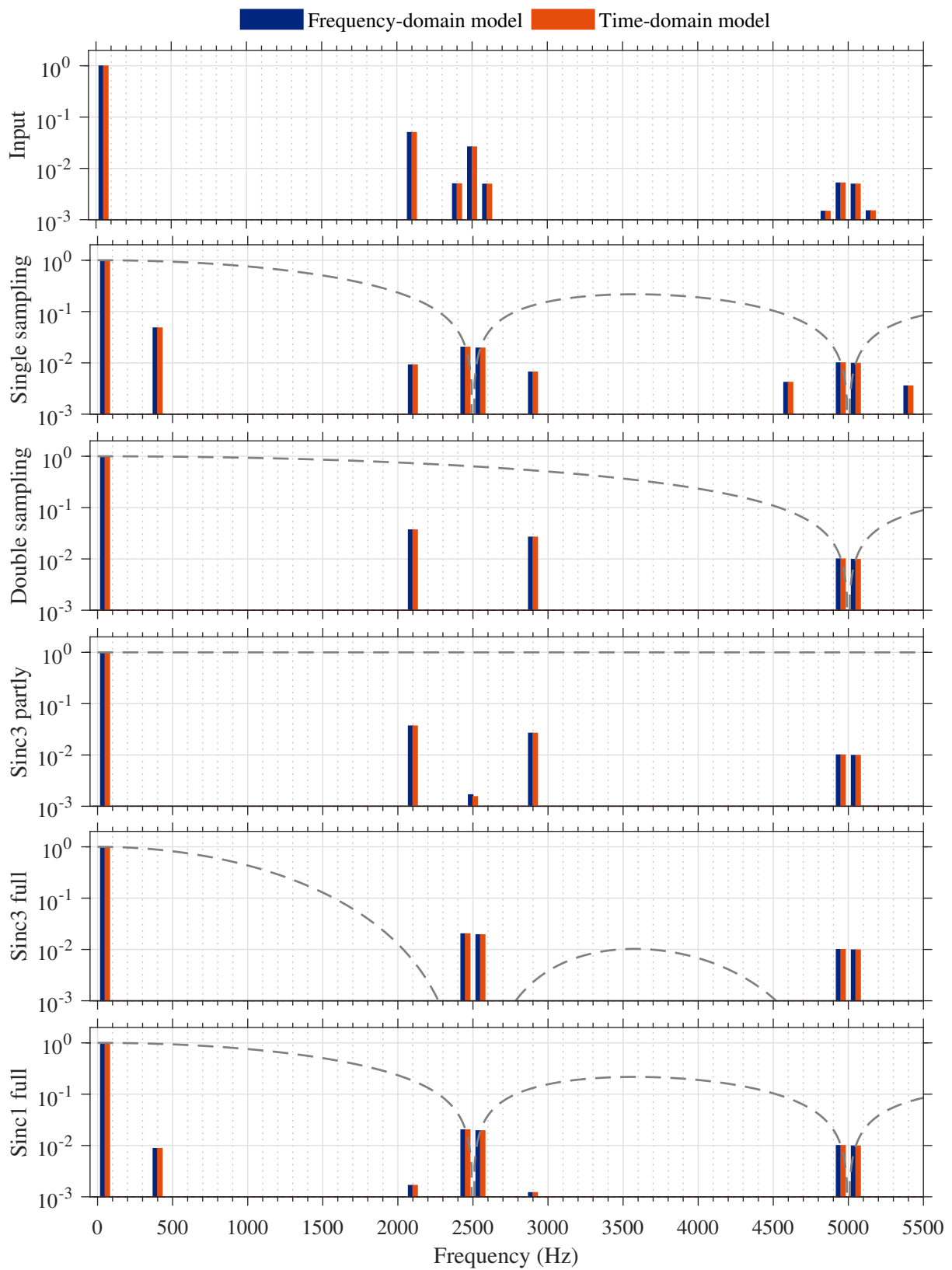
Figure 5.6: Results for various sampling and filtering methods. The input signal contains a fundamental component at 50 Hz, synchronized switching sidebands around multiples of 2500 Hz, and an unsychronized component at 2100 Hz.

Single sampling: The input signal is sampled and held once a switching period ($f_\mathrm{s} = f_\mathrm{sw}$). Because the sampling is synchronized with the switching process, the switching components are effectively reduced. The dashed line shows the attenuation introduced by the zero-order hold. Frequency components occur at $n \cdot f_\mathrm{s} \pm f_0, n \in \mathbb{Z}$, due to the sample and hold of the fundamental component. Aliasing occurs because the frequency of the unsychronized signal f_dis is larger than half the sampling frequency. Frequency components are generated at $n \cdot f_\mathrm{s} \pm f_\mathrm{dis}, n \in \mathbb{Z}$, including a low frequency component at $f_\mathrm{s} - f_\mathrm{dis} = 400\,\mathrm{Hz}$.

Double sampling: The input signal is sampled and held twice per switching period ($f_\mathrm{s} = 2 \cdot f_\mathrm{sw}$), synchronized with the switching process. The dashed line shows the attenuation introduced by the zero-order hold for double sampling. The fundamental frequency component is again present at $n \cdot f_\mathrm{s} \pm f_0, n \in \mathbb{Z}$, visible around $5000\,\mathrm{Hz}$. The frequency of the unsynchronized component is smaller than half the sampling frequency and aliasing to the baseband is avoided. The component appears at $2900\,\mathrm{Hz}$.

Sinc3 filter: Application of a sinc3 filter prior to the double sampling process introduces low-pass filtering and provides the necessary decimation from the high-frequency 1 bit signal to a lower sampled signal with a higher word size. Choosing a low decimation that results in an intermediate decimation frequency $f_\mathrm{D} >> f_\mathrm{s}$, the influence of the sinc3 filter on the frequency range discussed in this thesis is negligible. The graph "Sinc3 partly" shows the resulting spectrum when double sampling is applied. The dashed line represents the transfer function of the sinc3 filter with $f_\mathrm{D} = 500\,\mathrm{kHz}$. There is a small component present at f_sw due to a phase shift of the switching harmonics by the sinc3 filter. Again, aliasing occurs when single sampling is chosen (not depicted).

For a higher decimation that results in f_D being in the range of the sampling frequency, unsynchronized signals are more effectively damped. However, the benefit of synchronization can be lost when the switching ripple is averaged only over a part of the switching period. Thus, the intermediate decimation frequency is set to $f_\mathrm{D} = f_\mathrm{sw}$, even when double sampling is applied, and the switching harmonics cancel out over one switching period. The graph "Sinc3 full" shows the resulting spectrum, where the disturbance signal is effectively damped.

Sinc1 filter: When applying single sampling ($f_\mathrm{s} = f_\mathrm{sw}$) and an accumulate-and-dump circuit (sinc1 filter) over one switching period without utilizing any other filtering methods, the spectrum in the bottom graph results. The filtration effect is not as effective, as indicated by the dashed line. Thus, aliasing is visible, although the amplitude is low.

All results from the frequency-domain model [blue bars in Figure 5.6] are validated by time-domain simulations [red bars]. There is a perfect agreement between the frequency-domain and time-domain models and the deviation of the complex spectra is below 1e-4 for all harmonics (not depicted).

Although the sinc3 filter applied over the full sampling period has a good attenuation of out-of-band components, such as the unsychronized disturbance signals, it has an unwanted and

large impact on the baseband components. In comparison, the sinc1 filter has a flatter frequency response with a smaller impact on the baseband components and a lower attenuation of unwanted out-of-band components. Therefore, a combination can be applied, with a sinc3 filter to filter quantization noise, an additional digital filter to shape the damping behavior concerning out-of-band components, and an accumulate-and-dump circuit for decimation to the control frequency.

5.1.2 Control System

The control system in Figure 5.7 can be divided into the subtasks current control and duty-cycle calculation. The current control is performed in the rotating reference frame using PI controllers. The inputs are the measured ac-side currents $i_{\text{s ac}}$, the current setpoints $i_{\text{s sp}}$, and optional voltage signals for disturbance compensation $u_{\text{s comp}}$. The outputs are the setpoint voltages in 123 coordinates $u_{\text{s sp}}$, which are the inputs to the duty-cycle calculation. The outputs of the complete control block are the duty-cycle commands for the PWM process d_{s}.

Park Transformation

The current control utilizes the Park transformation to represent the signals in the rotating reference frame. The transformation comprises the Clarke transformation and a rotation matrix. Due to the omission of a neutral wire, there are only two independent currents in the three-phase system and the zero component can be truncated in the transformation matrices. The amplitude-invariant form of the Clarke transform, which allows for the expression of a three-phase signal x_ν, $\nu \in \{1, 2, 3\}$ in the stationary $\alpha\beta$ frame, is written in the time domain as

$$\begin{bmatrix} x_\alpha(t) \\ x_\beta(t) \end{bmatrix} = \frac{2}{3} \cdot \begin{bmatrix} 1 & -\frac{1}{2} & -\frac{1}{2} \\ 0 & \frac{\sqrt{3}}{2} & -\frac{\sqrt{3}}{2} \end{bmatrix} \cdot \begin{bmatrix} x_1(t) \\ x_2(t) \\ x_3(t) \end{bmatrix},$$
$$\vec{x}_{\alpha\beta}(t) = 2/3 \cdot \boldsymbol{T}_{\text{clarke}} \cdot \vec{x}_{123}(t). \tag{5.9}$$
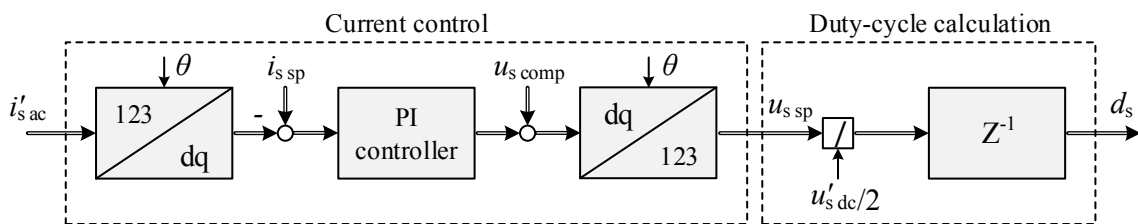

Figure 5.7: Block diagram for closed-loop control using PI current control and dc-link voltage feedback

The inverse transformation is written as

$$\begin{bmatrix} x_1(t) \\ x_2(t) \\ x_3(t) \end{bmatrix} = \begin{bmatrix} 1 & 0 \\ -\frac{1}{2} & \frac{\sqrt{3}}{2} \\ -\frac{1}{2} & -\frac{\sqrt{3}}{2} \end{bmatrix} \cdot \begin{bmatrix} x_\alpha(t) \\ x_\beta(t) \end{bmatrix},$$

$$\vec{x}_{\mathrm{abc}}(t) = \boldsymbol{T}_{\mathrm{clarke}}^{\mathrm{T}} \cdot \vec{x}_{\alpha\beta}(t).$$

(5.10)

The linear time-invariant Clarke transform can be applied to each frequency component individually and therefore can be expressed for the k-th Fourier coefficient as

$$\begin{bmatrix} X_{\alpha,k} \\ X_{\beta,k} \end{bmatrix} = \frac{2}{3} \cdot \begin{bmatrix} 1 & -\frac{1}{2} & -\frac{1}{2} \\ 0 & \frac{\sqrt{3}}{2} & -\frac{\sqrt{3}}{2} \end{bmatrix} \cdot \begin{bmatrix} X_{1,k} \\ X_{2,k} \\ X_{3,k} \end{bmatrix},$$

$$\vec{X}_{\alpha\beta,k} = 2/3 \cdot \boldsymbol{T}_{\mathrm{clarke}} \cdot \vec{X}_{123,k}.$$

(5.11)

The inverse transform results in

$$\vec{X}_{123,k} = \boldsymbol{T}_{\mathrm{clarke}}^{\mathrm{T}} \cdot \vec{X}_{\alpha\beta,k}.$$

(5.12)

The second component of the Park transform is a rotation into the dq reference frame with the rotating angle θ, resulting in the signal in dq coordinates, with

$$\begin{bmatrix} x_{\mathrm{d}}(t) \\ x_{\mathrm{q}}(t) \end{bmatrix} = \begin{bmatrix} \cos(\theta(t)) & \sin(\theta(t)) \\ -\sin(\theta(t)) & \cos(\theta(t)) \end{bmatrix} \cdot \begin{bmatrix} x_\alpha(t) \\ x_\beta(t) \end{bmatrix},$$

$$\vec{x}_{\mathrm{dq}}(t) = \boldsymbol{T}_{\mathrm{rot}}(\theta(t)) \cdot \vec{x}_{\alpha\beta}(t).$$

(5.13)

Assuming of the rotating angle has a constant gradient with $\theta(t) = \omega_{\mathrm{rot}}t$, where ω_{rot} is its angular frequency of the rotation, allows for the expression of the Fourier transform of the matrix elements as

$$\cos(\omega_{\mathrm{rot}}t) \quad \circ\!\!-\!\!\bullet \quad \frac{1}{2} \cdot \delta(\omega - \omega_{\mathrm{rot}}) + \frac{1}{2} \cdot \delta(\omega + \omega_{\mathrm{rot}}),$$

$$\sin(\omega_{\mathrm{rot}}t) \quad \circ\!\!-\!\!\bullet \quad -\frac{\mathrm{j}}{2} \cdot \delta(\omega - \omega_{\mathrm{rot}}) + \frac{\mathrm{j}}{2} \cdot \delta(\omega + \omega_{\mathrm{rot}}).$$

(5.14)

The Delta function is convolved with the spectrum of the signals in $\alpha\beta$ coordinates, which results in a frequency shift, with

$$\begin{aligned} X_{\mathrm{d}}(\omega) &= \frac{1}{2} \cdot X_\alpha(\omega) * \delta(\omega - \omega_{\mathrm{rot}}) + \frac{1}{2} \cdot X_\alpha(\omega) * \delta(\omega + \omega_{\mathrm{rot}}) ... \\ &\quad - \frac{\mathrm{j}}{2} \cdot X_\beta(\omega) * \delta(\omega - \omega_{\mathrm{rot}}) + \frac{\mathrm{j}}{2} \cdot X_\beta(\omega) * \delta(\omega + \omega_{\mathrm{rot}}) \\ &= \frac{1}{2} \cdot \left(X_\alpha(\omega - \omega_{\mathrm{rot}}) + X_\alpha(\omega + \omega_{\mathrm{rot}}) - \mathrm{j}X_\beta(\omega - \omega_{\mathrm{rot}}) + \mathrm{j}X_\beta(\omega + \omega_{\mathrm{rot}}) \right), \end{aligned}$$

(5.15)

$$X_q(\omega) = \frac{j}{2} \cdot X_\alpha(\omega) * \delta(\omega - \omega_{rot}) - \frac{j}{2} \cdot X_\alpha(\omega) * \delta(\omega + \omega_{rot})...$$

$$+ \frac{1}{2} \cdot X_\beta(\omega) * \delta(\omega - \omega_{rot}) + \frac{1}{2} \cdot X_\beta(\omega) * \delta(\omega + \omega_{rot}) \tag{5.16}$$

$$= \frac{1}{2} \cdot (jX_\alpha(\omega - \omega_{rot}) - jX_\alpha(\omega + \omega_{rot}) + X_\beta(\omega - \omega_{rot}) + X_\beta(\omega + \omega_{rot})) .$$

The application to Fourier components requires the rotation frequency to be an integer multiple of the fundamental frequency with $\omega_{rot} = n\omega_0, n \in \mathbb{N}$. The frequency-domain convolution of the rotating matrix results in a shift of n harmonic order, including a left-shift and a right-shift term

$$\begin{bmatrix} X_{d,k} \\ X_{q,k} \end{bmatrix} = \frac{1}{2} \cdot \begin{bmatrix} 1 & -j \\ j & 1 \end{bmatrix} \cdot \begin{bmatrix} X_{\alpha,(k-n)} \\ X_{\beta,(k-n)} \end{bmatrix} + \frac{1}{2} \cdot \begin{bmatrix} 1 & j \\ -j & 1 \end{bmatrix} \cdot \begin{bmatrix} X_{\alpha,(k+n)} \\ X_{\beta,(k+n)} \end{bmatrix} . \tag{5.17}$$

The inverse rotation describes the transformation from dq coordinates into αβ coordinates, with

$$\begin{bmatrix} x_\alpha(t) \\ x_\beta(t) \end{bmatrix} = \begin{bmatrix} \cos(\theta) & -\sin(\theta) \\ \sin(\theta) & \cos(\theta) \end{bmatrix} \cdot \begin{bmatrix} x_d(t) \\ x_q(t) \end{bmatrix},$$

$$\vec{x}_{dq}(t) = \boldsymbol{T}_{rot}(-\theta(t)) \cdot \vec{x}_{\alpha\beta}(t), \tag{5.18}$$

which can be expressed for the Fourier coefficients as

$$\begin{bmatrix} X_{\alpha,k} \\ X_{\beta,k} \end{bmatrix} = \frac{1}{2} \cdot \begin{bmatrix} 1 & j \\ -j & 1 \end{bmatrix} \cdot \begin{bmatrix} X_{d,(k-n)} \\ X_{q,(k-n)} \end{bmatrix} + \frac{1}{2} \cdot \begin{bmatrix} 1 & -j \\ j & 1 \end{bmatrix} \cdot \begin{bmatrix} X_{d,(k+n)} \\ X_{q,(k+n)} \end{bmatrix} . \tag{5.19}$$

The frequency-domain representation of the Park transformation is derived here for continuous-time signals. Due to the time invariance and linearity of the Clarke transform and equal CTFT and DTFT for cosine and sine [41] in (5.14), the results can be directly applied to discrete-time signals.

The derivation of the rotation matrix in the frequency domain is based on the assumption of a rotating angle with a constant gradient of ω_{rot}. This is valid in the first approximation because the rotating angle is determined by the grid frequency in grid-converter applications or the rotor speed in machine applications, which are stiff quantities in both cases. Nevertheless, the rotating frequency can contain harmonic components, especially in the presence of faults. The consequences of harmonic components in the rotating matrix are discussed and analyzed further in the context of a drive system with a synchronous machine in Chapter 6.

Proportional-Integral Control

Linear PI controllers can be described by a transfer function

$$H_{\mathrm{PI}}(\omega) = K_{\mathrm{P}} + \frac{K_{\mathrm{P}}}{T_{\mathrm{I}}} \cdot H_{\mathrm{I}}(\omega), \tag{5.20}$$

where K_{P} is the proportional gain and T_{I} is the integrator time constant. For digital control, the transfer function of the integrator $H_{\mathrm{I}}(\omega)$ depends on the choice of the integration method, all of which are summarized in Table 5.1. The table also provides the difference equations for the integration methods forward Euler, backward Euler, and Tustin, where $x[k]$ is the input signal and $y[k]$ is the output signal.

For a matrix representation, the PI controller is a diagonal matrix $\boldsymbol{H}_{\mathrm{PI}}$, where the diagonal elements are the sampled values $H_{\mathrm{PI}}[k\omega_0]$ of the transfer function in (5.20). The measured signals of the ac-side currents are transformed into dq coordinates $\vec{I}'_{\mathrm{d}}, \vec{I}'_{\mathrm{q}}$ by application of (5.11) and (5.17). The inputs of the current controllers are the deviations of the measured currents in dq coordinates from the setpoint signals $\vec{I}_{\mathrm{dsp}}, \vec{I}_{\mathrm{qsp}}$, with

$$\begin{aligned} \Delta \vec{I}'_{\mathrm{s\,d}} &= (\vec{I}_{\mathrm{s\,d\,sp}} - \vec{I}'_{\mathrm{s\,d}}) \\ \Delta \vec{I}'_{\mathrm{s\,q}} &= (\vec{I}_{\mathrm{s\,q\,sp}} - \vec{I}'_{\mathrm{s\,q}}). \end{aligned} \tag{5.21}$$

The outputs of the controllers are the setpoint voltages of the VSI in dq coordinates, with

$$\begin{aligned} \vec{U}_{\mathrm{s\,d\,sp}} &= \boldsymbol{H}_{\mathrm{PI}} \cdot \Delta \vec{I}'_{\mathrm{s\,d}} + \vec{U}_{\mathrm{s\,d\,comp}}, \\ \vec{U}_{\mathrm{s\,q\,sp}} &= \boldsymbol{H}_{\mathrm{PI}} \cdot \Delta \vec{I}'_{\mathrm{s\,q}} + \vec{U}_{\mathrm{s\,q\,comp}}. \end{aligned} \tag{5.22}$$

The equations contain additional components for disturbance compensation, which take into account the cross-coupling of the dq axes and a compensation of the measured disturbance

Table 5.1: Difference equations and transfer functions for different integration methods, cf [42].

Integration method	Difference equation	Transfer function
Forward Euler	$y[k] = T_{\mathrm{c}}\,x[k-1] + y[k-1]$	$H(\omega) = T_{\mathrm{c}}\dfrac{1}{\mathrm{e}^{\mathrm{j}\omega T_{\mathrm{c}}} - 1}$
Backward Euler	$y[k] = T_{\mathrm{c}}\,x[k] + y[k-1]$	$H(\omega) = T_{\mathrm{c}}\dfrac{\mathrm{e}^{\mathrm{j}\omega T_{\mathrm{c}}}}{\mathrm{e}^{\mathrm{j}\omega T_{\mathrm{c}}} - 1}$
Trapezoidal (Tustin)	$y[k] = \dfrac{T_{\mathrm{c}}}{2}\left(x[k] + x[k-1]\right) + y[k-1]$	$H(\omega) = \dfrac{T_{\mathrm{c}}}{2}\dfrac{\mathrm{e}^{\mathrm{j}\omega T_{\mathrm{c}}} + 1}{\mathrm{e}^{\mathrm{j}\omega T_{\mathrm{c}}} - 1}$

voltage in dq coordinates $\vec{U}_{\mathrm{ddis}}$ and $\vec{U}_{\mathrm{qdis}}$, with

$$\begin{aligned}
\vec{U}_{\mathrm{s\,d\,comp}} &= \vec{U}_{\mathrm{s\,d\,dis}} + \omega_{\mathrm{rot}} \cdot L_{\mathrm{ac}} \cdot \vec{I}'_{\mathrm{s\,q}}, \\
\vec{U}_{\mathrm{s\,q\,comp}} &= \vec{U}_{\mathrm{s\,q\,dis}} - \omega_{\mathrm{rot}} \cdot L_{\mathrm{ac}} \cdot \vec{I}'_{\mathrm{s\,d}}.
\end{aligned} \tag{5.23}$$

The dc component of the controller's transfer function has infinite gain, with $H_{\mathrm{I}}(\omega \to 0) \to \infty$. Thus, the dc components of the dq currents converge to

$$\begin{aligned}
I_{\mathrm{s\,d},0} &= I_{\mathrm{s\,d\,sp},0}, \\
I_{\mathrm{s\,q},0} &= I_{\mathrm{s\,q\,sp},0}.
\end{aligned} \tag{5.24}$$

Consequently, the dc components of the setpoint voltages cannot be calculated by (5.22). The solutions of $U_{\mathrm{s\,d},0}$ and $U_{\mathrm{s\,q},0}$ result instead from the complete equation system that incorporates the interaction of the control with the physical model of the VSI and its load.

The setpoint voltages $\vec{U}_{\mathrm{s\,d\,sp}}$ and $\vec{U}_{\mathrm{s\,q\,sp}}$ are transformed back into 123 coordinates by application of (5.19) and (5.12). The current setpoints are independent signals in this example system. Nevertheless, the approach can be extended to cascaded controllers that influence the current setpoints to control further signals of the plant, introducing additional equations with linear transfer functions.

Duty-Cycle Calculation

The duty cycle is the division of the setpoint voltage of phase ν by half the measured dc-link current. The calculated duty cycle is committed to the modulator within the control cycle and is applied to the switching pattern in the next control step, with

$$d_{\nu}[k] = \frac{u_{\mathrm{sp}\nu}[k-1]}{u'_{\mathrm{dc}}[k-1]/2}. \tag{5.25}$$

The division is the inverse operation of the multiplication in the time domain. For the equivalent operation in the frequency domain the inverse convolution is utilized. Applied to Fourier coefficients, this operation is represented by an inverse convolution matrix $\boldsymbol{C}(.)^{-1}$. The requirements for the existence of the inverse convolution are fulfilled [see inverse convolution in Section 2.3], because for a stable converter operation it is required that $u_{\mathrm{dc}}(t) \geq, \forall t$ and $1/u_{\mathrm{dc}}(t)$ is a slowly growing signal, since it is the state variable of an energy storage.

Finally, the delay block (z^{-1}) in Figure 5.7 takes the computational delay into account. The delay is considered in the frequency-domain models with a diagonal matrix $\boldsymbol{H}_{\mathrm{delay}}$. Accordingly, the calculation of the duty cycle results in

$$\vec{D}_{\mathrm{s}\nu} = 2 \cdot \boldsymbol{H}_{\mathrm{delay}} \cdot \boldsymbol{C}(\vec{U}'_{\mathrm{s\,dc}})^{-1} \cdot \vec{U}_{\mathrm{s\,sp}\,\nu}, \tag{5.26}$$

where the k-th diagonal element of the matrix is

$$H_{\text{delay},k} = \text{e}^{-\text{j}k\omega_0 T_\text{c}}. \tag{5.27}$$

5.2 Amplitude Quantization

In the digital control system, signals are represented by discrete values in a binary code. This leads to the generation of quantization noise, which can be classified by a number of effects. The analog input signals are transferred into discrete signals by the ADC. For uniform quantizers, the quantization step q is determined by the number of bits n and the full scale range FSR of the ADC [42], with

$$q = \frac{FSR}{2^n}. \tag{5.28}$$

Input quantization results in a quantization noise that can be modeled by a stochastic process, which superimposes the original signal. With the assumption that there is no correlation of noise and signal, the maximum signal to noise ratio (SNR) can be estimated as:

$$\text{SNR} = 10 \cdot \log_{10}\left(\frac{12}{8} \cdot 2^{2n}\right) (\text{dB}) \quad [42]. \tag{5.29}$$

The signal to noise ratio of the delta-sigma modulator was discussed previously. The output word size of the delta-sigma modulator is 1 and is subsequently increased by the decimator to the decimator's output word size p. When applying a sinc3 filter this results in

$$n = 3 \cdot \log_2(N) \quad [72]. \tag{5.30}$$

In the experimental system, a decimation ratio of $N = 40$ is applied, which results in a word size of approximately $n = 16$ bit and SNR $= 98$ dB. Therefore, the influence of input quantization on the measurement results is expected to be low.

A further influence of quantization noise can originate from rounding errors and truncations, because of the limited precision of variables and constants in the control process, which is called **arithmetic quantization noise** [42]. In the experimental setup, the digital control is implemented on an ARM Cortex-A9 processor [see Appendix B] with 32 bit floating point precision. For processors with access to floating point units, the influence of arithmetic quantization is considered negligible [42].

Output quantization results from the limited resolution in counter based PWM processes [42]. For a clock frequency of $f_{\text{clk}} = 100$ MHz, the switching instant can be executed with an accuracy of 10 ns. Using a control frequency of $f_\text{c} = 10$ kHz, the duty cycle has a resolution of

$f_{\mathrm{clk}}/f_{\mathrm{c}}$ points. The equivalent number of bits is represented by $\log_2(f_{\mathrm{clk}}/f_{\mathrm{c}}) \approx 13$, and the duty cycle resolution results in $f_{\mathrm{c}}/f_{\mathrm{clk}} = 0.01\,\%$ [34]. The resolution is higher for lower control frequencies, as they are used in the example cases and the influence of output quantization is expected to be low. However, it should be noted that for applications with a low ratio of $f_{\mathrm{clk}}/f_{\mathrm{c}}$, the effect can become significant and cause instabilities known as limit cycle oscillations [42].

5.3 Incorporation of the PWM Model

This section analyzes how to connect the output of the digital control, which is a discrete-time signal, to the input of the PWM model. The frequency-domain models for regularly-sampled PWM that incorporate multiple-frequency input signals were introduced in Section 3.2.2. As shown in the Simulink implementation of regularly-sampled PWM in Figure 3.13, its structure can be internally divided into a sampler, a ZOH, and a representation of naturally-sampled PWM.

Figure 5.8 shows two possibilities for adapting this arrangement to the frequency-domain model of regularly-sampled PWM. Subfigure a) shows the model presented in (3.60) in Section 3.2.2, where the input spectrum is the Fourier transform of the continuous-time duty cycle $D(f)$. Without loss of generality, the functions of the sampler and the ZOH can be applied outside the PWM model, providing the Fourier transform of the discrete-time duty cycle $D_{\mathrm{s}}(f)$ as input of a model of naturally-sampled double-edge PWM, which is used to calculate the switching function spectrum, as shown in subfigure b). In conclusion, regularly-sampled PWM is equivalent to naturally-sampled PWM with a 'distorted' duty cycle spectrum $D_{\mathrm{s}}(f)$ as its input.

A model for naturally-sampled double-edge PWM (ND-PWM) is derived by Song and Sarwate in [15, (61)]. Written in the nomenclature used in this thesis, the model results in

$$
\begin{aligned}
S_{\mathrm{ND}}(f, D) = {} & D(f) + S_{\mathrm{c}}(f) \cdot \mathrm{e}^{-\mathrm{j}\pi f T_{\mathrm{sw}}/2} + \sum_{m=1}^{\infty} (-1)^m \cdot \sum_{n=1}^{\infty} \dots \\
& \left(\frac{(\mathrm{j}2m\pi)^{2n-2}}{2^{2n-2} \cdot (2n-1)!} \cdot \left(D^{*(2n-1)}(f + 2mf_{\mathrm{sw}}) + D^{*(2n-1)}(f - 2mf_{\mathrm{sw}}) \right) \dots \right. \\
& \left. - \frac{(\mathrm{j}(2m-1)\pi)^{2n-1}}{\mathrm{j}2^{2n-1} \cdot (2n)!} \cdot \left(D^{*(2n)}(f + (2m-1)f_{\mathrm{sw}}) + D^{*(2n)}(f - (2m-1)f_{\mathrm{sw}}) \right) \right).
\end{aligned}
$$

(5.31)

In order to express the same switching function spectrum as for AD-PWM, with

$$
S_{\mathrm{AD}}(f, D) \approx S_{\mathrm{ND}}(f, D_{\mathrm{s}}),
$$

(5.32)

the Fourier transform of the discrete-time duty cycle is calculated and applied to the ND-PWM
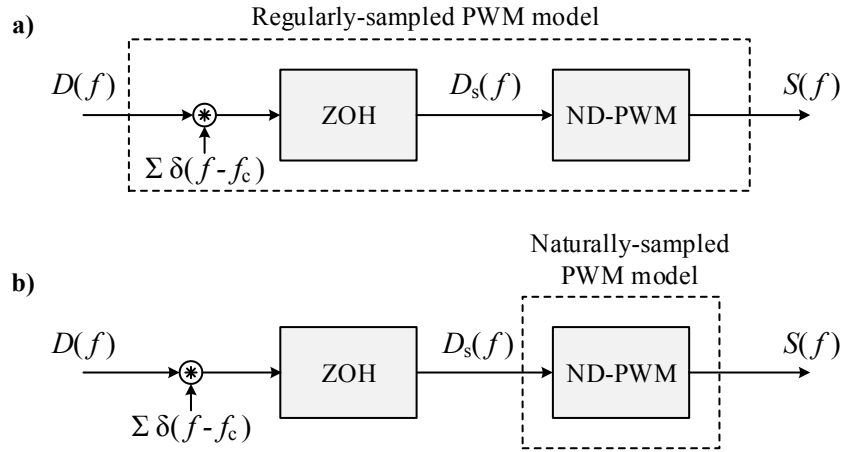
a)

b)

Figure 5.8: Equivalent methods to represent regularly-sampled PWM when the input is the CTFT of the duty cycle $D(f)$: **a)** The series connection of sampler, ZOH, and naturally-sampled PWM is combined in one mathematical expression. **b)** The CTFT of the duty cycle $D(f)$ is first converted into the DTFT of the duty cycle $D_s(f)$ using a model of the sampler and the ZOH. The resulting spectrum is used as the input for the naturally-sampled PWM model.

model. With the transfer function of the ZOH $H_{\mathrm{ZOH}}(f)$ and the sampler $H_s(f)$, this results in

$$D_s(f) = H_{\mathrm{ZOH}}(f) \cdot (H_s(f) * D(f)). \tag{5.33}$$

For the application of feedback control, the output of the digital controller is the duty-cycle spectrum $D_s(f)$ of the discrete-time signal, which interacts with the signals of the PWM and the plant. As previously discussed, the frequency-domain model for regularly-sampled PWM [Figure 5.8 a)] requires the duty-cycle spectrum $D(f)$ of the continuous-time signal $d(t)$ as the input. However, as shown in Figure 5.9 a), a naturally-sampled PWM model can be applied to express regularly-sampled PWM when the input is a discrete-time signal.

A numerical evaluation of the ND-PWM model is performed in an example case by converting (5.31) into the representation of discrete Fourier coefficients. The indeces of summation are limited to $m_{\max}$ and $n_{\max}$. The duty cycle is applied as the spectrum of the sampled signal, which is depicted in Figure 5.10. The duty cycle contains a fundamental frequency component with an amplitude of $|D_{,1}| = 0.7$ and a seventh harmonic component with an amplitude of $|D_{,7}| = 0.1$. The carrier to fundamental ratio is $f_{\mathrm{sw}}/f_{d0} = 3000/50 = 60$. These are the same parameters as used for the validation of the AD-PWM model in Figure 3.15. The duty-cycle spectrum contains sideband groups at multiples of the control frequency of $f_c = 2 \cdot f_{\mathrm{sw}}$.

The graphs on the left side of Figure 5.11 show the amplitude spectrum of the switching function for the first 80 harmonics for various numbers of considered harmonics. The first graph shows the comparison of the frequency-domain model with a time-domain model for $m_{\max} = 1$, $n_{\max} = 7$, $k_{\max} = 150$. Large deviations between the complex spectra are visible in the second
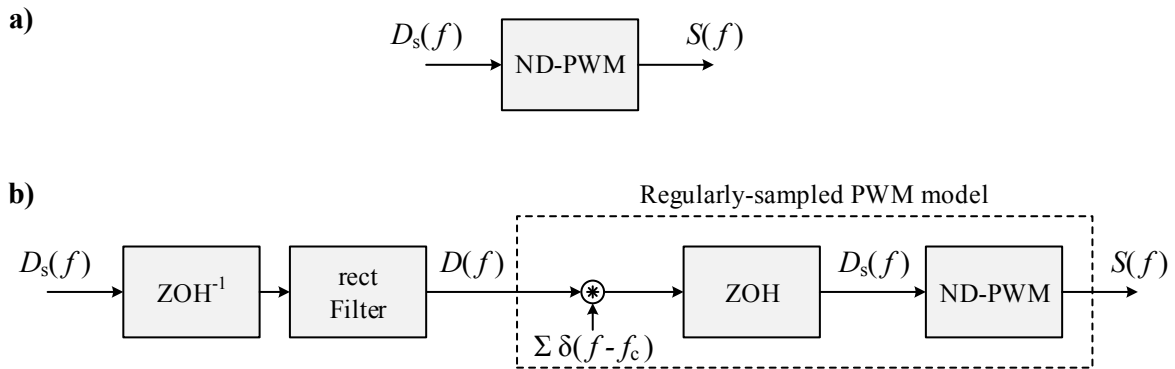
a)

b)

Figure 5.9: Equivalent methods to represent regularly-sampled PWM when the input is the DTFT of the duty cycle $D_s(f)$: **a)** A block expressing naturally-sampled PWM. **b)** The inverse ZOH and the rectangular filter compensate the sampler and the ZOH in the PWM model. These blocks are inserted prior to the frequency-domain model of regularly-sampled PWM that includes a ZOH block and a sampler [Figure 5.8 a)].
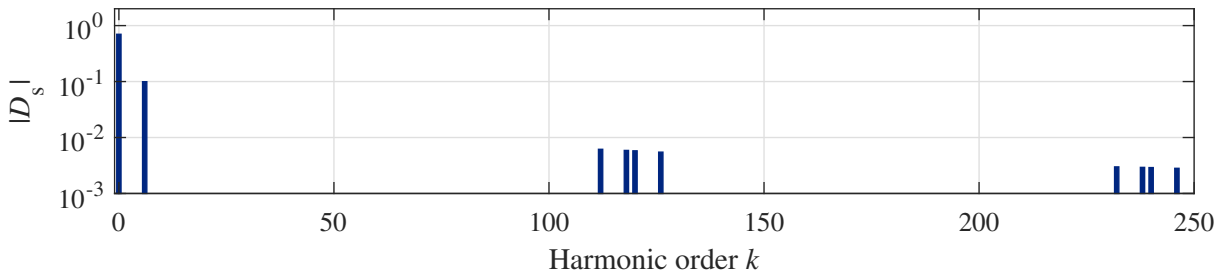

Figure 5.10: Spectrum of the sampled and hold duty cycle. The continuous duty cycle originally contains two components at $k = 1$ and $k = 7$. Due to sampling with the control frequency, components around multiples of the $f_c/f_0 = 60$ are present.

graph. As shown in the third and fourth graph, higher numbers of $m_{\max}$ and $n_{\max}$ lead to a minor improvement in the calculation. Nevertheless, large deviations occur, which can be explained by the low number of considered harmonics $k_{\max}$ of the duty-cycle spectrum. In this case, the second and third sideband groups shown in Figure 5.10 are neglected, which results in a incomplete calculation of the first carrier group for the switching function spectrum.

As shown in the fifth and sixth graphs, an increased number of $k_{\max} = 500$ is not sufficient when the indeces of summation ($m_{\max} = 1$, $n_{\max} = 7$) are low. This is because of the neglected interaction of the sideband groups of the duty cycle in the modulation process. The last two graphs show the spectra for $m_{\max} = 2$, $n_{\max} = 20$, and $k_{\max} = 500$. For very high numbers of $m_{\max}$, $n_{\max}$, and $k_{\max}$, the deviation decreases further (not depicted).

This numerical example shows that the model for ND-PWM requires a much higher number of harmonics $k_{\max}$ in the duty-cycle to reach the same accuracy as the AD-PWM model. Therefore, an alternative method is presented in Figure 5.9 b): The DTFT of the duty-cycle is converted into a CTFT, which is subsequently applied to the AD-PWM model. The conversion is performed
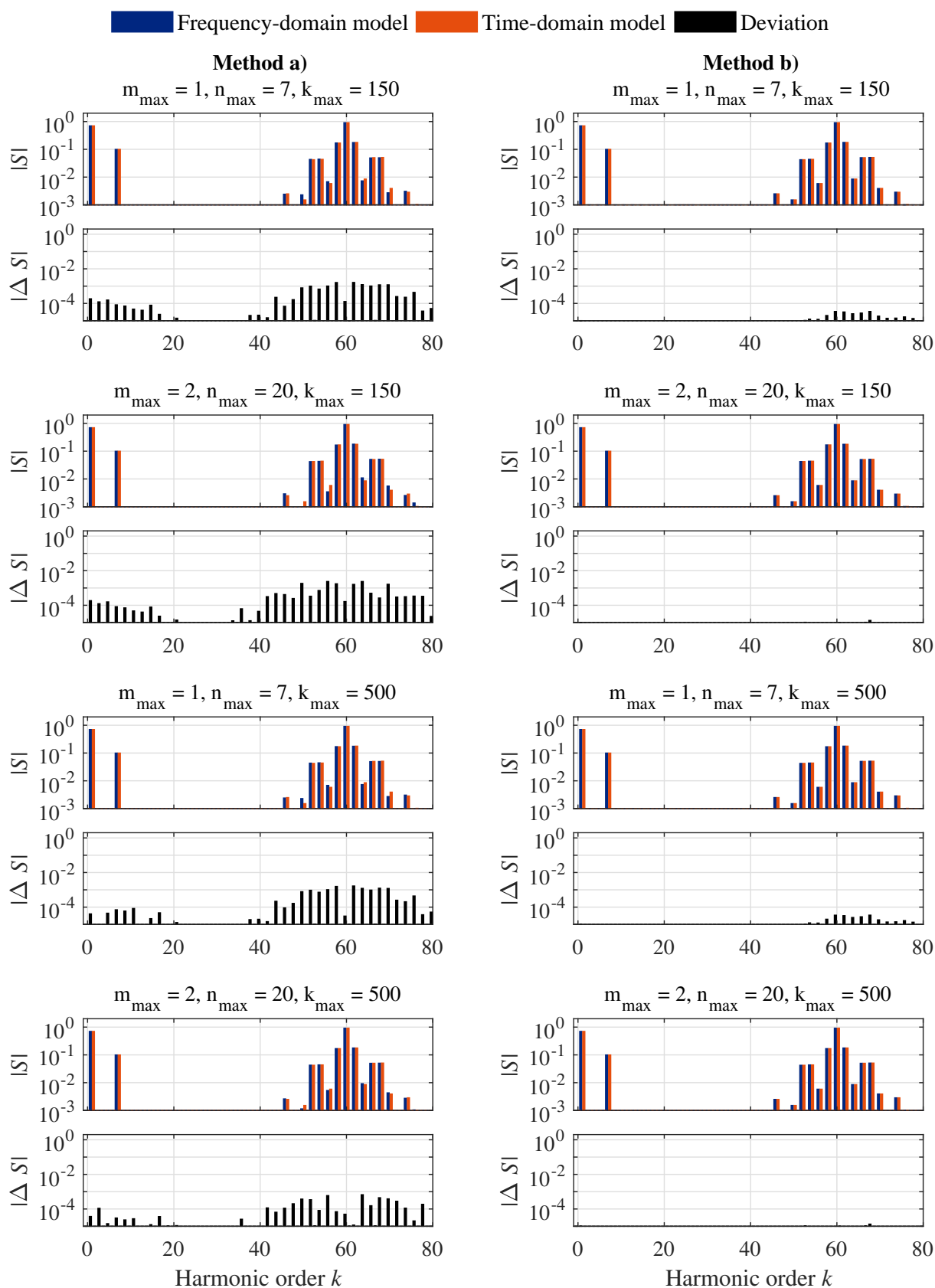
Figure 5.11: Evaluation of the models depicted in Figure 5.9, which represent regularly-sampled PWM when the input spectrum is the DTFT of the duty cycle $D_s(f)$. The parameters $m_{max}, n_{max}, k_{max}$ are varied from top to bottom. **Left graphs:** Method a) using a model for ND-PWM. **Right graphs:** Method b) using an inverse ZOH, a rectangular filter and a model for AD-PWM.

by application of the inverse transfer function of the ZOH

$$H_{\text{ZOH}}^{-1}(\omega) = \frac{j\omega T_c}{1 - e^{-j\omega T_c}}, \quad \omega \neq 0$$

$$H_{\text{ZOH}}^{-1}(0) = 1 \tag{5.34}$$

and the inversion of the sampling process. Because $D_s(f)$ is the DTFT of a band-limited signal, this can be represented by a rectangular filter

$$H_{\text{rect}}(\omega) = \begin{cases} 1 & \text{for} & -\omega_c/2 \leq \omega \leq \omega_c/2 \\ 0 & \text{otherwise} \end{cases}. \tag{5.35}$$

The graphs on the right side of Figure 5.11 show the results for this modeling approach for the same parameters as for the ND-PWM model. Although the model appears to be more complex, a high accuracy is reached for relatively low numbers of considered harmonics k_{max}. Due to the band-limiting effect of the rectangular filter, there are no duty-cycle components larger than $f_c/2$ that require consideration in the PWM model. The proposed approach is chosen for the evaluation of the total equation system presented in the next section, because a low number of k_{max} is crucial for the numerical solution process.

5.4 Numerical Evaluation

The frequency-domain model for closed-loop control is evaluated for the topology of Case I [Figure 3.26], where the ac-side phases are connected to a passive RL load and the dc link is fed by a three-phase diode rectifier. The parameters are listed in Table 5.2. The feedback loops incorporate the sensed ac-side currents and the dc-link voltage. The cut-off frequency of the sensors are f_{Icut} and f_{Ucut} for the ac-side current sensors and the dc-link voltage sensor, respectively. The PI controller is designed using the technical optimum, with

$$T_I = \frac{L_{\text{ac}}}{R_{\text{ac}}},$$

$$K_P = \frac{T_I \cdot R_{\text{ac}}}{2 \cdot 1.5 \cdot T_{\text{sw}}}. \tag{5.36}$$

Compensating voltages $\vec{U}_{\text{dcomp}}$ and $\vec{U}_{\text{qcomp}}$ are not used in this example case.

The mutual dependency of the nonlinear PWM process, the plant, and the controller requires the simultaneous solution of the nonlinear equation system, which is of the form written in (2.47). The equation system chosen for the following numerical evaluation describes $N = 13$ signals,

Table 5.2: Parameters of the example system for Case I

Parameter	Symbol	Values
Fundamental frequency	f_0	50 Hz
Switching frequency	f_{sw}	3 kHz
Control frequency	f_{c}	6 kHz
ac-side resistance	R_{ac}	5 Ω
ac-side inductance	L_{ac}	20 mH
dc-link capacitance	C_{dc}	480 μF
Grid voltage (line-to-line, rms)	U_{g}	400 V
Grid frequency	f_{g}	50 Hz
Grid-side inductance	L_{g}	260 μH
Current sensor cut-off frequency	f_{Icut}	240 kHz
Voltage sensor cut-off frequency	f_{Ucut}	100 kHz
Proportional gain (current control)	K_{P}	20 V/A
Integrator time constant controller	T_{I}	4 ms
Highest considered harmonic	k_{max}	70
Maximum carrier order	m_{max}	1
Maximum sideband order	n_{max}	7

collected in a vector

$$\vec{X} = [\vec{I}_{\mathrm{ac1}}, \vec{I}_{\mathrm{ac2}}, \vec{I}_{\mathrm{ac3}}, \vec{U}_{\mathrm{dc}}, \vec{D}_1, \vec{D}_2, \vec{D}_3, \vec{I}_{\mathrm{d}}, \vec{I}_{\mathrm{q}}, \vec{U}_{\alpha\mathrm{sp}}, \vec{U}_{\beta\mathrm{sp}}, \vec{U}_{\mathrm{dsp}}, \vec{U}_{\mathrm{qsp}}]^{\mathrm{T}}. \tag{5.37}$$

The size of the vector is $N \cdot l_{\mathrm{max}}$. All other signals are described as dependent variables and are not written explicitly in the equation system. They can however be calculated directly from the signals present in $\vec{X}$. The input signals of the system are the ac-side disturbance voltages, the dc-side disturbance current, the dc component of the dc-link voltage and the current setpoint in dq coordinates.

A large equation system results for large numbers of signals in the system and for large numbers of considered harmonics. This requires long computation times and increases the risk of a diverging solution process. For this reason, the fundamental frequency of the duty-cycle is set to 50 Hz (in comparison to 40 Hz in Chapter 3 and Chapter 4) and the fundamental frequency of the model results in $f_0 = 50$ Hz. This reduces the number of required harmonics k_{max} and therefore decreases the size of the equation system.

The numerical solution is performed in *Matlab* using the *trust-region algorithm*. This algorithm is chosen because it allows for the incorporation of information about the Jacobian matrix. The Jacobian consists of the partial derivatives

$$\frac{\partial f_i}{\partial x_j}, \quad i, j \in [1, N \cdot l_{\mathrm{max}}], \tag{5.38}$$

which are positioned in the i-th row and the j-th column.

An analytical description of the Jacobian is challenging due to the nonlinear operations of the PWM process and the convolution. In this work, a numerical calculation of the Jacobian is an inherent property of the *Matlab* function *fsolve*. Whereas the derivation of the analytical Jacobian is complex, it is straightforward to analyze if a dependency between two variables exists. This allows for the formulation of the sparsity pattern, where all partial derivatives that are nonzero are indicated in a sparsity matrix. When provided to the solver, the sparsity matrix determines which derivatives are calculated and which derivatives are known to be zero, accelerating the solution process. Figure 5.12 shows the sparsity pattern of the equation system. For clarity, the vector size of each signal is set to the low value of $l_{\max} = 9$. Each square drawn by the grid is a submatrix of size $l_{\max} \times l_{\max}$. Different forms of the submatrices are visible:

- **Blank fields:** No influence of the signal on the equation. The partial derivatives are zero.
- **Diagonal lines:** Linear influence of the signal on the equation. There is no coupling of the harmonics.
- **Double diagonal line:** Frequency-shift due to a coordinate rotation. The lines are on the first minor diagonals when the frequency shift is by one harmonic order.
- **Irregular hexagon:** Coupling of most harmonic components due to a convolution.
- **Squares:** Full coupling of all harmonics. In this case due to PWM or inverse convolution.

In this particular case, less than 15 % of the matrix elements are nonzero. The number of function calls, which are required to numerically calculate the Jacobian, is halved due to the use of the sparsity pattern.

The iterative solution process requires a vector of initial values $\vec{X}_0$ for the iterative process. A fundamental frequency model provides the fundamental frequency components for ac quantities and the dc component of dc quantities. All other harmonic components are set to zero.
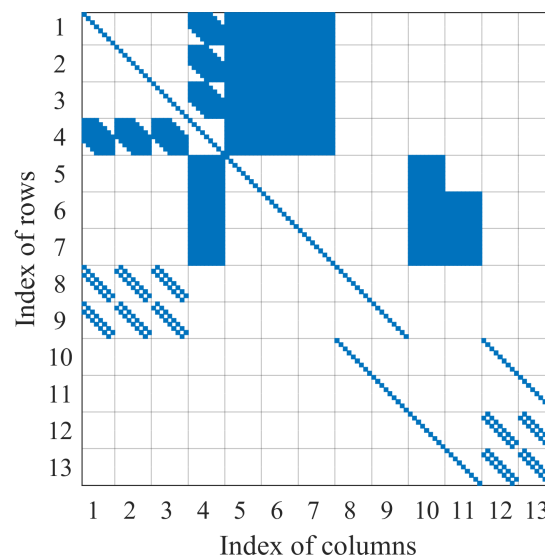

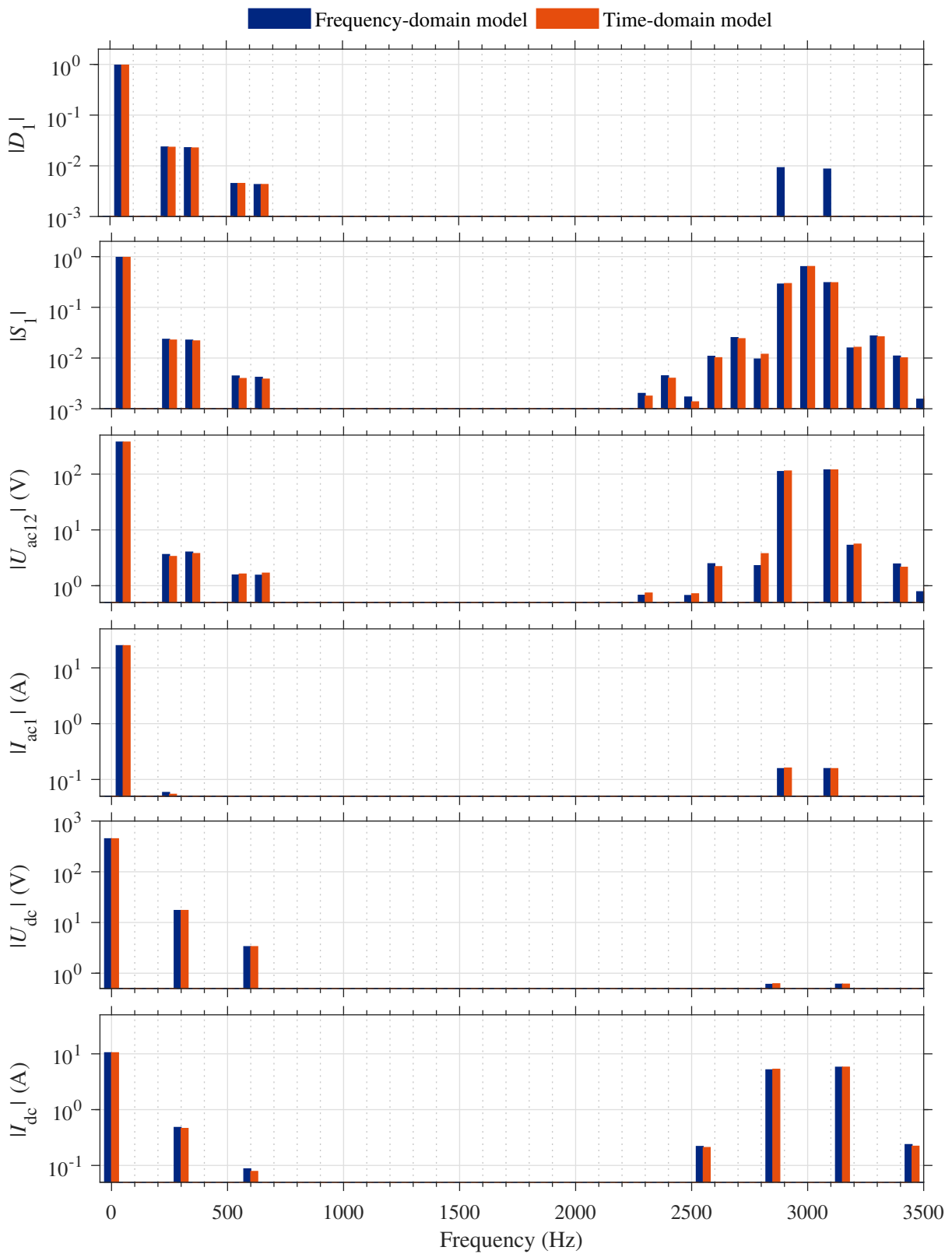**Figure 5.12:** Sparsity pattern of the nonlinear equation system.

Figure 5.13: Comparison of the results for closed-loop control using the frequency-domain model (blue) and the time-domain model (red).
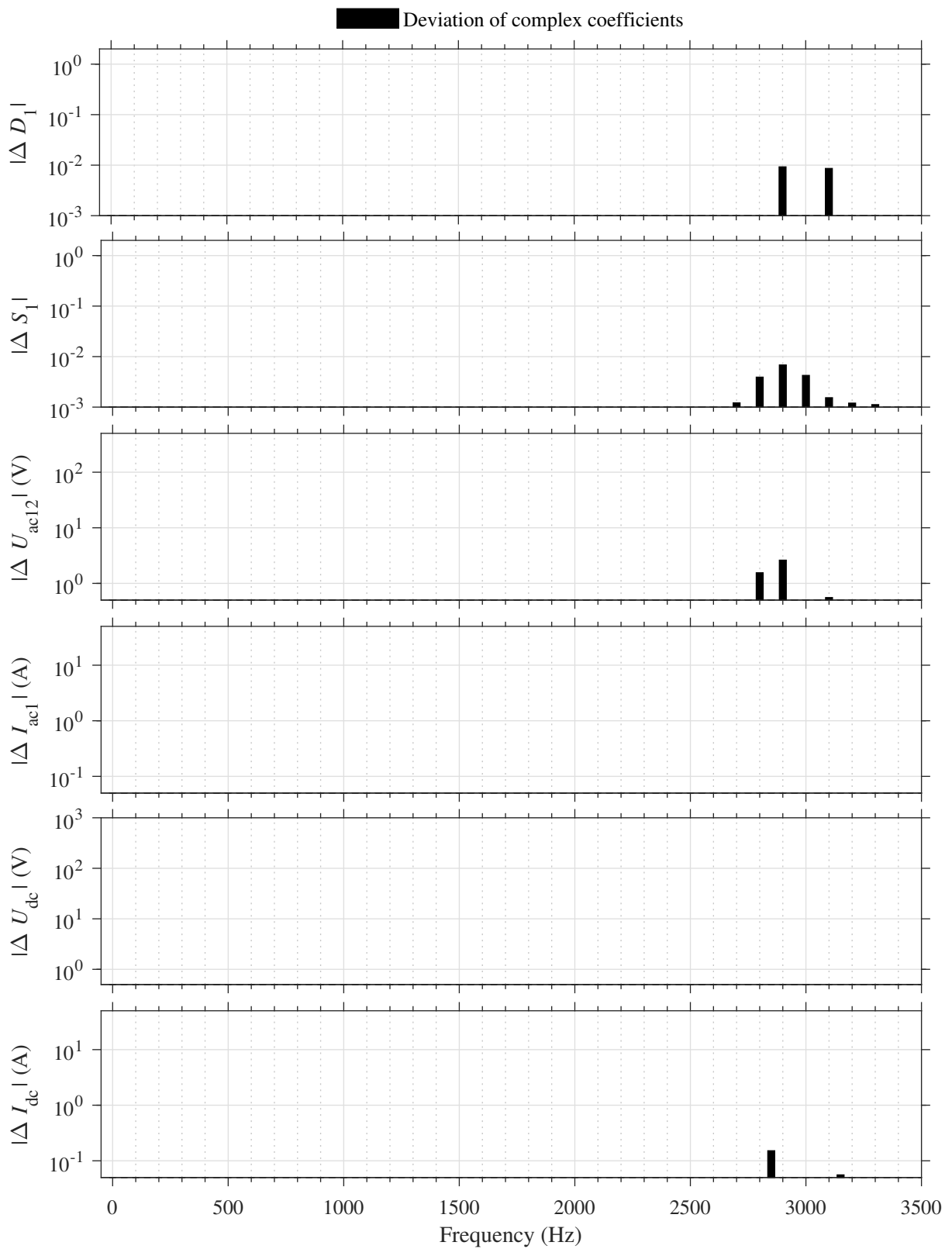
Figure 5.14: Deviation of the complex spectra of the frequency-domain model from the time-domain model presented in Figure 5.13 for closed-loop control.
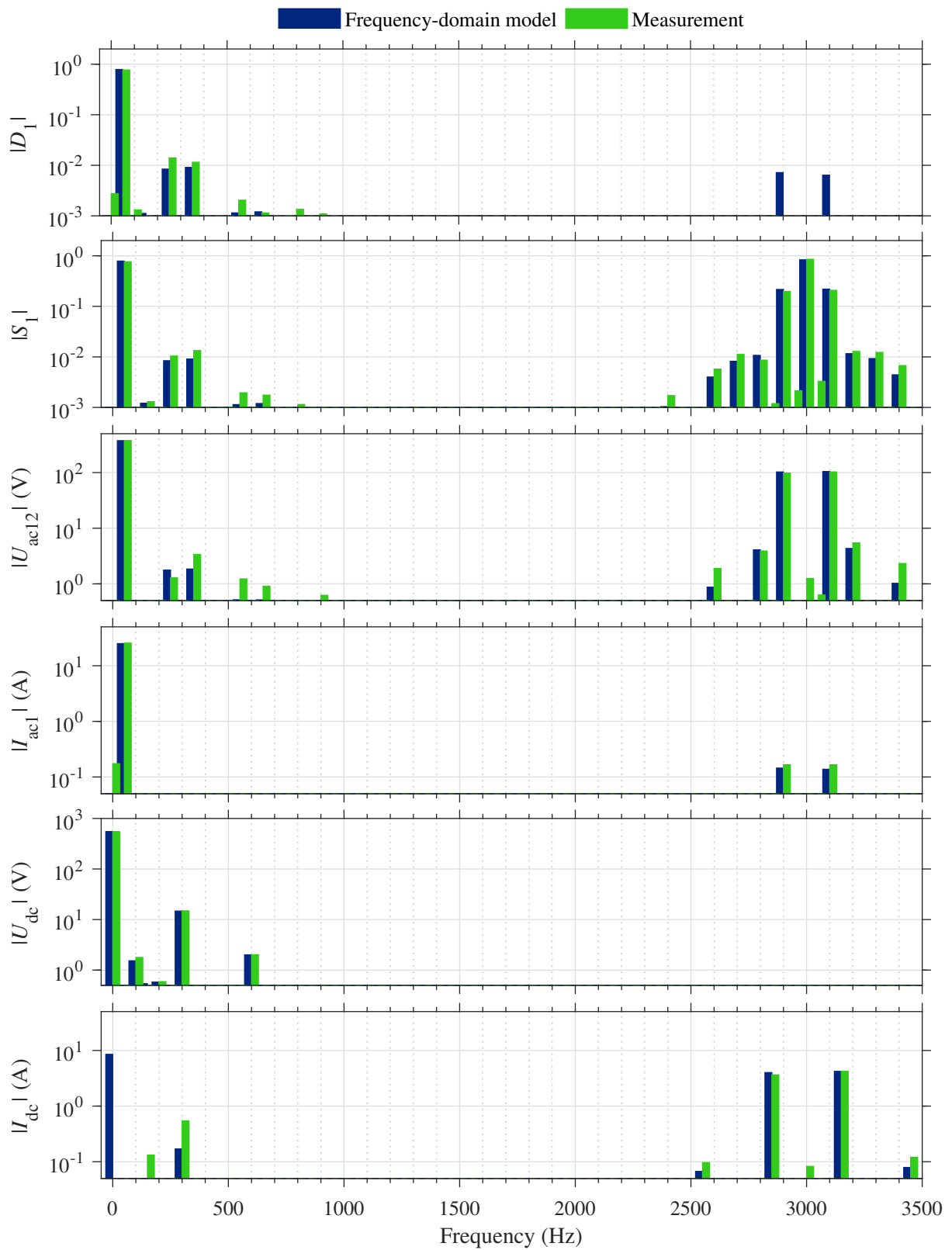
Figure 5.15: Comparison of frequency-domain model and measurements for a three-phase VSI with closed-loop control for Case I.
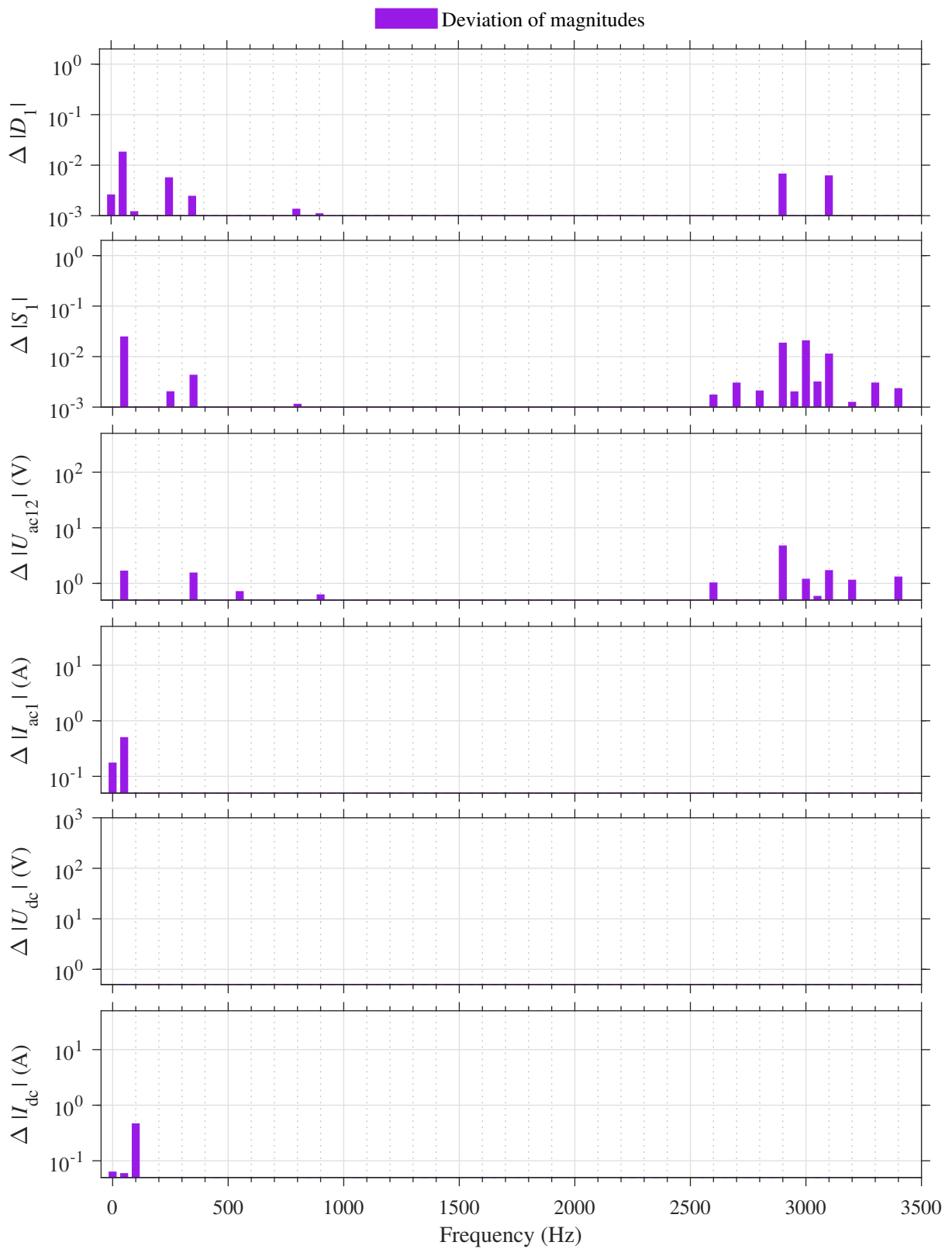
Figure 5.16: Deviations of the magnitude spectra shown in Figure 5.15 for a three-phase VSI with closed-loop control for Case I.

The magnitude spectra are depicted in Figure 5.13, comparing the results from the frequency-domain model to results from a time-domain simulation. The feedback loops of the ac-side currents and the dc-link voltage introduce low-frequency components into the duty cycle spectrum. These components result from the disturbance current of the diode rectifier, which are propagated to the sensed dc-link voltage and the sensed ac-side currents. Due to the nonlinear PWM process, the harmonic components of the duty cycle spectrum generate additional base-band and side-band harmonics in the switching function spectrum.

There is good conformity between the results of the two models, as indicated by the low deviations of the complex spectra shown in Figure 5.14. Minor deviations are visible around the switching frequency that can be explained by the low number of considered harmonics, as indicated by the previous examination presented in Figure 5.11.

A comparison of the frequency-domain results with measurement results is presented in Figure 5.15. The deviations of the magnitudes are illustrated in Figure 5.16.

To illustrate the influence of the propagated harmonics, Figure 5.17 presents a comparison of the "closed-loop" case to the "open-loop" case. For this, the fundamental component of the duty cycle is taken from the model with closed-loop control and used as an input in the model with open-loop control. The harmonic components are not included to mimic the missing feedback loop. The propagated harmonic components in the duty-cycle and their influence on the generation of baseband and carrier sideband harmonics in the switching function and ac-side voltage spectra is clearly visible. The lower baseband components in the ac-side voltage of the closed-loop case show the damping effect of the feedback control.

Figure 5.18 shows the duty cycle spectrum for three cases: For the first graph the current control and the voltage feedback is used as in Figure 5.13. In order to show the influence of the harmonics that are propagated by the current controller, the second graph depicts the resulting duty cycle when the voltage feedback is chosen to a set value of U_{dc0}. The third graph illustrates the harmonic components that are propagated by the voltage feedback. In this case, all harmonic components of the voltage setpoint provided by the current controller are neglected. Because the source of harmonic disturbances is located at the dc side, the majority of the harmonics are propagated through the voltage feedback. If the harmonic disturbance is located at the ac side, the current feedback loop would have a larger impact on the propagation of harmonic components.
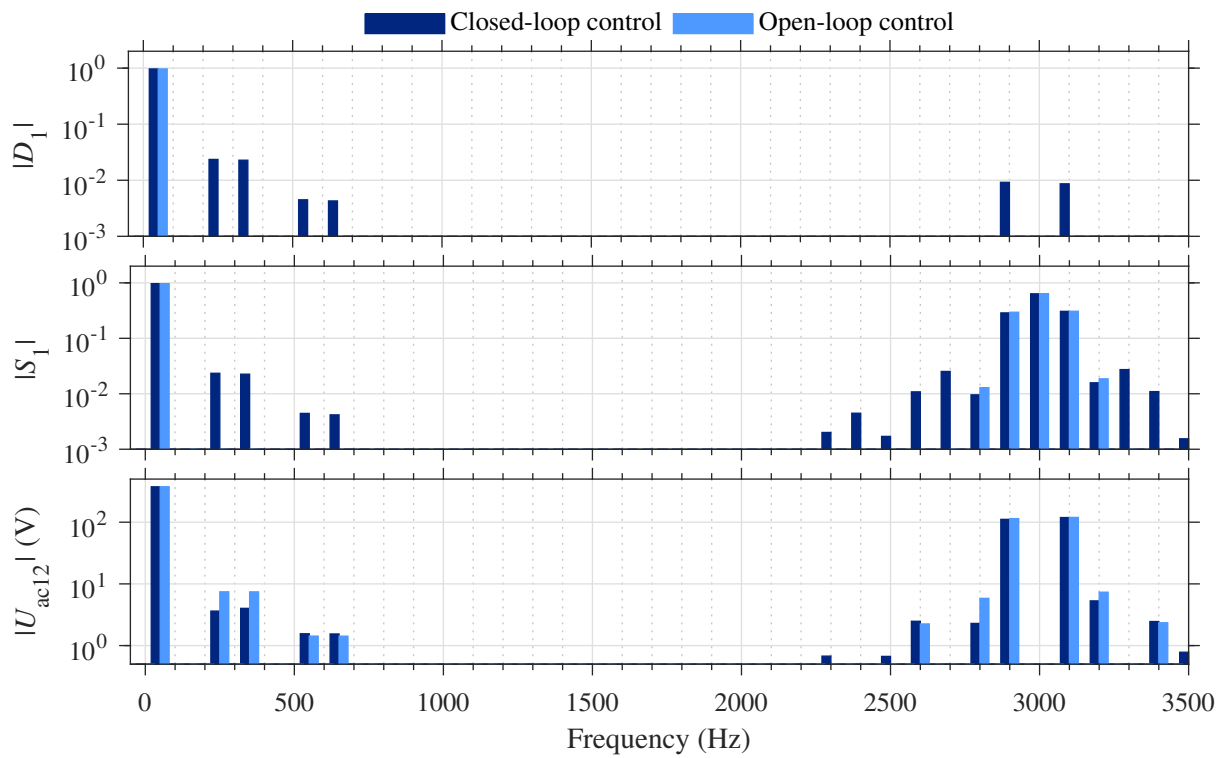
Figure 5.17: Comparison of frequency-domain models with closed-loop control (dark blue) and open-loop control (light blue).
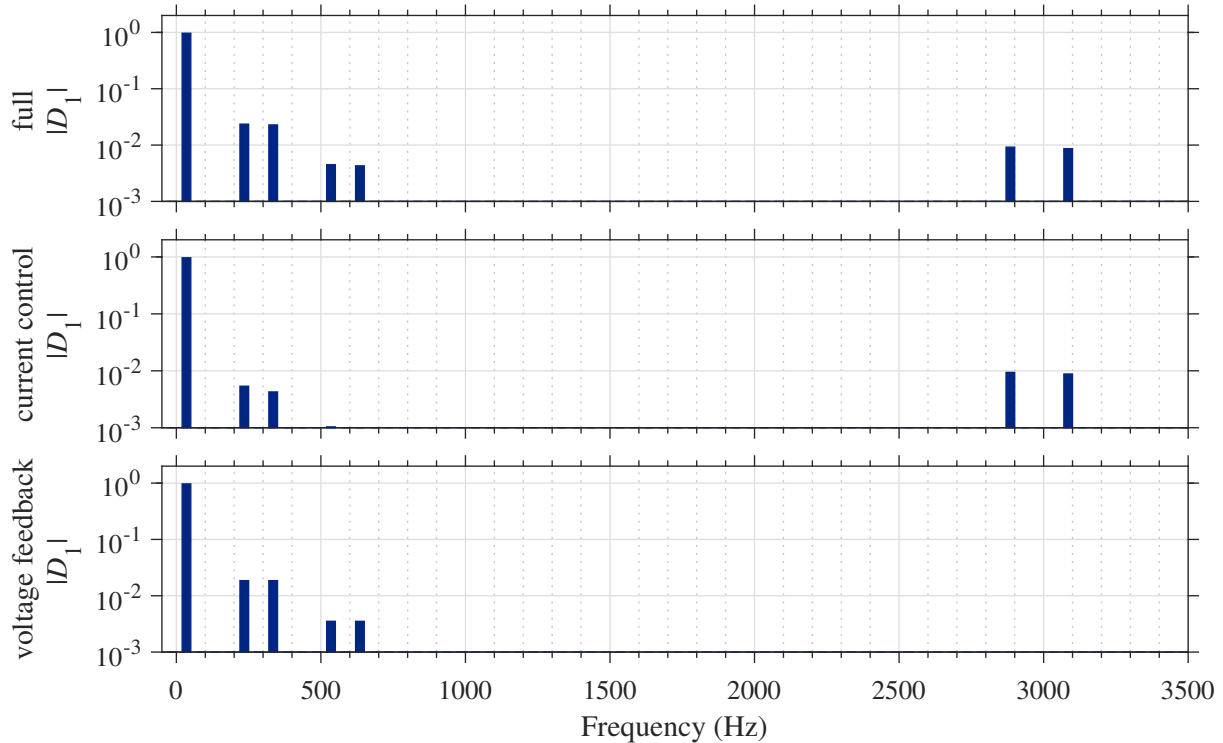

Figure 5.18: Comparison of duty cycle spectra when using current control and voltage feedback (first graph), only current control (second graph), only voltage feedback (third graph).

5.5 Discussion

This chapter demonstrated the incorporation of closed-loop control into the frequency-domain models, while considering the PWM process and the power electronic devices as ideal switches. Whereas previous approaches in the literature showed only unidirectional blocks for the individual components PWM, control, and plant, the method presented here includes their mutual dependencies and nonlinear interactions. These result in a nonlinear equation system, which can be numerically and simultaneously solved using iterative algorithms. The analysis shows how harmonics are propagated through the control loop to the duty cycle and how this changes the spectrum of the switching function.

High-frequency components that are not synchronized with the PWM process and the sampling process can occur when multiple converters are present in the system. Aliasing can result, generating low-frequency components in the sensed signals when these components are above the sampling frequency and when appropriate filtering methods are not implemented. The method presented here takes these components and the aliasing effect into consideration.

The detailed system description comes at the cost of a high computational effort, which depends on the number of harmonics considered and the number of system variables. Improvement of the solution process was achieved by exploitation of the sparsity of the equation system. This was done in the form of a derivation of the sparsity structure of the Jacobian, because it only requires the information of whether there is a dependency between two variables, without the need to give detailed information about this dependency. An analytical form of the partial derivatives that are collected in the Jacobian was not derived in this work, due to its complexity in the case of the PWM process.

6 Drive System

Electrical machines act as electromechanical energy converters connecting the electrical and mechanical domains. This power conversion is generally nonlinear, thus representing a common form of nonlinear load in converter system applications. Figure 6.1 shows a grid-connected drive system with a diode rectifier feeding a machine-side VSI. The PMSM is driven by the VSI and is connected to a mechanical load represented by the load torque m_l and the inertia J. Using a frequency converter as a variable-speed drive of the electrical machine allows for the decoupling of the rotor speed from the frequency of the feeding grid. Due to a finite control response and finite filter components, the decoupling is incomplete and frequency components of the machine subsystem can interact with frequency components of the grid side. The penetrated frequency components are considered to be interharmonics, since they are generally not an integer multiple of the subsystem's fundamental frequency [73].

Considerable interharmonic currents are introduced through the coupling dc link when an imbalance occurs in one of the subsystems. The impact of variable-speed drives on the grid current spectrum (drive input currents) when using a diode rectifier as a front-end converter is addressed in [38, 74, 75]. Periodic torque oscillations can occur due to parasitic load variations (e.g. wind shadow of a wind power plant's tower), loads connected to crank shafts (e.g. reciprocating compressors) [76–78], stator faults, and rotor faults [35, 36]. The resulting oscillation of the machine's speed leads to a phase modulation of the stator currents.

Therefore, the question arises of how to incorporate the drive system into the frequency domain modeling approach. In [39], a frequency-domain model of a synchronous machine is presented, which neglects the influence of the mechanical subsystem. This results in a linear frequency domain model of the synchronous machine. The goal of the modeling approach presented in this chapter is to provide a model of the drive system in the frequency domain covering the nonlinear interaction of the machine-side VSI and the electrical machine under the influence of load torque oscillations.
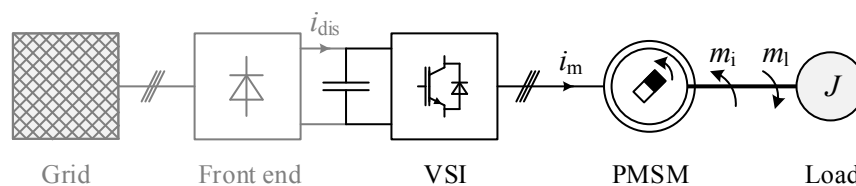

Figure 6.1: Grid-connected drive system with a diode rectifier (front end) coupled to a VSI feeding a PMSM.

This chapter is structured as follows: Section 6.1 reviews the differential equation system of the electrical machine for the example of a PMSM, provided by standard main spatial harmonic models in the literature like [79], followed by a transformation into the frequency domain. Saturation is neglected. The machine equations include a model of the mechanical subsystem with a single rotating inertia, which allows for the incorporation of mechanical load torque oscillations. The model of the VSI and its interaction with the electrical machine is developed in Section 6.2. To simplify the derivation in this chapter, the front-end converter is represented as a nonreactive current source. The VSI is assumed to be in open-loop control, thus there is no influence of the signals of the plant on the control signals. The model is developed in rotating dq coordinates and incorporates the system reaction to torque oscillations and its propagation to the dc link. Different assumptions on the strength of rotor speed oscillations and dc link voltage ripple result in the development of drive system models with various modeling depths, which are provided in Section 6.3. Finally, Section 6.4 evaluates the total equation system and compares the results to the spectra resulting from time-domain simulations and measurements.

6.1 Permanent Magnet Synchronous Machine

Figure 6.2 shows schematically a PMSM with one pole pair (number of pole pairs $p = 1$). The stator has three symmetrical phases $\nu \in \{1, 2, 3\}$ with the phase voltages $u_{\mathrm{m}\nu}$ described by

$$\begin{bmatrix} u_{\mathrm{m}1} \\ u_{\mathrm{m}2} \\ u_{\mathrm{m}3} \end{bmatrix} = R_{\mathrm{s}} \cdot \begin{bmatrix} i_{\mathrm{m}1} \\ i_{\mathrm{m}2} \\ i_{\mathrm{m}3} \end{bmatrix} + \frac{\mathrm{d}}{\mathrm{d}t} \begin{bmatrix} \psi_1 \\ \psi_2 \\ \psi_3 \end{bmatrix},$$
(6.1)

where $i_{\mathrm{m}\nu}$ are the stator phase currents and ψ_ν are the stator flux linkages. Because the skin effect and the proximity effect are neglected, the stator resistance R_{s} is assumed to be constant. The rotor is equipped with permanent magnets and rotates with an angular frequency ω_{m}. The permanent magnets generate a magnetic field that results in fluxes linked with the stator phases, which depend on the rotor position and have a constant amplitude of Ψ_{p}. The rotor position that results in the maximum flux linkage in phase 1 defines the direct axis (d-axis). This allows the mechanical rotor position to be described as an angle ε_{m} between the stator phase 1 and the d-axis (Figure 6.2). For machines with multiple pole pairs the maximum flux linkage in each phase occurs p-times during one full turn of the rotor. Thus, the electrical rotor position ε_{e} is introduced as $\varepsilon_{\mathrm{e}} = p\,\varepsilon_{\mathrm{m}}$. The electrical rotor position varies with the electrical angular frequency $\omega_{\mathrm{e}} = p\,\omega_{\mathrm{m}}$.

With the assumptions of symmetrical phases and the absence of zero sequence components, the equation system (6.1) can be simplified. The flux density of the stator phases and of the permanent magnets are symmetrically and sinusoidally distributed. The Park transformation, with the electrical rotor position as the transformation angle, enables the representation of the
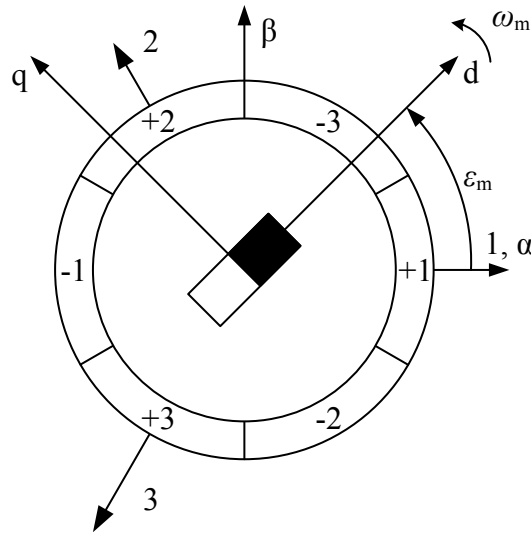
Figure 6.2: Illustration of a PMSM for $p = 1$ with different coordinate systems three-phase system: (123), stationary reference frame ($\alpha\beta$), and rotor reference frame (dq)

stator voltages in rotating dq coordinates $u_\mathrm{d}, u_\mathrm{q}$, with

$$
\begin{aligned}
u_\mathrm{d}(t) &= R_\mathrm{s} \cdot i_\mathrm{d}(t) + \frac{\mathrm{d}\psi_\mathrm{d}(t)}{\mathrm{d}t} - \omega_\mathrm{e}(t) \cdot \psi_\mathrm{q}(t), \\
u_\mathrm{q}(t) &= R_\mathrm{s} \cdot i_\mathrm{q}(t) + \frac{\mathrm{d}\psi_\mathrm{q}(t)}{\mathrm{d}t} + \omega_\mathrm{e}(t) \cdot \psi_\mathrm{d}(t).
\end{aligned}
\tag{6.2}
$$

When neglecting saturation of the machine's iron core, the flux linkages can be expressed by the product of the dq currents and constant inductances, with

$$
\begin{aligned}
\psi_\mathrm{d}(t) &= L_\mathrm{d} \cdot i_\mathrm{d}(t) + \Psi_\mathrm{p}, \\
\psi_\mathrm{q}(t) &= L_\mathrm{q} \cdot i_\mathrm{q}(t),
\end{aligned}
\tag{6.3}
$$

where L_d is the inductance in the d-axis and L_q is the inductance in the q-axis. Insertion of (6.3) into (6.2) yields the transient machine model with constant coefficients, with

$$
\begin{aligned}
u_\mathrm{d}(t) &= R_\mathrm{s} \cdot i_\mathrm{d}(t) + L_\mathrm{d} \cdot \frac{\mathrm{d}i_\mathrm{d}(t)}{\mathrm{d}t} - L_\mathrm{q} \cdot \omega_\mathrm{e}(t) \cdot i_\mathrm{q}(t), \\
u_\mathrm{q}(t) &= R_\mathrm{s} \cdot i_\mathrm{q}(t) + L_\mathrm{q} \cdot \frac{\mathrm{d}i_\mathrm{q}(t)}{\mathrm{d}t} + L_\mathrm{d} \cdot \omega_\mathrm{e}(t) \cdot i_\mathrm{d}(t) + \Psi_\mathrm{p} \cdot \omega_\mathrm{e}(t).
\end{aligned}
\tag{6.4}
$$

The following frequency-domain models are established through application of the model with constant coefficients.

The mechanical behavior is modeled with a single inertia J_m, which combines load and machine

inertia. The differential equation of the mechanical speed is described as

$$\frac{\mathrm{d}\omega_{\mathrm{m}}(t)}{\mathrm{d}t} = \frac{1}{J_{\mathrm{m}}} \cdot (m_{\mathrm{i}}(t) - m_{\mathrm{fr}}(t) - m_{\mathrm{l}}(t)), \tag{6.5}$$

with a load torque m_{l} and a speed-proportional friction torque m_{fr}, described by the friction constant K_{fr}, with

$$m_{\mathrm{fr}}(t) = K_{\mathrm{fr}} \cdot \omega_{\mathrm{m}}(t). \tag{6.6}$$

The mechanical rotor position is connected to the mechanical speed through the differential equation

$$\frac{\mathrm{d}\varepsilon_{\mathrm{m}}(t)}{\mathrm{d}t} = \omega_{\mathrm{m}}(t). \tag{6.7}$$

The machine torque can be calculated by

$$m_{\mathrm{i}}(t) = p \cdot \frac{3}{2} \cdot (\psi_{\mathrm{d}}(t) \cdot i_{\mathrm{q}}(t) - \psi_{\mathrm{q}}(t) \cdot i_{\mathrm{d}}(t)). \tag{6.8}$$

Substitution of the flux linkages with (6.3) results in

$$m_{\mathrm{i}}(t) = p \cdot \frac{3}{2} \cdot ((L_{\mathrm{d}} - L_{\mathrm{q}}) \cdot i_{\mathrm{d}}(t) \cdot i_{\mathrm{q}}(t) + \Psi_{\mathrm{p}} \cdot i_{\mathrm{q}}(t)). \tag{6.9}$$

6.1.1 Frequency-Domain Model

During stationary operation, the synchronous speed of the machine is impressed by the fundamental angular frequency of the feeding voltages $\omega_{\mathrm{e}0}$. Due to the electro-mechanical coupling the mechanical synchronous speed equals the direct component of the mechanical speed in steady state, with $\omega_{\mathrm{m}0} = \omega_{\mathrm{e}0}/p$. This fact simplifies the modeling process in the frequency domain, since $\omega_{\mathrm{m}0}$ is determined by the feeding voltages and is independent of the mechanical load.

To begin with, it is assumed that all signals can be expressed by a Fourier series with a fundamental angular frequency ω_0 and that all harmonics are integer multiples $k\omega_0, k \in \mathbb{Z}$. Transformation of the differential equations of the stator (6.4) and the differential equations of the mechanical system (6.5) and (6.7) into the vector representation of Fourier coefficients results in

$$\vec{U}_{\mathrm{d}} = \boldsymbol{Z}_{\mathrm{d}} \cdot \vec{I}_{\mathrm{d}} - L_{\mathrm{q}} \cdot \vec{\omega}_{\mathrm{e}} * \vec{I}_{\mathrm{q}}, \tag{6.10}$$

$$\vec{U}_{\mathrm{q}} = \boldsymbol{Z}_{\mathrm{q}} \cdot \vec{I}_{\mathrm{q}} + L_{\mathrm{d}} \cdot \vec{\omega}_{\mathrm{e}} * \vec{I}_{\mathrm{d}} + \Psi_{\mathrm{p}} \cdot \vec{\omega}_{\mathrm{e}}, \tag{6.11}$$

$$\boldsymbol{J}_{\mathrm{m}} \cdot \vec{\omega}_{\mathrm{m}} = p \cdot \frac{3}{2} \cdot \left((L_{\mathrm{d}} - L_{\mathrm{q}}) \cdot \vec{I}_{\mathrm{d}} * \vec{I}_{\mathrm{q}} + \Psi_{\mathrm{p}} \cdot \vec{I}_{\mathrm{q}} \right) - \vec{M}_{\mathrm{l}} - K_{\mathrm{fr}} \cdot \vec{\omega}_{\mathrm{m}}, \tag{6.12}$$

$$\boldsymbol{K} \cdot \vec{\varepsilon}_{\mathrm{m}} = \vec{\omega}_{\mathrm{m}}. \tag{6.13}$$

The frequency domain equation system contains linear impedances in d- and q-axes, described by diagonal matrices

$$\begin{aligned} \boldsymbol{Z}_{\mathrm{d}} &= \mathrm{diag}(Z_{\mathrm{d},-k_{\max}}, .., Z_{\mathrm{d},k_{\max}}), \\ \boldsymbol{Z}_{\mathrm{q}} &= \mathrm{diag}(Z_{\mathrm{q},-k_{\max}}, .., Z_{\mathrm{q},k_{\max}}), \end{aligned} \tag{6.14}$$

with the k-th elements

$$\begin{aligned} Z_{\mathrm{d},k} &= R_{\mathrm{s}} + \mathrm{j}k\omega_0 L_{\mathrm{d}}, \\ Z_{\mathrm{q},k} &= R_{\mathrm{s}} + \mathrm{j}k\omega_0 L_{\mathrm{q}}, \end{aligned} \tag{6.15}$$

and a diagonal matrix

$$\boldsymbol{J}_{\mathrm{m}} = \mathrm{diag}(J_{\mathrm{m},-k_{\max}}, .., J_{\mathrm{m},k_{\max}}), \tag{6.16}$$

with the k-th element

$$J_{\mathrm{m},k} = \mathrm{j}k\omega_0 J_{\mathrm{m}} \tag{6.17}$$

containing the inertia. The diagonal matrix $\boldsymbol{K}$ describes the differentiation in the frequency domain, with

$$\boldsymbol{K} = \mathrm{j}\omega_0 \cdot \mathrm{diag}(-k_{\max}, .., k_{\max}). \tag{6.18}$$

For the derivation it was assumed that all signals only contain harmonics that are integer multiples of ω_0. For a synchronous machine the electrical synchronous speed is inherently a multiple of the mechanical synchronous speed with the number of pole pairs as the proportionality factor $\omega_{\mathrm{e}0} = p\omega_{\mathrm{m}0}$. In general, the disturbances (the load torque m_{l} and the dc-link disturbance current i_{dis}) can introduce harmonics of the angular frequency $\omega_{\mathrm{l}0}$ and $\omega_{\mathrm{dis}0}$, which are not multiples of $\omega_{\mathrm{m}0}$. In this case, the fundamental angular frequency of the system model ω_0 is defined by the greatest common divisor

$$\omega_0 = \mathrm{gcd}(\omega_{\mathrm{m}0}, \omega_{\mathrm{l}0}, \omega_{\mathrm{dis}0}). \tag{6.19}$$

6.2 Converter Model in dq Coordinates

The previous section showed how the modeling of the PMSM in the rotor reference frame is beneficial, because it allows for the use of constant coefficients and the nonlinear behavior is reduced to a convolution of the vectors $\vec{I}_{\mathrm{d}}$, $\vec{I}_{\mathrm{q}}$, and $\vec{\omega}_{\mathrm{e}}$. However, this requires the feeding VSI to be modeled in the same reference frame as the machine. For this purpose, the VSI

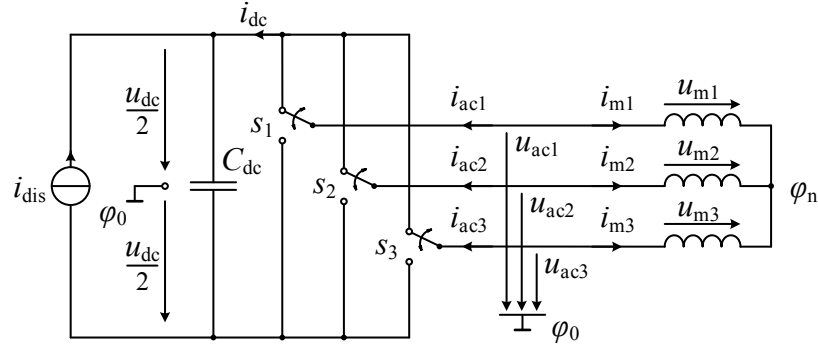**Figure 6.3:** Equivalent circuit of the drive system in 123 coordinate system

model developed in Chapter 3 is transformed into rotating dq coordinates. Figure 6.3 shows the equivalent circuit of the drive system in 123 coordinates for the definition of the variables.

At first, the switching function is expressed in $\alpha\beta$ coordinates using an amplitude-invariant Clarke transformation [see (5.9)], with

$$\begin{bmatrix} s_\alpha(t) \\ s_\beta(t) \end{bmatrix} = \frac{2}{3} \cdot \begin{bmatrix} 1 & -\frac{1}{2} & -\frac{1}{2} \\ 0 & \frac{\sqrt{3}}{2} & -\frac{\sqrt{3}}{2} \end{bmatrix} \cdot \begin{bmatrix} s_1(t) \\ s_2(t) \\ s_3(t) \end{bmatrix}. \tag{6.20}$$

Application of the Clarke transformation on both sides of the ac-side voltage equation [see (3.2)], with

$$\begin{bmatrix} u_{\mathrm{ac1}}(t) \\ u_{\mathrm{ac2}}(t) \\ u_{\mathrm{ac3}}(t) \end{bmatrix} = \begin{bmatrix} s_1(t) \\ s_2(t) \\ s_3(t) \end{bmatrix} \cdot \frac{u_{\mathrm{dc}}(t)}{2}, \tag{6.21}$$

leads to a voltage equation in $\alpha\beta$ coordinates, with

$$\begin{bmatrix} u_\alpha(t) \\ u_\beta(t) \end{bmatrix} = \begin{bmatrix} s_\alpha(t) \\ s_\beta(t) \end{bmatrix} \cdot \frac{u_{\mathrm{dc}}(t)}{2}. \tag{6.22}$$

The machine is star-connected with a floating star point voltage. Therefore, a zero-component in the ac-side voltages has no effect on the ac-side currents and the $\alpha\beta$ components of the ac-side voltages equal the $\alpha\beta$ components of the machine's phase voltages.

Secondly, a rotation [see (5.13)] with the PMSM's electrical rotor angle ε_e as the rotation angle is applied. This results in the switching function in dq coordinates, with

$$\begin{bmatrix} s_\mathrm{d}(t) \\ s_\mathrm{q}(t) \end{bmatrix} = \begin{bmatrix} \cos(\varepsilon_\mathrm{e}(t)) & \sin(\varepsilon_\mathrm{e}(t)) \\ -\sin(\varepsilon_\mathrm{e}(t)) & \cos(\varepsilon_\mathrm{e}(t)) \end{bmatrix} \cdot \begin{bmatrix} s_\alpha(t) \\ s_\beta(t) \end{bmatrix}, \tag{6.23}$$

and the voltage equation can be rewritten as

$$\left[\begin{array}{c} u_{\mathrm{d}}(t) \\ u_{\mathrm{q}}(t) \end{array}\right] = \left[\begin{array}{c} s_{\mathrm{d}}(t) \\ s_{\mathrm{q}}(t) \end{array}\right] \cdot \frac{u_{\mathrm{dc}}(t)}{2}. \tag{6.24}$$

Similarly, the machine currents $i_{\mathrm{m}\nu}$ are transformed into dq coordinates $i_{\mathrm{d}}, i_{\mathrm{q}}$. The dc-side current can then be expressed as a function of the phase currents and the switching functions in dq coordinates as

$$i_{\mathrm{dc}}(t) = -\frac{3}{2} \cdot \frac{1}{2} \cdot (s_{\mathrm{d}}(t) \cdot i_{\mathrm{d}}(t) + s_{\mathrm{q}}(t) \cdot i_{\mathrm{q}}(t)), \tag{6.25}$$

where the factor $3/2$ is introduced due to the fact that the amplitude-invariant Clarke transformation is applied. Finally, (6.24) and (6.25) can be expressed in the vector representation of Fourier coefficients, with

$$\vec{U}_{\mathrm{d}} = \frac{1}{2} \cdot \vec{S}_{\mathrm{d}} * \vec{U}_{\mathrm{dc}}, \tag{6.26}$$

$$\vec{U}_{\mathrm{q}} = \frac{1}{2} \cdot \vec{S}_{\mathrm{q}} * \vec{U}_{\mathrm{dc}}, \tag{6.27}$$

$$\vec{I}_{\mathrm{dc}} = -\frac{3}{4} \cdot \left(\vec{S}_{\mathrm{d}} * \vec{I}_{\mathrm{d}} + \vec{S}_{\mathrm{q}} * \vec{I}_{\mathrm{q}} \right). \tag{6.28}$$

6.3 Drive System Models

The drive system model that results from the connection of the machine model and the VSI model in dq coordinates is given in Figure 6.4. The challenge in this model results from the fact that the switching function in dq coordinates is a function of the rotor position, see (6.23). Therefore, the switching function (dq) depends on the system signals even for open-loop control and the model is nonlinear.

In this section the dq transform under the influence of oscillating rotor positions is derived, which leads to a complicated expression of the switching function spectrum. Therefore, simplified models are developed that can be used when the mechanical oscillations are small. These models of various modeling depth can then be chosen depending on the goal of the calculation, the influence of the disturbances, and the values of the parameters.

6.3.1 Park Transformation for Oscillating Rotor Positions

The rotation angle of the dq transformation contains harmonic components when the machine speed can be regarded as a periodically oscillating signal. The block diagram of the drive system in dq coordinates in Figure 6.5 illustrates the interaction of the signals. In the case of open-loop
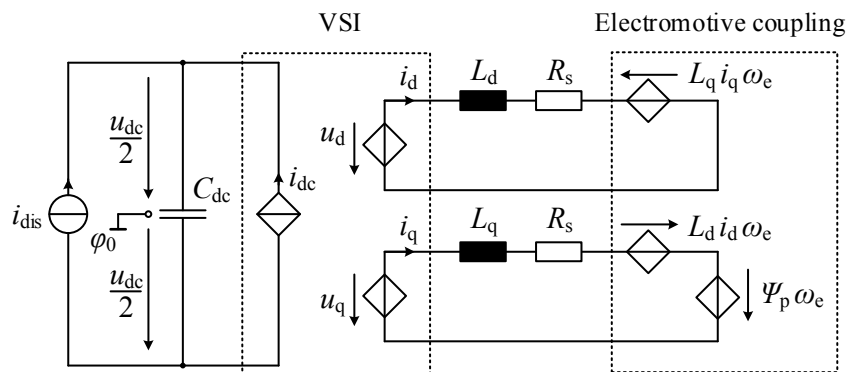
Figure 6.4: Equivalent circuit of the drive system in dq coordinates. The the diamond-shaped dependent sources in the left box are determined by the switching function in dq coordinates in (6.24) and (6.25). The electromotive coupling is described by dependent sources in the right box, representing (6.4).
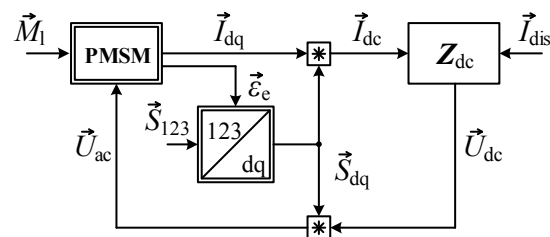

Figure 6.5: Block diagram of the drive system in dq coordinates

control, the switching function in 123 coordinates is independent of the system signals. The Park transformation leads to a dependency of the switching function in dq coordinates on the system signals. Therefore, the rotation matrix is further analyzed and a frequency domain expression is derived.

When expressing the machine's electrical angular frequency ω_e as a Fourier series, with

$$\omega_e(t) = \omega_{e0} + \sum_{\substack{k=-\infty, \\ k \neq 0}}^{\infty} \omega_{e,k} \cdot e^{jk\omega_0 t}, \tag{6.29}$$

the machine's electrical rotor angle ε_e can be calculated as its integral

$$\varepsilon_e(t) = \int \omega_e(t) dt,$$

$$= \int \left(\omega_{e0} + \sum_{\substack{k=-\infty, \\ k \neq 0}}^{\infty} \omega_{e,k} \cdot e^{jk\omega_0 t} \right) dt. \tag{6.30}$$
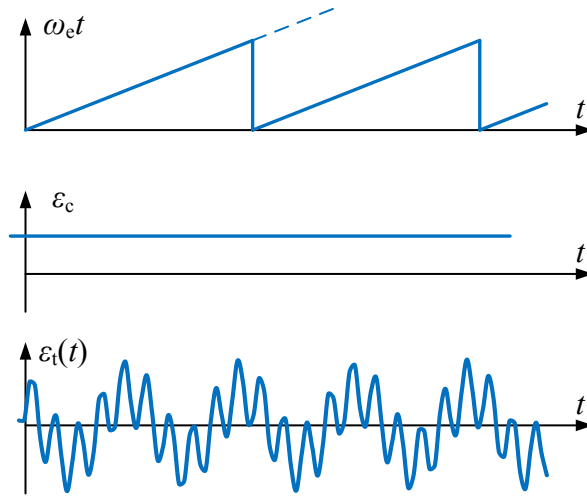
Figure 6.6: Separation of the electrical rotor angle into three parts when the rotor speed is periodically oscillating: Ramp of constant gradient ω_{e0} (top), a constant ε_c (middle), and time-dependent part ε_t (exaggerated, bottom).

The integral's solution

$$\varepsilon_e(t) = \omega_{e0}t + \varepsilon_c + \varepsilon_t(t) \tag{6.31}$$

can be divided into three components, with a ramp of constant gradient ω_{e0} as the first part, a constant second part ε_c to fulfill the initial condition, and a time-dependent third part

$$\varepsilon_t(t) = \sum_{\substack{k=-\infty, \\ k \neq 0}}^{\infty} \frac{\omega_{e,k}}{jk\omega_0} \cdot e^{jk\omega_0 t}. \tag{6.32}$$

Figure 6.6 shows the division of the electrical rotor angle ε_e into the three components. The time-dependent third part can be regarded as a Fourier series, with the complex coefficients

$$\varepsilon_{t,k} = \frac{\omega_{e,k}}{jk\omega_0}, \quad k \in \mathbb{Z}\backslash\{0\}. \tag{6.33}$$

Figure 6.7 illustrates the relationship between the rotor phase angle ε_e and the ac-side voltage in a phasor diagram. The voltage phasor and the rotor dq axes rotate with a constant angular frequency ω_{e0} that is superimposed by the harmonic components of the rotor speed. The position of the voltage phasor in reference to the d axis has a mean value that defines the constant component ε_c. Thus, the initial value of the electrical rotor position results in

$$\varepsilon_e(t=0) = \omega_{e0} \cdot 0 + \varepsilon_c + \varepsilon_t(t=0)$$
$$= \varepsilon_c + \sum_{\substack{k=-\infty, \\ k \neq 0}}^{\infty} \varepsilon_{t,k}. \tag{6.34}$$
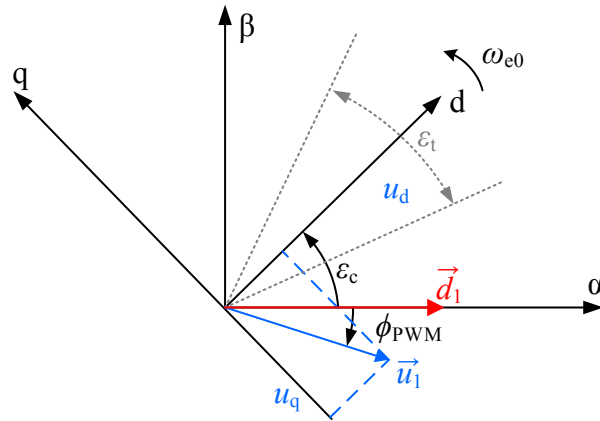
Figure 6.7: Phasor diagram of the stator voltage in the rotating reference frame

Using the partitioning in (6.31), the expression of the rotation matrix in (6.23) can be expressed as three individual rotation matrices. The first component leads to a rotation with a constant angular frequency w_0, with

$$
\begin{bmatrix} s'_{\mathrm{d}}(t) \\ s'_{\mathrm{q}}(t) \end{bmatrix} := \begin{bmatrix} \cos(w_0 t) & \sin(w_0 t) \\ -\sin(w_0 t) & \cos(w_0 t) \end{bmatrix} \cdot \begin{bmatrix} s_{\alpha}(t) \\ s_{\beta}(t) \end{bmatrix}.
\tag{6.35}
$$

With the requirement that the electrical radiant frequency be an integer multiple of the fundamental radiant frequency, $\omega_0 = n\omega_{\mathrm{e}0}, n \in \mathbb{N}$, the rotation is expressed by a shift of $\pm n$ harmonic orders in the frequency domain [see (5.17)]. This results in

$$
\begin{bmatrix} S'_{\mathrm{d},k} \\ S'_{\mathrm{q},k} \end{bmatrix} = \frac{1}{2} \cdot \begin{bmatrix} 1 & -\mathrm{j} \\ \mathrm{j} & 1 \end{bmatrix} \cdot \begin{bmatrix} S_{\alpha,(k-n)} \\ S_{\beta,(k-n)} \end{bmatrix} + \frac{1}{2} \cdot \begin{bmatrix} 1 & \mathrm{j} \\ -\mathrm{j} & 1 \end{bmatrix} \cdot \begin{bmatrix} S_{\alpha,(k+n)} \\ S_{\beta,(k+n)} \end{bmatrix}.
\tag{6.36}
$$

The constant part ε_{c} leads to a constant rotation of the switching function of

$$
\begin{bmatrix} s''_{\mathrm{d}}(t) \\ s''_{\mathrm{q}}(t) \end{bmatrix} = \begin{bmatrix} \cos(\varepsilon_{\mathrm{c}}) & \sin(\varepsilon_{\mathrm{c}}) \\ -\sin(\varepsilon_{\mathrm{c}}) & \cos(\varepsilon_{\mathrm{c}}) \end{bmatrix} \cdot \begin{bmatrix} s'_{\mathrm{d}}(t) \\ s'_{\mathrm{q}}(t) \end{bmatrix}.
\tag{6.37}
$$

In the frequency domain, the rotation is a simple matrix multiplication with the coefficients, with

$$
\begin{bmatrix} S''_{\mathrm{d},k} \\ S''_{\mathrm{q},k} \end{bmatrix} := \begin{bmatrix} \cos(\varepsilon_{\mathrm{c}}) & \sin(\varepsilon_{\mathrm{c}}) \\ -\sin(\varepsilon_{\mathrm{c}}) & \cos(\varepsilon_{\mathrm{c}}) \end{bmatrix} \cdot \begin{bmatrix} S'_{\mathrm{d},k} \\ S'_{\mathrm{q},k} \end{bmatrix}.
\tag{6.38}
$$

The frequency-domain expressions developed for the first two components allow the drive system to be modeled in dq coordinates when the rotor position is free of harmonic components, presented in Section 6.3.3. The rotation with the third, time-dependent part, with

$$
\underbrace{\begin{bmatrix} s_{\mathrm{d}}(t) \\ s_{\mathrm{q}}(t) \end{bmatrix}}_{\vec{s}_{\mathrm{dq}}(t)} = \underbrace{\begin{bmatrix} \cos(\varepsilon_{\mathrm{t}}(t)) & \sin(\varepsilon_{\mathrm{t}}(t)) \\ -\sin(\varepsilon_{\mathrm{t}}(t)) & \cos(\varepsilon_{\mathrm{t}}(t)) \end{bmatrix}}_{\boldsymbol{T}_{\mathrm{rot}}(\varepsilon_{\mathrm{t}}(t))} \cdot \underbrace{\begin{bmatrix} s''_{\mathrm{d}}(t) \\ s''_{\mathrm{q}}(t) \end{bmatrix}}_{\vec{s}''_{\mathrm{dq}}(t)},
\tag{6.39}
$$

allows for the incorporation of the oscillating rotor position. Its expression in the frequency domain requires a deeper investigation, which is conducted for a single-frequency oscillation first. Afterwards, an extension to multiple-frequency oscillations is presented.

Rotation Matrix for Harmonic Rotation Angles Containing a Single Frequency

Assuming $\varepsilon_t(t)$ is a sinusoidal function with $\varepsilon_t(t) = \hat{\varepsilon}_{,h} \cdot \cos(h\omega_0 t + \theta_{\varepsilon,h}), h \in \mathbb{N}$, the elements of the rotation matrix $\boldsymbol{T}_{\text{rot}}(\varepsilon_t(t))$ can be expressed as a Bessel series using the Jacobi-Anger expansion [12], with

$$\cos(\varepsilon_t(t)) = J_0(\hat{\varepsilon}_{,h}) + 2 \sum_{m=1}^{\infty} \cos(m \cdot \frac{\pi}{2}) \cdot J_m(\hat{\varepsilon}_{,h}) \cdot \cos(m \cdot (h\omega_0 t + \theta_{\varepsilon,h})), \tag{6.40}$$

$$\sin(\varepsilon_t(t)) = 2 \sum_{m=1}^{\infty} \sin(m \cdot \frac{\pi}{2}) \cdot J_m(\hat{\varepsilon}_{,h}) \cdot \cos(m \cdot (h\omega_0 t + \theta_{\varepsilon,h})). \tag{6.41}$$

In turn, (6.40) and (6.41) can be regarded as Fourier series, with the complex coefficients

$$F_{\cos,kh} = \begin{Bmatrix} J_k(\hat{\varepsilon}_{,h}) \cdot e^{jk(\theta_{\varepsilon,h}+\pi/2)} & \text{for} & k = m \cdot h; & m \text{ is even} \\ 0 & \text{otherwise} & & \end{Bmatrix}, \tag{6.42}$$

$$F_{\sin,kh} = \begin{Bmatrix} 0 & \text{otherwise} & & \\ J_k(\hat{\varepsilon}_{,h}) \cdot e^{jk(\theta_{\varepsilon,h}+\pi/2)} & \text{for} & k = m \cdot h; & m \text{ is odd} \end{Bmatrix}. \tag{6.43}$$

Following the general procedure, the Fourier coefficients are collected in vectors

$$\vec{F}_{\cos,h} = [F_{\cos,-k_{\max}h}, ..., F_{\cos,k_{\max}h}]^{\text{T}}, \tag{6.44}$$

$$\vec{F}_{\sin,h} = [F_{\sin,-k_{\max}h}, ..., F_{\sin,k_{\max}h}]^{\text{T}}. \tag{6.45}$$

Then the time-domain rotation of the switching function in (6.39) is represented by a convolution of the spectra, with

$$\vec{S}_d = \vec{F}_{\cos,h} * \vec{S}_d'' + \vec{F}_{\sin,h} * \vec{S}_q'', \tag{6.46}$$

$$\vec{S}_q = -\vec{F}_{\sin,h} * \vec{S}_d'' + \vec{F}_{\cos,h} * \vec{S}_q''. \tag{6.47}$$

Rotation Matrix for Harmonic Rotation Angles Containing Multiple Frequencies

For a time-dependent rotation angle with a finite number of $h_{\max}$ harmonics, the rotation matrix has the form $\boldsymbol{T}_{\text{rot}}\left(\sum_{h=1}^{h_{\max}} \hat{\varepsilon}_{,h} \cdot \cos(h\omega_0 t + \theta_{\varepsilon,h})\right)$. Through application of addition theorems, the total rotation matrix can be separated into individual rotation matrices for each harmonic h,

with

$$\boldsymbol{T}_{\mathrm{rot}} \left(\sum_{h=1}^{h_{\max}} \hat{\varepsilon}_{,h} \cdot \cos(h\omega_0 t + \theta_{\varepsilon,h}) \right) = \prod_{h=1}^{h_{\max}} \boldsymbol{T}_{\mathrm{rot}} \left(\hat{\varepsilon}_{,h} \cdot \cos(h\omega_0 t + \theta_{\varepsilon,h}) \right). \qquad (6.48)$$

In the frequency domain the rotation is represented by a vector of Fourier coefficients for each harmonic of $\varepsilon_{\mathrm{t}}(t)$. The switching function spectrum is calculated by extension of (6.46) and (6.47) into a recurring convolution for each harmonic h:

$$
\begin{aligned}
\vec{S}_{\mathrm{d}}^{(1)} &= \vec{F}_{\cos,1} * \vec{S}_{\mathrm{d}}'' + \vec{F}_{\sin,1} * \vec{S}_{\mathrm{q}}'', \\
\vec{S}_{\mathrm{q}}^{(1)} &= -\vec{F}_{\sin,1} * \vec{S}_{\mathrm{d}}'' + \vec{F}_{\cos,1} * \vec{S}_{\mathrm{q}}'', \\
\vec{S}_{\mathrm{d}}^{(h)} &= \vec{F}_{\cos,h} * \vec{S}_{\mathrm{d}}^{(h-1)} + \vec{F}_{\sin,h} * \vec{S}_{\mathrm{q}}^{(h-1)}, \\
\vec{S}_{\mathrm{q}}^{(h)} &= -\vec{F}_{\sin,h} * \vec{S}_{\mathrm{d}}^{(h-1)} + \vec{F}_{\cos,h} * \vec{S}_{\mathrm{q}}^{(h-1)}, \\
\vec{S}_{\mathrm{d}} &= \vec{S}_{\mathrm{d}}^{(h_{\max})}, \\
\vec{S}_{\mathrm{q}} &= \vec{S}_{\mathrm{q}}^{(h_{\max})}.
\end{aligned}
\qquad (6.49)
$$

Simplification of the Rotation Matrix Spectrum

The calculation of the Fourier coefficients of the rotating matrices and the large number of convolutions that are necessary to calculate the switching function spectrum result in a high computational effort. For this reason, a limitation of considered harmonic components is proposed.

According to (6.42) and (6.43), the amplitudes of the coefficients are determined by the Bessel function. For most applications it can be assumed that the speed oscillations have a relative amplitude $\hat{\omega}_{,h}/\omega_0$ that is much smaller than 1. Moreover, the harmonics of the rotating angle are connected with the speed oscillations via an integration, which leads to a damping by $1/h$. This strengthens the assumption of $\hat{\varepsilon} << 1$. Figure 6.8 shows the Bessel function $J_m(\hat{\varepsilon})$ for the orders $m = 0, 1, 2$ and for arguments $0 < \hat{\varepsilon} < 1$. For small arguments, the dc component J_0 approximates 1 and the magnitude reduces rapidly with higher orders, indicating that high order coefficients can be neglected.

This fact is illustrated in Figure 6.9, where the coefficients of the rotating matrix are depicted for speed oscillations with 5 % magnitudes in reference to the dc component, i.e. $\hat{\omega}_{,h}/\omega_0 = 0.05$. The coefficients of $F_{\cos}$ and $F_{\sin}$ are marked as blue and red crosses, respectively. The top graph shows the results for the first speed harmonic $h = 1$ illustrating that the coefficients of $F_{\cos}$ are present at even harmonics and dc, and the coefficients of $F_{\sin}$ are present at odd harmonics. The middle graph shows the results for the second speed harmonic $h = 2$, where the coefficients are damped by $1/h$ and the pattern is widened by $h \cdot k$. The convolution of both rotating matrices is depicted in the bottom graph.
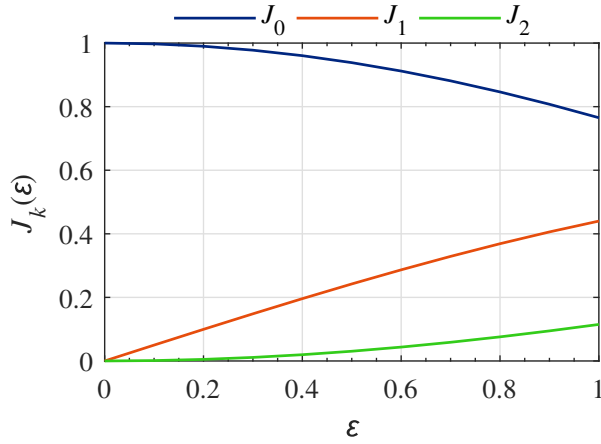
Figure 6.8: Bessel function for orders $k = 0, 1, 2$ and arguments $0 < \hat{\varepsilon} < 1$
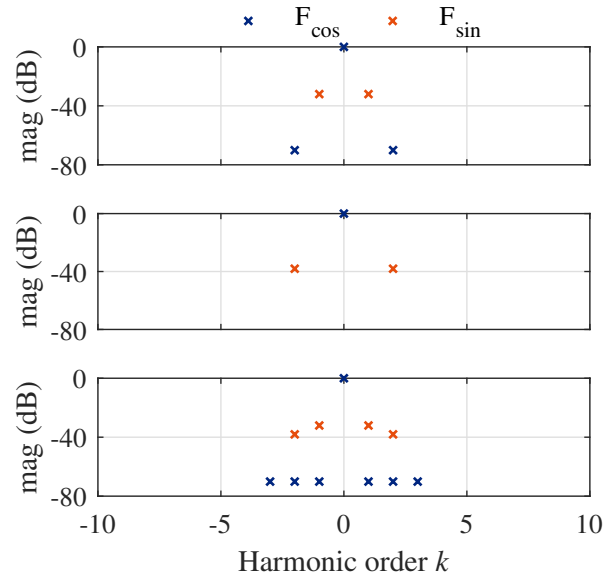
Figure 6.9: Fourier coefficients of the rotating matrix for $h = 1$ (top), $h = 2$ (middle), and their convolution (bottom)

In conclusion, it is proposed that the influence of speed harmonics can be neglected when the ratio of the speed oscillation's magnitude and its angular frequency $\hat{\omega}_{,h}/(h \cdot \omega_0)$ are below a specified limit. This limit is chosen in the numerical evaluations to 10^{-4}.

6.3.2 Fundamental-Frequency Model

A fundamental-frequency model of the drive system provides the initial values for the solution of the following multiple-frequency models. For this purpose, the frequency-domain equations of the PMSM (6.10)-(6.12) are evaluated for the dc component denoted with a '0' subscript, resulting in

$$U_{\mathrm{d0}} = -L_{\mathrm{q}} \cdot \omega_{\mathrm{e0}} \cdot I_{\mathrm{q0}} + R_{\mathrm{s}} \cdot I_{\mathrm{d0}}, \tag{6.50}$$

$$U_{\mathrm{q0}} = \quad L_{\mathrm{d}} \cdot \omega_{\mathrm{e0}} \cdot I_{\mathrm{d0}} + R_{\mathrm{s}} \cdot I_{\mathrm{q0}} + \Psi_{\mathrm{p}} \cdot \omega_{\mathrm{e0}}, \tag{6.51}$$

$$0 = p \cdot \frac{3}{2} \cdot ((L_{\mathrm{d}} - L_{\mathrm{q}}) \cdot I_{\mathrm{d0}} \cdot I_{\mathrm{q0}} + \Psi_{\mathrm{p}} \cdot I_{\mathrm{q0}}) - M_{\mathrm{L0}} - K_{\mathrm{fr}} \cdot \omega_{\mathrm{m0}}. \tag{6.52}$$

The magnitude of the VSI voltage

$$U_{\mathrm{d0}}^2 + U_{\mathrm{q0}}^2 = \left(M \cdot \frac{U_{\mathrm{dc0}}}{2} \right)^2 \tag{6.53}$$

is determined by the modulation index M and the dc-link voltage.

The four equations (6.50) - (6.53) form a nonlinear equation system, which can be solved for the four variables I_{d0}, I_{q0}, U_{d0}, and U_{q0} using, for example, the *trust-region algorithm*.

The fundamental frequency model also provides information about the relationship between the stator voltages and the electrical rotor position. For an analysis of this relationship, we revisit the phasor diagram depicted in Figure 6.7, which shows the voltage phasor and the corresponding dq components for a given rotor position. The constant component of the electrical rotor position ε_c is an angle in relation to the phasor of the ac-side voltage, with

$$\varepsilon_\mathrm{c} = -\phi_\mathrm{PWM} - \mathrm{atan}(\frac{U_{q0}}{U_{d0}}), \tag{6.54}$$

$$\phi_\mathrm{PWM} = \frac{\omega_{e0}}{2 \cdot f_\mathrm{c}}. \tag{6.55}$$

6.3.3 Model with Constant Machine Speed

If the harmonic speed components are low in the sense of a given application, a constant machine speed can be assumed and a simplification of the mathematical model is possible. Because of the constant speed, the switching function is independent of the system signals and $\vec{S}_\mathrm{dq} = \vec{S}''_\mathrm{dq}$ can be evaluated in (6.38) using the constant part of the rotor position as the rotating angle, calculated in (6.54).

With the assumption of a constant dc-link voltage U_{dc0}, the dq voltages in (6.26)-(6.27) are independent of the other system variables and can be evaluated a priori. Thus, the analytical model is described by (6.10) and (6.11), resulting in a linear equation system

$$\underbrace{\begin{bmatrix} \boldsymbol{Z}_\mathrm{d} & -L_\mathrm{q}\omega_0\boldsymbol{E} \\ L_\mathrm{d}\omega_0\boldsymbol{E} & \boldsymbol{Z}_\mathrm{q} \end{bmatrix}}_{\boldsymbol{A}} \cdot \underbrace{\begin{bmatrix} \vec{I}_\mathrm{d} \\ \vec{I}_\mathrm{q} \end{bmatrix}}_{\vec{X}} = \underbrace{\begin{bmatrix} \vec{U}_\mathrm{d} \\ \vec{U}_\mathrm{q} - \Psi_\mathrm{p}\omega_0\vec{k}_0 \end{bmatrix}}_{\vec{B}}, \tag{6.56}$$

where $\vec{k}_0$ represents a vector of length l. All elements of this vector are zero, with the exception of the centered element, which has a value of one, representing an existing dc component.

The execution of the frequency-domain model is explained in Figure 6.10 a) with a program flow chart. At first, the nonlinear fundamental frequency model is solved iteratively. Afterwards, the constant part of the rotor position is calculated, which is used to transform the switching function spectrum into dq coordinates. Because harmonic components in the rotor speed are neglected, the remaining equation system is linear and the *mldivide* function is applied for the solution in *Matlab*.
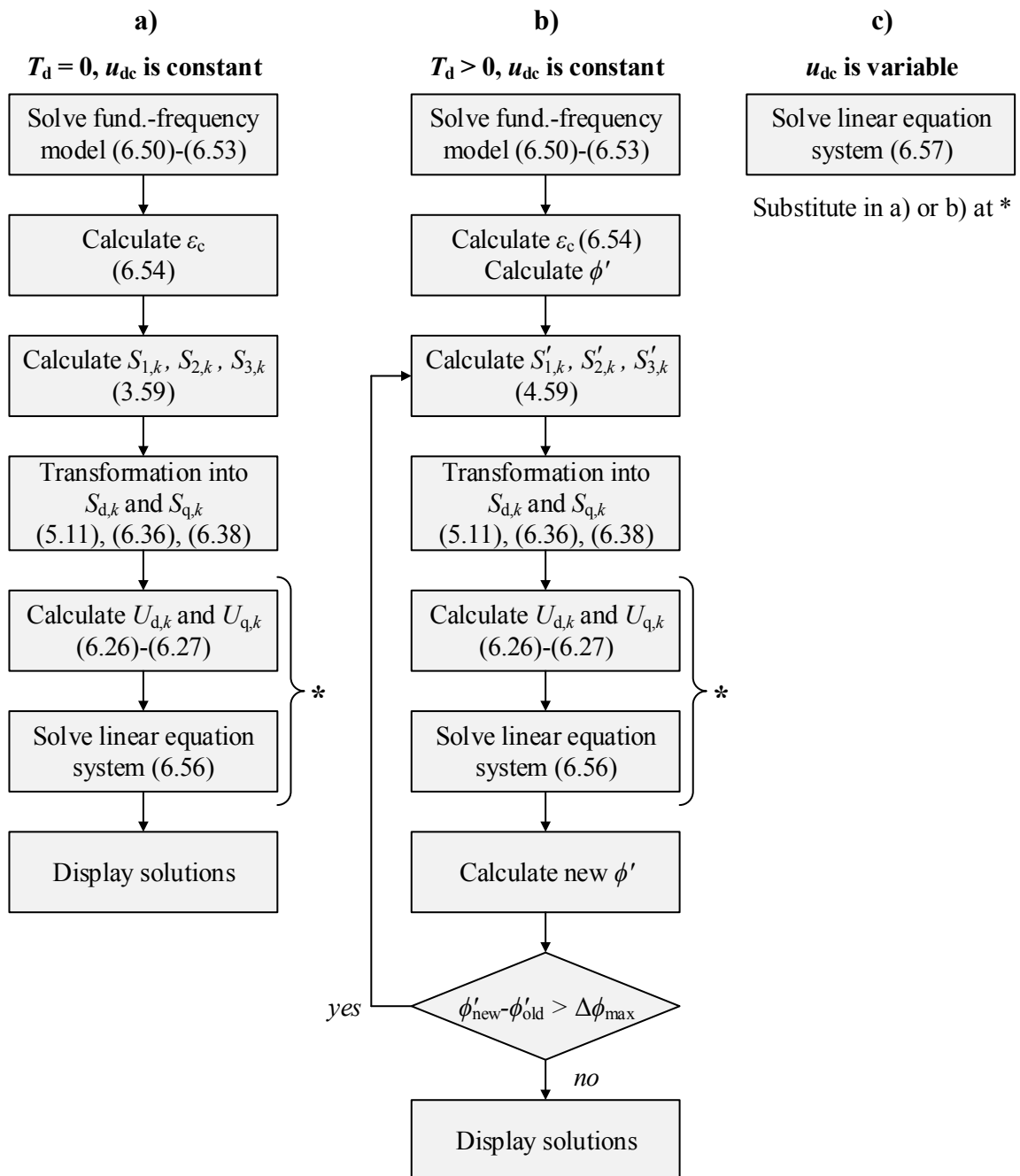
Figure 6.10: Program flow for model with constant machine speed with consideration of different effects:
    a) Without interlock times ($T_\mathrm{d} = 0$) and with a constant dc-link voltage
    b) With interlock times ($T_\mathrm{d} > 0$) and with a constant dc-link voltage
    c) For variable dc-link voltages, substitute the blocks in subfigure a) and b) that are marked with *.

Influence of Interlock Times

To consider interlock times in the model, the program flow in Figure 6.10 b) is executed. As introduced in Chapter 4, an iterative solution process is required to re-calculate the switching function spectrum, which depends on the zero-crossing of the phase currents. The phase angle ϕ' is recalculated from the ac-side currents in each step of the iteration. Using (4.59), the switching function is then calculated as a function of ϕ'.

Influence of Variable DC-Link Voltage

To take a variable dc-link voltage into account, the equation system in (6.56) is extended with (6.26)-(6.28), describing the interaction of the dc-side signals and the ac-side signals in dq coordinates. The equation covering the influence of the dc-link capacitance was previously introduced in (3.81). The equation system results in

$$\underbrace{\begin{bmatrix} \boldsymbol{Z}_\mathrm{d} & -L_\mathrm{q}\omega_\mathrm{e0}\boldsymbol{E} & -\frac{1}{2}\boldsymbol{C}(\vec{S}_\mathrm{d}) & \boldsymbol{0} \\ L_\mathrm{d}\omega_\mathrm{e0}\boldsymbol{E} & \boldsymbol{Z}_\mathrm{q} & -\frac{1}{2}\boldsymbol{C}(\vec{S}_\mathrm{q}) & \boldsymbol{0} \\ \boldsymbol{0} & \boldsymbol{0} & \boldsymbol{E} & -\boldsymbol{Z}_\mathrm{dc} \\ -\frac{3}{4}\boldsymbol{C}(\vec{S}_\mathrm{d}) & -\frac{3}{4}\boldsymbol{C}(\vec{S}_\mathrm{q}) & \boldsymbol{0} & \boldsymbol{E} \end{bmatrix}}_{\boldsymbol{A}} \cdot \underbrace{\begin{bmatrix} \vec{I}_\mathrm{d} \\ \vec{I}_\mathrm{q} \\ \vec{U}_\mathrm{dc} \\ \vec{I}_\mathrm{dc} \end{bmatrix}}_{\vec{X}} = \underbrace{\begin{bmatrix} \vec{0} \\ -\Psi_\mathrm{p}\omega_\mathrm{e0}\vec{k}_0 \\ \boldsymbol{Z}_\mathrm{dc}\cdot\vec{I}_\mathrm{dis} \\ \vec{0} \end{bmatrix}}_{\vec{B}} . \tag{6.57}$$

Elimination of variables can be performed to create a smaller equation system, as shown in Chapter 3. This step is excluded here, for the sake of brevity. The consideration of a variable dc-link voltage can be used with or without the consideration of interlock times, as indicated in Figure 6.10 c).

6.3.4 Model with Variable Machine Speed

The program flow chart for the model with variable machine speed is given in Figure 6.11. The beginning of the program is the same as for constant machine speed [Figure 6.10 a)]. First, the fundamental frequency model is solved and the constant part of the rotor angle ε_c is used to calculate the switching function in dq coordinates without oscillatory speed components $S''_{\mathrm{d},k}$ and $S''_{\mathrm{q},k}$. In contrast to the model with constant speed, the calculation of the switching function in dq coordinates considering oscillatory speed components ($S_{\mathrm{d},k}$ and $S_{\mathrm{q},k}$) is required. This is performed as a part of the nonlinear equation system that is solved in the following step. The second difference is the consideration of the mechanical equations (6.12) and (6.13). The equation system is solved using the *trust-region algorithm*.
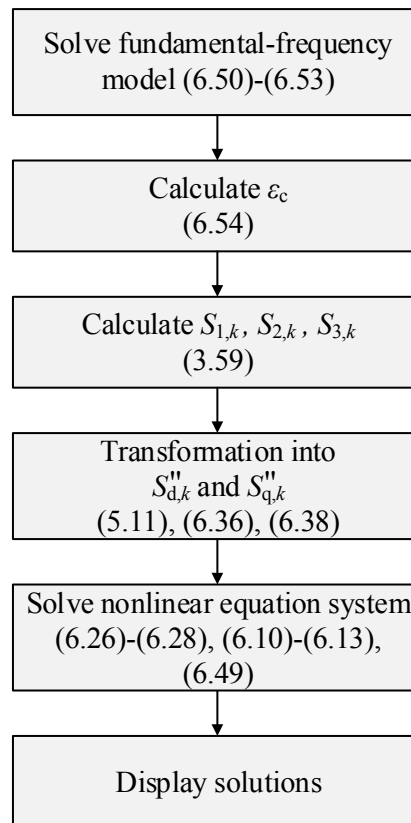
Figure 6.11: Program flow for model with variable machine speed.

6.4 Numerical Evaluation

The frequency-domain models of a drive system presented in this work are numerically evaluated and compared to time-domain simulations and measurement results. The general parameters of the electrical machine are summarized in Table 6.1.

6.4.1 Model with Constant Speed

First, the models with constant speed are evaluated. To do this, the fundamental frequency model is solved for a fundamental frequency of the duty cycle of 50 Hz, which results in a mechanical frequency of 10 Hz and a machine speed of 600 rpm. AD-PWM is applied with a switching frequency of 3 kHz. The load torque is set to $M_{\mathrm{L0}} = 15\,\mathrm{Nm}$. The constant part of the dc-link voltage is set to $U_{\mathrm{dc0}} = 440\,\mathrm{V}$ and the modulation index is $M = 0.2$.

Application of the fundamental frequency model provides an estimation of the dc-components of the currents and voltages in dq coordinates, with $I_{\mathrm{d0}} = -2.3\,\mathrm{A}$, $I_{\mathrm{q0}} = 17.7\,\mathrm{A}$, $U_{\mathrm{d0}} =$

Table 6.1: Parameters of the PMSM

Parameter	Symbol	Value
Pole pairs	p	5
Stator line resistance (dc)	R_s	$111\,\mathrm{m\Omega}$
Inductance d-axis (unsaturated)	L_d	$1.23\,\mathrm{mH}$
Inductance q-axis (unsaturated)	L_q	$2.11\,\mathrm{mH}$
PM flux linkage	Ψ_p	$0.129\,\mathrm{Vs}$
Total inertia	J_m	$0.0594\,\mathrm{kg\,m^2}$
Friction	K_fr	$40\,\mathrm{mN\,m\,/\,Hz}$

$-12.0\,\mathrm{V}$, and $U_\mathrm{q0} = 42.3\,\mathrm{V}$. Calculated from this, the constant part of the rotor position has a value of $\varepsilon_\mathrm{c} = -1.87$.

Constant dc-link voltage and negligence of interlock times

To begin with, the model with constant dc-link voltage and without interlock times is evaluated. The magnitude spectra are shown in Figure 6.12. The machine currents in dq coordinates, depicted in the top two plots, contain dc components and sideband harmonics at $f_\mathrm{sw} \pm 3 \cdot f_\mathrm{d0}$. The bottom two plots show the ac-side voltage and ac-side current spectra.

A comparison to time-domain simulations shows no differences in the results, as indicated by the deviations in Figure 6.13. The simulations are performed in *Simulink/Plecs*, where a constant speed source is connected to the rotor shaft. The simulation time is $200\,\mathrm{ms}$ and the results are sampled with $10\,\mathrm{MHz}$. Because of this, the mechanical load torque cannot be included in the system and the phase shift between the duty cycle of the VSI and the rotor position is a degree of freedom. By setting the phase shift to the value $\varepsilon_\mathrm{c} = -1.87$, both the frequency-domain model and the time-domain model are based on the same assumptions.

The dc values of the dq components result in $I_\mathrm{d0} = -2.3\,\mathrm{A}$, $I_\mathrm{q0} = 17.7\,\mathrm{A}$, $U_\mathrm{d0} = -12.0\,\mathrm{V}$, and $U_\mathrm{q0} = 42.3\,\mathrm{V}$. This confirms the previous calculation of the currents, voltages, and the constant angle of the rotor position using the fundamental frequency model.

Constant dc-link voltage and consideration of interlock times

Under the influence of interlock times, with $T_\mathrm{d} = 1\,\mathrm{\mu s}$, the frequency-domain model gives the results presented in Figure 6.14. The application of the model shows that the phase angle considering the current zero crossings has a value of $\Phi' = -0.063$. Results from time-domain simulations are included in the figure. The simulation time is $200\,\mathrm{ms}$ and the results are sampled with $100\,\mathrm{MHz}$. There are a considerable number of spectral lines that show differences between
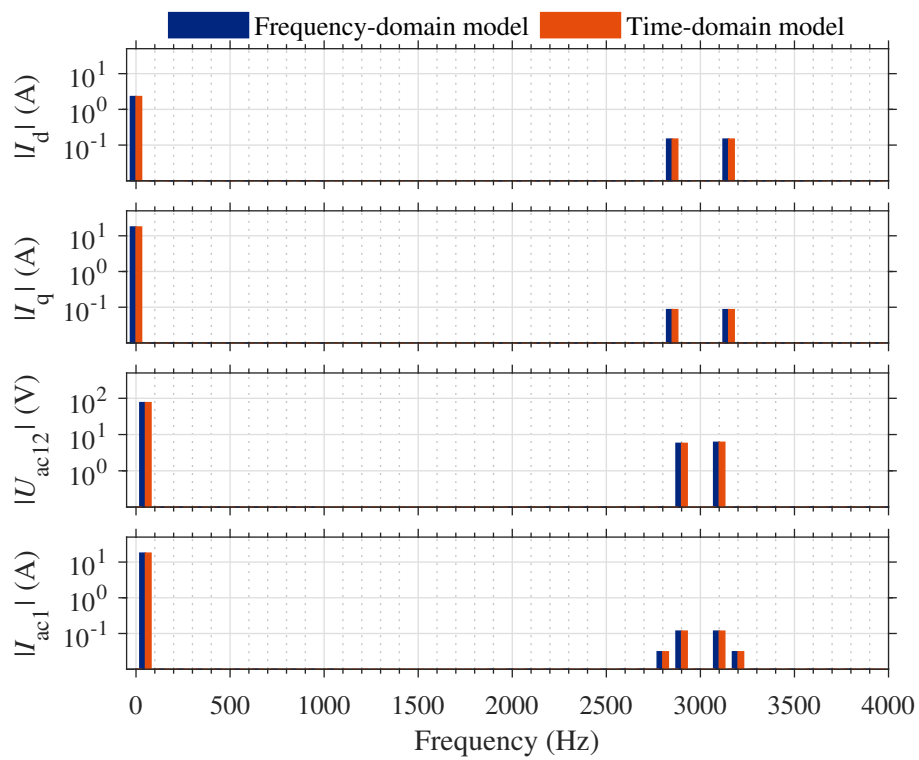
Figure 6.12: Comparison of the results for the drive system using the frequency-domain model (blue) and the time-domain model (red). The machine speed and the dc-link voltage are modeled as constant.
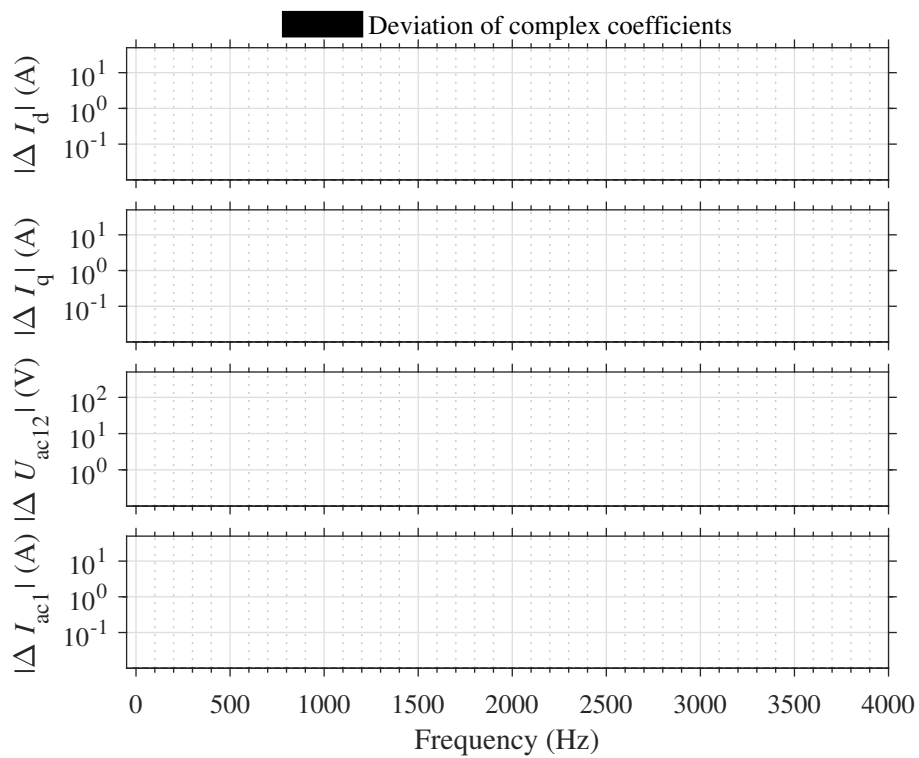

Figure 6.13: Deviation of the complex spectra shown in Figure 6.12.

the two models, as depicted in Figure 6.15. These differences include all depicted variables in the baseband and the switching sidebands.

To investigate these differences, a simulation model using the averaging method is used. The switching behavior is neglected and the power electronic devices are substituted with voltage sources. The effect of dead time is included additively by application of (4.6) to the reference voltage of the sources. The simulation time is $200\,\text{ms}$ and the results are sampled with $10\,\text{MHz}$.

The results are depicted in Figure 6.16 and the differences to the frequency-domain model are shown in Figure 6.17. As expected, the averaging model does not include the switching sideband harmonics. In the case of the line-to-line voltage spectra, there are no differences visible for the baseband harmonics between the models. The differences in the baseband components of the currents are very low. Therefore, it is likely that the differences that occur in the switched model for the line-to-line voltage spectra are due to an inaccuracy in the simulation model.

Variable dc-link voltage and negligence of interlock times

For the evaluation of the model with a variable dc-link voltage, a dc-side disturbance current introduces harmonic currents typical for a diode rectifier. The results of the time-domain model are sampled with $10\,\text{MHz}$ after a simulation time of $2\,\text{s}$. The results are shown in Figure 6.18. The differences between the frequency-domain model and the time-domain model are included in Figure 6.19.

The graphs show the line-to-line voltage spectrum and the phase current spectrum in the first and second graphs, respectively. The typical dc-link voltage spectrum under the influence of the rectifier current, as shown in the previous chapters, is depicted in the third graph. The bottom graph shows the dc-side current spectrum of the VSI. The differences between the results are lower than the chosen accuracy of the figures, which confirms the correct derivation of the equations of the drive system.

6.4.2 Model with Variable Speed

In order to confirm the correct derivation of the rotation matrix in the frequency-domain under the influence of speed harmonics, a test case with reduced models in the frequency domain and the time domain is conducted. The electrical angular frequency is the input of the models. It contains harmonics at the second and fourth harmonic of the mechanical angular frequency, as shown in Figure 6.20 in the first graph.

The value of ε_c is a degree of freedom, which is set to the same value in both models. In the time-domain model, this is accomplished by setting the initial rotor position to the value calculated
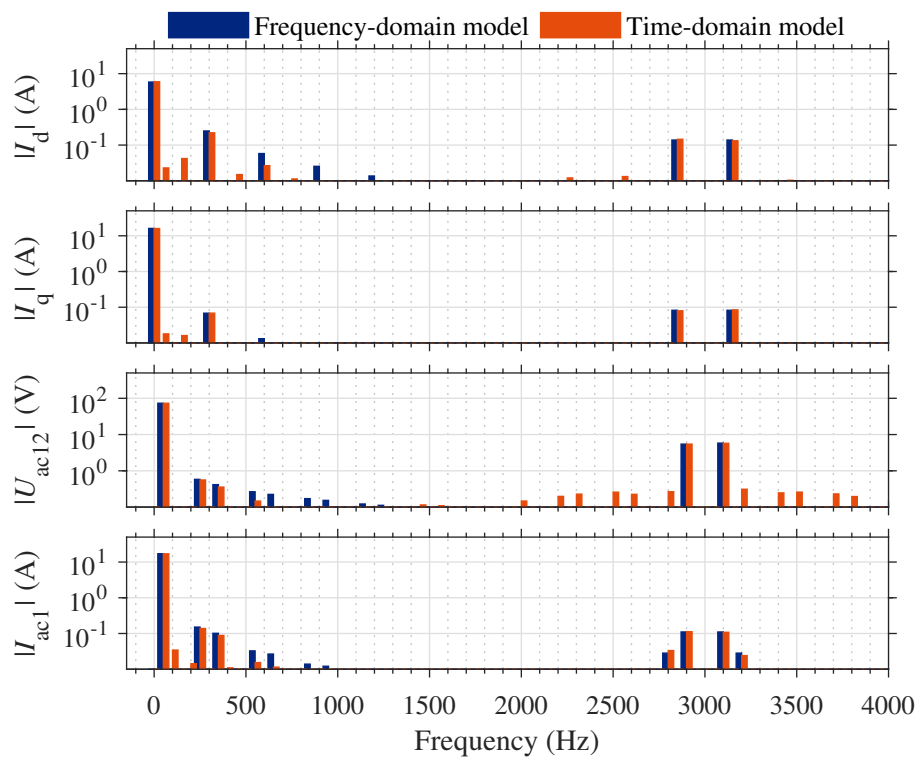
Figure 6.14: Comparison of the results for the drive system using the frequency-domain model (blue) and the switched time-domain model (red). The machine speed and the dc-link voltage are modeled as constant. An interlock time of $T_\mathrm{d} = 1\,\mu\mathrm{s}$ is considered.
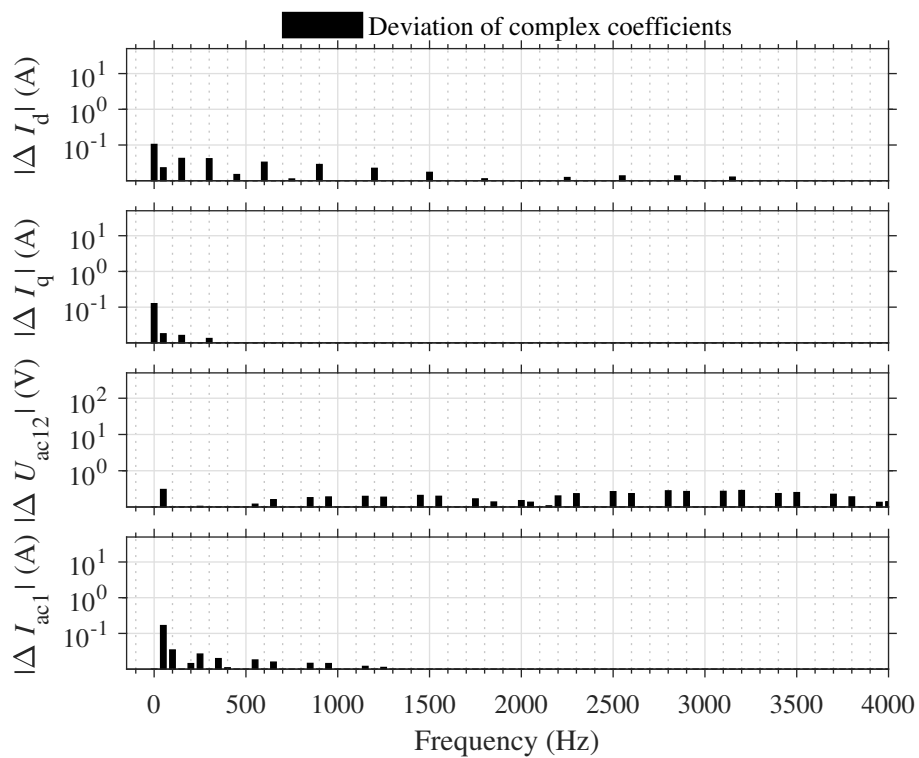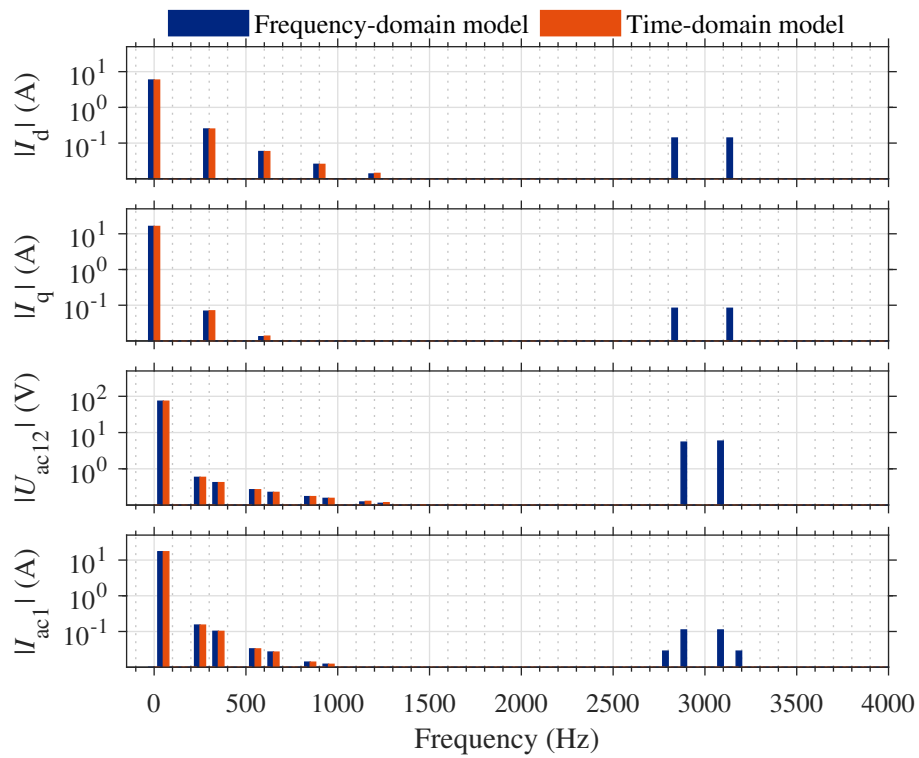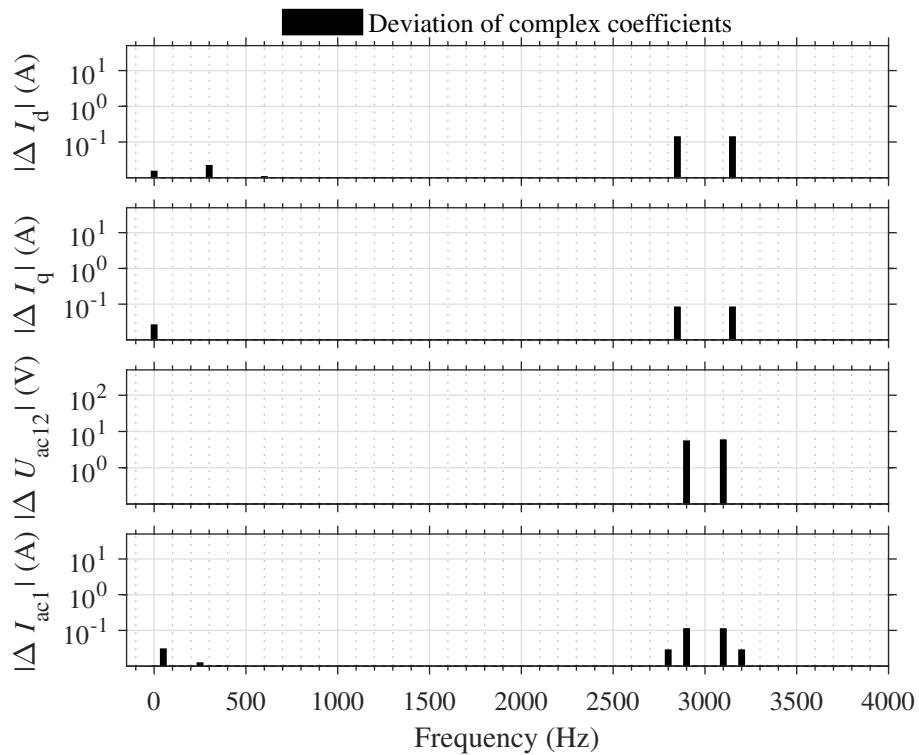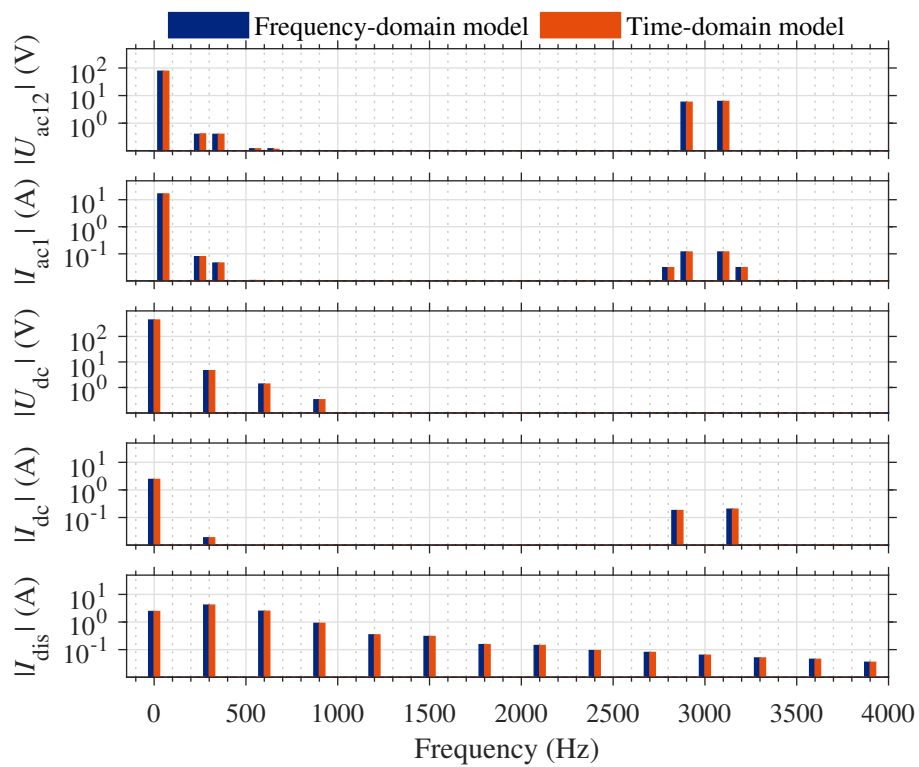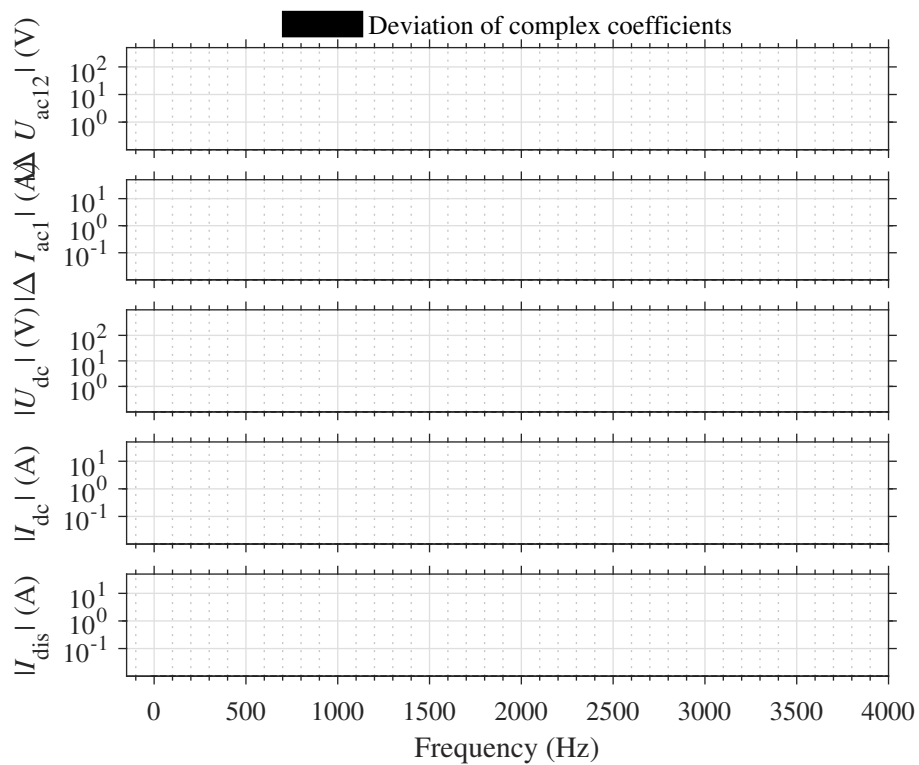

Figure 6.15: Deviation for the switched model with interlock times $T_\mathrm{d} = 1\,\mu\mathrm{s}$ in Figure 6.14

Figure 6.16: Comparison of the results for the drive system using the frequency-domain model (blue) and the averaging time-domain model (red). The machine speed and the dc-link voltage are modeled as constant. An interlock time of $T_d = 1\,\mu s$ is considered.

Figure 6.17: Deviation for the averaging model with interlock times $T_d = 1\,\mu s$ in Figure 6.16

Figure 6.18: Comparison of the results for the drive system using the frequency-domain model (blue) and the switched time-domain model (red). The machine speed is modeled as constant. The dc-link voltage is variable.

Figure 6.19: Deviation for model with variable dc-link voltage in Figure 6.18.

with (6.34).

The second and third graphs show the switching function spectra in dq coordinates under the negligence of the harmonic components in the angular frequency S_d'' and S_q''. The fourth and fifth graphs illustrate how the speed harmonics influence the switching function spectra S_d and S_q. The speed harmonic at 20 Hz is propagated to the switching function spectra. The amplitude of the harmonic at 40 Hz is too low to be visible. Any further harmonic components, as these are shown in Figure 6.9, are not visible here. Their amplitudes are too low to have a considerable impact. The differences between the spectra of the two models are negligible.

The evaluation of the complete drive system under the influence of harmonic torque yields the spectra depicted in Figure 6.21. In order to compare both models under the influence of the same input signals, the simulated load torque is used as an input signal of the frequency-domain model. The dc-link voltage is constant in both models. The influence of speed harmonics on the Park transformation is neglected in the frequency-domain model for ratios of the speed oscillation's magnitude and its angular frequency $\hat{\omega}_{,h}/(h \cdot \omega_0)$ under a value of 10^{-4}. There are no considerable differences between the results of the models.
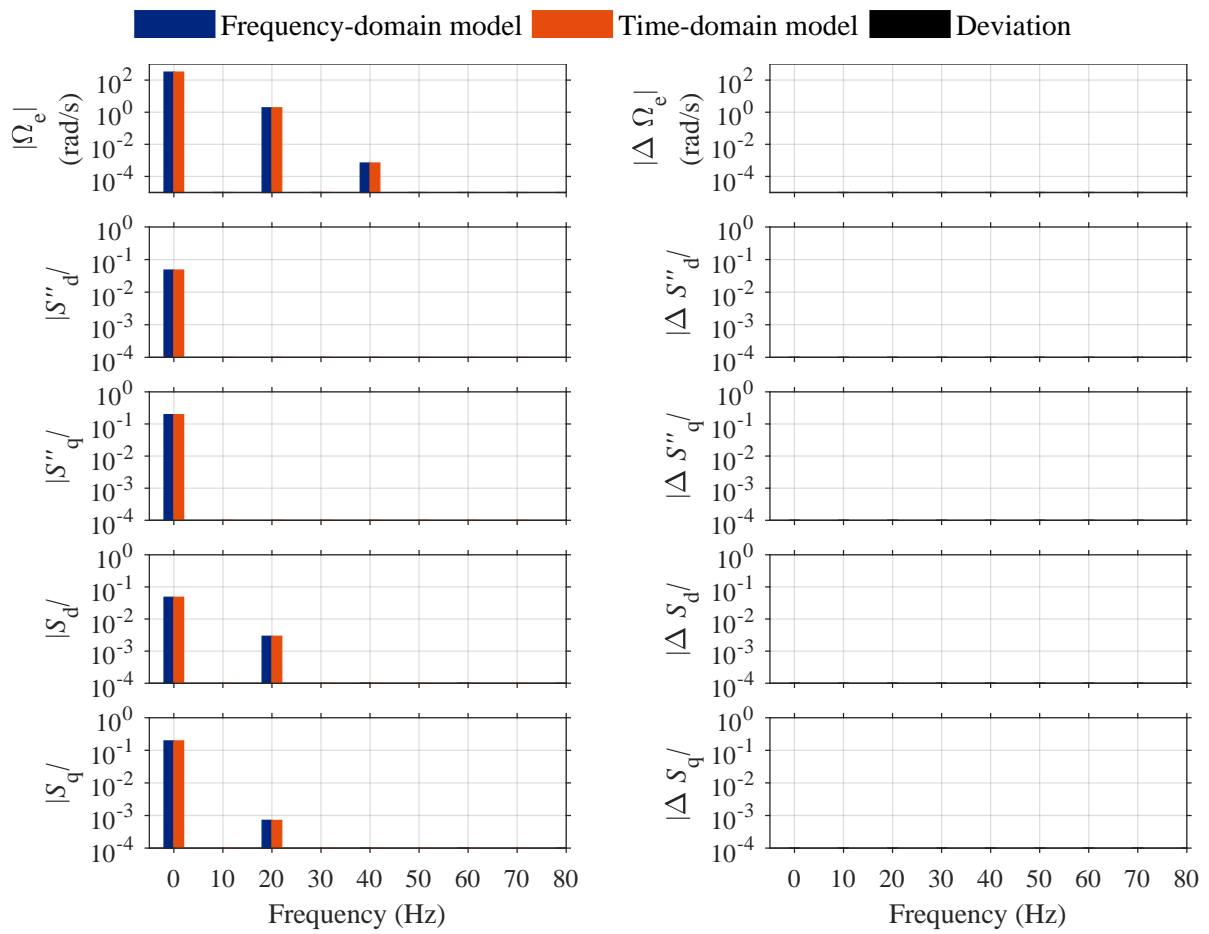
Figure 6.20: Switching function spectrum under the influence of speed harmonics. The speed is given as the same input signal in both models.
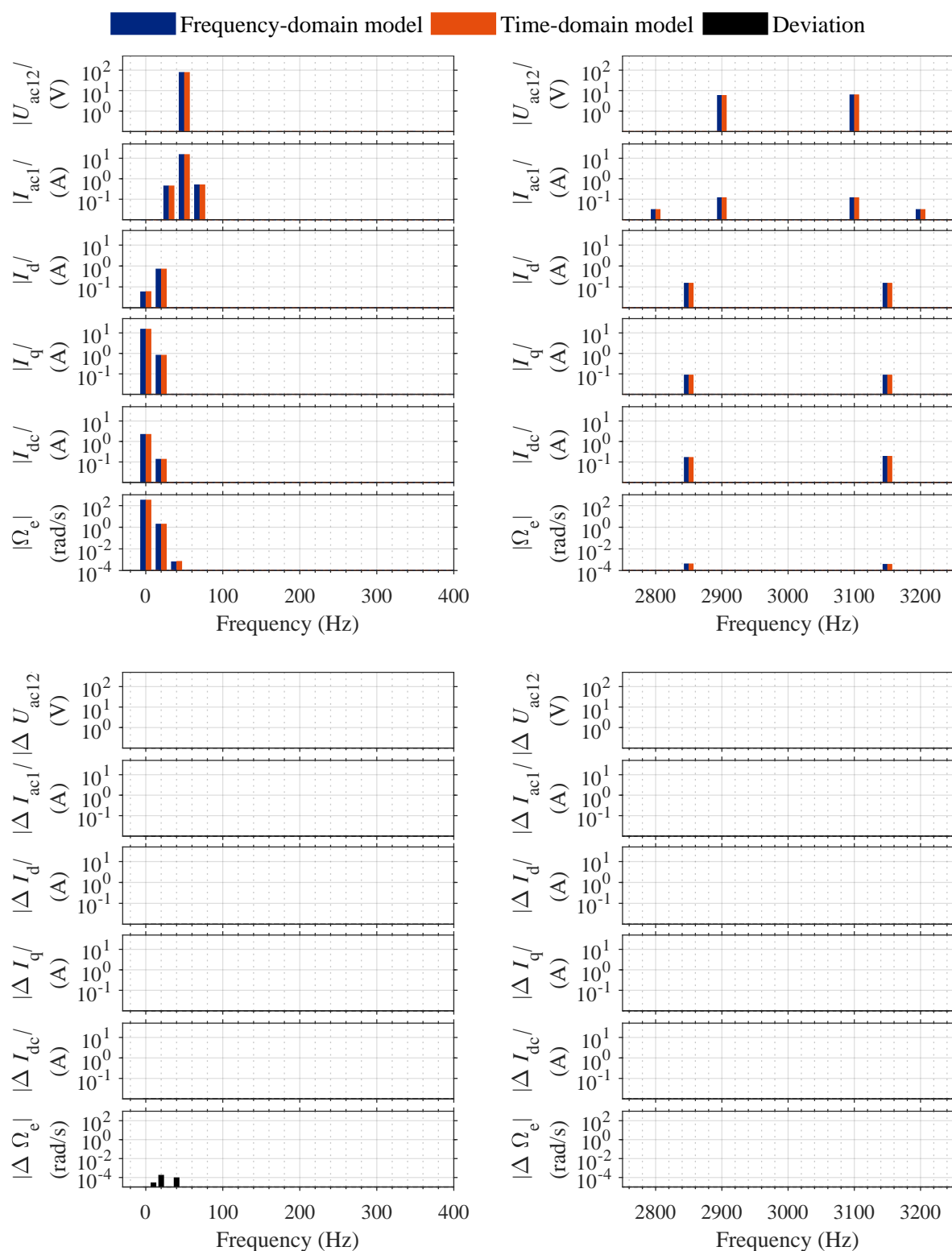
Figure 6.21: Results for the drive system model under the influence of oscillating load torque. The dc-link voltage is modeled as a constant input signal. There are no interlock times considered.

6.5 Discussion

In this chapter a model for the interaction of a VSI and a PMSM was developed in the frequency domain. The electrical machine was modeled with its main spatial harmonic behavior in the rotor reference frame (dq). The inductances and resistances of the model are considered as constant. The VSI's equation system, which was developed by using the switching function, was transformed into the same dq reference frame. The approach includes the influence of oscillating load torques on the rotor angle and as well as the reference frame rotation of the switching function. Each harmonic component leads to a rotation matrix consisting of Fourier coefficients that are described by a Jacobi-Anger expansion. The switching function in dq coordinates results in a convolution of these rotation matrices with the switching function that neglects these oscillating terms.

The excitation frequency is propagated from the load torque to the rotor speed and to the phase currents in dq coordinates. For the phase currents represented in 123 coordinates, the excitation occurs as sidebands around the fundamental frequency component. Additionally, multiples of the excitation frequency are generated. Nevertheless, these components are of much smaller amplitude and their generation can be considered a second-order effect. This fact allows for the simplification of the rotation matrix in dq coordinates, which results in a lower computational effort. The comparisons of the results from the frequency-domain and time-domain models showed very good conformity.

There is a number of nonlinear parasitic effects that are neglected in the machine model due to its underlying assumptions. The geometrical variation of the air gap due to rotor slots and the influence of the geometry of the permanent magnets leads to the generation of spatial harmonic components. In reality, the resistances and inductances depend on the frequency, due to skin effect and proximity effect. Saturation of the iron core was neglected, which simplifies the nonlinear relationship of current and flux linkage to a linear one. Moreover, saturation leads to a dependency of the effective magnetic permeance of the air gap, which introduces harmonic spatial components into the magnetic flux density [79]. A consideration of time harmonics and spatial harmonics requires a double Fourier series formulation and a detailed description of the relationships between the electrical and magnetic quantities of the machine.

7 Conclusions and Summary

Conclusions

The analysis of the VSI shows that there is a mutual dependency between the signals of the system: The ac-side quantities influence the dc-side quantities, and vice versa. The power conversion between the ac-side and the dc-side is a nonlinear process with the generation of baseband harmonics and switching sideband harmonics. It is remarkable that, despite this fact, the equation system of the VSI with open-loop control in the frequency domain is linear. This is made possible through definition of the switching function, which comprises the nonlinear PWM and power conversion processes and is independent of the system variables.

The switching function can be used even with the incorporation of dead-time effects. Nevertheless, their consideration sacrifices the linearity of the model: Under the influence of interlock times, the switching function depends on the sign of the phase current. This reaction of the system to the switching function can be reduced to the information of a single phase angle, which indicates the zero-crossing even under the influence of harmonics. However, this requires the assumption of two even zero-crossings (TEC mode), which might not be fulfilled under the influence of large harmonics.

Although the concept of the switching function is not new, its application in the analysis of PWM methods is rare. The common choice is to study the ac-side voltages, since these immediately impact the ac-side load. However, when analyzing the interaction of the ac-side and the dc-side, the definition of the switching function allows for a better understanding of the PWM and power conversion processes and the formulation of a compact equation system in the frequency domain.

In the case of a VSI with closed-loop control, the control and PWM signals depend on the signals of the physical system. A PWM model that considers multiple-frequency duty cycles is necessary to cover these interactions. Due to the nonlinearity of the PWM process, the overall equation system is nonlinear and iterative solution methods are required.

One might ask why it is important to consider the switching process and the interactions in such great detail. A motivation was found in the effects of aliasing, which can lead to an influence of the harmonics of the switching band on the baseband components due to the sampling process. The incorporation of sampling and aliasing effects was enabled in this thesis by distinguishing

continuous-time signals and discrete-time signals and their respective conversion processes. Both types of signals can be described by Fourier methods in the frequency domain, which allows for a simultaneous modeling of this hybrid system. Moreover, the importance of the correct representation of the sampling process in the PWM model should be stressed: If its input is already a discrete-time signal of correct sampling period, a model for regularly-sampled PWM would lead to faulty results, because the sampling process would be considered twice. It was demonstrated that a regularly-sampled PWM model with a continuous-time input signal can be approximated by a naturally-sampled PWM model combined with a sample-and-hold process applied to the input. In the case of a discrete-time input signal, it was preferable to apply an inverse sample-and-hold process combined with a regularly-sampled PWM model. This combination requires a lower number of considered harmonics than a naturally-sampled PWM model to acquire the same accuracy.

The influence of a PLL was neglected in this thesis. There are, however, similarities to the drive system model where oscillations can be present in the rotation angle. When these oscillations are described by harmonics, each harmonic component leads to a rotation matrix consisting of Fourier coefficients that are described by a Jacobi-Anger expansion. The switching function in dq coordinates then results in a convolution of these rotation matrices with the switching function that neglects these oscillating terms. Steps for simplification can be provided to allow for a more compact equation system. A more accurate representation of the electrical machine incorporates further nonlinear effects, such as saturation, spatial harmonics, and skin effect. These are neglected in the models presented due to the assumption of a magnetically linear machine on the basis of the fundamental spatial harmonic and of resistances independent of the frequency.

Summary

The modeling approach that was presented in this thesis proved to be a helpful tool for the calculation of steady-state spectra in VSI drives. It enables the consideration of harmonic interactions by simultaneous solution of the system equations. This stands in contrast with the prevailing unidirectional models found in the presented literature, which model the components with their input-to-output behavior, neglecting the bidirectional interactions. Multiple nonlinear effects were covered in this thesis, including the generation of switching harmonics in the PWM process, dead-time effects, the influence of feedback control, and the nonlinearity introduced by electromotive conversion.

The concept of the switching function is a center-piece of this thesis, which was adapted from the literature for describing the switching state of the converter half bridges. It was demonstrated in this thesis that dead-time effects can be incorporated into the switching function models in the frequency domain. In the case of a drive system, the switching function was transformed into the rotor reference frame. The influence of oscillatory components in the rotor angle on the coordinate transform were derived in the frequency domain, enabling modeling of the influence

of oscillating load torques on the voltages and currents of the drive system.

Applications of the presented method can be found where the interaction of the harmonic components cannot be neglected and when the base band harmonics and the switching band harmonics cannot be clearly separated. It was shown that interactions of switching-band harmonics and base-band harmonics are present when aliasing occurs.

In the case of unsynchronized inverter systems, e.g. parallel grid-tied VSI, the common method of avoiding aliasing through synchronization of PWM and sampling is not applicable between the individual VSI. The application of the presented method requires the development of a PLL model.

The nonlinear effects were analyzed individually in this thesis. A combination of effects, for example the incorporation of dead-time effects in closed-loop control, remains to be solved in future work.

For the presented method of numerical evaluation, integer ratios of the system frequencies are recommended. Although the choice of non-integer ratios does not lead to a more complicated system, the size of the equation system can become very large. A solution to this problem is strongly recommended to enhance practical applications. An enhancement of the speed of the solution process is desirable, when it comes to large numbers of considered harmonics and multiple nonlinear effects. For this, an improvement of the system description, the incorporation of an analytical Jacobian matrix, and an extensive study of solvers are recommended.

A Fourier Series

Table A.1 provides the conversion between different types of Fourier series representations.

	Fourier series	**Fourier coefficients**
a)	$x(t) = \dfrac{A_{,0}}{2} + \sum\limits_{k\in\mathbb{N}} A_{,k} \cdot \cos(k\omega_0 t)$ $+ \mathrm{j}B_{,k} \cdot \sin(k\omega_0 t)$	$\begin{aligned} A_{,k} &= \hat{X}_{,k} \cdot \cos(\theta_{x,k}) \\ &= 2 \cdot \Re\{X_{,k}\} \\ B_{,k} &= \hat{X}_{,k} \cdot \sin(\theta_{x,k}) \\ &= -2 \cdot \Im\{X_{,k}\} \end{aligned}$
b)	$x(t) = \dfrac{A_{,0}}{2} + \sum\limits_{k\in\mathbb{N}} \hat{X}_{,k} \cdot \cos(k\omega_0 t + \theta_{x,k})$	$\begin{aligned} \hat{X}_{,k} &= \sqrt{A_{,k}^2 + B_{,k}^2} \\ &= 2 \cdot \sqrt{\Re\{X_{,k}\}^2 + \Im\{X_{,k}\}^2} \\ \theta_{x,k} &= -\mathrm{atan}(\dfrac{B_{,k}}{A_{,k}}) \\ &= \mathrm{atan}(\Im\{X_{,k}\}/\Re\{X_{,k}\}) \end{aligned}$
c)	$x(t) = \sum\limits_{k\in\mathbb{Z}} X_{,k} \cdot \mathrm{e}^{\,\mathrm{j}k\omega_0 t}$	$X_{,k} = \begin{cases} \frac{1}{2}(A_{,-k} + \mathrm{j}B_{,-k}), & k < 0 \\ \frac{A_{,0}}{2}, & k = 0 \\ \frac{1}{2}(A_{,k} - \mathrm{j}B_{,k}), & k > 0 \end{cases}$ $= \begin{cases} \frac{1}{2}\hat{X}_{,-k}(\cos(\theta_{x,k}) - \mathrm{j}\sin(\theta_{x,k})), & k < 0 \\ \frac{A_{,0}}{2}, & k = 0 \\ \frac{1}{2}\hat{X}_{,k}(\cos(\theta_{x,k}) + \mathrm{j}\sin(\theta_{x,k})), & k > 0 \end{cases}$

Table A.1: Conversion of Fourier series representations using
    a) real coefficients $A_{,k}$ and $B_{,k}$,
    b) trigonometric coefficients magnitude $\hat{X}_{,k}$ and phase $\theta_{x,k}$,
    c) complex coefficients $X_{,k}$

B Experimental System

This appendix contains information about the experimental setup that was used for validation of the presented frequency-domain models. Figure B.1 shows the prototype setup of the VSI in its experimental environment.
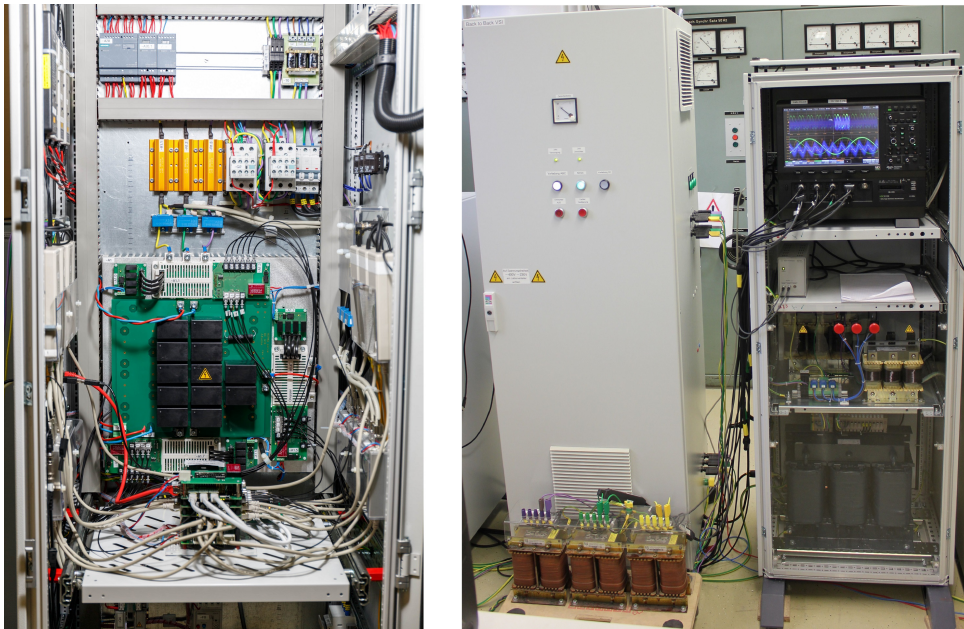

Figure B.1: The photo on the left shows the power stage of the VSI and its control unit. The photo on the right shows the closed cabinet of the power stage and a three-phase inductor in front of the cabinet. The cabinet on the right side contains an LCL filter and a transformer on the bottom, as well as the oscilloscope Teledyne Lecroy HDO8108 in the top part, which was used during the experiments.

Power stage

The power stage of the voltage-source inverter is depicted in Figure B.2. The back-to-back inverter system comprises three IGBT modules *Infineon IFS150V12PT4*. They are used as a grid-side VSI, a machine-side VSI, and an optional chopper module. The modules consist of three half-bridge modules. The minimum required interlock time and the minimum pulse width are both 1 µs.
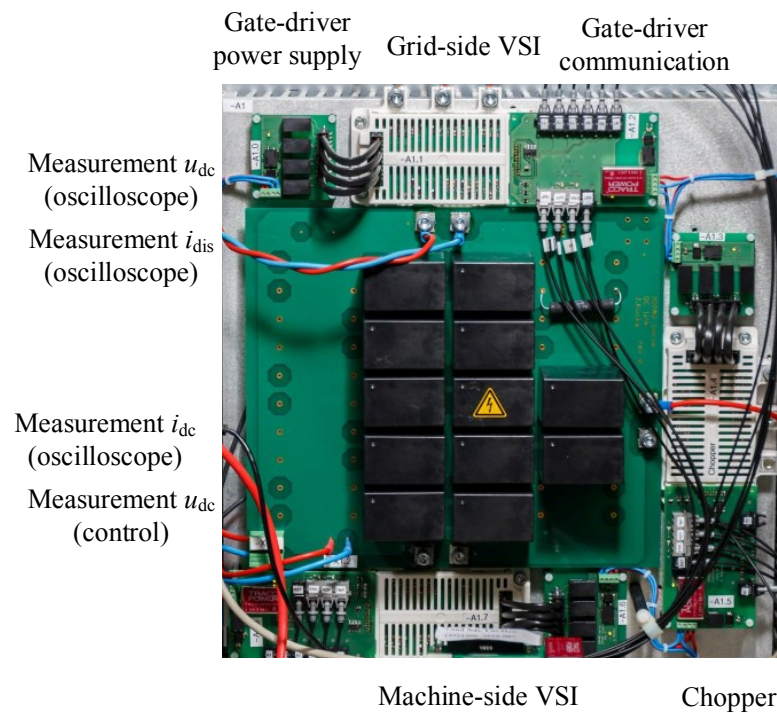
Figure B.2: Power stage of the back-to-back inverter system

Each IGBT module is equipped with a circuit board containing the optical transmitters and receivers for communication with the control system and a circuit board providing the insulated power supply of the gate drivers. The input signals of the gate drivers are generated on the FPGA unit of the control platform and transferred via optic fiber cables.

The dc link capacitance of $C_{dc} = 480\,\mu\text{F}$ is composed by a parallel connection of 12 individual film capacitors. A parallel $1\,\text{M}\Omega$ discharging resistor provides a slow discharging process.

Sensors of the control system

Current and voltage sensors are used for feedback control and synchronization with the utility grid or a grid emulation. The ac-side currents are measured by current transducers *LEM HASS 50-S*. The transducers have a 3-dB cut-off frequency of $f_{cut} = 240\,\text{kHz}$. Using an operational amplifier, the output voltage of the transducer is adapted to the required input voltage range of the ADC. The cut-off frequency of the ADC's input filter is much higher than the band-width of the current transducer and therefore negligible. Isolated $\Delta\Sigma$ modulators *Analog Devices AD7401A* are used as ADCs. They are operated at a clock frequency of $20\,\text{MHz}$ and are connected to the FPGA via RS-485 serial ports.

The ac-side voltages and the dc-link voltage are sensed by differential probes custom-made by

Protolar GmbH. Low pass filters with a cut-off frequency of 100 kHz are implemented in the probes and the same $\Delta\Sigma$ converters are used as for the current probes.

Digital control system

The control is implemented on the *Protolar ControlCube*. The hardware comprises four circuit boards, including a main board, one level of optic fiber transmitters and receivers, two boards with RS-485 ports for serial communication with the current and voltage probes, and a 24 V digital I/O interface. The key component is a system-on-chip unit *Xilinx Zynq 7000*, which is located on the main board. It contains an FPGA and an *ARM Cortex-A9* double-core processor. Via a 24 V digital IO interface, the ControlCube is connected to a programmable logic controller (PLC), which monitors basic operator clearance and operates contactors. The structure of the overall control system is depicted schematically in Figure B.3.
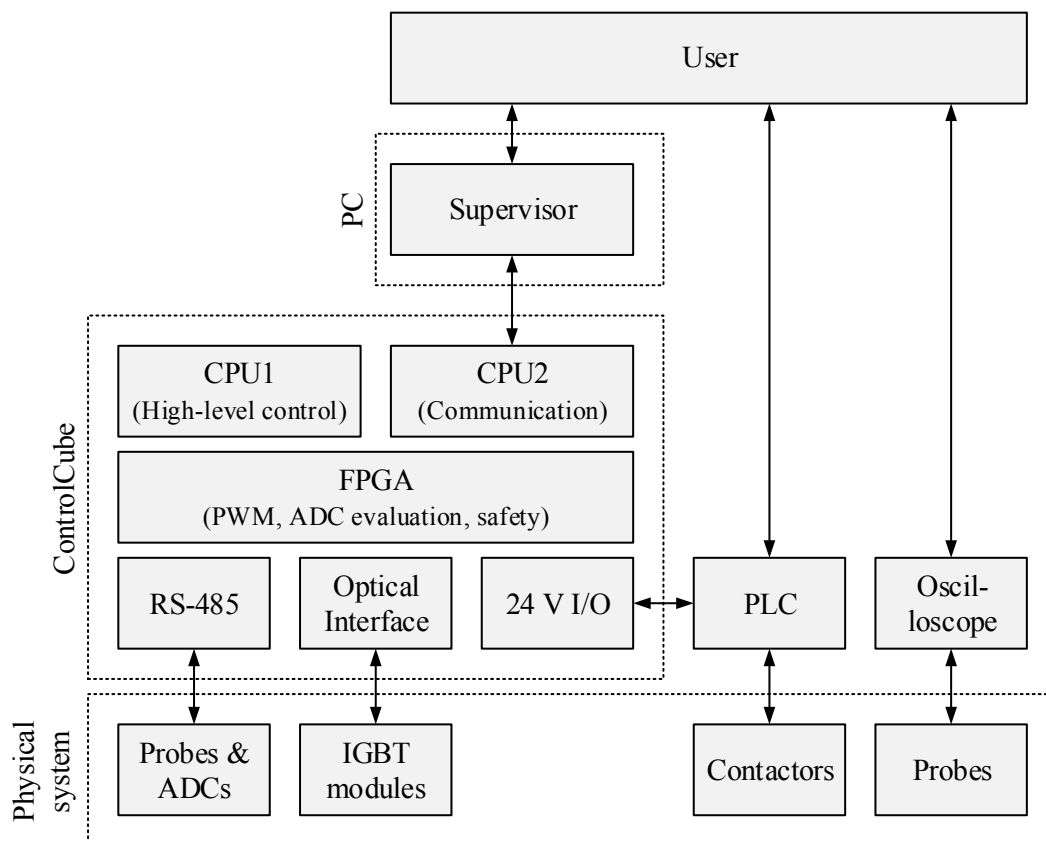

Figure B.3: Block diagram of the control structure

The FPGA incorporates the collection of measurement data from the ADCs. The digital filters (decimators) are implemented on the FPGA as Sinc3 filters or accumulate-and-dump filters. The FPGA also comprises the low-level control of the power converters, whereas the high level

control is implemented in CPU2, as an interrupt-based control algorithm written in C. The control algorithm provides a duty-cycle-equivalent sample point to the FPGA, where a counter determines the switching instant of the required duty cycle. The ControlCube is connected to a computer via Ethernet, allowing the user to observe control signals and change parameters and set-point values via the *Protolar* software *Supervisor*.

Data acquisition

The equipment used for data acquisition is independent of the measurement probes of the control system. Table B.1 lists the additional current and voltage probes used for this purpose. The table provides the -3 dB bandwidth of the probes. All high frequency cut-off frequencies are above 5 MHz, which is considered sufficiently high. All probes, except the Rogowski coils used to measure the dc-side current and the disturbance current, are specified for measuring dc signals. The Rogowski coils PEM CWT03LF have a peak current rating of 60 A and a low frequency (-3dB) bandwidth of 11 Hz. The measurement of dc currents is not inherently supported by Rogowski coils. Moreover, a considerable error is introduced into the angle information for low-frequency components, with an 18.6°(typical) phase lead at 50 Hz. Because the measurement results are used for validation of the amplitude information, the accuracy is considered sufficient for frequencies greater than 11 Hz.

The ac-side voltages are measured line-to-line between the ac-side terminals of the regarded IGBT module, assuring a low impedance coupling with the ac-side currents. Similarly, the dc-link voltage is measured between the dc-side terminals of the regarded IGBT module. Disturbance voltages are measured line-to-line at the disturbance-side terminals of the filter impedance that is inserted between the VSI and the disturbance. The gate signals of the top and bottom IGBTs of phase 1 are measured as the input signals of the gate driver, which are available as 5 V signals on the extension board containing the optic transmitters.

The data acquisition is performed on an eight channel 12 bit oscilloscope *Teledyne Lecroy HDO8108*, which is depicted on the right side of Figure B.1. A high number of 50 MS is used, which results in a sampling rate of 250 MS/s for the typically chosen acquisition window of 200 ms. Aliasing is avoided by using a 20 MHz analog input filter for the channels. Setting the acquisition height for voltage measurements to 1000 V and for current measurements to 100 A results in voltage quantization steps Q_u and current quantization steps Q_i of

$$Q_\mathrm{u} = 1000\,\mathrm{V}/2^{12} = 244\,\mathrm{mV},$$
$$Q_\mathrm{i} = 100\,\mathrm{A}/2^{12} = 24\,\mathrm{mA}.$$

The internal control signals are logged in *Supervisor* with a time-stamp protocol.

Table B.1: Current and voltage probes used for data acquistion.

Measured signal	Symbol	Probe	Bandwidth (-3 dB)
AC-side voltage	$u_{\text{ac}\nu}$	TESTEC TT-SI 9001	DC ... 25 MHz
DC-side voltage	u_{dc}	Tektronix P5200	DC ... 25 MHz
Disturbance voltage	$u_{\text{dis}\nu}$	TESTEC TT-SI 9001	DC ... 25 MHz
Bottom gate signal	g_{b}	TESTEC TT-SI 9001	DC ... 25 MHz
Top gate signal	g_{t}	TESTEC TT-SI 9001	DC ... 25 MHz
AC-side current	$i_{\text{ac}\nu}$	Agilent N2782B	DC ... 50 MHz
DC-side current	i_{dc}	PEM CWT03LF	11 Hz ... 5 MHz
Disturbance current	i_{dis}	PEM CWT03LF	11 Hz ... 5 MHz

a)   b)
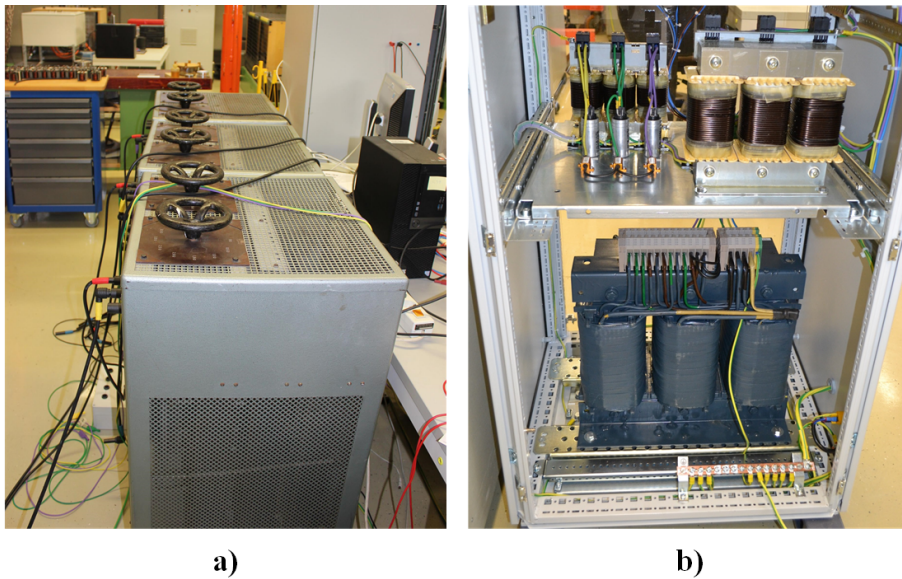
Figure B.4: Photographs of load and LCL filter: **a)** Adjustable resistors in star connection **b)** Three-phase LCL filter and isolating transformer

Loads

The VSI is loaded with three resistors in star connection [Figure B.4 a], which have a variable resistance of $0..5\,\Omega$. When using a first-order filter, the VSI is connected to the three-phase inductor placed in front of the rack in Figure B.1. It has a variable inductance of $5...20\,\text{mH}$ in $5\,\text{mH}$ steps. Alternatively, the third-order LCL filter shown in Figure B.4 b can be used. It consists of a converter-side inductor, a grid-side inductor, and shunt capacitors in series with damping resistors terminated in star connection. The grid-side inductor is connected to an isolation transformer in YNd5 connection. The transformer is modeled with its stray inductance and load-dependent losses as a series connection of an inductor and a resistor.

Bibliography

[1] M. Bierhoff and F. Fuchs, "DC-Link Harmonics of Three-Phase Voltage-Source Converters Influenced by the Pulsewidth-Modulation Strategy – An Analysis," *IEEE Transactions on Industrial Electronics*, vol. 55, no. 5, pp. 2085–2092, May 2008.

[2] B. McGrath and D. Holmes, "A General Analytical Method for Calculating Inverter DC-Link Current Harmonics," *IEEE Transactions on Industry Applications*, vol. 45, no. 5, pp. 1851–1859, Sep. 2009.

[3] R. Meyer, "Fault-Ride-Through-Regelung von Windenergieanlagen mit Vollumrichter und LCL-Netzfilter," Ph.D. dissertation, Leibniz Universität Hannover, 2014.

[4] F. Fuchs, "Converter Control for Wind Turbines when Operating inWeak Grids Containing Resonances," Ph.D. dissertation, Leibniz Universität Hannover, 2017.

[5] J. Song-Manguelle, J.-M. Nyobe-Yome, and G. Ekemb, "Pulsating Torques in PWM Multi-Megawatt Drives for Torsional Analysis of Large Shafts," *IEEE Transactions on Industry Applications*, vol. 46, no. 1, pp. 130–138, Jan. 2010.

[6] M. Odavic, M. Sumner, P. Zanchetta, and J. C. Clare, "A Theoretical Analysis of the Harmonic Content of PWM Waveforms for Multiple-Frequency Modulators," *IEEE Transactions on Power Electronics*, vol. 25, no. 1, pp. 131–141, Jan. 2010.

[7] F. Fnaiech, H. Y. Kanaan, K. Al-Haddad, S. Rahmani, F. Fnaiech, H. Y. Kanaan, K. Al-Haddad, and S. Rahmani, "A Comparative Study of Two PWM Techniques for Single-Phase Shunt Active Power Filters Employing Direct Current Control Strategy," in *2005 IEEE 36th Power Electronics Specialists Conference*, Jun. 2005, pp. 2758–2763.

[8] W. R. Bennett, "New results in the calculation of modulation products," *The Bell System Technical Journal*, vol. 12, no. 2, pp. 228–243, Apr. 1933.

[9] H. S. Black, *Modulation Theory*. Princeton, NJ: Van Nostrand, 1953.

[10] S. Bowes and B. Bird, "Novel approach to the analysis and synthesis of modulation processes in power convertors," *Proceedings of the Institution of Electrical Engineers*, vol. 122, no. 5, pp. 507–513, May 1975.

[11] G. Holmes, "A generalised approach to the modulation and control of hard switched converters," Ph.D. dissertation, Monash University, Australia, 1997.

[12] G. Holmes and T. A. Lipo, *Pulse Width Modulation for Power Converters: Principles and Practice*. Wiley-IEEE Press, 2003.

[13] F. Jenni and D. Wüst, *Steuerverfahren für Selbstgeführte Stromrichter*. vdf Hochschulverlag AG, 1995.

[14] S. M. Cox, "Voltage and current spectra for a single-phase voltage source inverter," *IMA Journal of Applied Mathematics*, vol. 74, no. 5, pp. 782–805, Oct. 2009. [Online]. Available: https://academic.oup.com/imamat/article/74/5/782/721962/ Voltage-and-current-spectra-for-a-single-phase

[15] Z. Song and D. V. Sarwate, "The frequency spectrum of pulse width modulated signals," *Signal Processing*, vol. 83, no. 10, pp. 2227–2258, Oct. 2003. [Online]. Available: http://www.sciencedirect.com/science/article/pii/S0165168403001646

[16] D. J. Kostic, Z. Z. Avramovic, and N. T. Ciric, "A New Approach to Theoretical Analysis of Harmonic Content of PWM Waveforms of Single- and Multiple-Frequency Modulators," *IEEE Transactions on Power Electronics*, vol. 28, no. 10, pp. 4557–4567, Oct. 2013.

[17] H. d. T. Mouton, B. McGrath, D. G. Holmes, and R. H. Wilkinson, "One-Dimensional Spectral Analysis of Complex PWM Waveforms Using Superposition," *IEEE Transactions on Power Electronics*, vol. 29, no. 12, pp. 6762–6778, Dec. 2014.

[18] C. Wu, W.-H. Lau, and H.-H. Chung, "Analytical technique for calculating the output harmonics of an H-bridge inverter with dead time," *IEEE Transactions on Circuits and Systems I: Fundamental Theory and Applications*, vol. 46, no. 5, pp. 617–627, May 1999.

[19] F. Koeslag, H. D. Mouton, and J. Beukes, "Analytical Modeling of the Effect of Nonlinear Switching Transition Curves on Harmonic Distortion in Class D Audio Amplifiers," *IEEE Transactions on Power Electronics*, vol. 28, no. 1, pp. 380–389, Jan. 2013.

[20] G. R. Ainslie-Malik, "Mathematical analysis of PWM processes," Ph.D. dissertation, University of Nottingham, Jul. 2013. [Online]. Available: http://eprints.nottingham.ac.uk/ 13021/1/Mathematical_Analysis_of_PWM_Processes.pdf

[21] D. C. Moore, M. Odavic, and S. M. Cox, "Dead-time effects on the voltage spectrum of a PWM inverter," *IMA Journal of Applied Mathematics*, vol. 79, no. 6, pp. 1061–1076, Dec. 2014. [Online]. Available: https://academic.oup.com/imamat/article/79/6/1061/845792/ Dead-time-effects-on-the-voltage-spectrum-of-a-PWM

[22] F. Chierchie, L. Stefanazzi, E. E. Paolini, and A. R. Oliva, "Frequency Analysis of PWM Inverters With Dead-Time for Arbitrary Modulating Signals," *IEEE Transactions on Power Electronics*, vol. 29, no. 6, pp. 2850–2860, Jun. 2014.

[23] G. W. Wester and R. D. Middlebrook, "Low-Frequency Characterization of Switched dc-dc Converters," *IEEE Transactions on Aerospace and Electronic Systems*, vol. AES-9, no. 3, pp. 376–385, May 1973.

[24] S. Cuk, "Modelling, analysis, and design of switching converters," Ph.D. dissertation, California Institute of Technology, 1977. [Online]. Available: http://resolver.caltech.edu/CaltechETD:etd-03262008-110336

[25] R. D. Middlebrook and S. Ćuk, "A general unified approach to modelling switching-converter power stages," *International Journal of Electronics*, vol. 42, no. 6, pp. 521–550, Jun. 1977. [Online]. Available: http://dx.doi.org/10.1080/00207217708900678

[26] R. W. Erickson and D. Maksimovic, *Fundamentals of Power Electronics*, 2nd ed. Springer US, 2001. [Online]. Available: //www.springer.com/de/book/9780792372707

[27] D. Maksimovic, A. M. Stankovic, V. J. Thottuvelil, and G. C. Verghese, "Modeling and simulation of power electronic converters," *Proceedings of the IEEE*, vol. 89, no. 6, pp. 898–912, Jun. 2001.

[28] Maksimovic, Zane, and Erickson, "Impact of digital control in power electronics," in *2004 Proceedings of the 16th International Symposium on Power Semiconductor Devices and ICs*, May 2004, pp. 13–22.

[29] D. Maksimovic and R. Zane, "Small-Signal Discrete-Time Modeling of Digitally Controlled PWM Converters," *IEEE Transactions on Power Electronics*, vol. 22, no. 6, pp. 2552–2556, Nov. 2007.

[30] S. Hiti, "Modeling and Control of Three-phase PWM Converters," Ph.D. dissertation, Virginia Tech, 1995.

[31] J. Sun, "Small-Signal Methods for AC Distributed Power Systems - A Review," *IEEE Transactions on Power Electronics*, vol. 24, no. 11, pp. 2545–2554, Nov. 2009.

[32] R. Teodorescu, M. Liserre, and P. Rodriguez, *Grid Converters for Photovoltaic and Wind Power Systems*. Wiley, 2011.

[33] W. Leonhard, *Control of Electrical Drives*, 3rd ed., ser. Power Systems. Berlin Heidelberg: Springer-Verlag, 2001. [Online]. Available: //www.springer.com/de/book/9783540418207

[34] L. Corradini, D. Maksimovic, P. Mattavelli, and R. Zane, *Digital Control of High-Frequency Switched-Mode Power Converters*.   Wiley-IEEE Press, Jul. 2015.

[35] R. R. Schoen and T. G. Habetler, "Effects of time-varying loads on rotor fault detection in induction machines," *IEEE Transactions on Industry Applications*, vol. 31, no. 4, pp. 900–906, Jul. 1995.

[36] M. Blodt, M. Chabert, J. Regnier, and J. Faucher, "Mechanical Load Fault Detection in Induction Motors by Stator Current Time-Frequency Analysis," *IEEE Transactions on Industry Applications*, vol. 42, no. 6, pp. 1454–1463, Nov. 2006.

[37] J. Song-Manguelle, G. Ekemb, D. L. Mon-Nzongo, J. Tao, and M. L. Doumbia, "A Theoretical Analysis of Pulsating Torque Components in AC Machines with Variable Frequency Drives and Dynamic Mechanical Loads," *IEEE Transactions on Industrial Electronics*, pp. 1–1, 2018.

[38] G. Chang, S.-K. Chen, H.-J. Su, and P.-K. Wang, "Accurate Assessment of Harmonic and Interharmonic Currents Generated by VSI-Fed Drives Under Unbalanced Supply Voltages," *IEEE Transactions on Power Delivery*, vol. 26, no. 2, pp. 1083–1091, Apr. 2011.

[39] J. Arrillaga, B. C. Smith, N. R. Watson, and A. R. Wood, *Power System Harmonic Analysis*.   Wiley & Sons Ltd, 1997.

[40] J. Ohm and H. D. Lüke, *Signalübertragung - Grundlagen der digitalen und analogen Nachrichtenübertragungssysteme*, 11th ed.   Berlin: Springer Vieweg, 2010.

[41] M. J. Roberts, *Signals and Systems: Analysis Using Transform Methods and MATLAB*, 2nd ed.   New York: McGraw-Hill Education, 2012.

[42] S. Buso and P. Mattavelli, *Digital Control in Power Electronics, 2nd Edition*.   Morgan & Claypool, May 2015.

[43] C. V. Garcia and J. Medel, "Matrix inverse operation convolution: Three Models description." in *WSEAS International Conference on signal processing, robotics and automation*, Cambridge, UK, Feb. 2009, pp. 246–253.

[44] R. Prost and R. Goutte, "Deconvolution when the convolution kernel has no inverse," *IEEE Transactions on Acoustics, Speech, and Signal Processing*, vol. 25, no. 6, pp. 542–549, Dec. 1977.

[45] Rüger, Niklas Erik, "Zur Anwendung eines bandseparierenden Modulationsverfahrens mit niedrigen Taktzahlen in der Leistungselektronik," Ph.D. dissertation, Leibniz Universität Hannover, 2012.

[46] H. W. v. d. Broeck, H. C. Skudelny, and G. V. Stanke, "Analysis and realization of a pulsewidth modulator based on voltage space vectors," *IEEE Transactions on Industry Applications*, vol. 24, no. 1, pp. 142–150, Jan. 1988.

[47] J. T. Boys and P. G. Handley, "Harmonic analysis of space vector modulated PWM waveforms," *IEE Proceedings B - Electric Power Applications*, vol. 137, no. 4, pp. 197–204, Jul. 1990.

[48] D. G. Holmes, "The general relationship between regular-sampled pulse-width-modulation and space vector modulation for hard switched converters," in *Conference Record of the 1992 IEEE Industry Applications Society Annual Meeting*, Oct. 1992, pp. 1002–1009 vol.1.

[49] S. R. Bowes and Y.-S. Lai, "The relationship between space-vector modulation and regular-sampled PWM," *IEEE Transactions on Industrial Electronics*, vol. 44, no. 5, pp. 670–679, Oct. 1997.

[50] A. M. Hava, R. J. Kerkman, and T. A. Lipo, "Carrier-based PWM-VSI overmodulation strategies: analysis, comparison, and design," *IEEE Transactions on Power Electronics*, vol. 13, no. 4, pp. 674–689, Jul. 1998.

[51] A. Kwasinski, P. T. Krein, and P. L. Chapman, "Time domain comparison of pulse-width modulation schemes," *IEEE Power Electronics Letters*, vol. 1, no. 3, pp. 64–68, Sep. 2003.

[52] T. Itkonen, J. Luukko, A. Sankala, T. Laakkonen, and R. Pöllänen, "Modeling and Analysis of the Dead-Time Effects in Parallel PWM Two-Level Three-Phase Voltage-Source Inverters," *IEEE Transactions on Power Electronics*, vol. 24, no. 11, pp. 2446–2455, Nov. 2009.

[53] F. Chierchie, E. E. Paolini, and L. Stefanazzi, "Dead-Time Distortion Shaping," *IEEE Transactions on Power Electronics*, pp. 1–1, 2018.

[54] J. M. Guerrero, M. Leetmaa, F. Briz, A. Zamarron, and R. D. Lorenz, "Inverter nonlinearity effects in high-frequency signal-injection-based sensorless control methods," *IEEE Transactions on Industry Applications*, vol. 41, no. 2, pp. 618–626, Mar. 2005.

[55] D. Wang, P. Zhang, Y. Jin, M. Wang, G. Liu, and M. Wang, "Influences on Output Distortion in Voltage Source Inverter Caused by Power Devices' Parasitic Capacitance," *IEEE Transactions on Power Electronics*, vol. 33, no. 5, pp. 4261–4273, May 2018.

[56] K. Wiedmann, "Positionsgeberloser Betrieb von permanentmagneterregten Synchronmaschinen," Ph.D. dissertation, Leibniz Universität Hannover, 2012.

[57] A. Guha and G. Narayanan, "Impact of dead-time on inverter input current, DC-link dy-

namics and light-load instability in rectifier-inverter-fed induction motor drives," *IEEE Transactions on Industry Applications*, vol. PP, no. 99, pp. 1–1, 2017.

[58] S.-G. Jeong and M.-H. Park, "The analysis and compensation of dead-time effects in PWM inverters," *IEEE Transactions on Industrial Electronics*, vol. 38, no. 2, pp. 108–114, Apr. 1991.

[59] A. Porst, "Power Semiconductor Devices," in *Silicon: Evolution and Future of a Technology*. Berlin Heidelberg: Springer-Verlag, 2004. [Online]. Available: //www. springer.com/de/book/9783540405467

[60] N. Mohan, T. M. Undeland, and W. P. Robbins, *Power Electronics: Converters, Applications, and Design*, 3rd ed. Wiley, Oct. 2002.

[61] D. Salt, D. Drury, and D. Holliday, "The nonlinear voltage distortion effect of an extended IGBT turn-off time in sinusoidal PWM VSI applications," in *2009 IEEE International Electric Machines and Drives Conference*, May 2009, pp. 1497–1502.

[62] A. R. Munoz and T. A. Lipo, "On-line dead-time compensation technique for open-loop PWM-VSI drives," *IEEE Transactions on Power Electronics*, vol. 14, no. 4, pp. 683–689, Jul. 1999.

[63] J.-W. Choi and S.-K. Sul, "Inverter output voltage synthesis using novel dead time compensation," *IEEE Transactions on Power Electronics*, vol. 11, no. 2, pp. 221–227, Mar. 1996.

[64] B. Weber, "Positionsgeberlose Regelung von permanentmagneterregten Synchronmaschinen bei kleinen Drehzahlen mit überabtastender Stromerfassung," Ph.D. dissertation, Leibniz Universität Hannover, 2018.

[65] K. Yamamoto, K. Shinohara, and H. Ohga, "Effect of parasitic capacitance of power device on output voltage deviation during switching dead-time in voltage-fed PWM inverter," in *Power Conversion Conference - Nagaoka 1997., Proceedings of the*, vol. 2, Aug. 1997, pp. 777–782 vol.2.

[66] N. Bedetti, S. Calligaro, and R. Petrella, "Self-Commissioning of Inverter Dead-Time Compensation by Multiple Linear Regression Based on a Physical Model," *IEEE Transactions on Industry Applications*, vol. 51, no. 5, pp. 3954–3964, Sep. 2015.

[67] S. Almér and U. Jönsson, "Harmonic analysis of pulse-width modulated systems," *Automatica*, vol. 45, no. 4, pp. 851–862, Apr. 2009. [Online]. Available: http: //www.sciencedirect.com/science/article/pii/S0005109808005396

[68] X. Yue, D. Boroyevich, F. C. Lee, F. Chen, R. Burgos, and F. Zhuo, "Beat Frequency

Oscillation Analysis for Power Electronic Converters in DC Nanogrid Based on Crossed Frequency Output Impedance Matrix Model," *IEEE Transactions on Power Electronics*, vol. 33, no. 4, pp. 3052–3064, Apr. 2018.

[69] P. M. Aziz, H. V. Sorensen, and J. v. d. Spiegel, "An overview of sigma-delta converters," *IEEE Signal Processing Magazine*, vol. 13, no. 1, pp. 61–84, Jan. 1996.

[70] S. J. Orfanidis, *Introduction to Signal Processing*. Prentice Hall, 2010. [Online]. Available: http://www.ece.rutgers.edu/~orfanidi/intro2sp

[71] J. C. Candy and G. C. Tmes, *Oversampling delta-sigma data converters: theory, design, and simulation*. Piscataway, New Jersey: IEEE Press, Wiley-Interscience, 1992.

[72] M. Oljaca and T. Hendrick, "Combining the ADS1202 with an FPGA Digital Filter for Current Measurement in Motor Control Applications," Texas Instruments, application report SBAA094, Jun. 2003.

[73] A. Testa, M. F. Akram, R. Burch, G. Carpinelli, G. Chang, V. Dinavahi, C. Hatziadoniu, W. M. Grady, E. Gunther, M. Halpin, P. Lehn, Y. Liu, R. Langella, M. Lowenstein, A. Medina, T. Ortmeyer, S. Ranade, P. Ribeiro, N. Watson, J. Wikston, and W. Xu, "Interharmonics: Theory and Modeling," *IEEE Transactions on Power Delivery*, vol. 22, no. 4, pp. 2335–2348, Oct. 2007.

[74] G. W. Chang and S.-K. Chen, "An analytical approach for characterizing harmonic and interharmonic currents generated by VSI-fed adjustable speed drives," *IEEE Transactions on Power Delivery*, vol. 20, no. 4, pp. 2585–2593, Oct. 2005.

[75] D. Basic, "Input Current Interharmonics of Variable-Speed Drives due to Motor Current Imbalance," *IEEE Transactions on Power Delivery*, vol. 25, no. 4, pp. 2797–2806, Oct. 2010.

[76] P. G. Cummings, "Power and Current Pulsations of an Induction Motor Connected to a Reciprocating Compressor," *IEEE Transactions on Industry Applications*, vol. IA-14, no. 3, pp. 213–219, May 1978.

[77] L. B. Farr and M. Fanslow, "Power factor control of synchronous motors powering large reciprocating compressors," in *Record of Conference Papers Industry Applications Society 52nd Annual Petroleum and Chemical Industry Conference*, Sep. 2005, pp. 321–325.

[78] W. E. Lockley, T. S. Driscoll, W. H. Wharran, and R. H. Paes, "Harmonic torque considerations of applying a 6000-HP induction motor and drive to a high-speed compressor," *IEEE Transactions on Industry Applications*, vol. 31, no. 6, pp. 1412–1418, Nov. 1995.

[79] G. Müller and B. Ponick, *Theorie elektrischer Maschinen.* Berlin: Wiley-VCH, Jan. 2009.

Curriculum Vitae

Name:	Malte John
Date of birth:	3 September 1988
Place of birth:	Emden, Germany

Work Experience:

02/2014 - 01/2019	Research associate Leibniz University Hannover Institute for Drive Systems and Power Electronics
12/2012 - 03/2013	Internship – Basic Design of HVDC Plus Siemens AG

Education:

Since 01/2014	Doctoral studies Leibniz University Hannover
10/2009 - 01/2014	Electrical Engineering – Diplom Leibniz University Hannover
06/2013 - 11/2013	Visiting Scholar Wisconsin Electric Machines and Power Electronics Consortium University of Wisconsin-Madison
10/2008 - 09/2009	Business Administration and Engineering Technische Universität Braunschweig